Melt Pool Geometry and Microstructure Control Across Alloys in Metal Based Additive Manufacturing Processes

Submitted in partial fulfillment of the requirements for the degree of

Doctor of Philosophy

in

Mechanical Engineering

Sneha Prabha Narra

B.E., Civil Engineering, Osmania University

M.S., Computational Mechanics, Carnegie Mellon University

M.S., Mechanical Engineering, Carnegie Mellon University

Carnegie Mellon University

Pittsburgh, PA

(May, 2017)

Dedication

To my parents, Sharada Devi and Prabhakar Reddy

Who are my inspiration and instilled the values of honesty and perseverance in me

Acknowledgements

First, I would like to thank my thesis adviser, Jack Beuth for giving me the opportunity to do research under his guidance. Without his advice, this thesis would not be complete. His encouraging words -- “If you are not naturally good at something, and if you put effort in it, you will do better than what you would have done if you were naturally good at it,” motivated me to do good work and develop interest in new areas of research. I am also grateful to the other members of my committee, Professor Anthony Rollett, Professor Maarten de Boer, Professor Burak Kara and Professor Fred Higgs, for their insightful comments and timely advice, which improved the quality of my work. The financial support for this research is provided by the National Science foundation under grant CMMI-1335298, and also in part by the Research for Additive Manufacturing in Pennsylvania (RAMP), prime award number FA8650-12-2-7230, subaward number 543105-78001.

I would like to acknowledge the support of Dr. Tom Nuhfer, Director of Microscopy in Materials Science Department for not just helping with microscopy, but also for asking me questions which encouraged me to think beyond my work. Without his support, the EBSD results presented in this work would not be possible. I would also like to thank Dr. Adam Wise and Dr. Betsy Clark for being available when I had questions about microscopy. I would also like to thank William Pingitore in the Undergrad Material Science Lab for his help with sample preparation. I would like to thank Professor Rollett for answering countless number of my questions and for his support. In addition, for allowing me to use their group’s auto-polisher, which saved lot of time. I would like to acknowledge Wayne Meyers from Arcam for sharing useful insights on operating the machine successfully which was crucial for the experiments performed as part of this work. I would like to acknowledge the support of machine shop crew: Jim Dillinger, John Fulmer and Ed

Wojciechowski for helping me with using machine shop equipment. I would like to thank Chris Hertz (for answering all administrative related questions), Bobby Kostyak (for taking care of orders) and other Mechanical Engineering department staff who took care of administrative details and made my PhD process smooth. I would also like to thank Maxine Reinhart Leffard (Civil and Environmental Engineering) and Melissa Brown (Mechanical Engineering) for making me feel at home when I first arrived to CMU, and more importantly, for their support and encouragement throughout my stay at CMU.

The best part of my Ph.D. experience was working with an amazing group of Ph.D. students in Professor Jack Beuth's group. I would like to thank Luke Scime and Brian Fisher for reviewing majority of my thesis and providing insightful comments. I would also like to thank them for being part of good research discussions. I would like to thank Zack Francis for contributing his finite element models which were used in this work and helping with etching the countless number of samples without any complaints. I would like to acknowledge Colt Montgomery for performing all the Inconel 718 experiments in the laser powder bed process which were crucial in completing this work and also for useful discussions related to research. I would also like to thank Dr. Joy Gockel and Dr. Jason Fox who were crucial in my first couple of years in the Ph.D. program when they were senior Ph.D. students in the group and for their continuing advice when I need even after their graduation. I am grateful to Prince Shaival Singh (Mechanical Engineering) and Shivram Kashyap (Material Science and Engineering) for teaching me the fundamentals of EBSD which helped me a lot in my self-learning process to interpret the EBSD results presented in this work. I am grateful to Recep Onler (Mechanical Engineering) for helping with using the Alicona InfiniteFocus Microscope. I would also like to acknowledge Ross Cunningham and Ming Tang in Material Science and Engineering who were part of the collaborative projects that I worked on.

I would like to thank the CMU Graduate Student Assembly leadership (2016-2017) for appointing me as the International Student Advocate and giving me the opportunity to represent international students. This was a great experience that helped me learn new things and above all I got to know and work with the best people. Specially, I would like to mention Nicole Rafidi who was a great pillar of support when I was in need of help. I would also like to acknowledge Mechanical Engineering Graduate Student Organization (MEGSO) 2016-2017 group for being a great group of people to work with and take my mind off research for some time.

I would like to thank my parents and specially my mom, Sharada Devi who was an inspiration for me to pursue great things in life without any reservations. Her hard work and countless number of sacrifices made it possible for me to earn the doctorate degree from the reputed university in the world. I am very grateful to my undergraduate adviser and mentor Professor Murali Krishna Namuduri for recognizing my capabilities and encouraging me to pursue a Ph.D. His constant support and encouragement were critical in this journey. I would like to thank my sister Chaitanya Narra and my best friend Saketha Pingali for their unwavering support over the years. I am grateful to my aunts Poojitha Reddy and Sridevi, who are my first friends, and also the biggest support all through my life. I would like to acknowledge my friends Akshay Gundla, Minkyung Kang, Luke Scime, Deepak Patil, Dr. Narayan Ramasubramanian aka 'Nada', Sudhandhu Nahata, Neil Patel, Akanksha Garg, Priya Manaswini Kambham, Vinod Vemuru, Narisi Pallerla, Sushma Thipparathy and many others whom I have met on this journey and who made my stay in USA, a great experience so far.

Lastly, I would like to thank Varun Kasireddy who was by my side at all times, both good and bad. Thank you for your unwavering support and belief in my capabilities. I cannot imagine completing this dissertation work without your love, support and great advice.

Abstract

There is growing interest in using additive manufacturing for various alloy systems and industrial applications. However, existing process development and part qualification techniques, both involve extensive experimentation-based procedures which are expensive and time-consuming. Recent developments in understanding the process control show promise toward the efforts to address these challenges. The current research uses the process mapping approach to achieve control of melt pool geometry and microstructure in different alloy systems, in addition to location specific control of microstructure in an additively manufactured part. Specifically, results demonstrate three levels of microstructure control, starting with the prior beta grain size control in Ti-6Al-4V, followed by cell (solidification structure) spacing control in AlSi10Mg, and ending with texture control in Inconel 718. Additionally, a prediction framework has been presented, that can be used to enable a preliminary understanding of melt pool geometry for different materials and process conditions with minimal experimentation. Overall, the work presented in this thesis has the potential to reduce the process development and part qualification time, enabling the wider adoption and use of additive manufacturing in industry.

Table of Contents

List of Tables

List of Figures

1 Introduction

1.1 Additive Manufacturing

Additive Manufacturing (AM), colloquially known as 3D printing, has recently become an area of intense research in both the aerospace industry as well as academia. For instance, General Electric (GE) invested ~$1.3B in two major metal AM manufacturers Arcam AB and Concept Laser in the year 2016 to advance their AM business and research [1]. As its name suggests, AM is a process by which a final part is constructed by adding material successively in a layer-by-layer fashion as shown in Figure 1-1. This is in contrast to traditional machining processes in which excess material is removed to produce the final part. The layer-wise nature of AM makes it extremely favorable for producing light-weight and complex geometries (e.g. hollow parts, cellular structures etc.), thus offering an unparalleled level of design freedom while also reducing material waste and weight of the part which reduces fuel consumption for aircrafts. This design flexibility makes AM particularly attractive to the aerospace industry since major airline companies prefer a lighter design, which also meets the safety and strength requirements, to save fuel. Apart from aerospace industry, AM also has applications in the biomedical, automobile and energy industries.

AM processes can be classified into various categories depending on the materials and process used for fabrication. A wide variety of materials ranging from plastics to composites to metal alloy systems can be used in AM systems. Metal AM can be further classified into nano particle jetting, binder jetting, powder bed fusion and direct energy deposition processes [2]. These processes are discussed in the following sections with a focus on the powder bed fusion processes studied in this thesis work.

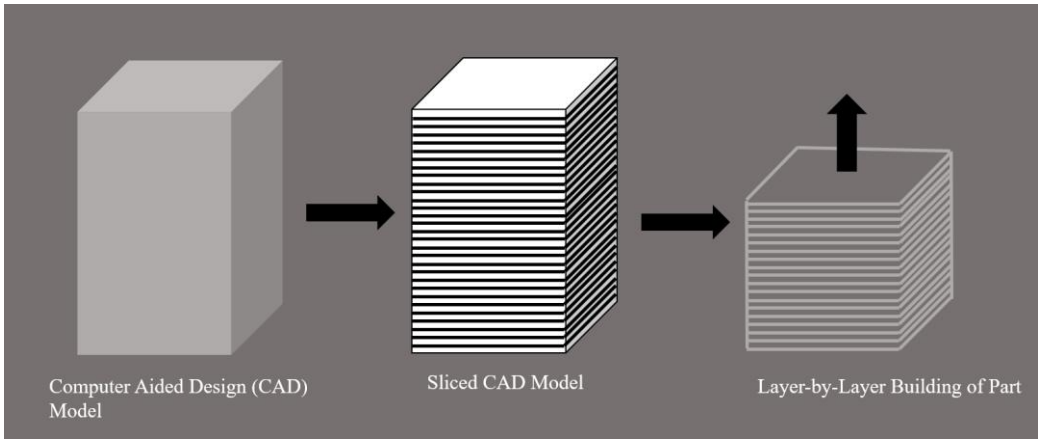

Figure 1-1: Layer-by-Layer building of the component in Additive Manufacturing.

1.1.1 NanoParticle Jetting™ Process

In the nanoparticle jetting™ process, first, droplets containing the nanoparticles are deposited onto the build-tray. Then, very high temperatures in the build envelope evaporate the liquid surrounding the nano-sized particles within a droplet and brings the particles together. This process repeats at every layer resulting in a final component. This can be used for fabricating components with fine features and better surface finish than the processes that use larger powder sizes such as power bed AM processes. XJET patented the technology and commercially manufactures the nanoparticle jetting machines [3].

1.1.2 Binder Jetting Process

In the binder jetting process, liquid binder droplets are selectively deposited onto a powder bed within the boundaries, described by the Computer aided design (CAD) model, to bind the powder particles together [4]. This process is repeated for every layer. At the end of the process, a green part is obtained which consists of powder particles which are held together by a binding agent. This green part is transferred to a curing oven to set the glue followed by a sintering or infiltration process. During the sintering process, binder material evaporates and the powder particles sinter together leaving the metal part behind. This results in shrinkage on the order of ~30% - 40%.

During the infiltration process, the bronze melts and gets wicked into the part. This has less shrinkage (on the order of 2%) when compared to sintering process. ExOne™ is the commercial manufacturer of the binder jetting machines to print components from metallic materials [5].

1.1.3 Direct Energy Deposition Process

In the direct energy deposition process, the heat source is typically a laser or electron beam. A travelling heat source is used to form a melt pool and feedstock material is fed into the melt pool. This is similar to welding processes. Feedstock material can be in the form of powder or wire. Typically, when laser beam is used as the heat source, feedstock material is powder. This powder is fed into the melt pool at every layer of the part during the deposition process. This process known as Laser Engineered Net Shaping (LENS) [6], was developed by Sandia National Labs and commercially manufactured by Optomec®. On the other hand, when the electron beam is the heat source, feedstock material is metal wire and this process is knows as Electron Beam Wire Feed process (EBF3) [7]. This was developed by the National Aeronautics and Space Administration (NASA) at Langley and commercially manufactured by Sciaky INC.

1.1.4 Powder Bed Fusion Processes

1.1.4.1 Powder Bed Electron Beam Melting Process

Arcam AB® is the only commercial manufacturer of electron beam melting (EBM) machines in the current market. Figure 1-2 shows the details of the Arcam S12 machine. In powder bed EBM, an electron beam is used to melt the powder layer. Before the build is started, a vacuum level on the order of 10^{-4} mbar is maintained in the build chamber. During the build, to allow for conductive environment and to avoid accumulation of electrons on the build surface, Helium is introduced into the build chamber, which will increase the pressure to $2x10^{-3}$ mbar. This results in a clean and

inert build environment minimizing the possibility of contamination of the fabricated component [8].

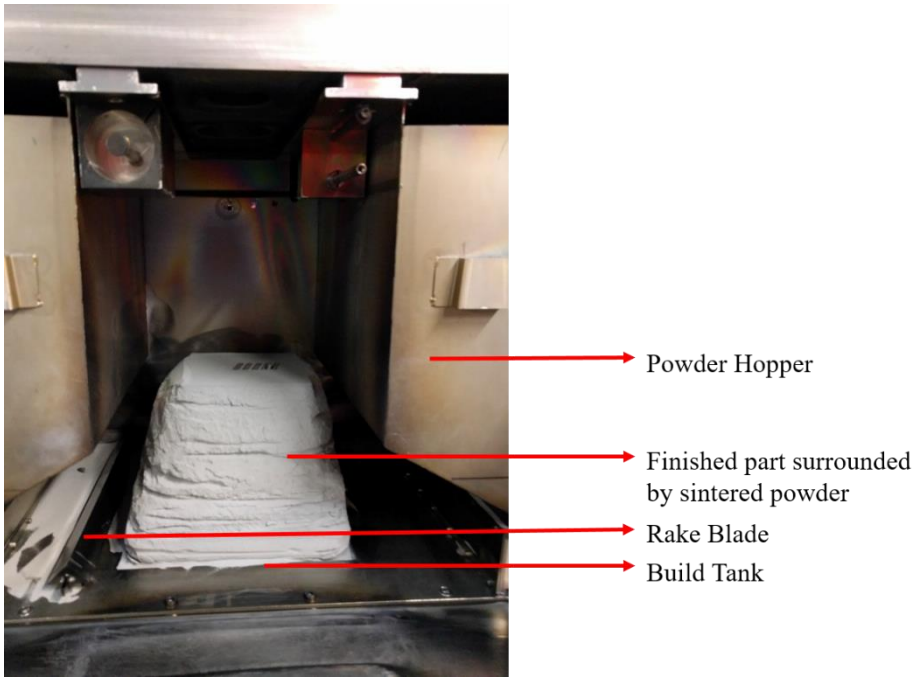

Figure 1-2: Interior of the Arcam S12 build chamber with various components identified.

The process starts with heating of a start plate to a specific temperature depending on the material that is used for fabrication. For instance, in Ti-6Al-4V builds, the start plate is heated to a temperature of 750 °C. Once the start plate reaches the specified temperature, the process starts with spreading a powder layer on to the start plate. The thickness of the powder layer can vary between 50 – 100 microns. The powder layer is then preheated using a high power, defocused (larger beam spot size), and high speed electron beam. The purpose of this step is to increase the conductivity of the powder and facilitate the flow of electrons from the top surface of the plate to electrical ground. This will prevent accumulation of the electrons on the top surface and their interaction with the incoming electron beam which will result in repulsion and thus flying off the powder in the build chamber resulting in "smoke" [9]. After the preheating step is complete, a focused electron beam with lower power and velocity melts the powder layer as per the CAD

model. Once, the melting process is complete, the build tank carrying the build plate moves down by a distance which is equal to the layer thickness and a new layer of powder is spread on to the build plate. This process is repeated for successive layers until the part fabrication is complete. At the end of the process, the built part is surrounded by a block of powder as shown in Figure 1-3. This block is then transferred to a powder recovery system (PRS), where a stream of high velocity Ti64 powder particles are used to break the solid powder block into powder particles which are collected at the end of the process. This recovered powder is sieved and used again for the next build.

Figure 1-3: Finished part surrounded by preheated powder being cleaned in the Powder Recovery System (PRS).

Some of the advantages of the EBM process are:

1. Background temperatures are high in the EBM process which results in nearly residual stress-free parts. For the same reason, parts built by this process do not need support structures to prevent warping due to residual stresses. However, heat transfer supports, as shown in Figure 1-4, are added to the part to enhance the transfer of heat from the melted region to the bottom of the part to prevent any excess heat buildup resulting in poor part quality. An example of a

poor surface finish is shown in Figure 1-4, which resulted from inadequate heat transfer supports.

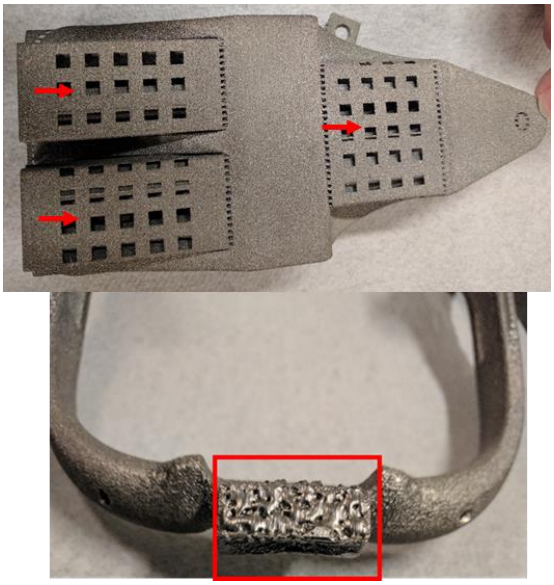

Figure 1-4: Part consisting of heat transfer supports (top) and poor surface finish resulting from excess heat accumulation.

2. This process can be used to build fine mesh/cellular structures [10] without adding any support structures since support is provided by the preheated powder as shown in Figure 1-5.

Figure 1-5: Mesh/cellular structures supported by preheated powder bed.

3. Higher build temperatures result in a martensitic structure-free part except for the top region, which does not experience enough number of heat cycles and still contains martensitic structure [11].
4. Deposition rates are higher when compared to laser beam melting processes due to the ability to control the electron beam motion accurately and instantaneously via electromagnetic field.
5. The maximum power delivered by an electron beam melting machine is higher when compared to the laser beam processes which will also result in higher deposition rates due to the ability to melt larger area and melt through thicker powder layers.
6. There are no losses due to reflection in electron beam. Efficiency of the electron beam is reported to be ~95% which is higher than a laser beam efficiency [12].

The EBM process also has some limitations as listed below:

1. Evaporation of components in the alloy material with lower vapor pressures since process environment is vacuum. This will affect the composition of the alloy and resulting microstructure. For instance, evaporation of aluminum is a prevalent problem during the deposition of Ti64 in EBM process [13].
2. Currently, there are only three alloy systems that can be used for building parts in the Arcam machine [14]. Process development for other alloy systems is still a work in progress [9].
3. Due to the "smoking" problem, there is a lower-limit on the size of powders that can be used in the EBM process. This imposes limits on the minimum layer thickness can be used for building parts. Layers less than 50 microns are not used, which in turn constrains the ability to deposit using lower deposition energy. Thus, parts produced from an EBM machine have rougher surface when compared to the parts produced on the laser melting machine. This is illustrated in Figure 1-6.

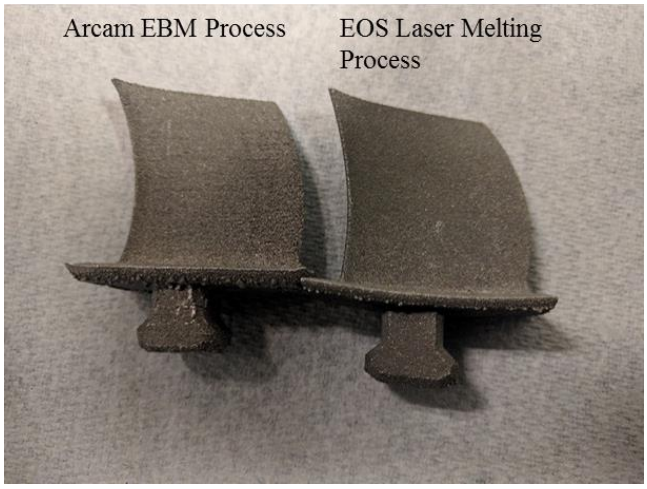

Figure 1-6: Generic GE compressor blades manufactured by electron (left) and laser (right) powder bed processes.

4. There is a limit on the minimum feature size that can be built in the EBM process. Smaller feature sizes and enclosed spaces are not ideal for complete powder removal during the powder recovery process [15]. In addition, layer size and melt pool size also controls the minimum feature size that can be deposited successfully.

1.1.4.2 Powder Bed Laser Beam Melting Process

There are multiple machine manufacturers in the current market that produce laser powder bed fusion (LPBF) machines. EOS's laser melting machine is used for experiments in this work. Hence, details pertaining to this process are discussed here. In LPBF processes, a laser beam is used to melt the powder layer. The process starts with purging the build chamber with inert gases such as nitrogen and argon depending on the material that is used for building the parts. Nitrogen is used for Steels and for other materials like Ti64, nickel superalloys and aluminum alloys, argon is used to maintain inert atmosphere. After the purging step, the build plate is heated to temperatures up to 200 °C depending on the material that is used for fabrication. This step is an attempt to reduce the residual stresses during the build process. In the next step, powder is spread on the build plate using a recoater blade shown in Figure 1-7. The layer thickness ranges from 20-

60 microns. Then, a laser beam melts the powder layer in the pattern specified by the CAD model. Typically, after a layer is melted, the build tank moves down and a new layer of powder is spread on the build plate which is then melted using a laser beam. These steps repeat until the part is complete. Figure 1-7 shows the details of the EOS's laser powder bed machine. At the end of the process, powder is removed from the build plate using a brush and parts are cleaned of any powder remnants.

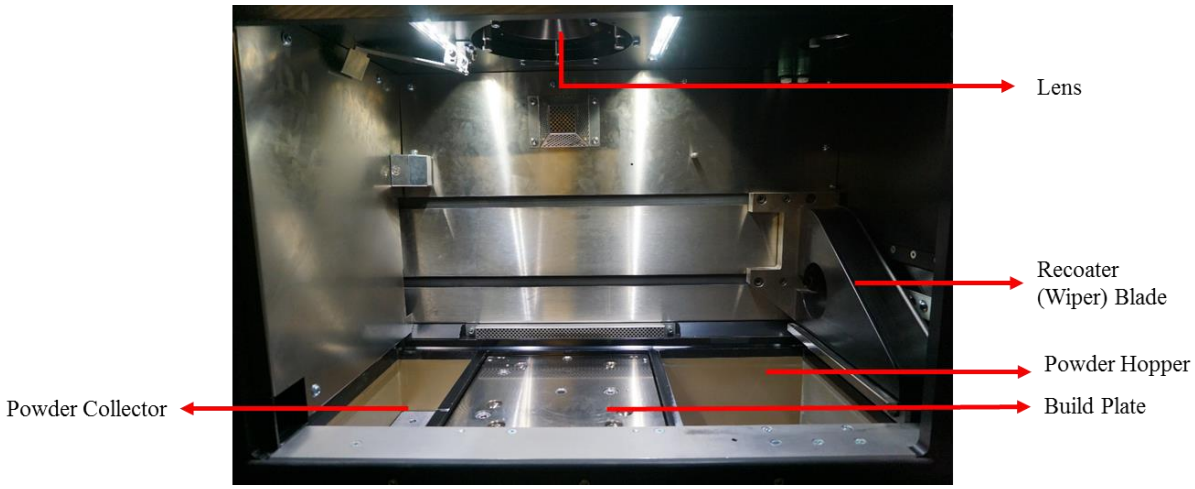

Figure 1-7: Interior of the EOS M290 machine with various components identified.

Some of the advantages of LPBF process are:

1. It can build with wide range of materials including titanium, aluminum, steel, and nickel alloys among many other materials [16].
2. Due to the ability to use smaller powders, smaller layer thicknesses are possible and hence can deposit dense parts using lower energy density. This will result in parts with a smoother surface finish when compared to the EBM process as shown in Figure 1-6.
3. Minimum feature size that can be built using laser melting machine is lower when compared to the EBM process for two reasons. One is the ability to deposit dense parts at

lower energy densities when compared to EBM process and the second reason is the ability to remove the powder from tiny openings by simply shaking the part.

4. Evaporation of materials is not prevalent when compared to EBM process because the build chamber is maintained at a pressure which is on the order of atmospheric pressure.

Some of the limitations of the LPBF process are:

1. Enclosed spaces without openings are not ideal for this process since loose powder has to be removed from the fabricated component.
2. Efficiency of the laser beam is around 10 – 60 % due to major losses from reflection [17].
3. Bulky support structures are required in the laser melting processes to prevent part deformation due to warping as illustrated in Figure 1-8, which results in wastage of material for support structures.

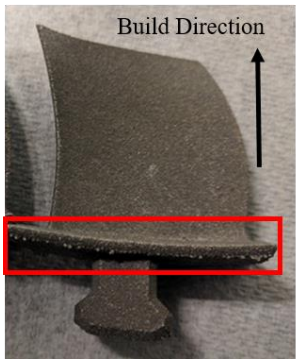

Figure 1-8: Component with warping.

4. Unlike the EBM process, in laser process, powder particles are not held together by applying heat. Hence, it is not possible to build overhangs and larger meshes successfully without adding support structures.
5. The mirrors, which are mechanically operated, control beam motion. Thus, there is lag in beam scanning, when the scanning velocity changes and increases. Further, this imposes a

limitation on the maximum scanning velocity that can be used which affects the deposition speed.

6. Fabricated parts contain martensitic structure in materials like Ti64, since process takes place at lower temperatures when compared to EBM [18].

1.2 Applications of Direct Metal Additive Manufacturing

AM's ability to: (i) create parts with reduced material waste, (ii) build composite parts [19], (iii) create parts with increased efficiency and (iv) build parts with intricate design features, sets it apart from conventional manufacturing techniques such as forging, casting and machining. AM is also proven to be an efficient method to repair damaged parts [20], especially in the aerospace industry, where the parts are complex and require long delivery times [21]. Due to these unique advantages, AM has the potential to revolutionize the biomedical, aerospace, automobile and other industries [22,23].

Figure 1-9 shows an example of a GE bracket - which is redesigned for reduction in weight with no compromise in strength when compared to the forged bracket [24]. These are manufactured using Ti-6Al-4V in electron beam melting process. This modified design results in 85% reduction in weight which in turn will decrease fuel consumption resulting in an increase in profit [25].

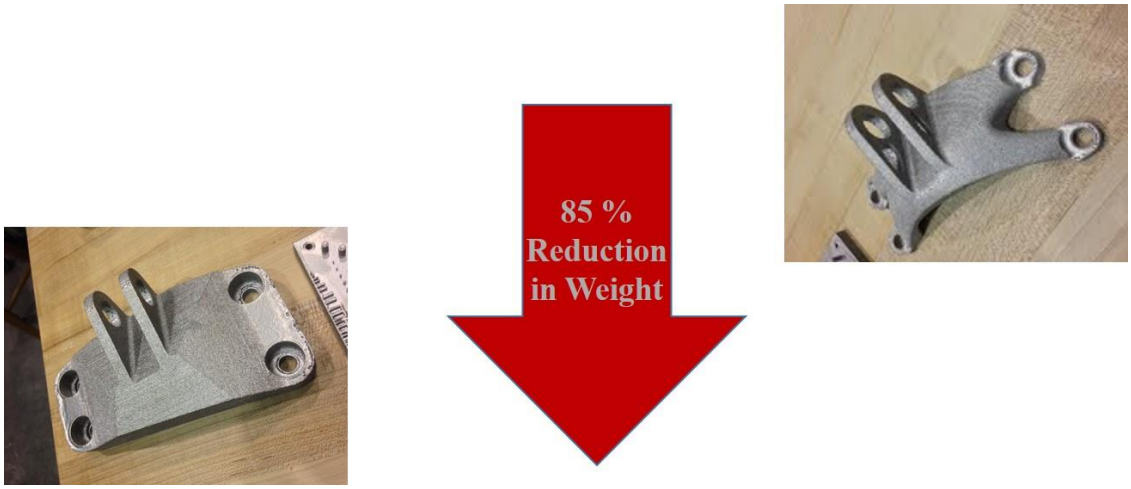

Figure 1-9: Traditional (left) and redesigned (right) brackets manufactured on Arcam EBM machine using Ti64 powder.

Various materials, which are difficult to machine, and hence are not suitable for traditional subtractive manufacturing processes, like Ti-6Al-4V, can now be used for building components with complex geometries due to the layer-by-layer deposition of AM using high input energy density. These high energy densities will also allow for using materials with higher melting points for building components.

Figure 1-10 shows the mesh structures which can be manufactured using AM processes without the need to machine the extra material. These mesh structures have wide variety of applications such as improving the thermal efficiency in heat exchange media, for lightweight structures, in biocompatible inserts to promote cell growth, mechanical damping and many more [26]. For biomedical industry, major application of metal AM is in patient specific implants which will allow for easier placement of implants in the patient's body and for tailoring the mechanical properties of the implant to match with that of the bone. The surface of the metal implants can be controlled to improve the bone ingrowth selectively based on the purpose of the implant [27]. The mesh structures that are possible to manufacture through metal AM as shown in Figure 1-11 allows for bone ingrowth into the metal implant.

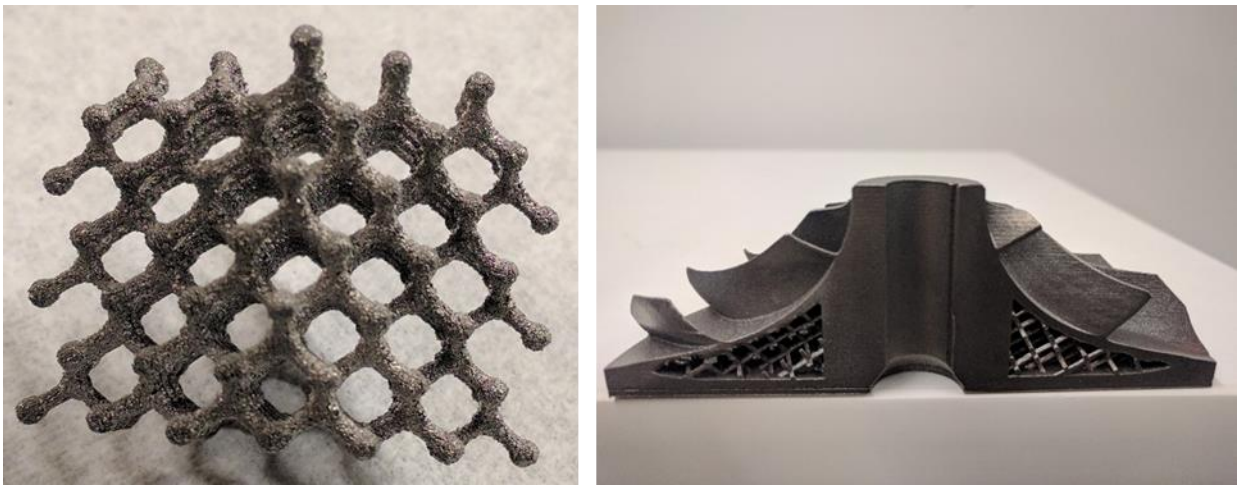

Figure 1-10: Components with cellular/mesh structures fabricated using AM.

Figure 1-11: Figure demonstrating the applications of AM in medical implant industry.

1.3 Motivation

With the rapid increase in the use of AM in the industry, more materials, many of which are otherwise not feasible to be manufactured or processed, have started to appear in the catalogue of materials qualified for use in various AM equipment. There has also been great progress in using in-situ monitoring technologies to collect build-related information that can be used in process control and qualification. Typically, this information is thermal and image based which does not provide details related to the microstructure and resulting part properties. Hence there is a

significant need to integrate melt pool geometry and microstructure control to improve process outcomes and also for part qualification with reduced experimentation and testing [28]. Existing work on process outcomes control is generally alloy and process specific, as well as heavily dependent on experimentation which is time consuming and also not an economic proposition. These tedious procedures must be repeated for each alloy system and process. In order to create process control strategies efficiently, there is a need for a generalized approach for process parameter development that can be used to generate a preliminary knowledge base for any new material or process.

The major issues that are unaddressed so far are:

1. Being able to develop process themes (process variable sets) for a new alloy system with minimal experimentation and utilizing the process knowledge base of the existing alloy systems. Development of process parameters for a new material system and for new process conditions, is associated with large number of experiments and simulations, which is time consuming and expensive. The current standard portfolio of materials used in Arcam machines include Ti-6Al-4V, Ti-6Al- 4V ELI, Titanium Grade 2, and Cobalt-Chrome [14]. Laser melting processes support multiple materials such as maraging steels, stainless steels, IN718, IN625, cobalt chrome, Ti-6AL-4V, Ti-6Al-4V ELI and AlSi10Mg [16]. With the projected increase in the use of AM in industry, new materials will be developed further for use in AM equipment and it is important to have a framework that can be used to transfer process knowledge from known materials to new material systems.
2. At this point, it is well known that AM allows design flexibility and offers geometric freedom. However, fabrication of components with performance flexibility is still not a reality. In other words, fabrication of components with location specific properties, depending on the loading

they experience, is not yet available. Also, a relationship between process variables and resulting microstructure will advance the process development, optimization and qualification methods. To be able to build parts to meet stipulated performance requirements:

a. It is essential to understand the solidification microstructure that forms during the build to reduce the time spent in analysis procedures and how microstructure varies with the process variables. Additionally, these processes have very high solidification rates which is an area not explored in detail in the past.
b. It is also critical to know the transition between microstructures resulting from different process settings in a single component.

1.4 Contributions

This work is aimed toward adding more process related knowledge to the existing AM knowledge base and demonstrating the capabilities of the AM processes which were not investigated in the past. The main contributions of this thesis are:

1. With the advancement of AM processes, not just new materials, but also different process conditions for existing material systems will be of interest. This process development involves extensive experimentation and computation. To address this issue, a non-dimensional framework is presented to predict the melt pool characteristics for a wide range of material and process parameters. This aids in minimizing the number of experiments and simulations that need to be performed for process parameter development.
2. Along with predicting melt pool geometry, solidification microstructure is also predicted for three different alloy systems in two different powder bed metal AM processes. Specifically, prior beta grain size control in electron beam melted Ti64, cell spacing control in laser melted AlSi10Mg and texture control in laser melted IN718 are studied in this work. Fundamental

ideas of integrated melt pool geometry and microstructure control are explored and extended to multiple alloy systems in this thesis work. This work is useful in:

   a. Correlating microstructure to melt pool geometry which can be observed using in-situ monitoring techniques. This will provide an estimate of the properties to be expected without seeking any intensive post processing characterization and testing.
   b. Extending the process space to optimize the properties of interest such as creep strength, surface finish, hardness, deposition rate and many more.

3. To fabricate components with location-specific properties, it is critical to understand both the control of microstructure and also the transitions in microstructure with respect to changes in process parameters. Work done in this thesis demonstrates these concepts through an example study on transition in prior beta grain sizes when implementing location-specific microstructure control in electron beam melted Ti64.

1.5 Thesis Outline

This thesis is divided into 8 chapters. Chapter 1 provides background on additive manufacturing with a focus on powder bed AM processes followed by relevant review of materials and existing state of knowledge in Chapter 2. This provides background for the research carried out as part of this thesis.

Chapters 3, 4, 5 & 6 discusses the three aspects of microstructure control ranging from grain size control in Ti64 (Chapter 3), transition in grain size for location specific control of microstructure (Chapter 4), cell spacing (solidification structure) control in AlSi10Mg (Chapter 5) and texture control in IN718 (Chapter 6). The common theme of integrated melt pool geometry and microstructure control is demonstrated in all the 3 alloy systems.

After demonstrating that melt pool geometry control is not just important for controlling the part precision and porosity, but it is also important to understand the resulting microstructure, focus is shifted in Chapter 7 to developing a framework for predicting melt pool characteristics for different materials and process conditions. This will allow AM users to obtain preliminary values for melt pool geometry with minimal to no experimentation and simulation work.

Finally, in Chapter 8, implications of the research performed as part of this thesis are explained by presenting major conclusions. The scope of future work is also outlined in this chapter.

Polishing procedures and additional measurements from experiments and are provided in the Appendix.

2 Background

This chapter provides background related to the solidification theory and materials studied in this work. In addition, relevant review of the existing knowledge on process control is provided, which summarizes the state of existing knowledge on this topic.

2.1 Solidification Theory

Molten material solidifies through grain nucleation and growth. There are two types of nucleation: homogeneous and heterogeneous. In homogeneous nucleation, once the temperature drops below the freezing temperature, nucleation can occur randomly throughout the liquid, whereas in heterogeneous nucleation, nucleation occurs on the surface of a foreign object such as impurities in the liquid or other solid interface which is in contact with the liquid. It requires high amount of undercooling in order to achieve homogeneous nucleation [29]. In welding processes, nucleation is reported at very low undercooling on the order of 1-2 K, when compared to $\geq$ 200 K for homogeneous nucleation [30]. Hence, based on the observations from welding processes, it is expected that heterogeneous nucleation is prevalent during solidification in AM processes.

The crystal structure is formed by the growth of nuclei into grains. Depending on the morphology of the growing structure, which changes with the conditions at the solid-liquid interface, growth can be classified into different types: planar, cellular or dendritic solidification as shown in Figure 2-1. With increase in solidification rate, the instability in the solidification front increases and it is no more planar. In castings, dendritic solidification is prevalent [31]. AM has higher cooling rates than castings and planar solidification is only observed over a small region as a thin layer at the bottom of the melt pool [32]. The reason for this can be the lower solidification rate and higher thermal gradient at the bottom of the melt pool. Similarly, grain morphology is

also affected by the thermal gradient and solidification rate which is first presented by Hunt [33]. In Chapter 6, the change in grain growth direction with changing solidification conditions is discussed for laser melted Inconel 718.

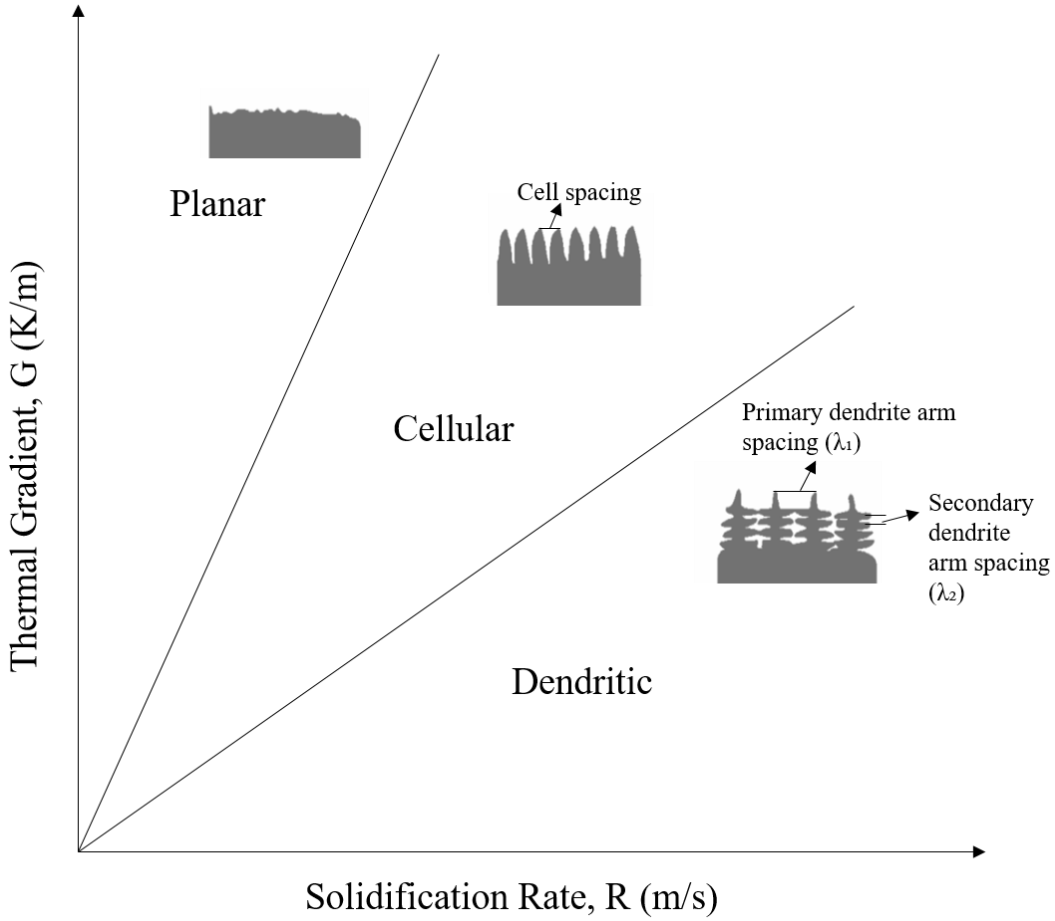

Figure 2-1: Qualitative presentation of the nature of solidification front with change in solidification conditions[30]**.**

In dendritic solidification, a tree-like structure forms during the solidification process. The distance between the primary trunks is known as primary dendrite arm spacing and the distance between the adjacent branches that grow out the primary trunk are known as secondary dendrites. The spacing between these is known as secondary dendrite arm spacing. A grain consists of one or many dendrites growing along the same crystallographic direction. Dendrites that have different orientation are separated by grain boundaries. Secondary dendrite arm spacing (λ_2) is critical for

mechanical properties of the material such as ultimate strength, ductility, elongation and homogenization times [31]. During columnar dendritic solidification, primary dendrite arm spacing (λ_1) secondary dendrite arm spacing are determined whereas for equiaxed grains, grain size and secondary dendrite arm spacing are measured [29]. In dendritic solidification, primary dendrite arm spacing in columnar growth and cellular dendritic growth are estimated using Equations 2.1 and 2.2. Secondary dendrite arm spacing is known from Equation 2.3**.** In these equations, c, k and m are constants, V is the solidification rate and G is the thermal gradient.

$$\lambda_1 = cV^{-1/4}G^{-1/2} \tag{2.1}$$

$$cell\ spacing = kV^{-1/3}G^{-1/3} \tag{2.2}$$

$$\lambda_2 = mV^{-1/3}G^{-1/3} \tag{2.3}$$

In general, with increase in cooling rate (G.V), cell spacing and dendrite spacing decreases. For more details on the derivation of these equations, refer to [29] or other standard solidification text books/literature. These are the primary solidification features which can be altered by indirectly controlling the thermal gradient and solidification rate by modifying the process parameters. These also provide information about the thermal conditions during solidification since resulting microstructure does not change much post solidification process [29].

AM has the unique ability to tailor the microstructural features of an as-built part by adjusting the process settings before the start of the build or during the build. Hence it is important to quantify the effect of primary process variables on the primary solidification microstructure. These results can also be for validating solidification models that can be used for predicting the microstructure and properties. The information on microstructure length scales and morphology are used in the mechanical property models that are used for design optimization [34].

2.2 Materials

2.2.1.1 Titanium Alloy Ti-6Al-4V (Ti64)

Titanium alloy Ti-6Al-4V (Ti64) is two phase (α + β) alloy which is used extensively in aerospace, biomedical and automotive industries [35]. As the material solidifies, it initially forms a BCC (body centered cubic) β-phase which upon reaching the beta transus temperature transforms to HCP (hexagonal close packed) α phase. The temperature at which the transformation occurs depends on the composition of the alloy. Aluminum is the α stabilizer and Vanadium is the β stabilizer. This means that as the concentration of Vanadium increases, the temperature at which β transforms to α decreases and vice versa. The different stages of this transformation is illustrated in Figure 2-2.

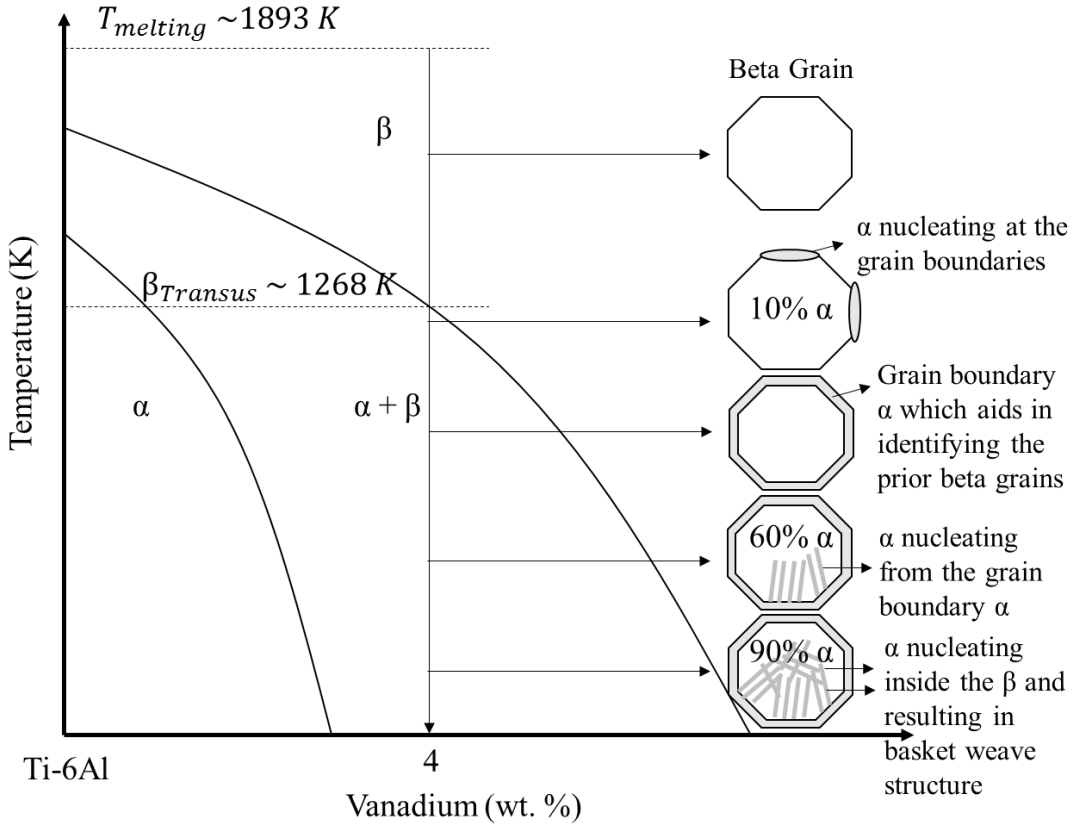

Figure 2-2: Transformations in Ti64 as the material solidifies [30,35]**.**

First, α nucleates at the grain boundaries and grows along the grain boundaries. This is known as grain boundary α (α_{gb}). This is continuous along the beta grain boundary and while analyzing the prior beta grain sizes in this work it aided in identifying the grain boundaries. An illustration of this is shown in Figure 2-3 which is similar to the cast microstructure of Ti64 except for the epitaxial columnar growth which depends on the solidification conditions. As the cooling continues, α starts nucleating from the grain boundaries and the growth continues inside the grain resulting in a network of α which is known as primary α, also identified in Figure 2-3. Depending on the arrangement of the α, the primary α can be categorized into colony α or basket weave (widmanstätten) α. The description provided above is for diffusion based transformations which results in a structure that is found in electron beam melted Ti64 deposits studied in this work. However, depending on the solidification conditions, different types of transformations are possible such as martensitic (α') and massive (α_m) structures [30].

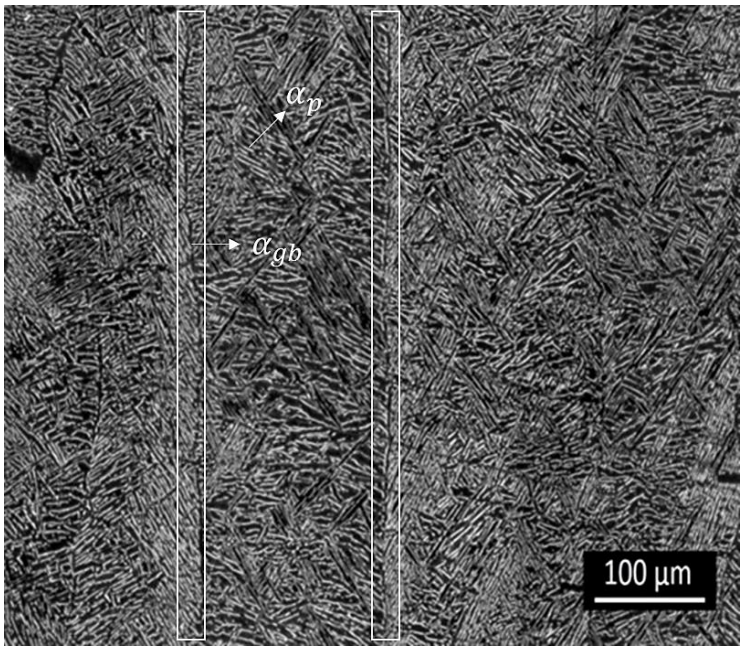

Figure 2-3: Optical micrograph of electron beam melted Ti64 with grain boundary and primary alpha identified[36]**.**

2.2.1.2 Aluminum Alloy AlSi10Mg

AlSi10Mg is extensively used in casting thin wall components and complex geometries. This is a hypo-eutectic alloy that consists of 10% Si, 0.35% Mg, 0.16% Fe, 0.01% Ti) [37]. The high fluidity, low shrinkage, smaller solidification interval (~40K) when compared to other Aluminum alloys reduces the susceptibility of AlSi10Mg to hot cracking or hot tearing. Therefore, AlSi10Mg is favorable for casting. For the same reasons, AlSi10Mg is also the major alloy of interest for laser melting processes [38]. This material is used in aerospace and automobile industries among others [39].

The equilibrium phase diagram for AlSi10Mg is shown in Figure 2-4. During the solidification the α-Al nucleates first and continues to grow (Figure 2-5- left) and during this process the concentration of silicon increases in the liquid and at some point β phase nucleates. The α phase continues to grow in between the β phase resulting in the eutectic α+β matrix identified in Figure 2-5 (left) [29]. However, as shown in Figure 2-5 (right), the structure of rapidly solidified AlSi10Mg is different from its cast counterpart. In laser melted AlSi1Mg, silicon is segregated at the aluminum cell boundaries. This fine structure in AlSi10Mg is due to the high cooling rates in laser melting process [40,41].

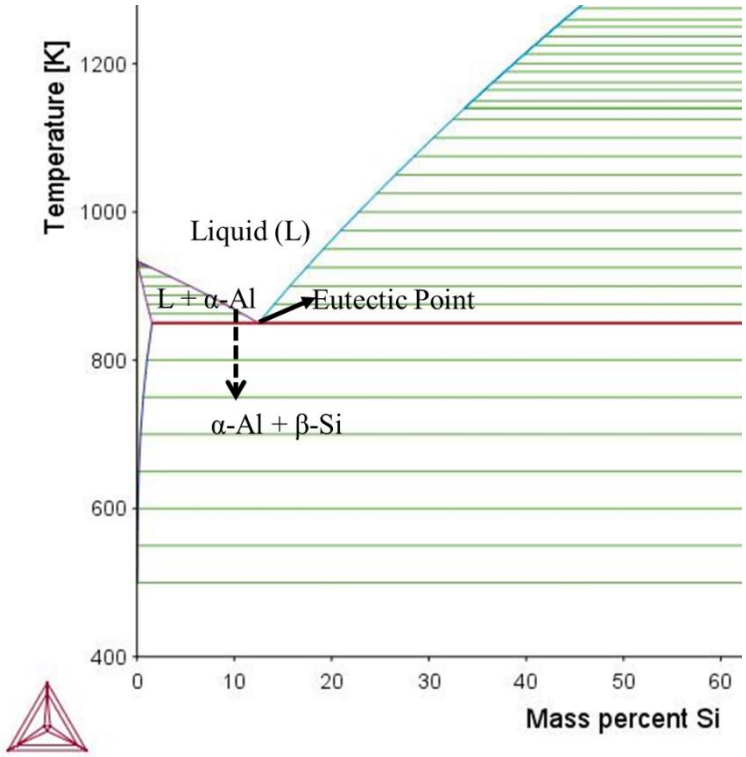

Figure 2-4: Equilibrium binary phase diagram for AlSi10Mg.

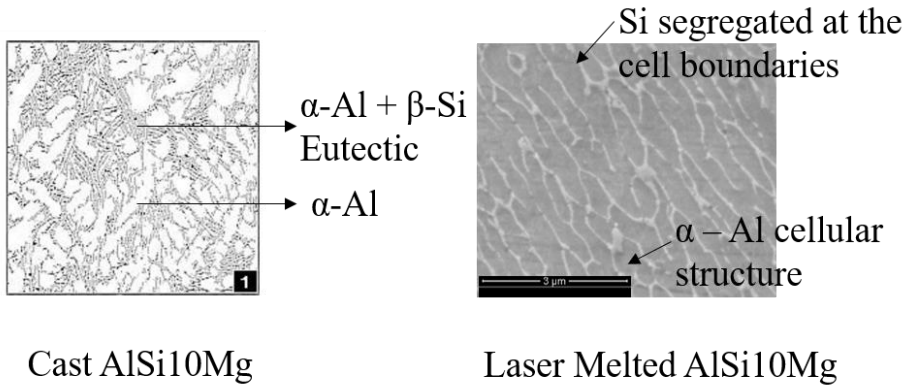

Figure 2-5: Comparison of as-cast taken at 50 X magnification (left) and laser melted (right) AlSi10Mg microstructure [39,42,43]**.**

2.2.1.3 Nickel Super Alloy Inconel 718 (IN718)

Inconel 718 is high-temperature, high-strength alloy that can be used in structural applications. Typical composition of IN718 is: 53.44 % Ni, 18.92% Cr, 5.10% Nb+Ta, 2.99% Mo, 0.93% Ti, 0.46% Al, 0.03% C, and 18.13% Fe. It is not easy to fabricate complex parts using this alloy due to the difficulty to machine this material [44]. However, using additive manufacturing, it is

possible to fabricate intricate geometries using IN718 such as heat exchangers [45]. The main phases present in wrought and cast IN718 are [46–50]:

(i) ϒ with composition Ni-Cr-Fe

(ii) ϒ′ with composition Ni_3 (Al, Ti) - intermetallic precipitate

(iii) ϒ″ with composition Ni_3Nb – intermetallic precipitate

(iv) δ with composition Ni_3Nb –intermetallic precipitate

(v) laves phase with composition $(Ni, Fe, Cr)_2$ (Nb, Mo, Ti) – brittle intermetallic phase

(vi) carbide precipitates with composition NbC and $M_{23}C_6$

ϒ′, ϒ″ and δ are the strengthening phases, the formation of which is governed by the heat treatment methods and the size of the ϒ′ and ϒ″ precipitates is on the order of *nm* [51,52]. On the other hand Laves phase is not preferred due to its undesirable impact on various mechanical properties of the material [47]. Similarly, carbide precipitates which form during ageing are reported to reduce the notch ductility of the IN718 and affect the fracture mode [48]. It is important to note that the precipitation of different phases discussed here depend on the processing conditions and using a time-temperature-transformation (TTT) diagram [53]. Due to the presence of strengthening precipitate phases and alloying element Cr and Mo, IN718 can sustain high temperature environments and is corrosion resistant. Therefore, these properties make IN718 suitable for applications in oil, natural gas, aerospace, nuclear and other industries [49,50,53,54]

Figure 2-6 shows the difference between typical IN718 microstructure and as-deposited laser melted IN718 microstructure. Fine dendritic and cellular solidification substructure due to high cooling rates is observed in the laser deposited material and the bright regions are rich in Nb and Mb and this is reported as δ phase. In the interdendritic regions, laves phase and carbides are observed. The presence of ϒ′ and ϒ″ was also reported. [49,50,55–59].

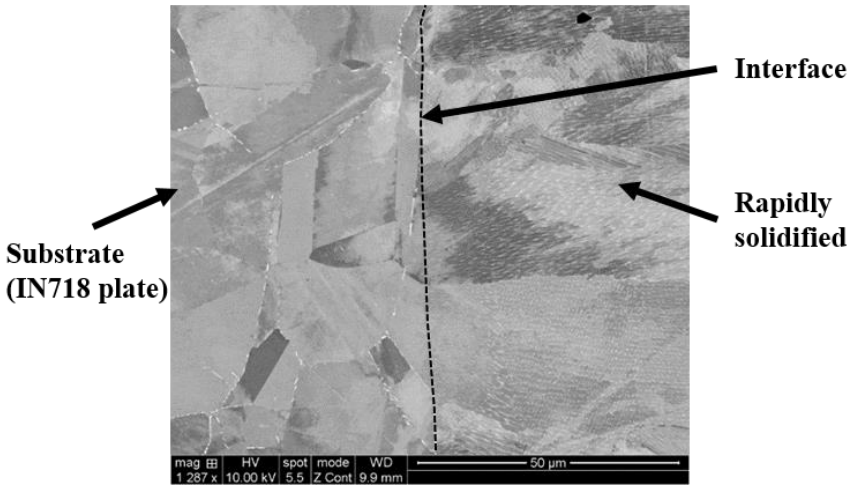

Figure 2-6: Example micrograph showing the contrast between typical IN718 and laser melted IN718 microstructure.

2.3 Relevant Literature Review from Additive Manufacturing

The current research covers various aspects of process control in additive manufacturing such as melt pool geometry and microstructure for multiple alloys. With respect to melt pool geometry, goal is to predict geometry with minimal experimentation. On the other hand, for microstructure, the focus is on enabling location-specific control and predicting microstructure from process parameters. Several researchers contributed to the existing body of knowledge on these topics. This section reviews relevant literature and identifies gaps in the current knowledge from the perspective of melt pool geometry and microstructure control.

Temperate distribution during the melting process provides information about melt pool geometry. One of the early works on welding processes, Rosenthal [60] presented an analytical solution for temperature distribution in the case of a moving point heat source. The primary inputs for this model are: (i) power delivered by the beam, (ii) travel velocity, (iii) thermophysical properties of the material, and (iv) background temperature. Based off of Rosenthal's analytical solution, Christensen et.al [61] developed dimensionless graphs for predicting melt cross-sections over a range of welding conditions and material properties. This can be treated as a generalized

version of Rosenthal's analytical solution in an effort to test its applicability over a range of welding conditions and materials. However, Rosenthal's analytical solution does not take into account of the change in the thermo-physical properties of the material with temperature, latent heat and the assumed point source does not take into account the beam distribution effects. Tsai et.al [62] developed a modified version of Rosenthal's analytical solution with an additional distribution parameter to include the distribution effects of the heat source on the temperature field. These analytical models often need to be used carefully with appropriate modifications to include the effect of temperature dependent properties [28,63]. Nevertheless, researchers in AM field have used these simple analytical models to estimate melt pool dimensions [64,65]. On the other hand, many researchers have worked on numerical modeling of the AM processes. These models range from simple and less expensive finite element models to estimate the melt pool characteristics [28,66–72] to sophisticated and expensive models that demonstrate particle level interactions which are important to study defects generated during the process that are associated with fluid flow inside the melt pool and particle-fluid interaction [73–75]. However, these models must be run and verified with experiments for different process conditions and materials each time there is a change in either the material or the process parameter. This is not an efficient proposition when different materials and processing conditions are being explored. Therefore, further work needs to be done to predict the melt pool geometry characteristics with minimum assumptions and experimentation.

Microstructure generally affects the mechanical properties of a part. AM microstructure is different from microstructures formed in cast, rolled and other traditional manufacturing methods. This is due to the rapid solidification and resulting higher cooling rates. This difference in microstructure results in a difference in properties of the part [76]. Therefore, there has been great

interest in studying the AM microstructure and resulting mechanical properties [77–81]. These studies range from understanding the evolution of microstructure to changing the process conditions to control the microstructure and resulting mechanical properties in an additively manufactured part. In electron beam melting process, Ti64 is the aerospace alloy of major interest. Electron beam melted Ti64 consists of highly textured columnar prior beta grains which are aligned along the build direction and filled with randomly oriented α laths [11,30,82]. It is also reported that for nominal build parameters, with increase in back ground temperature, the mechanical properties degrade [11]. The microstructure and resulting properties are effected by energy density, part thickness/size, scanning pattern, build orientation , distance from the build plate, location on the build plate and other process parameters [78,83–86]. Most of this research focused on studying specific process variable combinations and part geometries. These works lack a framework to combine the effect of processing conditions, part geometry and other factors on microstructure quantitatively. Using process mapping approach [87,88], Bontha et al. [89,90] developed solidification maps that predict grain morphology in Ti64. Building on that, an integrated melt pool geometry and microstructure control was demonstrated for Ti64 in both EBM and EBF3 process [28,91,92]. The main focus of these works was on controlling prior beta grain size in single bead deposits of Ti64 via melt pool geometry control. This allowed for predicting the microstructure for different process conditions in single bead geometry and these concepts are extended to solid parts [36]. This opens up the opportunity for location specific control of microstructure in AM, which is not yet explored in detail.

Solidification conditions which control the size scale of the structure formed at solidification can be modified on the fly in AM. Because of the rapid solidification fine and more homogeneous solidification substructure is observed in additively manufactured components

[50,93,94]. Due to the fine microstructure, the mechanical properties are better or comparable to the as-cast properties of AlSi10Mg [40,42,95,96]. Similarly, for laser melted IN718, the room temperature mechanical testing properties exceeded that of as cast and forged IN718 due to the fine grain structures and at high temperatures the performance is similar to forged IN718 and better than cast IN718 [55]. The scale of the fine structures can be controlled by controlling the solidification conditions. This was explored for dendrite spacing in IN718 and cell spacing in AlSi10Mg in the laser melting process [41,50]. For AlSi10Mg, Tang et al. [41] showed that that cell spacing can be refined by increasing the cooling rate and the relationship with cooling rate follows the trend presented in literature for splat cooling process [97]. However, these results for cell spacing dependence on cooling rates are presented for single bead samples. Thus, more work needs to be done to test their validity in solid builds. In addition, there is still potential to utilize these cell spacing control techniques to achieve location specific control of microstructure in a single component.

It is clear that columnar growth is typical in additively manufactured components. This results in anisotropy in the properties of the part where it is not desired. Given the nature of AM, the beam parameters can be controlled to control the solidification conditions which affect the grain growth and thus resulting texture of a part. Previous works have demonstrated the control of grain texture in laser melted 316 stainless steel [32] and in nickel super alloy IN718 using electron beam melting[98–100]. However, in these works, the control was achieved through modulating the beam spot size, shape and scanning pattern. Another means to achieve control via melting parameters: beam power and velocity was demonstrated by Gockel [28]. Results from that work indicated that beam power and velocity can be used to control the thermal gradients and solidification rates which in turn affect the grain morphology. In addition, relationships between

melt pool shape and grain morphology was also presented for Ti64. Similar work by Liu et al. [101] on super alloy single crystals demonstrated the effect of melt pool geometry on growth pattern and microstructure in a melt pool. The results from these works are on single melt tracks. Therefore, more work is needed to test the control of texture via control of melting parameters in solid components and link it back to melt pool geometry control.

To summarize, the major issues that are unaddressed so far are (i) developing process themes (process variable sets) for a new alloy system with minimal experimentation and utilizing the process knowledge base of the existing alloy systems (ii) a quick way to extend the standard process theme limits while using the machine (iii) relating the process themes across different AM processes [88]. With the projected increase in the use of AM in industry, new materials will be developed further for use in AM equipment and it is important to have a framework that can be used to transfer process knowledge from known materials to a new material system. It is also important to understand the solidification microstructure that forms during the build to reduce the time spent in post-processing procedures. Along with the above mentioned requirements, relationship between, process variables, resulting microstructure and properties will advance the process development and qualification methods

3 Location Specific Solidification Microstructure Control in Powder Bed Electron Beam Melting of Ti-6Al-4V

3.1 Overview

In this work, relationships between prior beta grain size in solidified Ti-6Al-4V and melting process parameters in the Arcam Electron Beam Melting (EBM) process are investigated. Toward this goal, samples are built on an Arcam S12 machine at Carnegie Mellon University by varying the Arcam proprietary speed function and beam current over process space for a variety of test specimens listed in Table 3-1. Optical microscopy is used to measure the prior beta grain widths and assess the number of prior beta grains present in a melt pool in the raster region of the build. Results show that despite the complicated evolution of beta grain sizes in solid parts, beta grain widths still scale with melt pool size. This highlights the controlling role of solidification cooling rate (which scales with melt pool cross sectional area) and yields an important insight on the control of prior beta grain widths in raster regions of bulky parts. The resulting understanding of the relationship between primary machine variables and prior beta grain widths (also referred to as grain size in this Chapter) is then used to demonstrate spatial control of as-built microstructure in the EBM process. Part of this chapter is published in the proceedings of the Solid Freeform Fabrication symposium [36].

Table 3-1: Terminology to refer to experiments.

Experiment Designation	Description
No added powder single beads	Beam on plate with no powder
Solid blocks	Multi-layer pad experiments (blocks)
Donut	Component with donut shaped region lying inside a square

3.2 Methods

3.2.1 Integrated Melt Pool Geometry and Microstructure Control via Process Mapping

The process mapping technique developed by Beuth et al. [87] relates identified primary process variables: beam power (P), travel speed (V), background temperature, material feed rate or layer thickness and local part geometry to main process outcomes such as process precision, build rate, microstructure, and flaw formation [88]. Previous work done by Gockel [28] demonstrated that the process maps for cooling rate which govern grain size follow similar trends to process maps of melt pool size for Ti64 in electron beam melting processes. This means, if the melt pool size can be controlled, grain size can also be controlled; this is referred to as integrated melt pool geometry and microstructure control. These ideas are used for prior beta grain width control in the electron beam melted Ti64.

3.2.2 Experiments

Experiments performed consists of no-added powder single beads, solid blocks and a donut sample with location specific variation of process parameters. Details of the experiment parameters and layouts are discussed in the following sections. All the experiments are performed on an Arcam S12 machine with EBM control software 3.2.2 at Carnegie Mellon University. Gas atomized Ti64 powder with size range 50 – 100 μm [82] was used for solid blocks and the donut sample. This powder was used for multiple builds, so the composition of powder might differ slightly from the standard powder supplied by Arcam. 70 micron thick powder layers were used in this build. Except for the melting parameters of the beam, additional parameters which control the part fabrication such as start plate heating, heating of powder layers, scanning pattern, hatch spacing etc. follow the standard Ti64 process parameters available on the Arcam S12 at Carnegie Mellon University.

The purpose of these tests is to vary the melt pool geometry by controlling the amount of energy that is being delivered by the electron beam which in turn is shown to affect the cooling rates and thus the solidification microstructure.

The primary variables for beam control in the EBM process are beam speed, beam current, speed function and focus offset as shown in Figure 3-1. Beam speed and beam current parameter values are used only when the builds are done in manual mode which means the operator has to explicitly communicate with the machine to execute different steps during the build process. For regular builds, the automatic mode is used. When a part is built in the automatic mode, beam current and beam velocity are changed with part height based on a thermal model embedded in the machine's control software. Speed function controls the change in beam velocity with change in beam current. The focus offset controls the spot size of the electron beam. In this work, the effect of focus offset is not discussed in detail and for more details on the effect of focus offset, readers can refer to work done by Francis [102]. Because the main goal of the work is to enable the process control in automatic mode, the speed function is varied in the experiments to study the control of prior beta grain size. This will enable any user with basic Arcam user training to modify the process conditions and thus control the final part microstructure.

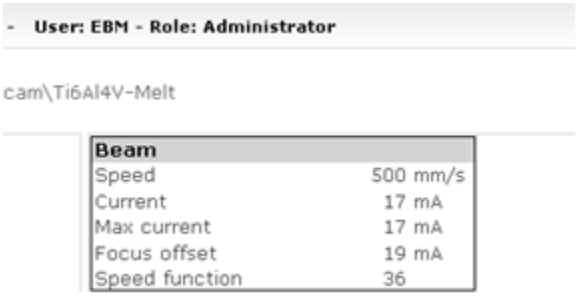

Figure 3-1: Primary beam parameters on the Arcam S12 machine.

Previous work by Gockel [28] concluded that melt pool grain size scales with effective melt pool width for single beads in the EBM process. This demonstrates that prior beta grain size

can be controlled by controlling the melt pool size. In that work, the author conducted experiments by directly varying beam power (current) and velocity (speed) to maintain a constant cross-sectional area of the melt pool whereas, in this work, velocity is not controlled explicitly by the user, but the machine parameter speed function is changed to vary the velocity to yield a melt pool with constant cross-section area.

3.2.2.1 No Added Powder Single Bead Experiments

The speed function parameter was studied in the past by some researchers working in the area of EBM[9,30]. It was observed that for a constant speed function, melt pool size remains constant. However, the explicit relationship between the speed function and melt pool geometry is not available. This served as the motivation to perform no-added powder single bead experiments to map out the relationship between melt pool area and speed function.

No-added-powder single bead tests were performed for different speed function and beam current combinations as listed in Table 3-2 on an Arcam S12 machine at Carnegie Mellon University. The specks of powder that are present in the Figure 3-2 are those which fell on the top when the door was opened after the build was completed. The beam carrying a specified current and operating at a given speed function traveled from one end of the plate to the other leaving rectangular melt tracks as shown in Figure 3-2. The base of the plate was maintained at a temperature of approximately 750 °C.

Table 3-2: Experiment parameters for no-added material single bead experiments.

Sample No.	Beam Current (mA)	Speed Function	Focus Offset (mA)
1 (Nominal)	17	36	19
2	17	17	19
3	17	7	19
4	17	75	19
5	17	154	19
6	8.5	36	19

7	8.5	17	19
8	34	36	19
9	34	17	19
10	12	30	0
11	12	13	0
12	12	4	0
13	12	64	0
14	12	130	0
15	6	30	0
16	6	13	0
17	24	30	0
18	24	13	0

Figure 3-2: Ti64 plate (~210W×210L mm) with melt tracks formed at different beam parameters.

3.2.2.2 Multi-Layer Pad Experiments (Solid Blocks)

Figure 3-3 shows the top view of the experimental layout of 9 multi-layer blocks of dimensions 30W×30L×20H mm built by varying the speed function and beam current in the build theme (shown in Figure 3-1) while holding other melting parameters constant. As detailed in Table 3-3, out of 9 samples, 5 samples were built with varying speed function at a constant beam current. The remaining 4 samples were built with varying beam current at constant speed function. Sample 1 was built using the nominal build conditions for the Ti64 alloy that are available on the Arcam S12 machine. It is important to note that the number of test samples reduced when we moved from

single beads to multi-layer pads. Single bead experiments are easy to perform and do not require powder which results in a quick and inexpensive tests. However, multi-layer pads are time-consuming to build and they require powder which makes these tests more expensive. Additionally, not many multi-layer blocks fit on the 210 mm x 210 mm build envelope in the Arcam S12 machine. Hence, information from single layer pads is used to develop an experiment plan for multi-layer pads in which prior beta grain size is varied systematically.

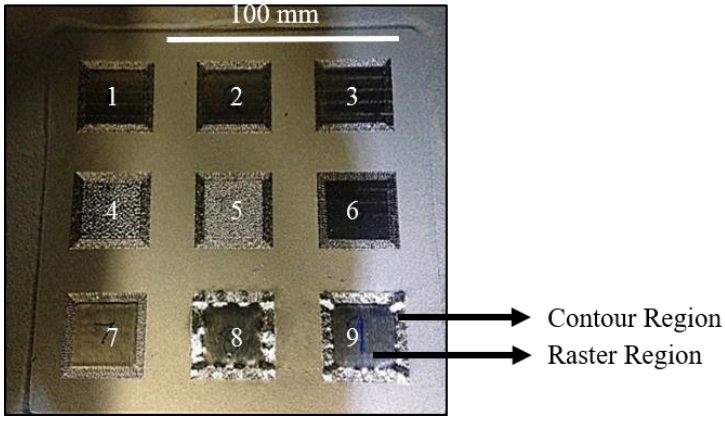

Figure 3-3: Above view of multi-layer (solid) blocks in the build chamber.

Table 3-3: Experiment parameters used in solid build tests.

Block No.	Beam Current mA	Speed Function
1 (Nominal)	17	36
2	17	17
3	17	7
4	17	75
5	17	154
6	8.5	36
7	8.5	17
8	34	36
9	34	17

Figure 3-3, it can be observed that for the bottom 2 samples the edges have wave-like discontinuities in the contour region which are identified in the layout. This is caused by the

melting parameters in the contour region for samples 8 and 9 resulting in excess heat buildup - affecting the surface finish of the sample. However, contour regions are not studied in this work and since raster regions are of interest in this work, samples 8 and 9 can still be used for analysis of the raster regions.

3.2.2.3 Donut Sample

Based on the information obtained from single beads and multi-layer pads, it is now possible to achieve a single chosen prior beta grain width in a test block by varying the melt pool cross-sectional area. The next goal was to confirm that microstructure can be varied spatially in a single part, i.e. test the ability to obtain different grain sizes in a single part. Toward this goal, the part geometry as shown in Figure 3-4 was built on the Arcam S12 machine. Dimensions are 18W×18L×10H mm. The objective of this experiment is to vary the prior beta grain size by a factor of 4 in different regions on the block. Each region is loaded as a separate part file onto the machine and melted with region-specific parameters. Region 1 is melted first followed by Region 3 and finally Region 2.

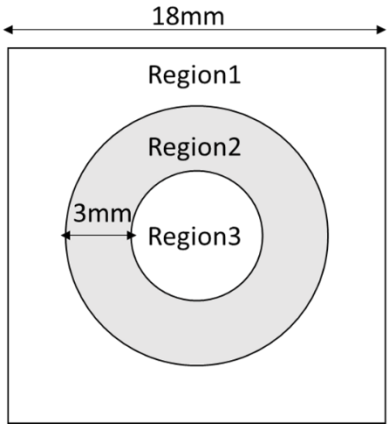

Figure 3-4: Experiment layout for the donut sample.

Parameters shown in Table 3-4 are developed based on the results from single bead and multi-layer block experiments. It is observed that with an increase in focus offset values, the beam

spot size increases. At very low speed functions, energy density is high and result in evaporation of material which leaves pores inside the melt pool and results in deep melt pools shown in Figure 3-5. This leads to keyholing porosity [103] in the final component that affects the fatigue life of the part. Hence, for Region 1 and Region 3 where the speed function is very low, the focus offset was increased to spread out the beam over a larger area to avoid keyholing [104]. Adjustments to the focus offset are based on the work presented in [105]. It is important to note that all process parameters were changed in-plane and not along the build direction of the sample.

Table 3-4: Experiment parameters used in fabricating the component.

Region Designation	Speed Function	Focus Offset (mA)
Region1	2	38
Region2	36	19
Region3	2	38

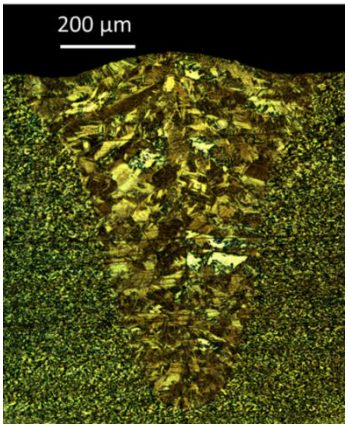

Figure 3-5: Example of high aspect ratio (depth to width ratio) melt pool that corresponds to keyholing.

3.2.3 Sample Preparation and Characterization Techniques

Single bead melt lines were sectioned along the transverse direction of the melt track at locations well away from the plate edges where the melt pool reaches steady-state conditions using Wire Electrical Discharge Machine (Wire EDM). The solid blocks were sectioned vertically at the center plane along the build direction using a diamond wafer blade. Single bead samples and the donut

sample were mounted in Konductomet™ mounting compound via hot compression mounting. Solid builds were mounted using epoxy because they were larger than the allowable size in hot press mounting equipment. The samples were then polished using a Buehler auto-polisher. Details of the polishing procedure are provided in Appendix A. Polished samples were etched for 15-20 seconds using Kroll's reagent which is comprised of 92 mL of deionized water, 6 mL of Nitric Acid (HNO_3) and 2 mL of Hydrofluoric Acid (HF) [28].

Single bead images were taken using an Alicona InfiniteFocus optical microscope. An example melt pool is shown in Figure 3-6. In single beads, the melt pool is marked along the solidification boundary, where the morphology is different from the start plate as shown in Figure 3-6. The melt pool dimensions of cross-sectional area, width and depth were measured. Grains grew from the melt pool boundary upward and toward the center and, qualitatively, a majority of the grains appear to be columnar. Using ImageJ software, the average prior beta grain width was measured in the melt pool cross-section using the line intercept method [106] where each intercept value is recorded rather than just estimating the average value.

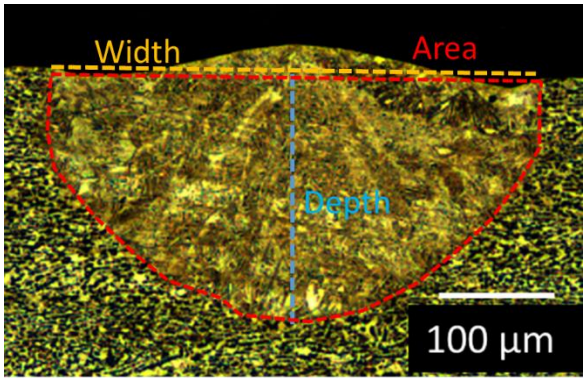

Figure 3-6: Example melt pool marked with cross-section dimensions.

Solid blocks images were taken both with a 20X objective using a Zeiss Light Optical Microscope (LOM) and an Alicona InfiniteFocus optical microscope. In the LOM, dark field mode was used to increase the contrast of boundary alpha phase, which aids in identifying the prior beta

grains, and phase colors were reversed to identify the grain boundary alpha clearly. An example micrograph of a solid block with columnar prior beta grains is shown in Figure 3-7. Grain widths were measured from the blocks using the line intercept method [106] at heights of 19 mm, 17 mm, 15 mm, and 12.5 mm (above the build plate) across the bulk raster region as illustrated in Figure 3-8. In order to avoid the edge effects when beam turns around to melt the next track, measurements were taken at least 2mm away from the edge. This is based on the visual observation of the grain growth direction from the optical micrograph. Near the edges, grains are curved towards the center of the block which slowly transitions to grains that grow along the build direction. Prior beta grain sizes were measured in the top half of each block, where it was expected that a steady-state value of beta grain widths might exist as shown in Figure 3-8.

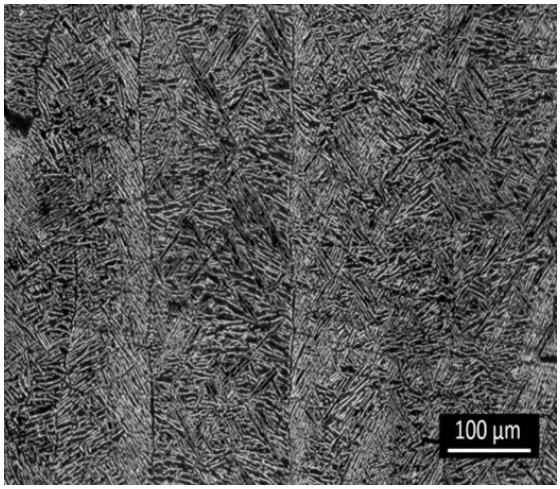

Figure 3-7: Columnar grains growing along build direction in Ti64.

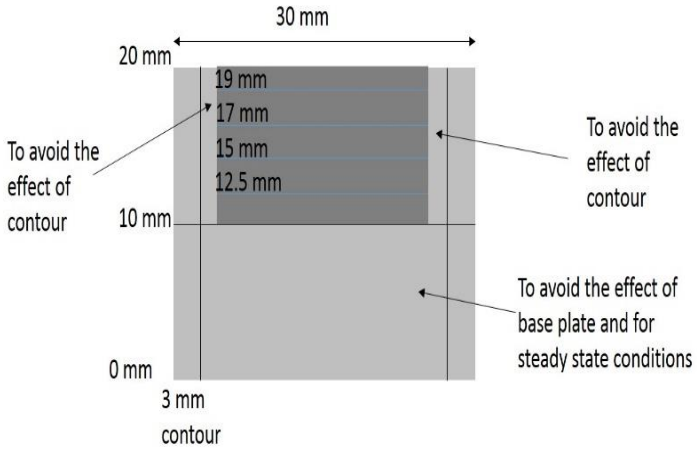

Figure 3-8: Illustration of region considered for measurement of prior beta grain widths in solid blocks.

The donut sample is not sectioned along the build direction. Instead, it is mounted such that the polished section presented the view from above as shown in Figure 3-9. This image was captured with 2.5X objective using an Alicona InfiniteFocus optical microscope. The sample is polished 2.5 - 3 mm deep into the part. The circular intercept method [106] was used to measure the average prior beta grain width in different regions of the component. The black colored circles in Figure 3-9 denote the boundaries between different regions, whereas white circles denote regions where average prior beta grain widths were measured. It is important to note that, the region of interest is small and not many circles can be drawn to obtain information on variability. Hence, coordinates of the grain boundaries intercepting the circle were used to measure the length of each grain intercept and this data is recorded for all the circles. The line intercept method could not be used owing to the small length of a line that could be drawn in the region of interest. This in turn results in not being able to include a sufficient number of grains. Mounting the sample to facilitate the above view aids in understanding the overlap between different regions; this is discussed in results section.

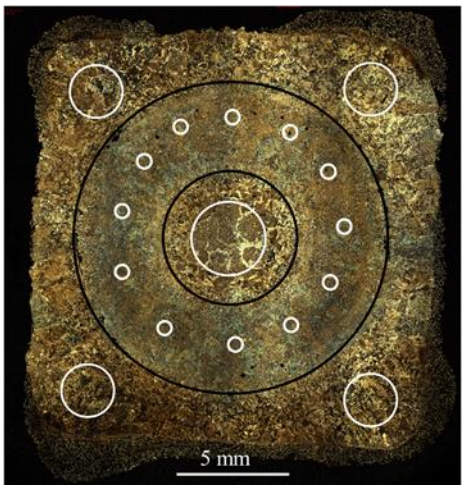

Figure 3-9: Illustration of region considered for measurement of prior beta grain widths in a single component.

3.3 Results: Solidification Microstructure

3.3.1 Single Bead Experiments

No-added material single bead experiments are used to map out the effect of the speed function on melt pool size and the variation of prior beta grain size with the speed function. Both of these results are discussed in detail in the follow sections.

3.3.1.1 Melt Pool Geometry Mapping

Melt pool geometry characteristics which are estimated from the cross-section of the single bead melt track are width, depth and area. Table 3-5 details these estimates for all of the single melt tracks. From Figure 3-2, it can be seen that for every process variable combination, the scan trace is rectangular in shape. When these rectangular boxes are sectioned to observe the cross-section of the melt track, it results in 2 melt pool cross sections per track. Measurements in Table 3-5 are an average of the measurements obtained from the two melt pools at the cross-section. Samples 4, 5 and 8 resulted in melt pools which are particularly shallow, making it difficult to identify the exact melt pool boundary. Hence, measurements from those three samples are not provided.

For a constant speed function, if beam current is increased, the melt pool width increased and depth decreased though the change in area is not significant. In cases with a focus offset of 0 mA where the beam spot size is expected to be minimized, at lower speed functions, the change in area caused by a change is beam current is significant. This is because of the keyholing phenomena [107]. In the keyholing process region, the change in melt pool area is not negligible. This is evident from samples 11, 16 and 18 where the melt pool area changed by more than 10%. In these cases melt pool area is taken from the cases where the melt pool is not too deep and is on the threshold of keyholing.

Table 3-5: Cross-section dimensions of the melt pool from single bead experiments.

Sample Designation	FO (mA)	Beam Current (mA)	SF	Width (µm)	Depth (µm)	Average Area (µm²)
1	19	17	36	1047	57	4.8E+04
2	19	17	17	1172	110	1.2E+05
3	19	17	7	1265	268	2.7E+05
6	19	8.5	36	702	95	4.9E+04
7	19	8.5	17	777	175	1.0E+05
9	19	34	17	1865	96	1.4E+05
10	19	12	30	608	194	9.0E+04
11	0	12	13	557	397	1.7E+05
12	0	12	4	890	912	4.8E+05
13	0	12	64	537	92	3.0E+04
14	0	12	130	454	52	1.5E+04
15	0	6	30	442	217	7.9E+04
16	0	6	13	647	234	1.9E+05
17	0	24	30	1089	83	7.2E+04
18	0	24	13	1228	185	1.6E+05

Though the focus offset variable is known to control the beam spot size, these experiments show that beam current also affects the spot size for a given focus offset value. To be specific, for a given focus offset, if the beam current is increasing, spot size also increases as evidenced by the increase in melt pool width and decrease in melt pool depth. However, it is observed in the previous study by Francis [105] that the change in spot size has less impact on melt pool area when compared to width and depth. This is also evident from the melt pool dimension values in Table 3-5.

For estimating the melt pool area, the average of the melt pool areas is calculated from those melt pools whose area is not affected by the change in beam spot size. These area calculations are outlined in Table 3-6. Figure 3-10 shows the plot of speed function versus melt pool area from these experiments. Since there are only two melt pools that are used in measurement, a variability analysis is not provided.

Table 3-6: Measurement of melt pool areas for different speed functions.

SF	Average Area (μm²)
4	4.8E+05
7	2.7E+05
13	1.7E+05
17	1.1E+05
30	7.6E+04
36	4.8E+04
64	3.0E+04
130	1.5E+04

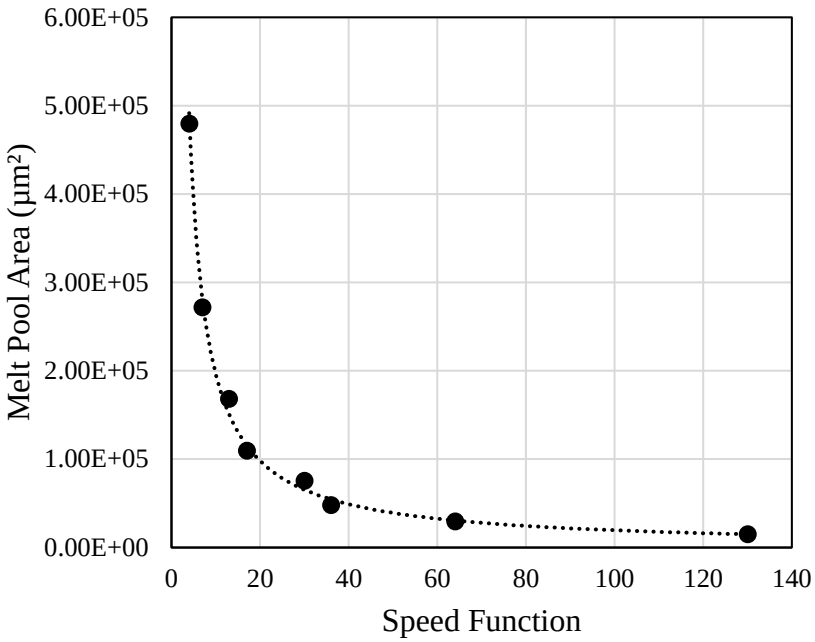

Figure 3-10: Variation of melt pool area with speed function on Arcam S12 machine.

3.3.1.2 Solidification Microstructure Mapping

Grain sizes are measured from the melt pools in which the prior beta grain boundaries were easily identifiable. Using the line intercept method [106], a line is drawn across the grains in the melt pool and each grain width is measured using ImageJ software. This data provides information about both the average prior beta grain width and also existing variability. Table 3-7 provides the details of the prior beta grain width measurement along with standard deviation and standard error values.

Table 3-7: Measurements of average prior beta grain widths for single beads.

Sample Designation	Effective Width (µm)	Average Grain Width (µm)	Standard Deviation (µm)	Standard Error (µm)	Grains per Width
2	528	25	9	2	21
3	832	37	11	2	22
11	654	34	13	3	19
15	439	22	9	2	20

Figure 3-11 shows the plot of prior beta grain width variation with speed function in single beads. This plot illustrates a distinct relationship between melt pool area and prior beta grain size. Instead of melt pool area, effective width is used to be able to compare the results with previous work on integrated melt pool geometry and microstructure control in electron beam melting of Ti64 [28]. Effective width is calculated by assuming a semi-circular melt pool where diameter is equal to width of the melt pool. It was found that prior beta grain width scales with effective width such that the average number of grains per effective melt pool width is approximately 21 for all the measured melt pools. Error bars in the plot represent a 95% confidence intervals (CI) about the average grain width. Only 2 values for melt pool width were available since only 2 melt pools are available for measurement and hence insufficient data is available to present the CI.

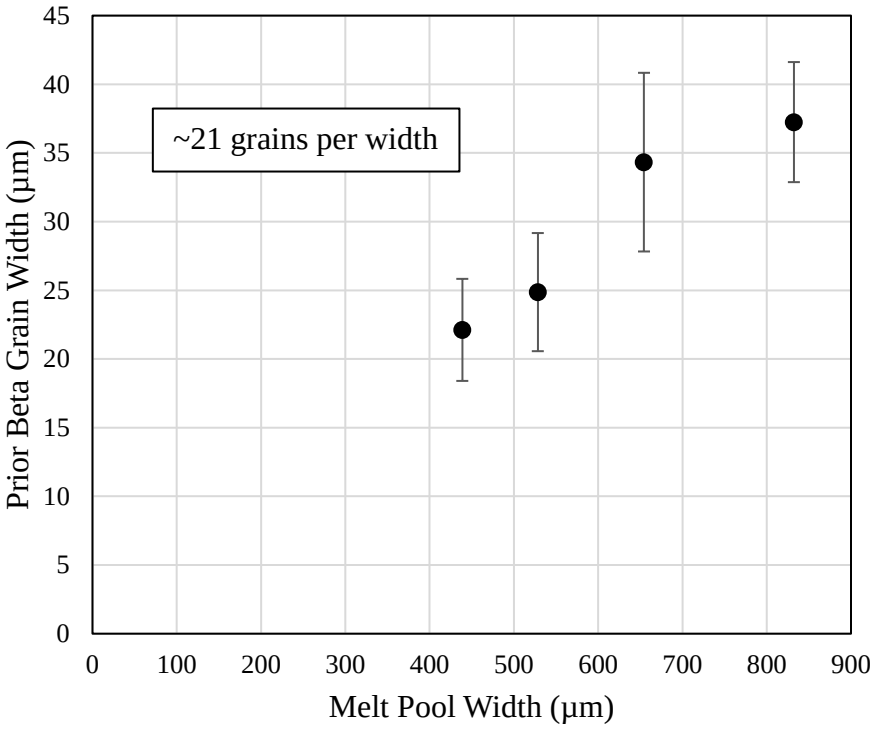

Figure 3-11: Variation of prior beta grain width with melt pool width in single beads.

Previous work done by Gockel [28] found that melt pool grain size scales with melt pool effective width for single beads in the Arcam process, however the number of grains per width of

the melt pool was found to be 7 instead of 21, as reported in this document. In that work, the author conducted experiments by directly varying power and velocity to maintain a constant cross-sectional area of the melt pool. An example melt pool which has a similar cross-sectional area to the melt pool from the present study is shown in Figure 3-12.

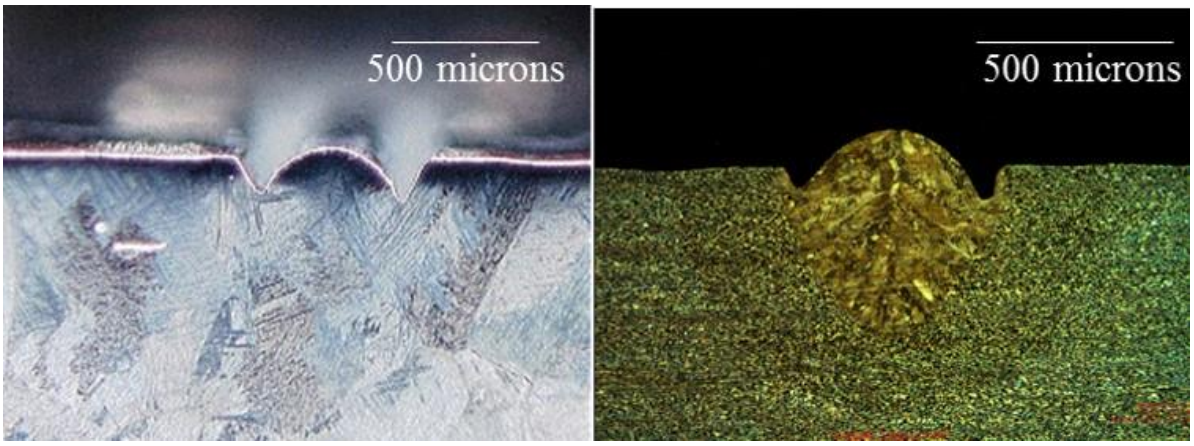

Figure 3-12: Illustration of the effect of substrate grain size on prior beta grain width in melt pool.

For similar build conditions, there is change in the grain size in both of the melt pools. It can be seen that there are differences between the grain sizes of the start plate in both the cases. Grains are bigger in the substrate used by Gockel [28], resulting in fewer grains (7) per melt pool when compared to the substrate used in the current study which resulted in higher number of grains (21) per melt pool. This is likely due to the higher number of nucleation sites available in the start plate with finer grains when compared to the start plate with coarser grains. These results provide a great motivation for studying the effect of grain size in the substrate or the previous layers during the layer-by-layer building process. Chapter 4 investigates this topic in detail and the implications it has on the location specific-control of solidification microstructure in the donut sample.

3.3.2 Multi-Layer Pad Experiments (Solid Blocks)

It was observed from Figure 3-7 that the solid build microstructure consists of columnar grains growing along the build height. This has been reported in previous work [30,82] focusing on understanding Ti64 solidification microstructure. There were no traces of individual melt pools or powder layers in the final build because the grains grow through layers. This can be due to remelting caused by the pre-heating step and heat from melting subsequent layers during the build process [108][82]. In all the samples, the grain growth pattern is similar to that observed in the nominal case, with the exception of samples built with higher speed functions, yielding shallower melt pools. These specimens experienced significant porosity due to lack-of-fusion as shown in Figure 3-12. In these cases, heat transfer pathways are different from that of fully-melted samples, which leads to irregular microstructure close to these pores compared to the fully-melted cases. Measurements in these samples were taken in regions well away from the pores to avoid their effect on microstructure.

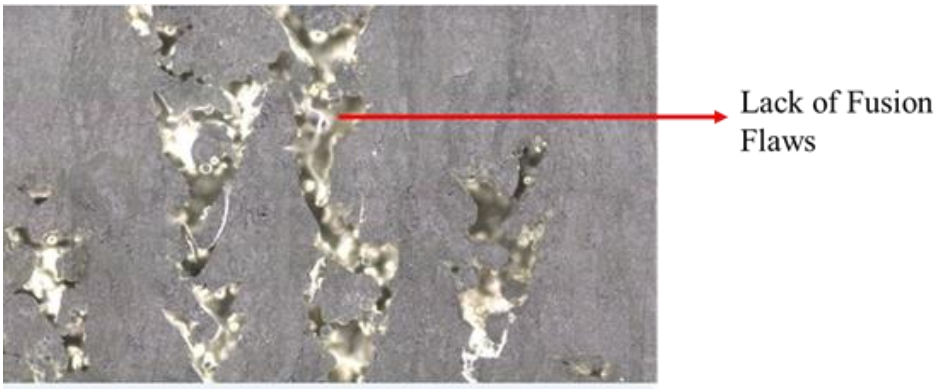

Figure 3-13: Lack of fusion porosity in solid blocks with shallow melt pools.

At the part heights considered, there is a large variation in grain width values across the width of the sample. This is evident from an example grain size distribution plot shown in Figure 3-14 for Sample 1. There is wide dispersion in the grain size values and they follow close to log-normal distribution and grain sizes from different heights overlap which means steady-state

conditions were achieved. This variation can be either because of the natural variability observed in the grain growth or because the grain sizes were measured from a 2D section. With the available information, it is not possible to distinguish quantitatively between the variability resulting from these two sources. Grains at the lower tail of the distribution are likely (i) the ones which are either growing along directions other than the build direction and only part of the grain is available for measurement in the cross-section used for analysis or (ii) those which did not survive during the competitive grain growth. They also come from the grains which have just started growing and are narrow. Hence, grain size distributions are important to understand the probability of occurrence of grain sizes as well as the range which includes the majority of the grains. Even though there is variability in grain widths at different heights of the sample, the variability of the average grain widths across all heights in a single test block is low as illustrated in Figure 3-15.

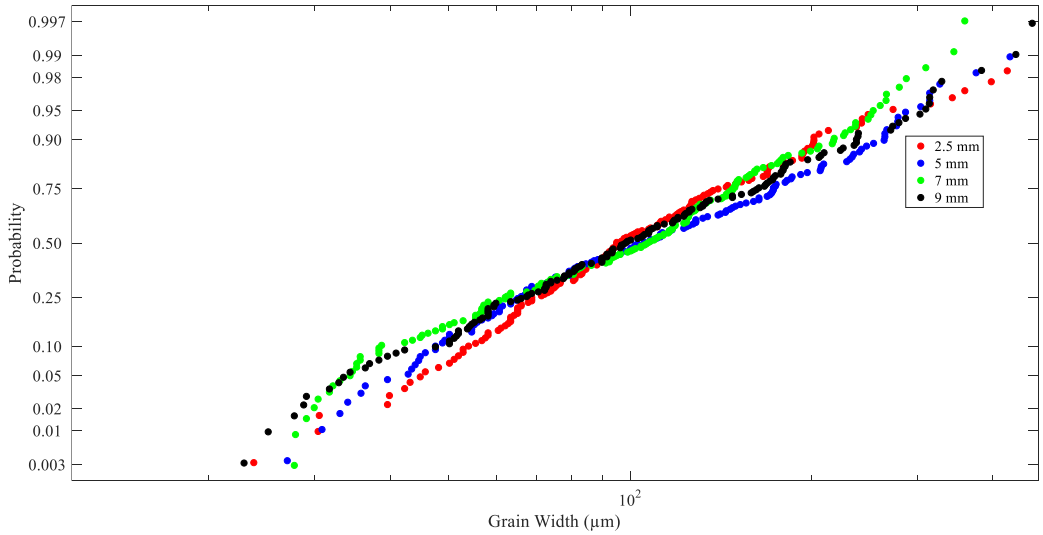

Figure 3-14: Probability plot (cumulative) of the of the grain size distributions at different heights for sample 1.

Based on the large-sample theory [109], a 95% CI is estimated using the general procedure for a normal distribution even though the actual grain width distribution is log-normal. In this analysis, blocks 7 and 8 are not analyzed since blocks 6 and 9 address the case where beam current

is being varied for the same speed function. It is expected that within the bottom 5mm of each block, a transition occurred between the small grains seen in the single bead tests to the much larger widths observed in this study. This is investigated in detail in Chapter 4.

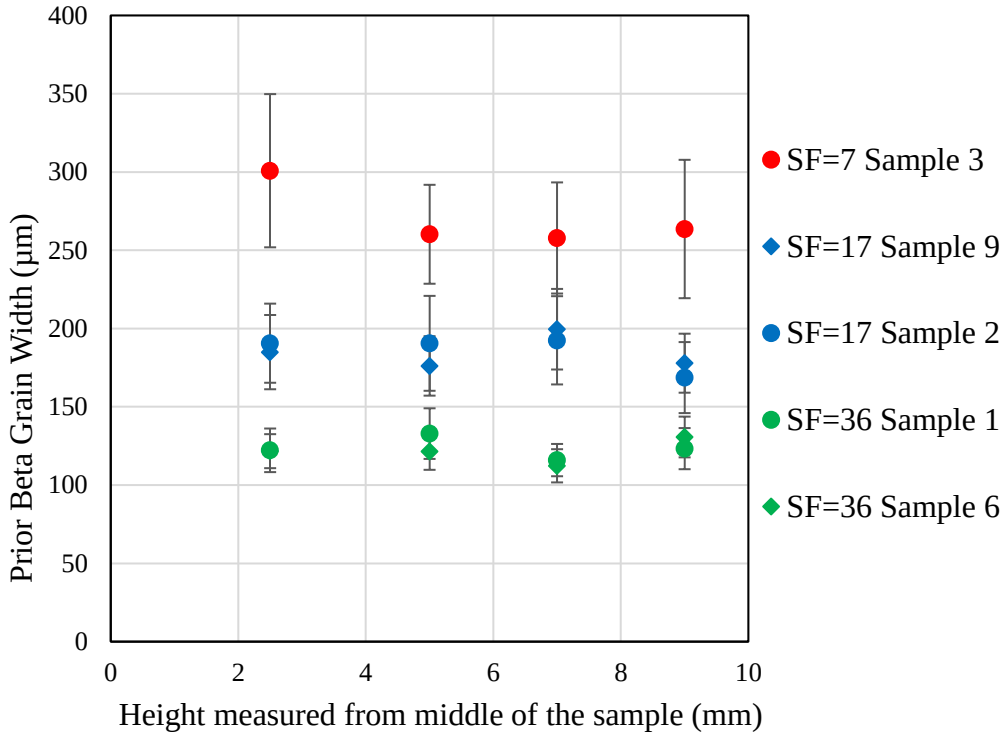

Figure 3-15: Variation of average prior beta grain widths with part height for different melt conditions.

Since the variation in average grain widths at different heights is not significant, all the grain width values from different heights are combined in each sample to estimate the average grain width. Details of these measurements are provided in Table 3-8 and grain size distributions in steady-state regions for different samples is shown in Figure 3-16. Grain widths follow log-normal distribution and there is wide dispersion in all the samples. For different beam currents and the same speed function, grain size distributions overlap which implies that there is no effect caused by the beam current parameter specified in the process theme at the beginning of the build

for these samples. With an increase in speed function, the grain size distribution curves shift toward lower values.

Table 3-8: Measurement of average prior beta grain widths in solid blocks.

Sample Designation	Effective Width (µm)	Average Grain Width (µm)	Standard Deviation (µm)	Standard Error (µm)	Grains per Width
1	350	123	84	3	3
2	528	183	121	6	3
3	832	268	164	12	3
4	257	91	22	4	3
5	180	69	20	6	3
6	350	121	73	3	3
9	528	184	109	5	3

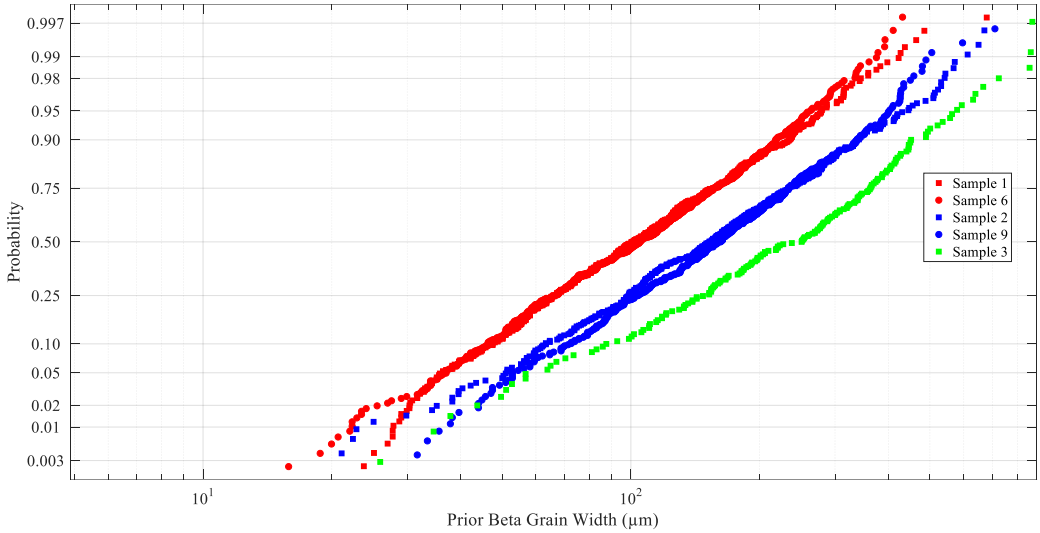

Figure 3-16: Probability plot (cumulative) of the grain sizes in solid blocks built with different melt parameters.

Grain width values from solid blocks are plotted against the melt pool width from single beads as shown in Figure 3-17. It is interesting to note that the grain width still scales with melt pool width and the number of grains per melt pool width is 3. A comparison of the number of grains per melt pool width from single beads and solid blocks is shown in Figure 3-18. The decrease in number of grains per width in solid blocks can be explained by the fact that in multilayer builds, columnar prior beta grains span multiple layers of the build and increase in width

due to competitive growth. As they grow, they take the place of some grains that narrow and die out because their crystal growth direction is not aligned with the direction of heat transfer. What is most interesting is that despite the complicated evolution of beta grain sizes in solid parts, beta grain widths still scale with melt pool widths. This highlights the controlling role of solidification cooling rate (which scales with melt pool cross sectional area) and yields an important insight into how to control beta grain widths in raster regions of bulky parts. Control of melt pool cross sectional area (and the related effective melt pool width) results in the control of beta grain width.

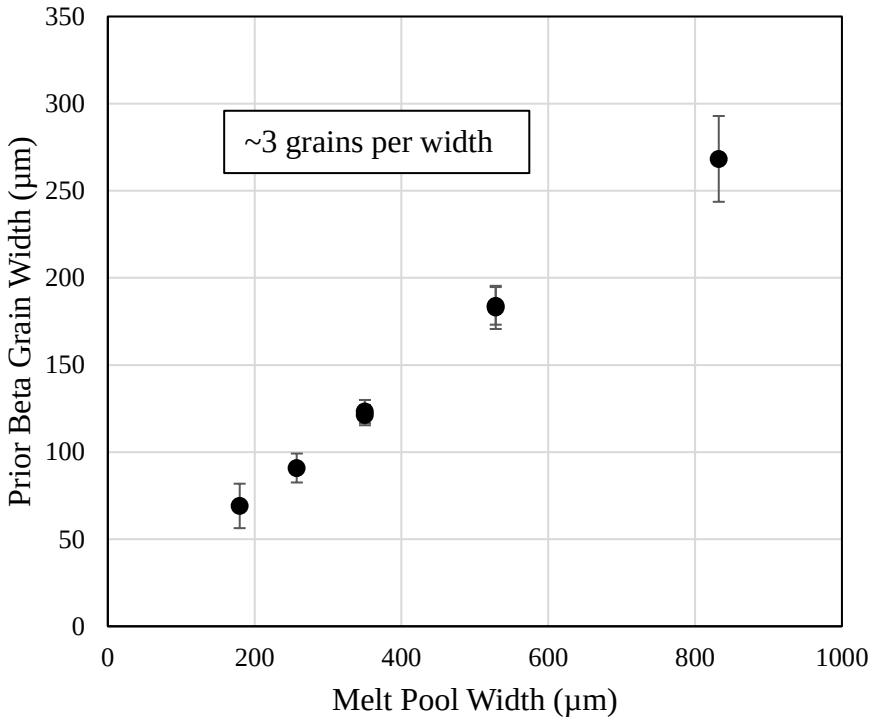

Figure 3-17: Variation of prior beta grain width with melt pool width for solid blocks.

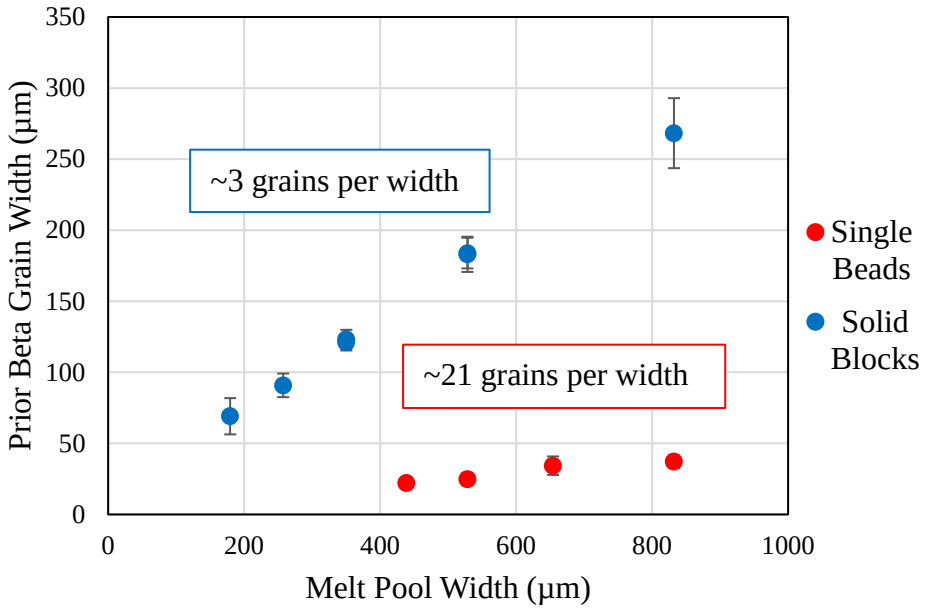

Figure 3-18: Comparison of number of grains per melt pool width in single beads and solid blocks.

Using this knowledge, average grain width in the solid blocks can be varied over any range of values. Figure 3-19 shows example micrographs of the samples with average widths ranging from 91 – 277 microns.

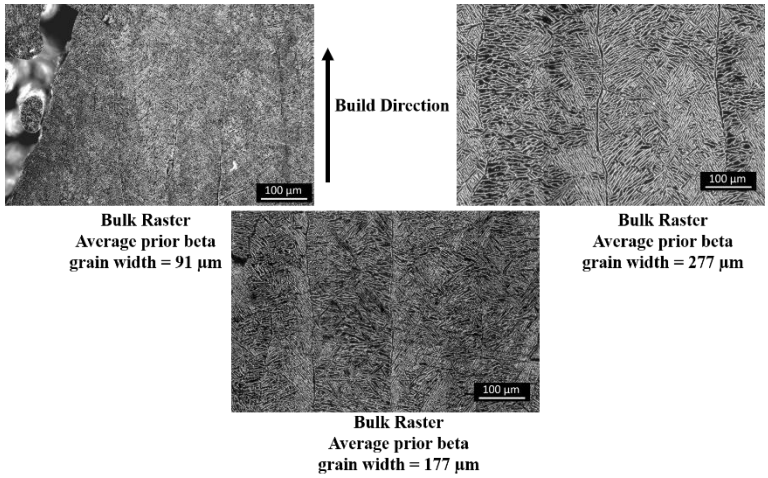

Figure 3-19: Location specific variation of prior beta grain size over a range of values in solid builds.

3.3.3 Location Specific Solidification Microstructure Control in Ti-6Al-4V

The donut sample consisted of three different regions in which Region 1 and Region 3 are expected to have a grain size which is 4 times that in Region 2. From Table 3-9, the ratio of average prior beta grain width between Region 1 and Region 2 is 3.5 which is 12.5% less than the expected ratio of 4. Since, large number of grain widths are used for analysis, standard error values are not significant and 95% CIs about the average grain widths are not large in Region in 1 and Region 2. On the other hand, it can be observed from Figure 3-20 (left) that the grains in Region 3 are 2.5 times than the grains in Region 1 though the melting parameters are the same. This is likely due to the heat buildup in this region. This shows that deposition path and part geometry are critical for cooling rate control.

Table 3-9: Measurement of average prior beta grain width in component.

Region Designation	Average Grain Width (µm)	Standard Deviation (µm)	Standard Error (µm)
Region 1	430	165	21
Region 2	121	63	5
Region 3	1066	299	106

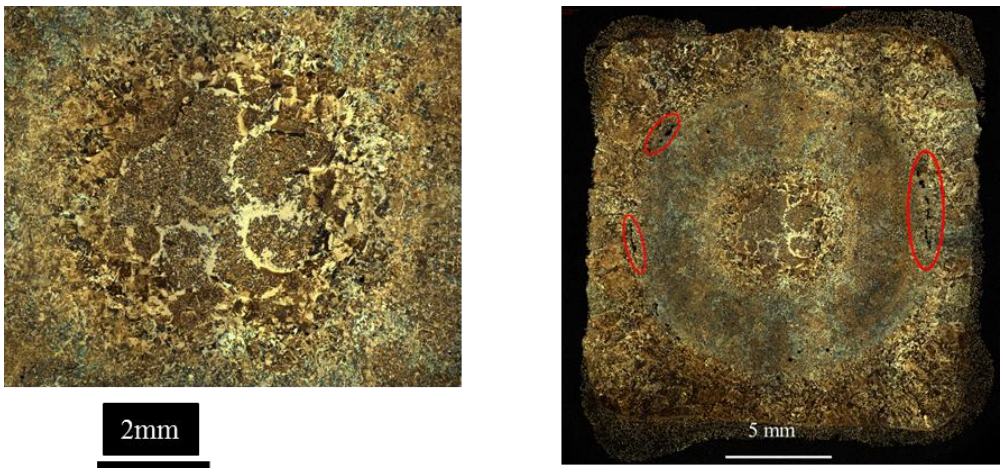

Figure 3-20: Central region of the component (left) and lack of overlap regions identified across the boundaries (right).

At the prior beta transus temperature, beta transforms to α+β morphology. Thus, α morphology also depends on the post-solidification heat transfer which is determined by non-melting parameters such as build height, build duration and build geometry. In these experiments, apart from prior beta grain size, there is also a difference in α morphology at different energy densities as shown in Figure 3-21. These morphological features are identified in Figure 3-21 for both high and low energy density scenarios. The micrograph on the left is of a higher cooling rate sample and has both grain boundary α (α_{gb}), basket weave and colony α(α_p). Micrograph on the right is of a lower cooling rate sample and has comparatively coarser α both nucleating at the grain boundaries and inside the beta grain resulting in basket weave morphology. Thus, α structures are coarser in lower cooling rate region when compared to the higher cooling rate region. This means constraining beta grains can also significantly affect alpha grains, which have a much more direct tie to mechanical properties.

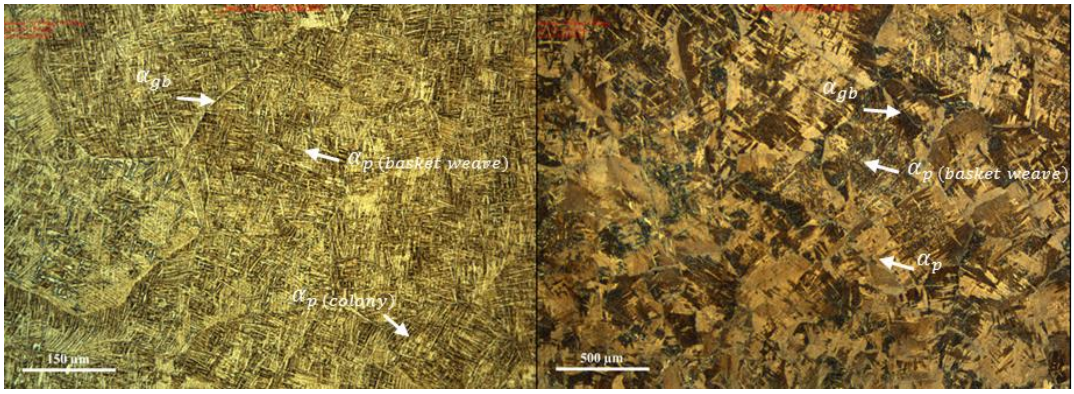

Figure 3-21: Comparison of prior beta grain widths and alpha morphology in Region 2 (left) and Region 1 (right) which have different cooling rates.

The transition between interfaces is discussed in detail in Chapter 8. From Figure 3-20 (right), it can be observed that there is porosity in some locations at interfaces between different regions. This is due the poor adjustment of the overlap between the part files at the beginning of the experiment. Thus, along with deposition path and turn-around effects, there should be proper

overlap between the different locations of the component to minimize porosity due to lack of overlap between the components.

3.4 Effect of Changing Prior Beta Grain Size on Mechanical Properties

Cunningham et al. [110] had studied the effect of changing prior beta grain size on mechanical properties via tensile testing. Results from that work show an increase in α lath width with increase in prior beta grain size. To be specific, by increasing the grain size by a factor of 2, resulted in a 20-30% decrease in the yield strength and ultimate tensile strength. This study also reported a possible slight increase in elongation with increase in prior beta grain size. Thus, it is critical to understand the prior beta grain size control to the α lath and thus, the properties of the part. This result can be explained based on the scaling of cooling rate at solidification and at beta-transus temperature. Cooling rates at the beta-transus temperature control the α structure. This means, lower cooling rates at solidification resulting in coarser prior beta grains result in lower cooling rates at beta transus resulting in a coarser α. This will decrease the yield strength and ultimate tensile strength of the part [111].

3.5 Conclusions

Part qualification is critical for widespread commercialization of AM and knowledge about as-built properties is critical in speeding up the qualification process. This study contributes to understanding and controlling as-built microstructure in the Arcam EBM process space for Ti64, with a focus on prior beta grain size.

The role of Arcam-defined beam parameters in controlling melt pool geometry and microstructure have been determined in detail through literature review and experimentation. Based on the concept of prior beta grain width scaling with melt pool width for single-bead

geometries for the Arcam EBM process and an electron beam wire feed process, prior beta grain width control has been extended to multi-layer blocks, i.e. multi-layer solid build geometries filled by raster patterns. Results demonstrate that prior beta grain width scales with effective melt pool width (melt pool size) in solid builds. This greatly simplifies the strategy for controlling beta grain widths to one of controlling melt pool size. These results are further used to vary the microstructure methodically in different locations of a single part which was successful. Further, this integrated melt pool dimension and microstructure control strategy is demonstrated to be achievable by modifying Arcam-defined beam variables that are accessible for any Arcam user with basic operational training.

4 Transitions in Solidification Microstructure of Ti-6Al-4V in Powder Bed Electron Beam Melting Process

4.1 Overview

In chapter 3, location-specific control of prior beta grain size in Ti-6Al-4V is demonstrated. Two important things to note are: (i) the part design for location-specific control involved varying the parameters in the x-y plane and not along the build direction and (ii) for the test blocks, measurements are taken in the top half of the block where the grain dimensions have reached steady-state. Achieving location specific control of microstructure in a component, however, will involve changing the process parameters both in the x-y plane and along the build direction. In addition, this knowledge will provide insights into the effect of existing substrate grain size on the as-built part grain size, which has implications for developing process parameters for repair of components. Hence, it is critical to study the response of microstructure to changes in process variables within a single component.

This chapter investigates the response of prior beta grain size to change in process parameters, which in turn change the thermal conditions in a single component. Methodical mapping of grain response distance along the build direction is performed through experimentation. Additionally, in-plane transition is also studied. This response distance knowledge is then used to achieve location-specific control of prior beta grain size in the dove tail region shown in Figure 4-3 of the generic General Electric (GE) compressor blade.

4.2 Methods

4.2.1 Experiment Progression

In chapter 4, experiment progression included the process flow from single beads to multi-layer pads to solid builds to a component in which region-specific grain size control was demonstrated. However, a critical component which is missing in the experiment progression are experiments to understand transition in microstructure with changes in process parameters. In this chapter, transition experiments are added to the experiment progression for location-specific control of solidification microstructure which is highlighted in Figure 4-1. These experiments are discussed in detail in the following sections.

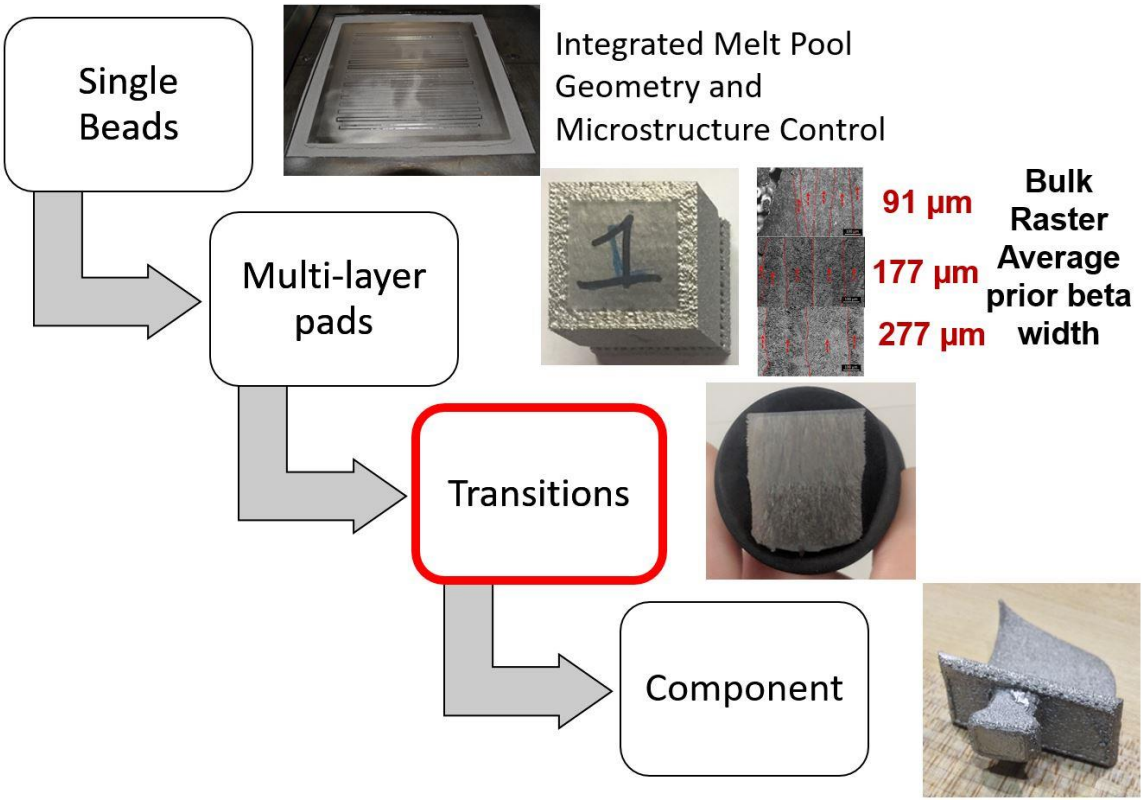

Figure 4-1: Experiment progression for location specific control of microstructure.

The Arcam S12 machine with EBM control software 3.2.2 was used to conduct the experiments presented in this chapter. Gas atomized Ti64 powder with size range 50 – 100 μm [82] was used. This powder was used for multiple builds, so the composition of powder might differ slightly from the standard powder supplied by Arcam. 70 micron thick powder layers were used in this build. Except for the melting parameters of the beam, additional parameters which control the part fabrication such as start plate heating, heating of powder layers, beam focus offset, scanning pattern, hatch spacing etc. follow the standard Ti64 process parameters available on the Arcam S12 at Carnegie Mellon University.

4.2.1.1 Transition Experiments

The main objective of these tests is to study the response (transition) distance along both the build and in-plane directions when process parameters are changed to vary the grain size in different locations of the component. In-plane variation was investigated using the donut sample discussed in Chapter 3. Hence, in this section, transition experiments are conducted with the main focus on the build direction transition.

Table 4-1: Experiment parameters for build direction transition experiments.

Scaling Factor (X=124 μm)	Speed Function	Focus Offset (mA)
X	36	19
2X	9	27
4X	2	38

Table 4-1 details the process parameters and Figure 4-2 (left) illustrates the layout for these experiments. X here refers to the average grain size calculated from the nominal melting parameters used on the Arcam S12, 2X means the parameters were adjusted to result in a nominal

average grain size that is 2 times larger than the nominal grain size and likewise for 4X. The beam spot size was increased by increasing the focus offset for the 2X and 4X samples to eliminate porosity resulting from the key holing [105]. The red blocks in Figure 4-2 (left) are samples that failed during the build due to excess heat buildup that caused part deformation and thus affected the spreading of powder and resulted in deformed components as shown in Figure 4-2 (right). Hence, these blocks were not used for any further analysis. Samples 1-3 were used to map the response distances for changes in microstructure.

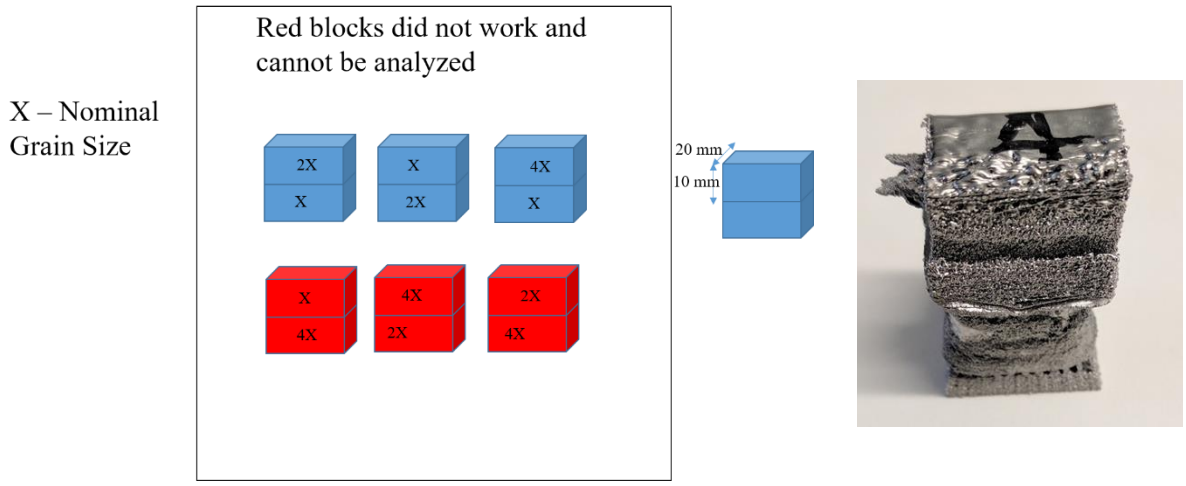

Figure 4-2: (left) Layout for transition experiments and (right) deformed sample due to excess heat buildup and incorrect spreading.

4.2.1.2 Fabricating a Component

The dove tail region of the generic GE compressor blade shown in Figure 4-3 is used as a case study to implement location specific control with knowledge of the transitions and response distance for grain size. The dimensions are modified to increase the size of the dove tail by 2 times for fabrication and characterization purposes. The goal is to have fine grains at the stress concentrators in order to increase the yield strength in that location. At the same time, process parameters had to be selected such that there will be enough grains for measurement since these regions are only 1.64 mm wide as identified in Figure 4-3. Parameters used in this test are outlined

in Table 4-2. During the fabrication process, for the middle section which consists of the stress concentration region (identified by arrows in Figure 4-3), the entire section was first melted with parameters that result in finer grain sizes. After that, the middle section excluding the stress concentration regions was remelted with parameters which result in coarse grains. This was done in order to eliminate any overlap porosity between the fine grain and coarse grain regions. This component was built without any contours and thus has rougher surface on the edges when compared to samples built with contours. This roughness at the edges can be observed in Figure 4-5.

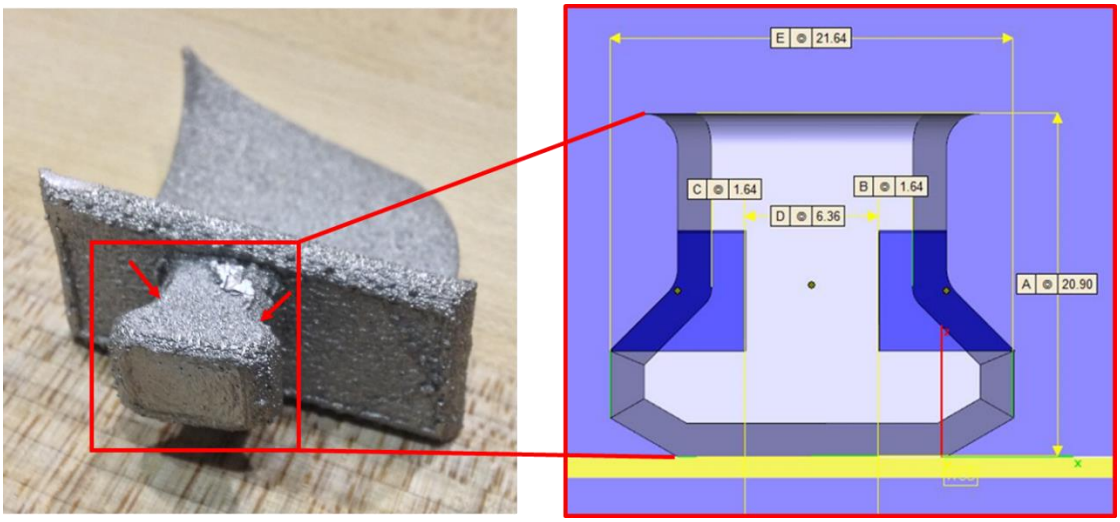

Figure 4-3: The dovetail region highlighted in the generic GE compressor blade and the computer aided drawing (CAD) model showing dimensions.

Table 4-2: Experiment parameters used in fabricating the dovetail component.

Region Designation	Speed Function	Target Average Prior Beta Grain Size (µm)	Focus Offset (mA)
Stress Concentrators	51	109	19
Coarser Grain Region	12	212	19

4.2.2 Sample Preparation and Characterization

The solid blocks and the dovetail were sectioned vertically at the center along the build direction using a diamond wafer blade in order to study the grain size response along the build direction for different processing conditions. The sectioned samples were mounted in Konductomet™ mounting compound via compression mounting. The samples were then polished using a Buehler auto-polisher. Details of the polishing procedure are provided in Appendix A. The polished samples were etched for 15-20 seconds using Kroll's reagent which is comprised of 92 ml of deionized water, 6 ml of Nitric Acid (HNO_3) and 2 ml of Hydrofluoric Acid (HF) [28]. An example image of the etched sample is shown in Figure 4-4 and Figure 4-5. In Figure 4-4, coarser grains were followed by the finer grains and it can be observed that the transition between the two grain sizes is clearly visible.

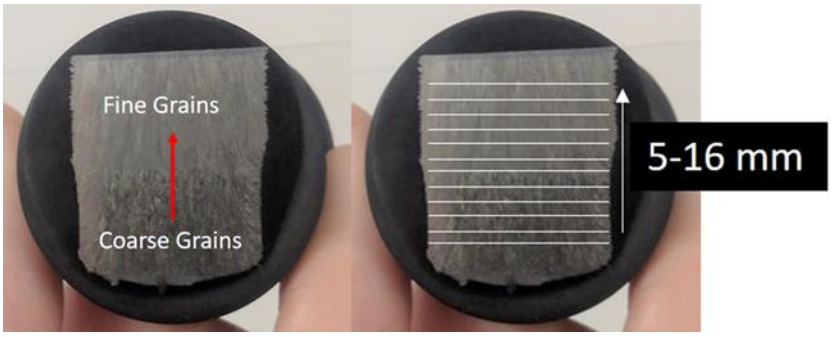

Figure 4-4: (left) Polished and etched cross-section and (right) illustration of region considered for measurement of prior beta grain widths at different heights.

Figure 4-5: Polished and etched cross-section of the stress concentrator region in the dovetail component.

Images were taken using an Alicona InfiniteFocus optical microscope. For the solid blocks grain widths were measured from the blocks using the line intercept method [106] at heights of 5 mm – 16 mm from the bottom of the sample, across the bulk raster region as illustrated in Figure 4-4 (right). When using the line intercept method, each intercept is measured in order to construct the grain size distribution plots and understand the dispersion in the grain sizes. Since the focus is on understanding the transition in grain sizes, for the dovetail region, the grain sizes were calculated from the interface towards the stress concentrator region until the measurements reached a steady state value.

4.3 Results

4.3.1 Solidification Microstructure

In Chapter 3, Ti64 solidification microstructure is discussed with the main focus on changes in prior beta grain size with changes in process parameters which control the melting process. Using different process parameters within a single component yields different types of microstructure due to the change in solidification conditions. However, it is important to note that there is a transition region between areas with different solidification conditions. This work discussed the

two types of transitions in the microstructure with changes in process variables: in-plane transition and transition along the build direction that are discussed in detail in the following sections.

4.3.1.1 In-plane transition

The donut shaped sample shown in Figure 4-6 with melting pattern from Chapter 3 is used to study in-plane transitions. In this experiment, the surrounding block (Region1) and circular region (Region3) inside the donut are melted first, followed by the melting of the donut region (Region2). Region1 and Region3 are deposited with melting parameters which will result in larger prior beta grains when compared to Region2.

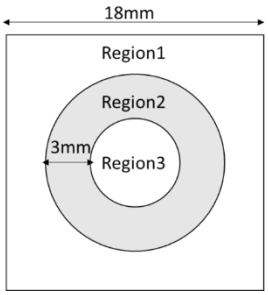

Figure 4-6: Experiment layout for the component.

There is a zone between the different regions which has grain sizes that are smaller than the coarse grain regions but larger than the fine grain region. This can be due to the heat transfer from one region to the other region during the melting process. This will result in a transition region between the two areas with different melting conditions and it can be referred to as an in-plane transition. Examples of such transitions between different regions in the donut sample are shown in Figure 4-7. The image on the left shows the example transition region between the donut and the circular region inside the donut whereas the image on the right shows the example transition region between the donut and the surrounding block.

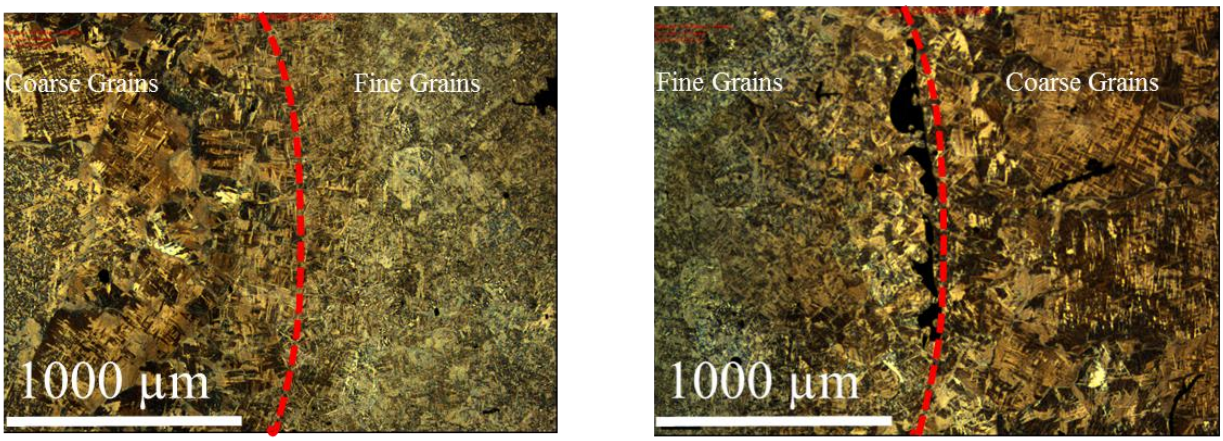

Figure 4-7: Transition region between: (left) the donut and the circular region inside the donut and (right) the donut and the surrounding block.

This transition distance is on the order of 600 microns, which is approximately equal to the typical melt pool width (refer to Chapter 3 for melt pool width measurements) in the electron beam melting process. It is important to note that this transition region looks qualitatively similar at both the interfaces. Interfaces are marked based on the dimensions from the computer aided design (CAD) model used to print the parts.

4.3.1.2 Transition along the build direction

This section discusses the transitions along the build direction. Figure 4-8 shows an example micrograph from the sample where the melting parameters were changed such that the average prior beta grain size changes from X to 2X where X is 124 microns based on the measurements for nominal parameters in Chapter 3. It can be observed that the number of grains at each height gradually decreased as we move from the bottom to the top region of the image; 8 mm, 9 mm…13 mm represent the heights at which these images were taken and stacked together to result in the comprehensive image. The average grain size measurements at different heights are also provided in this figure.

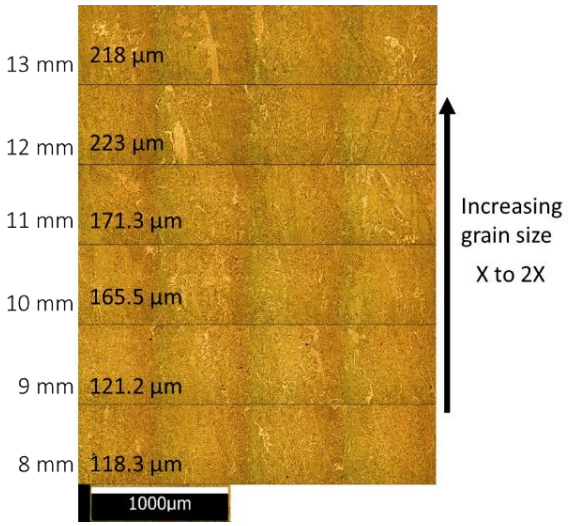

Figure 4-8: Example stacked image with micrographs from different heights for Sample 1 (X→2X transition).

Table 4-3 to Table 4-5 detail the grain size measurements at different heights for the samples 1-3 respectively. The standard deviation and standard error values are also provided to understand the dispersion about the average grain size and the confidence in the average grain size measurement respectively. Figure 4-9 provides the average grain size measurements with a 95% Confidence Interval (CI) for all three samples. Based on the large-sample theory [109], 95% CI is estimated using the general procedure for a normal distribution despite the fact that the actual grain width distribution is log-normal based on results from Chapter 3. The dashed red, blue and green vertical lines represent the point at which the melting parameters are changed. From the experiment set up it can be seen that for all the samples, changes in process parameters are initiated midway through the build, which is at 10 mm. However, in Figure 4-9, it can be seen that the transition position is marked at 7 mm for one sample. This is due to the shift in the transition point during the build resulting due to the sagging of the bottom section due to larger melt pools. By measuring the amount of sagging at the bottom of the sample, the transition location is identified. Also, there is an increase in the standard error value with increase in prior beta grain size when compared to the cases with smaller prior beta grains. This can be explained by the fact that the number of grains

available at a cross-section decreases with an increase in grain size and this results in an increase in standard error. It can also be observed that the transition distance from X→4X is almost 2 times the transition distance from X→2X. This can be explained using nucleation and grain growth concepts in solidification theory which is discussed in the following section.

Table 4-3: Details of the average prior beta grain size at different heights for sample 1 (X→2X transition).

Distance from the Base (mm)	Average Prior Beta Grain Size (µm)	Standard Deviation (µm)	Standard Error (µm)
5	127	91	9
6	128	71	7
7	125	68	6
8	118	61	6
9	121	66	6
10	166	91	10
11	171	87	10
12	223	111	14
13	218	119	15
14	213	123	16
15	255	176	24
16	217	139	17

Table 4-4: Details of the average prior beta grain size at different heights for sample 2 (2X→X transition).

Distance from the Base (mm)	Average Prior Beta Grain Size (µm)	Standard Deviation (µm)	Standard Error (µm)
5	239	138	19
6	224	108	14
7	223	142	19
8	218	142	18
9	142	93	10
10	113	62	6
11	120	79	7
12	114	72	7
13	122	89	9
14	105	71	6
15	124	73	7
16	111	74	7

Table 4-5: Details of the average prior beta grain size at different heights for sample 3 (X→4X transition).

Distance from the Base (mm)	Average Prior Beta Grain Size (µm)	Standard Deviation (µm)	Standard Error (µm)
5	135	69	7
6	131	74	7
7	145	86	9
8	138	65	6
9	184	94	11
10	310	157	24
11	295	147	15
12	335	204	35
13	393	262	48
14	470	320	63
15	516	262	54
16	477	274	52

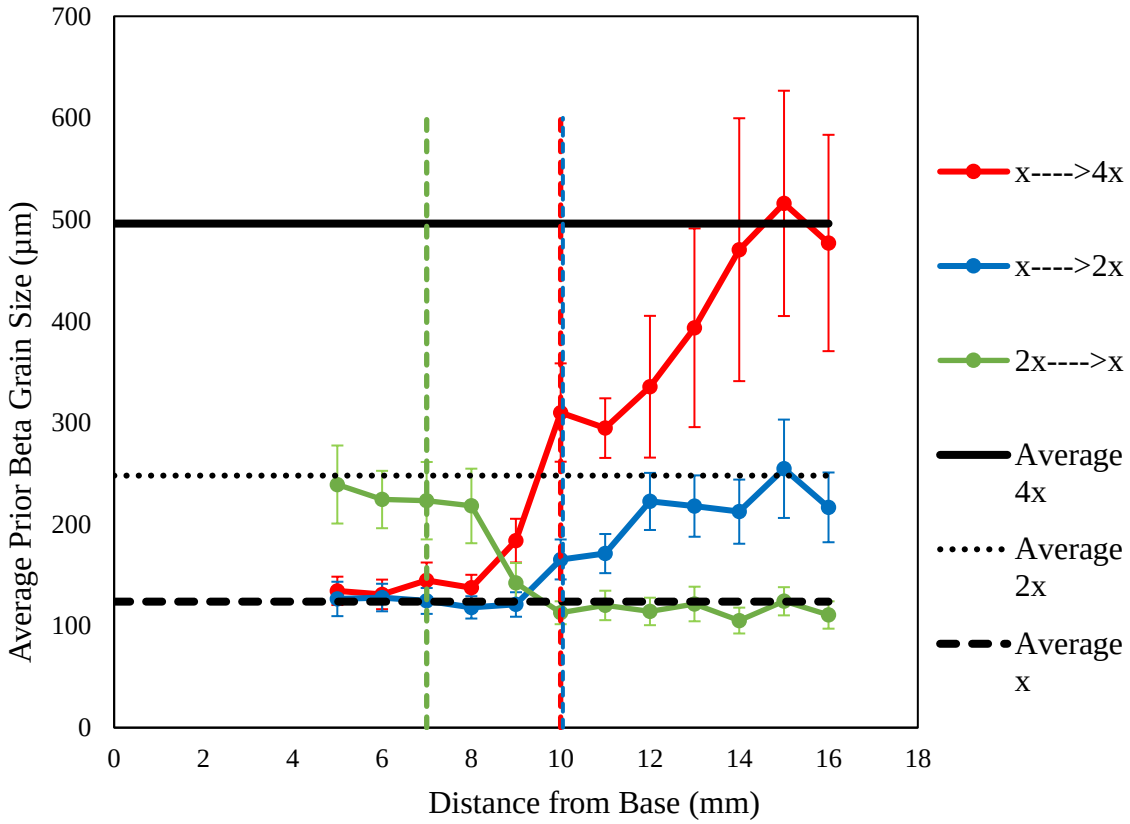

Figure 4-9: Average prior beta grain sizes at different heights for samples 1-3.

If we consider the X→2X example. At the interface, dendrites growing in 2X region nucleate from the grains in the X region and are large in number when compared to the dendrites nucleating from coarser grains. These dendrites have to grow through a few layers before they reach a steady state in 2X region. The transition distance from X→2X is the same as the transition distance from 2X→X. Also, it is important to note from Figure 4-9 that for the X→4X transition, there is an increase in the average prior beta grain size even before the point of transition in the process parameters. The 4X melt pools are bigger and they remelt the previous (lower) layers which will increase the grain size in the previous layers. Apart from the above observations, these types of measurements can be used to perform a non-dimensionalization of the grain sizes that would potentially allow for the estimation of transition distance for any initial and final value of average grain sizes. However, in this work, only two different grain size transitions are explored and hence it did not result in enough data points to test if non-dimensionalization, or rule of thumb, can be developed to estimate the transition distance.

When collecting the grain size data to estimate the average prior beta grain size, individual intercepts were also estimated which were then used to construct the cumulative probability distribution plots for grain sizes. At the part heights considered, there is a large variation in grain width values across the width of the sample. This is evident from the grain size distribution plots shown in Figure 4-10 to Figure 4-12 for samples 1-3 respectively. There is wide dispersion in the grain size values and they follow close to log-normal distribution since the points form a straight line in the plot. These distributions are provided at the steady-state region in the bottom block, at the point of transition, and at the steady-state region in the top block. It can be observed from these plots that there is a gradual shift in the cumulative probability distributions with changes in melting parameters that result in different prior beta grain sizes. It is expected that the distributions will

overlap for steady state region measurements. This information is not provided in the plots here, however steady-state region behavior is discussed in Chapter 3. It is also interesting to note from the x-2x and 2x-x plots that the large grains in the transition region tend to take longer to transition than the small grains (blue and red curves overlap at large grain size in both plots). This agrees well with the solidification theory because large grains take longer to die out.

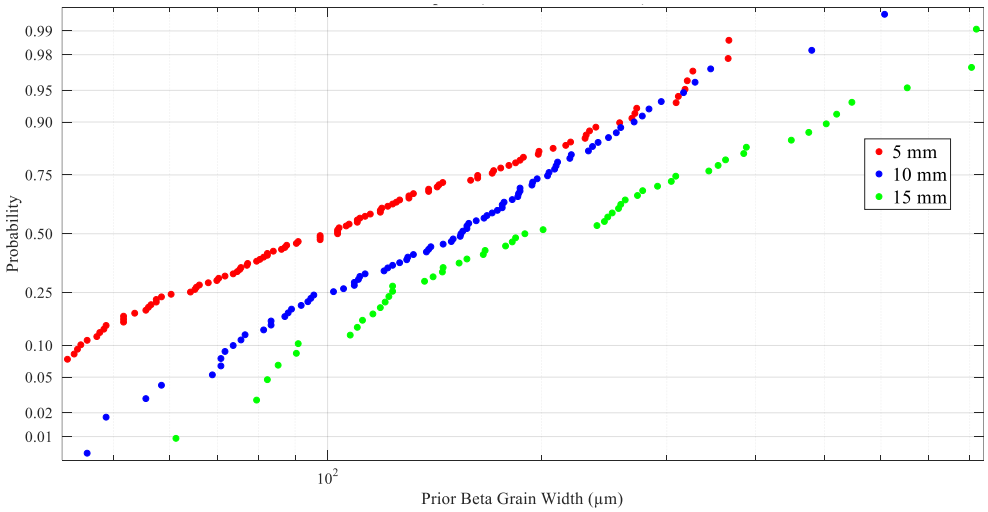

Figure 4-10: Grain width distributions at different heights in sample 1 (X→2X transition).

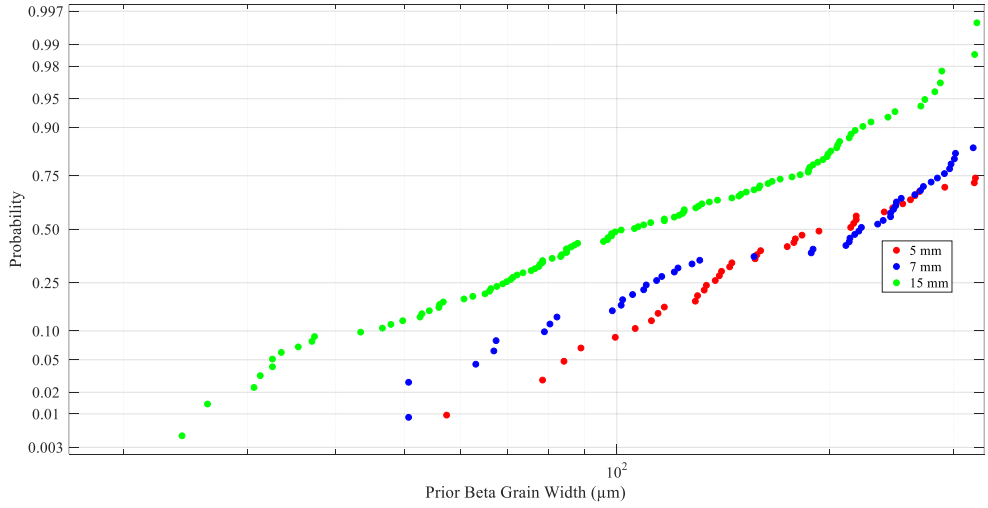

Figure 4-11: Grain width distributions at different heights in sample 1 (2X→X transition).

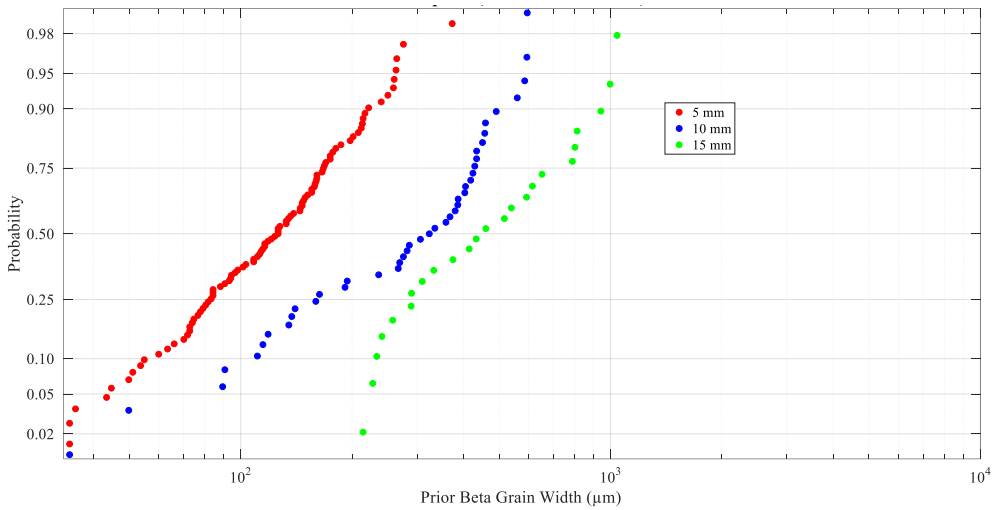

Figure 4-12: Grain width distributions at different heights in sample 1 (X→4X transition).

4.3.2 Dovetail Component

Using the knowledge from in-plane and along the build direction transitions, the dove tail component was manufactured such that the stress concentrator regions have finer prior beta grains when compared to the rest of the dove tail, as shown in Figure 4-13. The red arrows identify the interfaces between the stress concentration regions and the rest of the component. Based on the transition distance knowledge from the previous section, a response distance of 2 mm was allowed for grains in the stress concentration region from the location where parameter change is initiated.

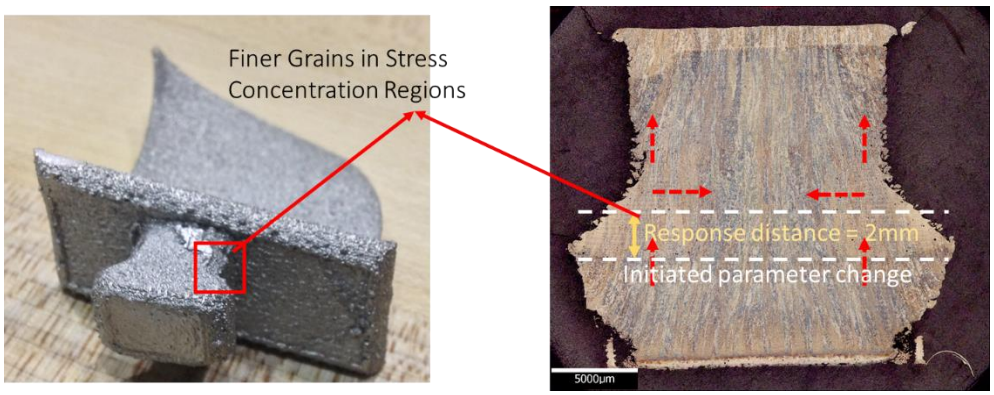

Figure 4-13: Generic compressor blade and the polished and etched cross-section of the dovetail region with stress concentration regions identified.

Details of the measured grain sizes from the interface region are summarized in Table 4-6. It can be observed from these measurements that the grains in the stress concentrator region are finer than the targeted grain sizes in Table 4-2. This can be explained based on the fact that the targeted grain size is measured from the central region of the solid blocks away from the edges whereas the stress concentrator is the edge region of the component. In the edge regions, during the solidification process, grains nucleate from the neighboring powder particles which results in finer and larger number of grains when compared to the central section of the solid blocks where grains grow bigger with part height. From Figure 4-14 it can also be observed that grains near the edge are bent inwards since solid material has higher thermal conductivity when compared to the surrounding powder material and dendrites grow in the direction of maximum thermal gradient.

Table 4-6: Prior beta grain size measurements in the dovetail region from the interface.

Height from the Interface (mm)	Average Prior Beta Grain Size (µm)	Standard Deviation (µm)	Standard Error (µm)
0	157	73	11
1	92	59	6
2	60	59	6
4	60	37	4

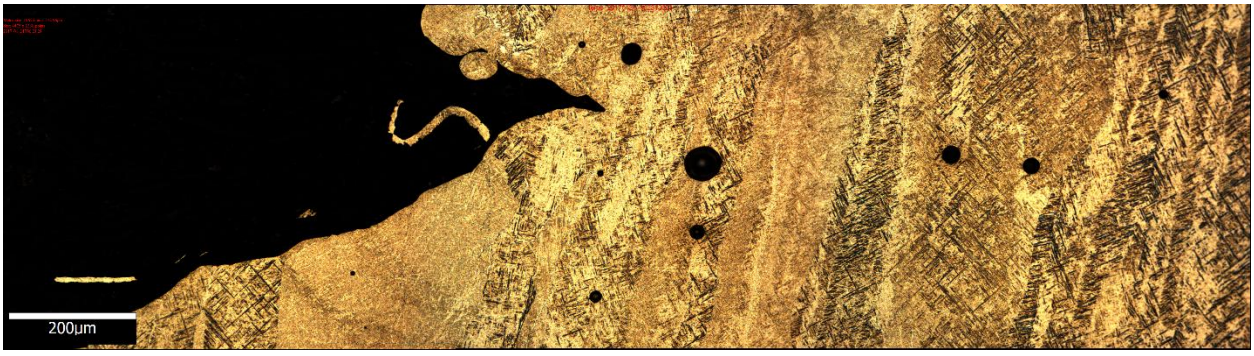

Figure 4-14: Example micrograph of the stress concentrator region.

Average prior beta grain sizes are plotted against the distance from the interface in Figure 4-15. On the x-axis, 0 mm refers to the interface where the change in melting parameters was initiated during the build. It can be observed from the plot that the average grain size reaches a steady-state within 2 mm which agrees with the estimated distance from the previous section.

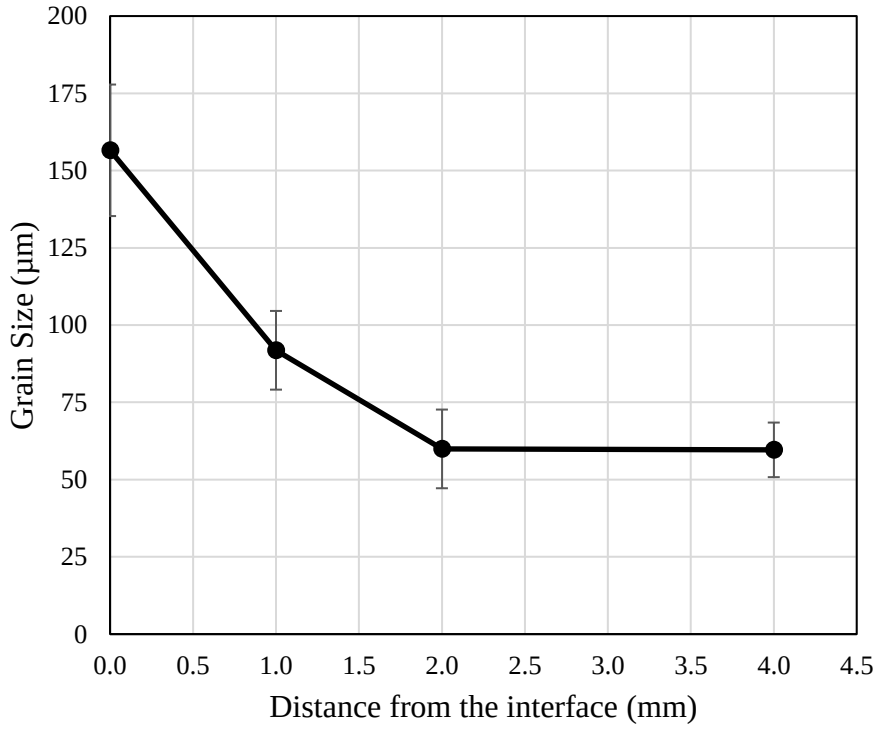

Figure 4-15: Average prior beta grain sizes at different heights from the interface.

4.4 Conclusions

This study contributes to the understanding of the transition/response in prior beta grain size with changes in process parameters during location-specific control of as-built solidification microstructure in the Arcam EBM process space for Ti64. Two different types of transitions are identified based on the plane in which process parameters are changed: in-plane transition and build direction transition. Results demonstrate that in-plane transition is on the order of the melt pool widths (microns) whereas the build direction transition depends on the initial and final prior beta grain sizes and is typically on the order of multiple melt pool depths (millimeters). The

response distance for transition along build direction depends on the initial and final grain size. These results are further used to vary the microstructure in different locations of the dovetail region of the generic GE compressor blade in order to achieve steady-state fine grains in the regions that act as stress concentrators when compared to the rest of the dovetail region. This work is not only applicable for location-specific microstructure control in a single component, it also provides relevant information for understanding the effect of existing substrate microstructure for repair of components where new material is deposited onto the existing substrate.

5 Location Specific Control of Solidification Microstructure in Laser Powder Bed Fusion of Aluminum Alloy AlSi10Mg

5.1 Overview

In Chapter 3, location-specific control of prior beta grain size in a single component made of Ti64 was achieved by means of integrated melt pool geometry and microstructure control. In this chapter, solidification microstructure control through melt pool geometry control is investigated in detail for the AlSi10Mg alloy in a laser melting process. First, melt pool geometry control across the available selective laser melting process space was studied utilizing both modeling and experimental techniques, followed by examination of solidification cooling rates from the thermal model which govern the size scale of the features that are formed at solidification. After that, single bead, single layer pad, and multi-layer pad experiments were performed and analyzed for melt pool geometry, variability in melt pool geometry, defect identification and solidification microstructure.

This work (i) identified the regions in available processing space that will minimize the defects due to under-melting and keyholing porosity and produce a high quality part and (ii) established concepts of integrated melt pool geometry and microstructure control in laser melted AlSi10Mg. Results from this work will help the user to optimize the process for desired outputs instead of just using the nominal parameters recommended by the machine manufacturer.

5.2 Methods

The following section discusses the process mapping approach, finite element model and experiments that are used in this Chapter.

5.2.1 Process Mapping Approach

The process mapping technique developed by Beuth et al. [87] relates identified primary process variables: beam power (P), travel speed (V), background temperature, material feed rate or layer thickness and local part geometry to main process outcomes like process precision, build rate, microstructure, and flaw formation [88]. These identified process outcomes are critical in determining the overall part quality. Using this approach, both numerical modeling results and experiments can be mapped with minimal data to characterize a process. These maps are especially useful in opening up the process space and utilizing the available space to meet application-specific requirements [112].

5.2.2 Finite Element Model

Finite element (FE) simulations were run in the ABAQUS [113] environment. This model is based on the thermal model developed by [71] for the electron beam wire feed process. In this model, a laser beam carrying a specified power moves along the length of the plate in a straight line with a specified travel speed. This simulates the no-added single bead tests where no powder is added to the substrate. A three dimensional solid element type DC3D8 for diffusive heat transfer is used in the model. This is an 8-node linear brick element. Energy delievered by the laser beam is modeled as a uniformly distributed circular heat flux which is applied on the top face of the elements [105] as shown in Figure 5-1. This heat flux travles along the axis of symmetry. The diameter of the ciruclar heat flux is made equivalent to the estimated spot size on the EOS machine which is 100 μm [114]. The model is large enough to avoid the effect of free edges on the melt pool. The mesh is biased toward the region of interest and a symmetry condition is imposed on the along the mid-plane of the melt pool, which allows only half of the melt pool to be modeled, thus saving computation time. An example biased mesh is shown in Figure 5-1 and Figure 5-2.

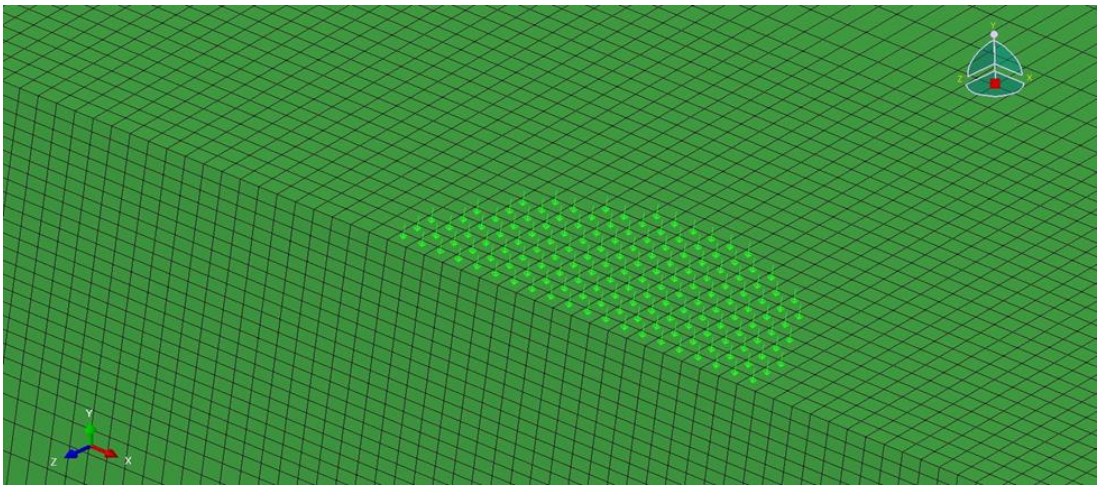

Figure 5-1: 3D FE model showing uniform circular heat flux distribution.

Simulation parameters are summarized in Table 5-1. The temperature-dependent thermo-physical properties are available for an aluminum alloy composed of 7% Silicon [115], while the alloy of interest is composed of 10% Silicon. This was the closest estimate possible from the available information. It is expected that there will be a difference in the liquidus and solidus temperatures on the order of 20 K [116]. Nevertheless, this minor difference should not have a significant effect on the geometry and cooling rate related output from the model which are the primary interest in this work.

Table 5-1: Simulation Parameters.

Input Parameter	**Range**
Absorbed power (W)	30 - 111 (3 levels)
Travel velocity (mm/s)	200 – 1400 (6 levels)
Spot size (μm)	100, uniform circular heat distribution
Preheat temperature (K)	308
Melting range (K)	840-887
Latent heat (J/Kg)	425000
Thermal conductivity (W/m K)	163-73.9 W/m K for T ranging from 298-1273 K
Specific heat (J/kg K)	880-1190 J/kg K for T ranging from 298-1273 K
Density (kg/m^3)	2680-2300 kg/m^3 for T ranging from 298-1273 K

Radiation and convection to the surroundings are not modeled since the primary heat transfer pathway is conduction into the substrate. These phenomena do not have a significant effect on melt pool geometry for laser based AM processes [117] . Apart from the radiation and convection at the surfaces, there are temperature dependent fluid flow effects inside the melt pool which affect the melt pool depth which is discussed in detail by [73]. These phenomena are not included in the current model. However, when the model results are compared against the experiments, these affects are factored in as "effective absorptivity" which is discussed in detail in § 5.3. Also, it is observed that fluid flow in the melt pool decreases the surface temperatures of the melt pool, especially at the location where heat flux is being applied [73]. In the present work, cooling rates are extracted at the tail end of the melt pool away from the point where the heat source is applied and hence they should not be significantly affected if fluid flow inside the melt pool is not considered in the heat transfer model.

A melt pool is identified by the region which has temperatures above or equal to the melting temperature of the alloy considered for the analysis. Figure 5-2 (Left) shows an example of the FE model with melt pool identified as well as the cross-section of the melt pool perpendicular to beam travel direction. The cross-sectional area is the maximum area of the steady-state melt pool perpendicular to the beam travel direction as marked in Figure 5-2 (Right). Likewise, melt pool width and depth are also estimated from the FE model. The cooling rate (dT/dt) is calculated from the distance (Δx) between the solidus and liquidus isotherms as identified in the Figure 5-3 for a specific beam power (P) and beam travel speed (V) as in Equation 5.1. ΔT is the solidification interval in this equation.

$$\frac{dT}{dt} = \frac{\Delta T * V}{\Delta x} \tag{5.1}$$

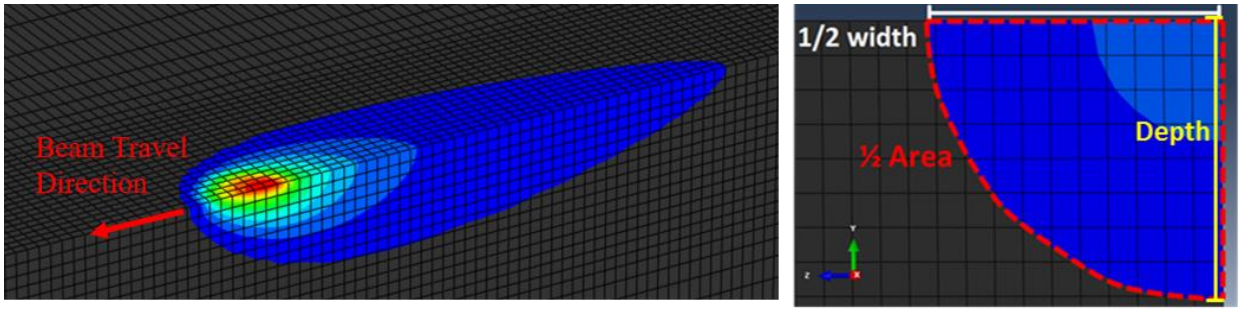

Figure 5-2: (Left) Simulated steady-state melt pool shown with beam travel direction and (Right) cross-section.

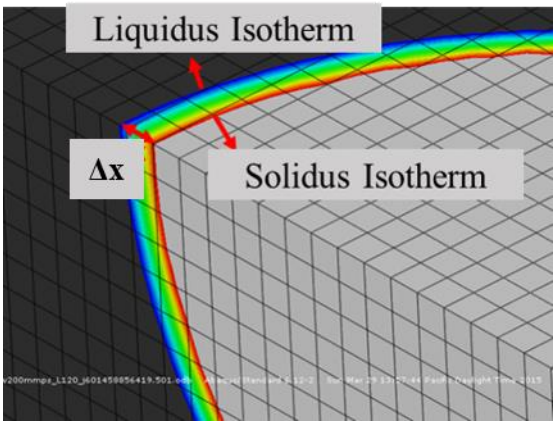

Figure 5-3: Illustration of distance calculation between solidus and liquidus isotherm.

5.2.3 Experiments

Simple single melt track experiments were performed by varying beam power and velocity on an AlSi10Mg substrate without adding any powder. This was done to find the process window that will result in continuous and good quality melt tracks. Also, process maps to control melt pool geometry and solidification microstructure were developed using these experiments. Single track experiments were then followed by single layer pad experiments to study the variability in melt tracks in one layer. Knowledge from the single track and single layer pad experiments was used to deposit solid blocks which are either rectangular or cubic samples. Depending on the part quality and expected microstructure, process inputs were further narrowed down to build the final test geometry which is that of a real part to test the applicability and limitations of the concepts

developed from single beads and multi-layer pads. Thus, these experiments were performed in succession to systematically develop a process knowledge database as shown in Figure 5-4.

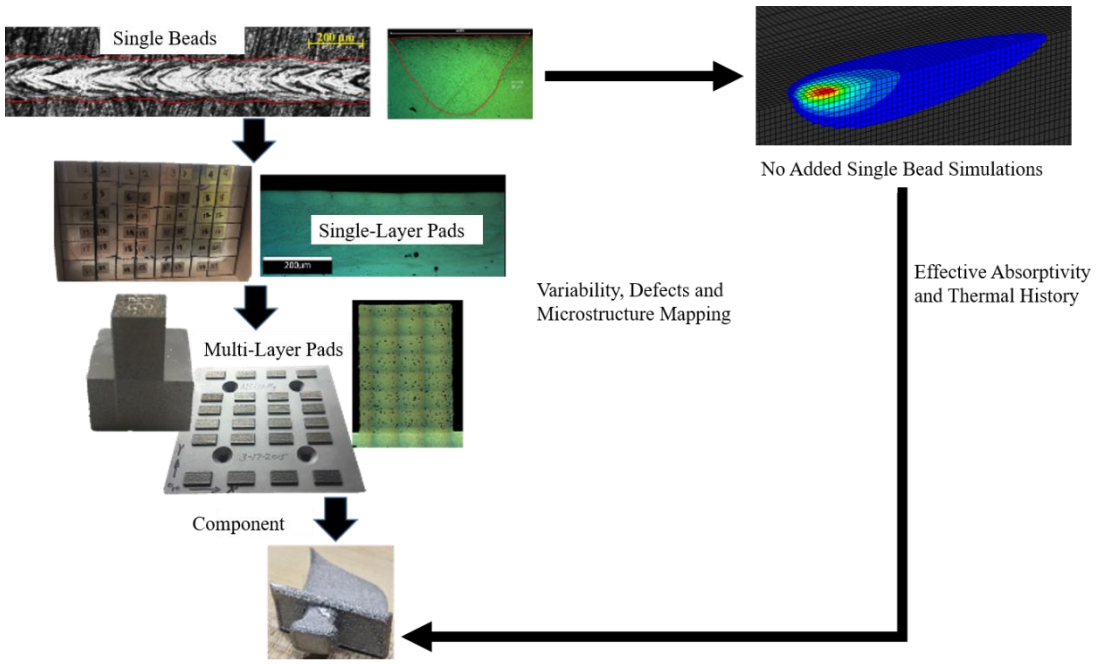

Figure 5-4: Progression of test geometries and integration of simulation results.

Single beads, single layer pads and multi-layer pad experiments were performed on an EOS M280 at the Alcoa Technical Center in New Kensington, PA whereas, the component is fabricated on EOS M290 machine at Carnegie Mellon University. The feedstock powder used for the experiments is spherical, gas atomized powder produced in an inert Argon gas. This is the standard powder supplied by the EOS machine manufacturer. The build chamber was ventilated with Argon during the experiments. Details of the test layouts and parameters are discussed in detail in the following sections.

5.2.3.1 Single Beads

The goal of the experiments is to characterize the process throughout the available process space. These experiments are used to analyze the melt pool geometry and primary solidification

microstructure that is controlled by cooling rates at solidification. Process parameters are outlined in Table 5-2 and illustrated in Figure 5-5.

Table 5-2: Process Parameters Used in Experiments.

Parameter	Range
Beam power (W)	100 – 370 (see Figure 5-5)
Beam travel velocity (mm/s)	200 – 1400 (see Figure 5-5)
Preheat temperature (K)	308
Focus diameter (μm)	100 [114]

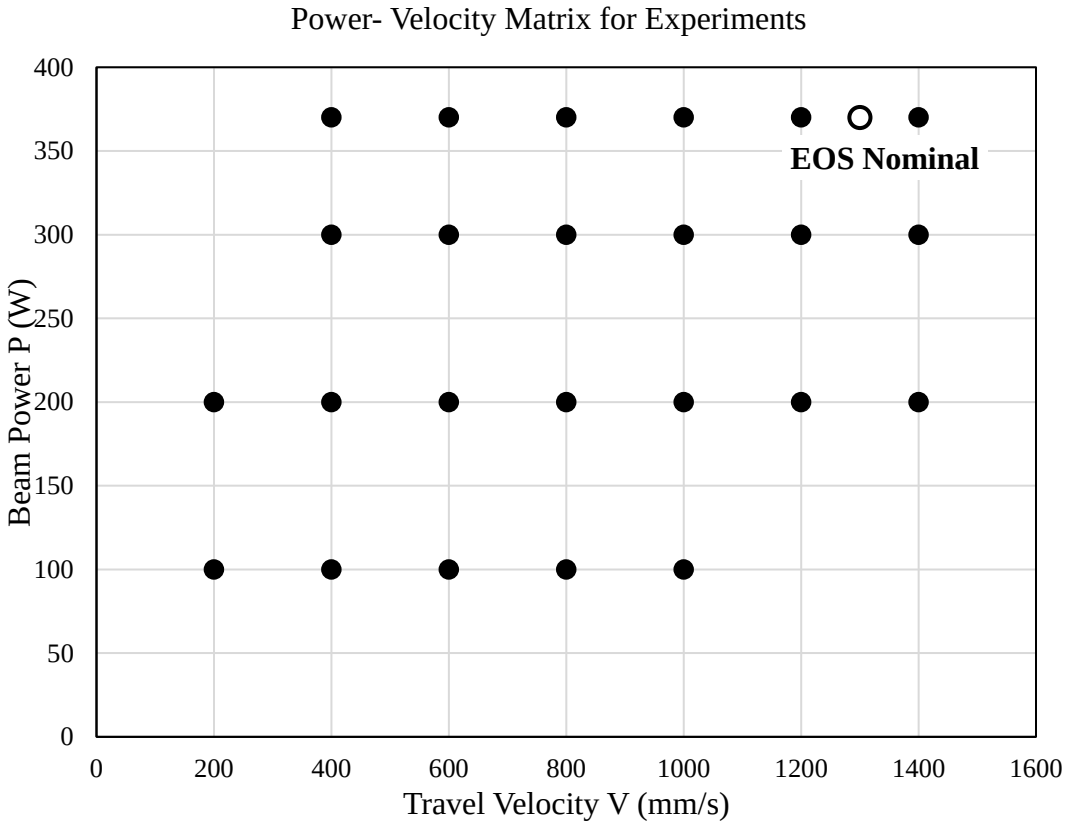

Figure 5-5: Experiment matrix in the Power-Velocity space at which single bead, single layer pad and multi-layer pad tests were performed.

No added powder single bead experiments were run on plates that are made of the material of interest. Usually plates are manufactured by rolling and AlSi10Mg is a typical casting alloy which made it difficult to obtain a plate that can be used. As an alternative, 2 mm tall AlSi10Mg blocks were built on an Al5083 plate using standard EOS parameters outlined in Table 5-3. These

blocks act as AlSi10Mg substrate on which single beads can be deposited. To avoid depositing on a rougher surface which makes it difficult to identify the melt track precisely, the top surface of the blocks was surfaced using a mill before depositing the single beads at different power and velocity combinations. Figure 5-6 shows the layout of the experiments along with an example image of the alternate set up to create AlSi10Mg substrate for single bead experiments.

Table 5-3: Nominal Parameters for AlSi10Mg on EOS M280.

Parameter	Value
Beam power (W)	370
Beam travel velocity (mm/s)	1300
Preheat temperature (K)	308
Focus diameter (µm)	100 [114]
Layer thickness (µm)	30
Hatch spacing (µm)	190
Scan rotation	67°
Sky writing	On

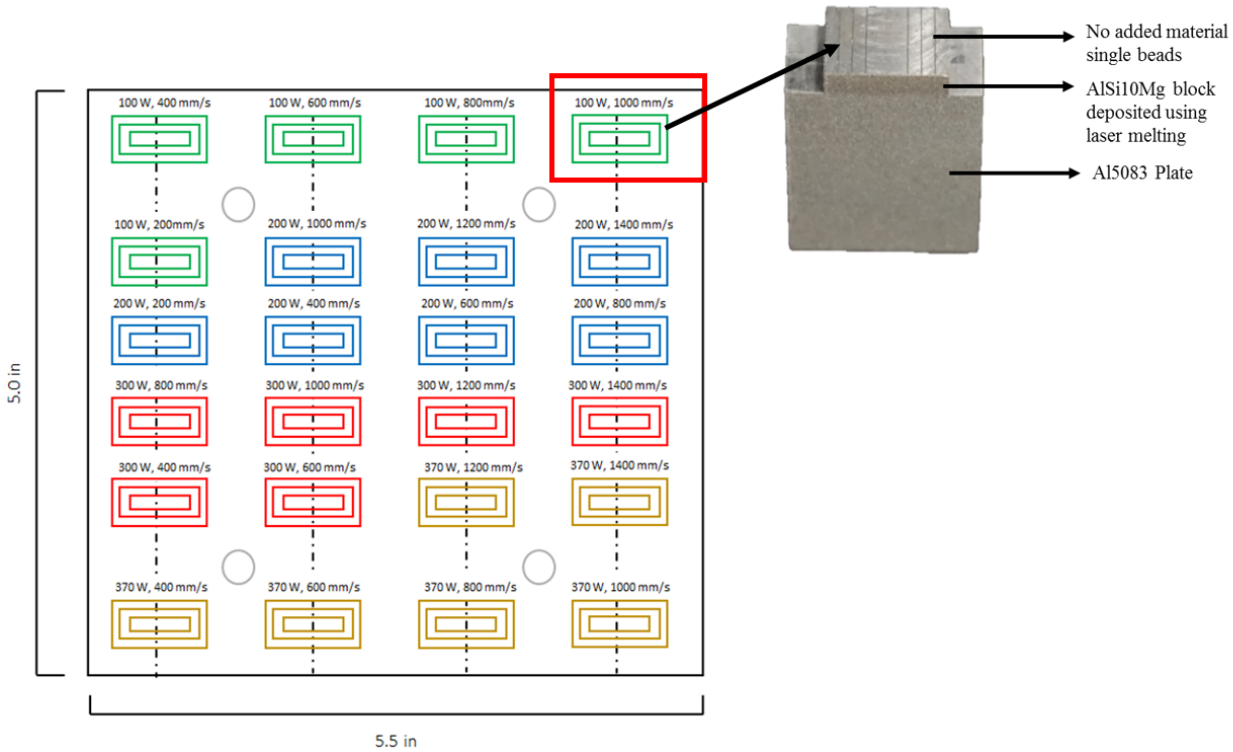

Figure 5-6: Experiment layout for single bead tests; Example single bead experiment where beads are deposited on a laser deposited AlSi10Mg block.

5.2.3.2 Single Layer Pads

Based on the analysis of the single bead tests, single layer pad tests were done for the same 24 PV combinations that were used for single bead tests as shown in Figure 5-5. In these tests, the hatch spacing is adjusted such that the overlap between the adjacent melt pool tracks for different process parameters is consistent with the overlap for nominal process parameters which is 7%. The adjusted hatch spacing values and resulting overlap are illustrated in Figure 5-7. Different colored pads in this layout correspond to different power levels used in the experiment. On the EOS machine, hatch spacings can only be entered as multiples of 10 and hence some of the hatch spacing values have to be rounded off to the nearest multiple of 10. This resulted in some pads having the same hatch spacing value which is evident from Figure 5-7. The overlap shown in Figure 5-8 (left) refers to the overlap between the adjacent melt tracks which is calculated using the equation shown in the figure (right).

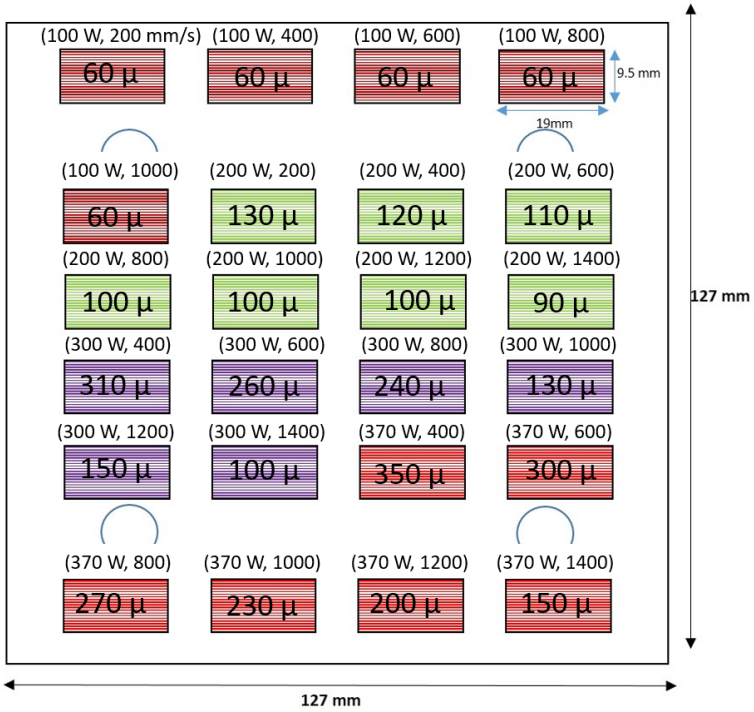

Figure 5-7: Pad experiment layout, the adjusted hatch spacings noted in the figure were chosen to produce pads with the nominal 7% overlap.

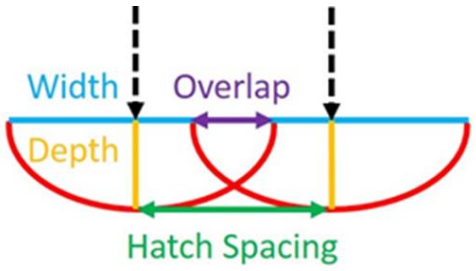

$$Overlap\ (\%) = \frac{(Width - Hatch\ Spacing)}{Width} * 100$$

Figure 5-8: (Left) Illustration of the overlap between the adjacent melt tracks and (Right) Equation to measure the overlap between adjacent melt tracks for a given melt pool width and hatch spacing.

These experiments are especially useful to study the variability in melt pool dimensions such as melt pool width and depth which is critical to avoid porosity in the fabricated components using the geometric model for porosity [65]. These experiments also provide useful information on whether there is heat buildup that affects the melt pool geometry and microstructure when depositing the melt tracks side by side. An example single layer pad along with the cross-section is shown in Figure 5-4.

5.2.3.3 Multi-Layer Pads (Solid Blocks)

Similar to single layer pad tests, multi-layer pad tests or solid blocks were built for 24 PV combinations that were used for single bead tests as shown in Figure 5-5. In these tests, the hatch spacing is adjusted such that the overlap between the adjacent melt pool tracks for different process parameters is consistent with the overlap for nominal process parameters. Apart from beam power, velocity and hatch spacing, all other process parameters are maintained at nominal values provided in Table 5-3. An example cross-sectioned multi-layer pad is shown in Figure 5-4. These experiments are useful to study the process defects and solidification microstructure in bulk components.

5.2.3.4 Component (US Thirteen Star "Betsy Ross" Flag)

The main goal of the present work is to achieve good quality parts along with controlling the solidification conditions in different locations of the component resulting in different solidification microstructures. Utilizing knowledge from the prior experiments, a US Thirteen Star "Betsy Ross" flag shown in Figure 5-9 was fabricated with different processing conditions in different components of the flag. In order to avoid any defects due to lack of overlap between different components that were built with different parameters, the entire flag was built with smaller size melt pools and then the larger size melt pools were deposited selectively in the regions where coarser microstructure is desired. Details of the process parameters are outlined in Table 5-4.

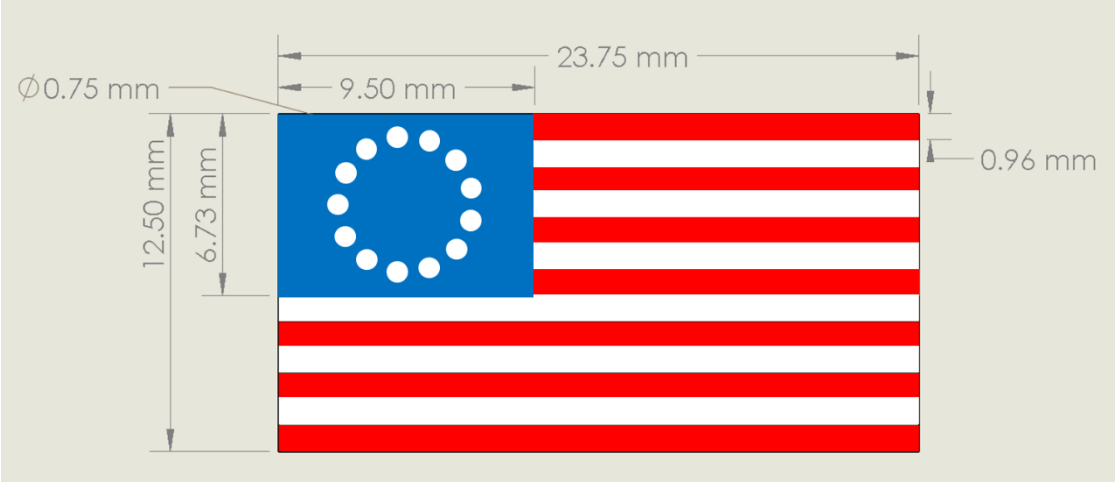

Figure 5-9: Experiment layout for the Flag.

Table 5-4: Experiment parameters used for fabrication of the Flag.

Location	Power (W)	Velocity (mm/s)	Hatch Spacing (µm)	Layer Thickness (µm)	Estimated Coarse to Fine Cell Spacing Ratio
Stars	300	1400	60	20	1
White Stripes	300	1400	60	20	1
Red Stripes	370	1000	140	20	1.33

Blue Background for Stars	370	1000	140	20	1.33

5.2.4 Sample Preparation and Characterization

Black dashed lines across the plate in Figure 5-6 are the locations where melt tracks are sectioned to observe the cross-sections of the single bead, single layer pad and multi-layer pad experiments. Sectioning is done using a wire-cut Electrical Discharge Machine (EDM) at the Alcoa Technical Center. An example of the sectioned sample is shown in Figure 5-6. For the component, in order to retain the entire flag, sectioning was not done. Instead the sample is mounted such that after polishing, the top view of flag can be imaged. All samples were mounted in Konductomet™ mounting compound via compression mounting.

Single beads and single layer pads are polished using the Struer's auto-polisher. The polishing procedure is outlined in Appendix A. Multi-layer pads and component are polished using Buehler's auto-polisher following the standard procedure laid out by Buehler as shown in Appendix A. Once the samples are polished, they are etched using Barker's reagent for 60 seconds. Barker's reagent consists of 2% aqueous flouoroboric acid (HBF_4) [38]. Deionized water is used to prepare the aqueous solution.

A Zeiss AX10 optical microscope was used to image the top surface of the single beads before sectioning the samples. These images are taken at the middle section of the tracks so that there are no turn around or edge effects and the melt pool has reached a steady state. An Example image of the top surface of the no added material single bead is shown in Figure 5-10. The red lines at the border of the melt track were manually added using GIMP software as a new layer in the image. After that, the layer was filled with black color and the distance between the red lines

was measured automatically using an image processing script to calculate the melt pool width along the melt track [70].

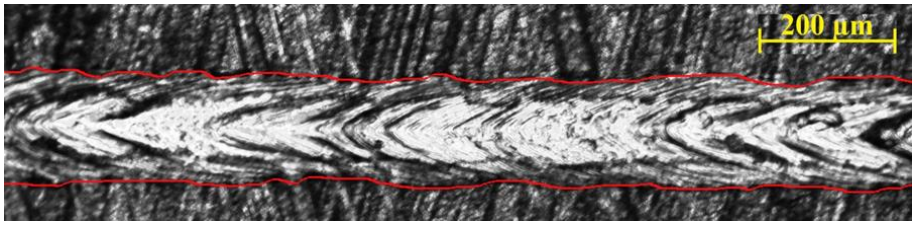

Figure 5-10: An optical microscope image of the surface of an AlSi10Mg melt pool track with the edges manually highlighted in red. The melt pool width (distance between the red lines) was measured at every pixel along the length of this image, the results of which were then averaged together. This single bead track was melted using a beam power or 370 W and a velocity of 1400 mm/s.

Polished samples were imaged using an Alicona InfiniteFocus optical microscope. Figure 5-11 shows example micrographs of the single bead, single layer pad and multi-layer pad samples with melt pools identified along with melt pool geometry characteristics that are of interest. Melt pool geometry was measured using ImageJ software.

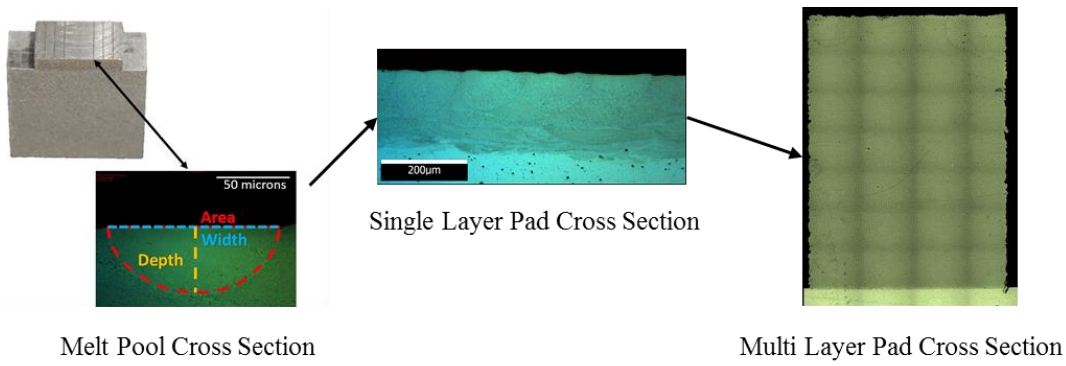

Figure 5-11: Example images of the melt pool cross-sections for single bead → single layer pad → multi-layer pad tests.

A Quanta 600 Scanning Electron Microscope (SEM) was used for obtaining micrographs in secondary electron imaging mode since it captures the contrast from surface topography resulting from etching. For cell spacing measurements in single beads and multi-layer pads, the line intercept method [106] is used. However, to improve the efficiency and reduce the human bias

when measuring the flag component, ImageJ and Matlab routines were used to measure cell sizes by utilizing image processing and particle analysis methods. For the component, Figure 5-12 shows the sequence of the steps used in the cell-size analysis with example micrographs. A technique which involves dilation of the image followed by erosion was used to close the gaps between cells that were not connected due to non-uniform or insufficient etching at few locations. After the edges are closed, particle analysis in ImageJ was used to analyze the cells. Quantities of interest from particle analysis are Equivalent Projected Circle Diameter (EQPC), maximum caliper diameter (Feret Diameter) and minimum caliper diameter (Min Feret). This technique not only provides the average measurement values, but also provides information on cell size distributions.

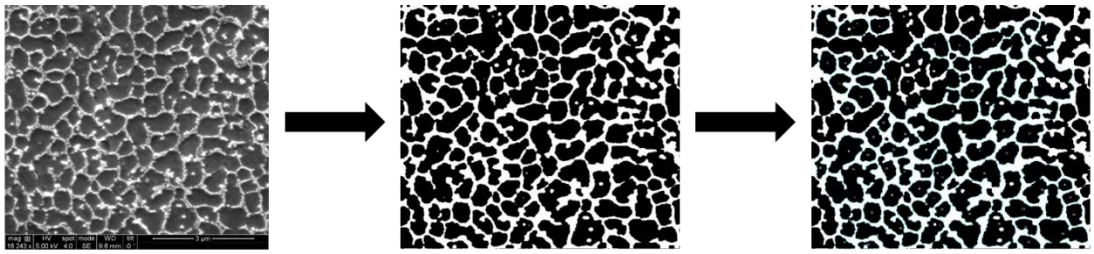

Figure 5-12: Sequence of steps used in cell size measurement in the *Flag* component.

It is important to note that these routines could not be used on single beads and multi-layer pads because cell shape deviated from circular or close to circular shape in some images depending on the growth direction. This variation in cell shape is due to the fact that cross section of the bead or pad is imaged as opposed to the above view image from the component. This change in cell shape led to threshold values varying widely between different images, which in turn prevented automatic extraction of measurement values.

5.3 Results

5.3.1 Process Mapping of Melt Pool Geometry

Process maps are developed for melt pool width, depth and area using the information from experiments and simulations. Comparison between the maps resulting from experiments and simulations is also provided in this section providing insights on the thermal model used in this work.

5.3.1.1 Simulations

Figure 5-13 to Figure 5-15 show the process maps for maximum melt pool area, width and depth estimated from the simulations respectively. It can be observed that there are power-velocity combinations in the machine process variable space that yield constant melt pool dimensions. Most of the machine manufacturers suggest a standard parameter set to be used for fabrication for every material the manufacturer supports. However, not all components require the same properties. These parameters need to be changed based on the application of the component and it is important to understand the process input and output relationships to optimize the parameters for the quantity of interest [112]. Thus, process maps can be used to extend the process limits and utilize the full potential of the process to optimize the quantity of interest during the build.

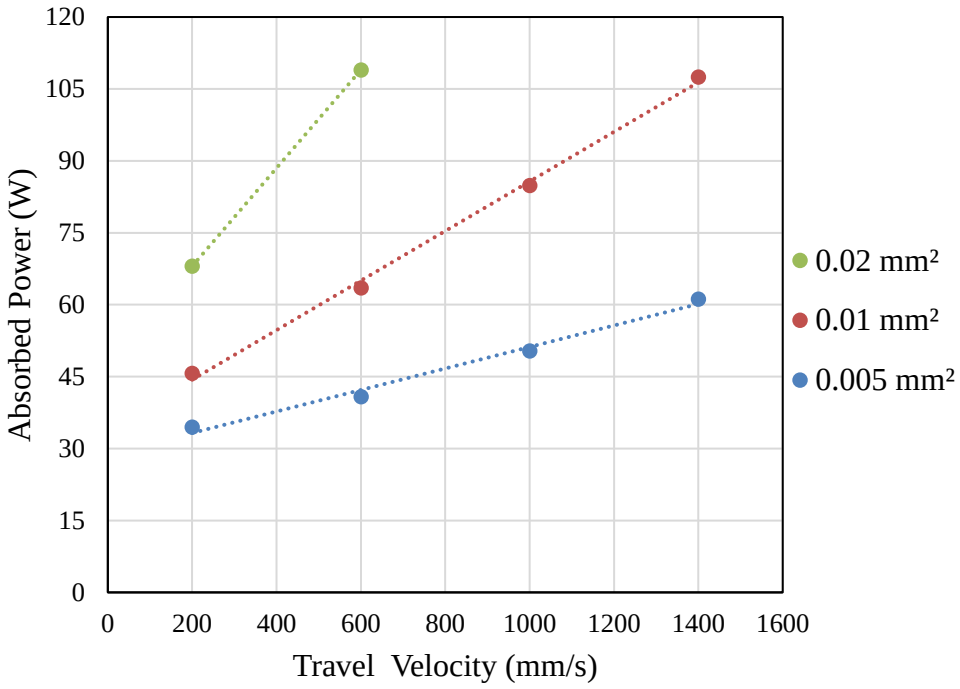

Figure 5-13: Process map of melt pool area for AlSi10Mg. Area remains constant along each line in the map.

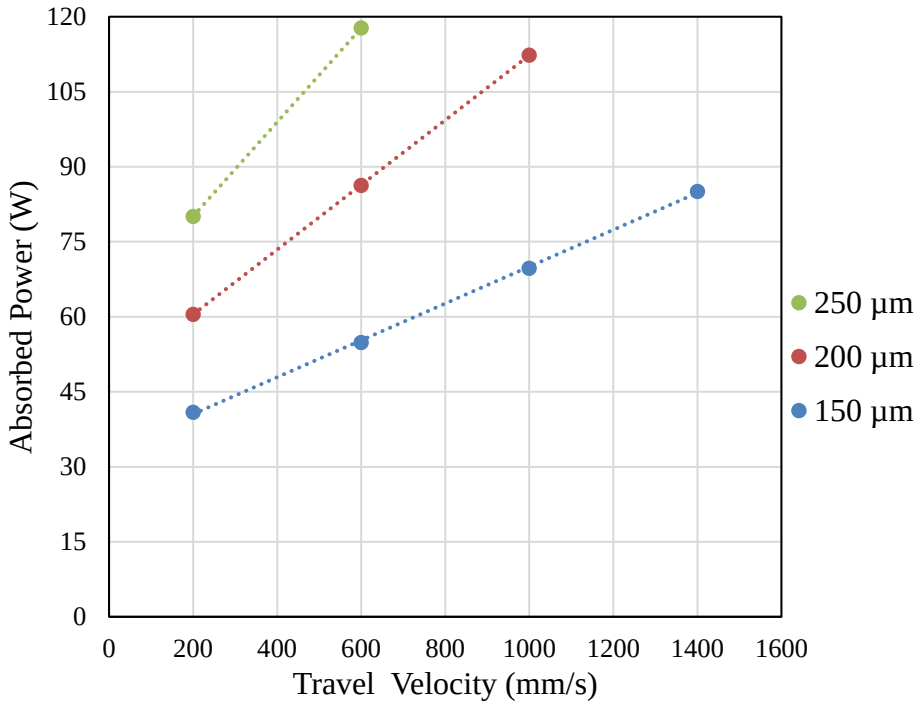

Figure 5-14: Process map of melt pool width for AlSi10Mg. Width remains constant along each line in the map.

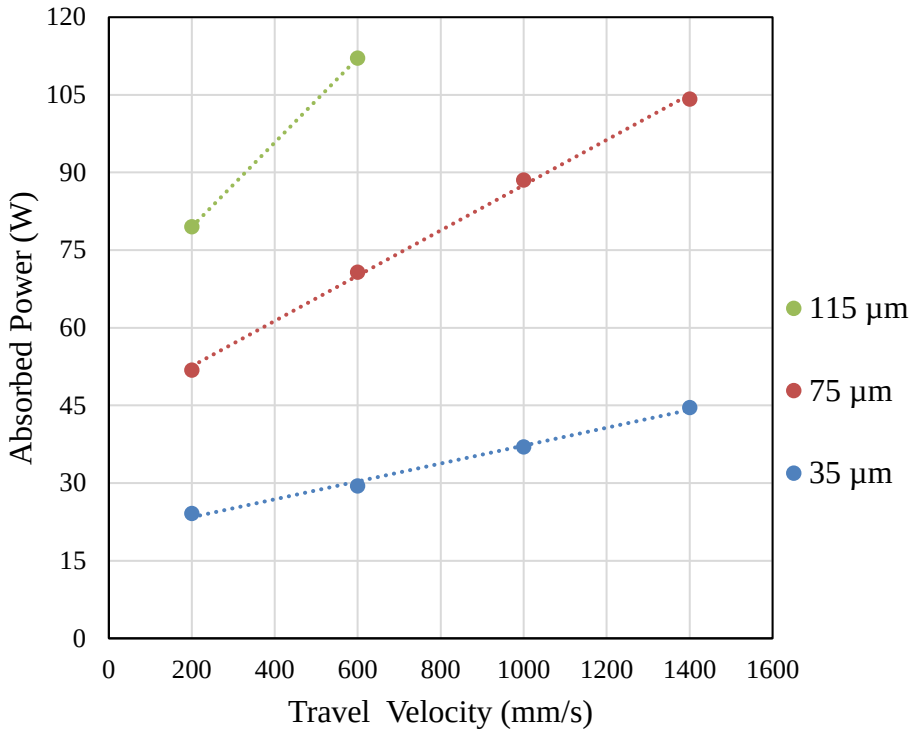

Figure 5-15: Process map of melt pool depth for AlSi10Mg. Depth remains constant along each line in the map.

5.3.1.2 Experiments

First, measurement for melt pool width is discussed for single beads and single layer pads. In single beads, width is measured both at the surface and at the cross-section. In single-layer pads, cross-section widths across the pad are measured to study the variability of melt pool width for a single layer deposition. The number of melt pools available for measurement in a single layer pad depends on the size of the melt pool. Pads with smaller melt pools consist of more melt pools compared to pads with larger melt pools. However, it was ensured that at least 20 melt pools were measured to capture the variability to a statistically significant extent. The melt pool width measurements described above are outlined in Table 5-5.

Table 5-5: Summary of melt pool widths from single beads and single layer pad experiments.

Sample Designation	Beam Power (W)	Travel Velocity (mm/s)	Average Width at the Surface ± 2σ (µm)	Average Cross-sectional Width (Single Layer Pad) (µm) ± 2σ	Single Bead Cross Section Width (µm)
1	100	200	79 ± 4	69 ± 6	67
2	200	200	156 ± 8	183 ± 122	143
3	100	400	75 ± 6	64 ± 8	64
4	200	400	135 ± 4	140 ± 24	126
5	300	400	350 ± 16	351 ± 40	334
6	370	400	410 ± 18	395 ± 36	377
7	100	600	72 ± 2	64 ± 4	63
8	200	600	126 ± 4	131 ± 8	119
9	300	600	295 ± 14	305 ± 26	284
10	370	600	338 ± 16	345 ± 28	326
11	100	800	71 ± 6	64 ±8	70
12	200	800	114 ± 6	111± 14	110
13	300	800	261 ± 6	264 ± 18	256
14	370	800	291 ± 14	308 ± 20	288
15	100	1000	71 ± 10	59 ± 6	65
16	200	1000	105 ± 4	109 ± 10	106
17	300	1000	186 ± 66	196 ± 64	144
18	370	1000	239 ± 8	271 ± 28	245
19	200	1200	98 ± 6	99 ± 6	109
20	300	1200	156 ± 22	140 ± 40	166
21	370	1200	222 ± 16	232 ± 26	220
22	200	1400	95 ± 4	94 ± 10	97
23	300	1400	126 ± 14	120 ± 14	112
24	370	1400	158 ± 14	180 ± 32	161

It can be observed that the shaded rows are examples of melt tracks that have comparatively high variability. These cases are discussed in detail below with melt pool images. In Table 5-5, σ refers to the standard deviation. For Sample 2, though the surface width measurement from the single bead has a smaller amount of variability, the melt pools in the single layer pad are highly variable. The reason for this behavior is not known. Since, for the single beads, the variability is

minimal, this sample is treated as an outlier resulting from the laser malfunctioning or manual error while assigning process parameters on the machine. Hence, measurements from the single layer pad for Sample 2 were not considered in developing the process maps. Figure 5-16shows the melt pools from single beads and the single layer pads from Sample 2. For Sample 17, the variability is higher and on the same order of magnitude for both single beads and single layer pads. An example melt pool for this case is shown in Figure 5-17. Similarly, for Sample 20, the variability in melt pool width found in the single layer pad is higher than the variability measured from surface widths. However, the variability is still on the same order of magnitude. Figure 5-18 illustrates the example melt pool for Sample 20. Samples 17 and 20 were melted at a higher velocity range of 1000 mm/s. Hence, for these samples, variability could be resulting from the higher travel velocity of the laser. From Table 5-5, it can be inferred that the general trend is higher velocities result in higher melt pool variability. Previous works have shown that bead-up of the melt pool due to surface tension effects [118,119] results in irregular melt tracks for lower width to length melt pools. However, melt pool cross section images of these samples did not show any bead up. Thus, the reason for this melt pool variability is not clear. Nevertheless, it is important to consider this variability to control the lack of fusion porosity [65][120].

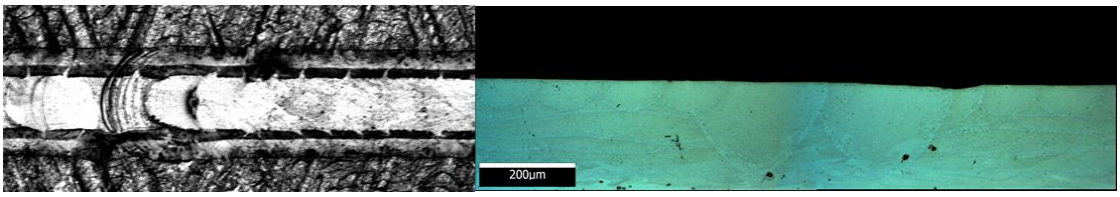

Figure 5-16: (Left) Image of the melt pool track at the surface, (Right) Image of the cross-section of the melt track from single layer pad tests. Tracks in both the images are melted using a beam power of 200 W and a velocity of 200 mm/s.

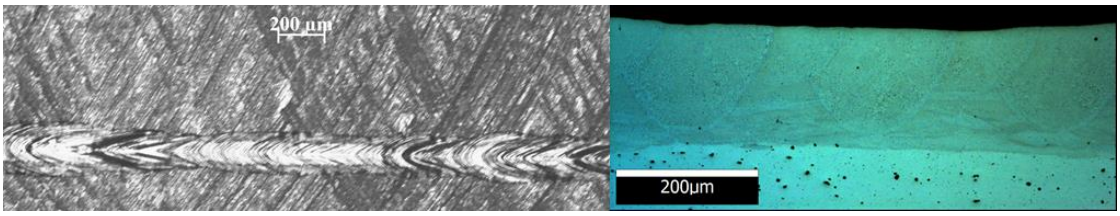

Figure 5-17: (Left) Image of the melt pool track at the surface, (Right) Image of the cross-section of the melt track from single layer pad tests. Tracks in both the images are melted using a beam power of 300 W and a velocity of 1000 mm/s.

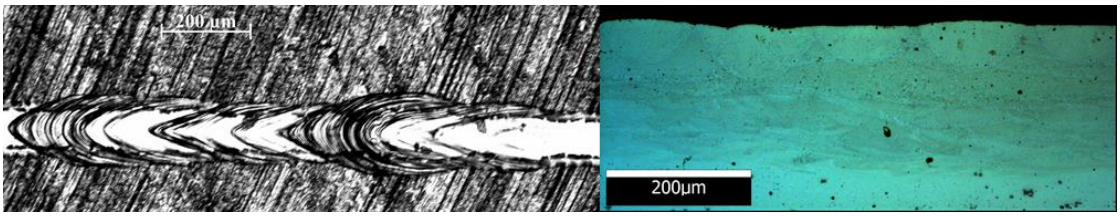

Figure 5-18: (Left) Image of the melt pool track at the surface, (Right) Image of the cross-section of the melt track from single layer pad tests. Tracks in both the images are melted using a beam power of 300 W and a velocity of 1200 mm/s.

Surface width measurements provide insight into melt pool variability. Process maps are developed for surface width and cross-section width of the melt pools from the experiments as shown in Figure 5-19. Dashed lines represent the maximum and minimum possible width (95% bounds) for the process parameter combinations. In other words, they represent the variability in the melt pool width. Process maps show that the variation is more pronounced at higher beam travel velocities. At low velocities, there is agreement between the average width and the cross-section width while this is not necessarily the case in the higher velocity region. However, the cross-section measurement is always within the window prescribed by the surface widths. This can be explained based on the fact that we are looking at one cross-section of the melt pool along the melt track. Hence, a single cross-section measurement does not provide sufficient information to ensure overlap between the melt pools, especially at higher velocities. It is worth noting that the lower bounds of the width values are the critical values when operating in the higher velocity space if the user wishes to guarantee an acceptable overlap between adjacent melt tracks and mitigate lack-of-fusion porosity.

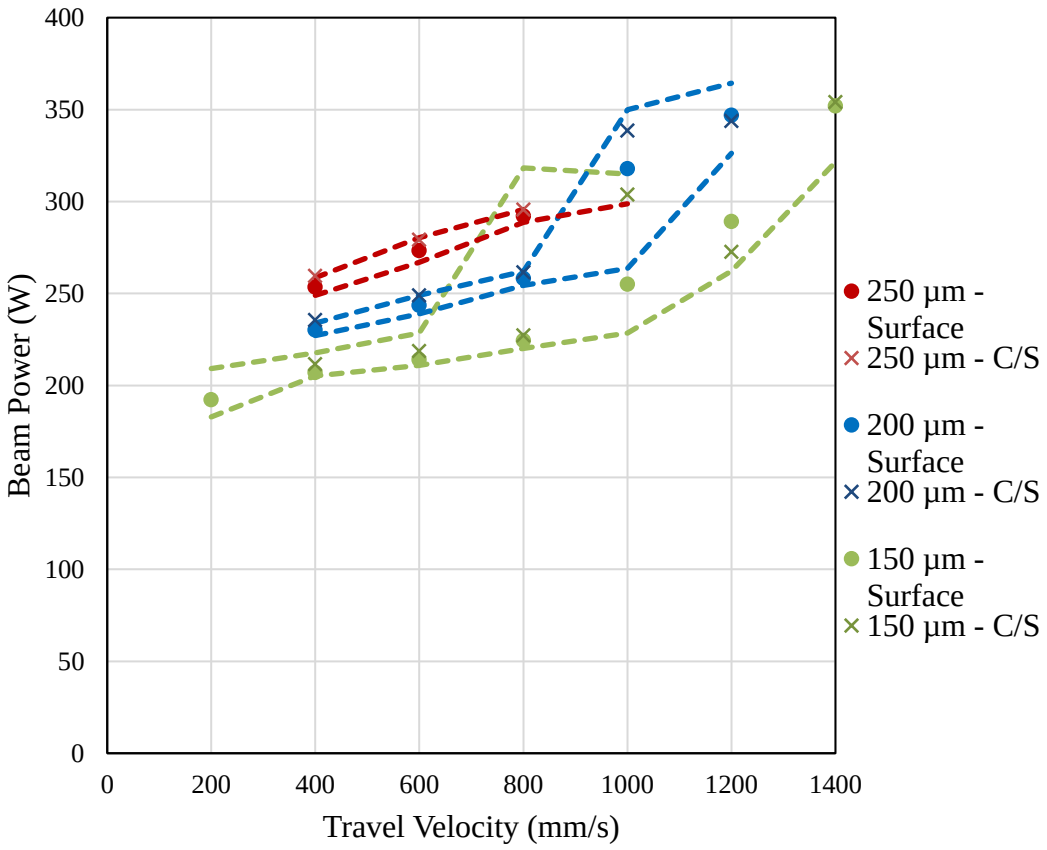

Figure 5-19: Process map for constant melt pool widths at the surface and the cross section for single melt tracks. Dashed lines depict the variation in the melt pool widths.

Surface width measurements provide information about the variability along the melt track. However, variability can be expected across the layer too which can be obtained from the single layer pad measurements at a cross section. Figure 5-20 shows the comparison between the melt pool width measurements at the surface and across the single layer pad. Dashed and solid lines represent the maximum and minimum possible width (95% bounds) for surface measurements from single beads and cross section measurements from single layer pads respectively. It can be observed that variability is almost the same in both the cases and the average measurements agree well. This means, studying the surface width from the single beads is sufficient to understand the variability in melt pool width.

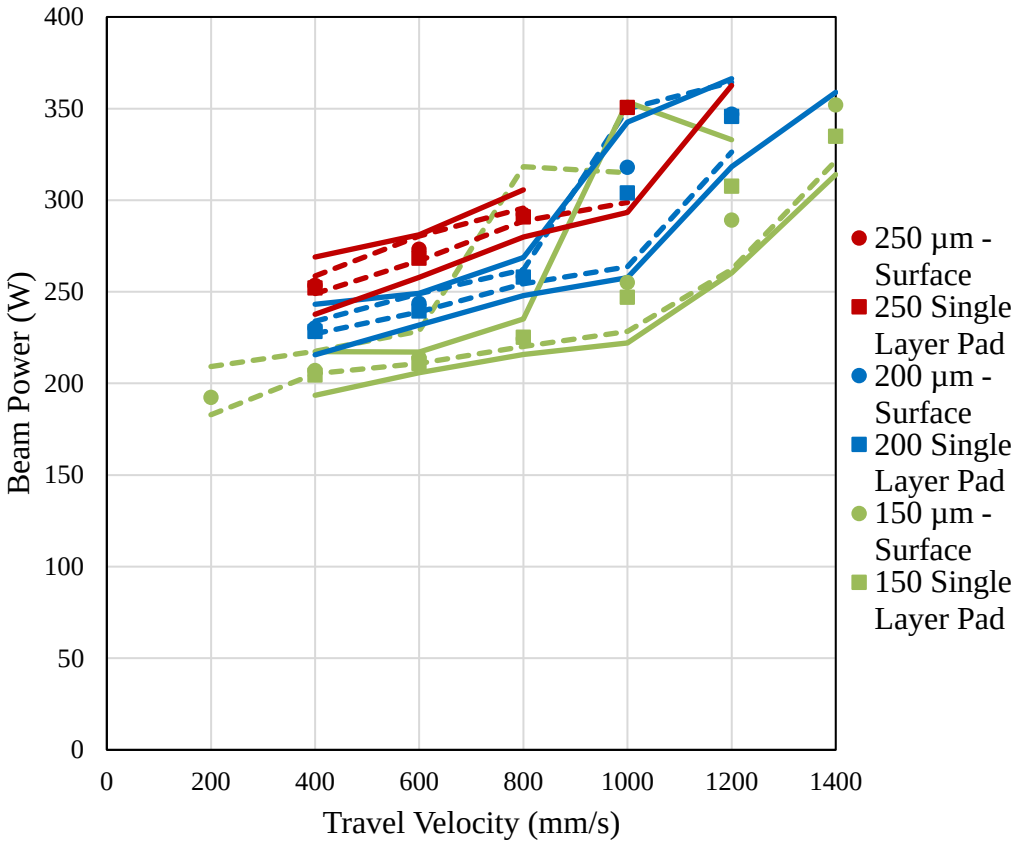

Figure 5-20: Process map for constant melt pool widths at the surface and the cross section for single layer pads. Dashed lines and solid lines around the data markers depict the variation in the melt pool widths.

The discussion on melt pool widths leads into the discussion on melt pool depths. Similar to variability in width, understanding the variability in depth is critical to ensure complete melting of powder and sufficient overlap between successive layers. This was studied by developing process maps for melt pool depth using the cross section depth measurements outlined in Table 5-6 for single beads and single layer pads. From the depth process map in Figure 5-21, it can be observed that variability in depth also follow similar trends to variability in width where variability is comparatively higher at higher velocities. At other regions in the process space, melt pool depth measurements from single beads are in agreement with the average melt pool depth from single layer pads. From the results on melt pool width and depth, it can be concluded that at higher

velocities it is especially useful to know the minimum depth and width in order to adjust the hatch spacing and layer thickness to ensure proper overlap between adjacent tracks and for complete melting of the powder layer.

Table 5-6: Summary of melt pool depths from cross sections of single beads and single layer pad experiments.

Sample Designation	Power (W)	Velocity (mm/s)	Depth (Single Layer Pad C/S) ± 2σ (µm)	Std. Dev (µm)	Depth Single Bead (C/S) (µm)
1	100	200	18 ± 4	2	20
2	200	200	90 ± 102	51	58
3	100	400	16 ± 2	1	17
4	200	400	53 ± 20	10	53
5	300	400	297 ± 22	11	329
6	370	400	414 ± 36	18	460
7	100	600	15 ± 2	1	17
8	200	600	47 ± 4	2	46
9	300	600	228 ± 22	11	225
10	370	600	282 ± 38	19	344
11	100	800	14 ± 4	2	16
12	200	800	40 ± 8	4	40
13	300	800	168 ± 36	18	179
14	370	800	238 ± 28	14	232
15	100	1000	13 ± 4	2	12
16	200	1000	38 ± 4	2	40
17	300	1000	111 ± 72	36	66
18	370	1000	175 ± 20	10	158
19	200	1200	35 ± 4	2	35
20	300	1200	64 ± 28	14	97
21	370	1200	137 ± 16	8	142
22	200	1400	31 ± 6	3	31
23	300	1400	49 ± 8	4	49
24	370	1400	87 ± 22	11	87

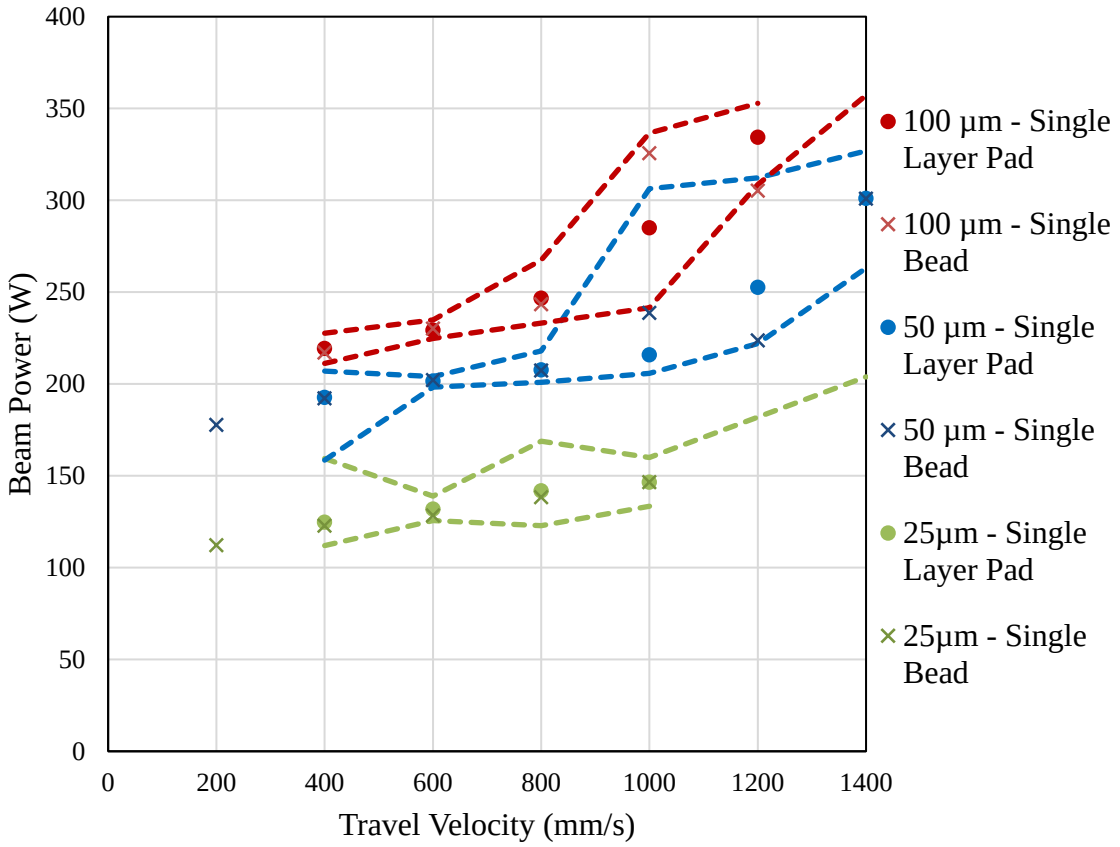

Figure 5-21: Process map for constant melt pool depths for single beads and single layer pads. Dashed lines around the data markers depict the variation in the melt pool depth.

Melt pool area process maps are developed to study the effect of process variables on melt pool cross-section area. Figure 5-22 illustrates the process map for melt pool area developed for data outlined in Table 5-7. Sample 17 shaded in grey in the table has more variability when compared to other samples and it is not considered for the melt pool area analysis. Within the available information from single bead cross-section, it can be observed that lines of constant melt pool area follow linear trend below 1000 mm/s. Since, the melt pools are variable at higher velocities, the reported area of such melt pools depends on the location where the track is sectioned to observe the cross section and trends in that region for melt pool area cannot be determined from the available information.

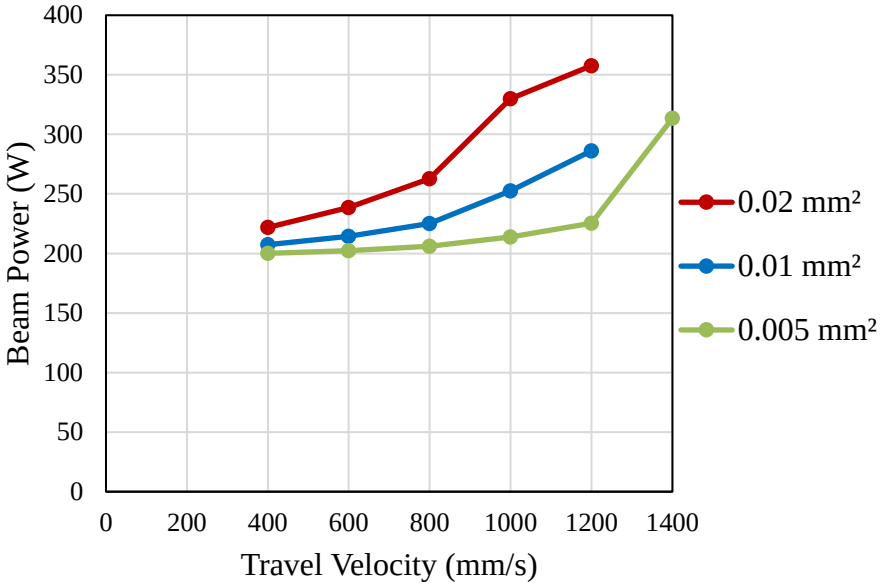

Figure 5-22: Process map for melt pool area developed from cross section data of single bead experiments.

Table 5-7: Summary of melt pool areas from cross sections of single bead experiments.

Sample Designation	Power (W)	Velocity (mm/s)	Area (mm²)
1	100	200	9.4E-04
2	200	200	6.4E-03
3	100	400	7.9E-04
4	200	400	4.9E-03
5	300	400	7.4E-02
6	370	400	1.1E-01
7	100	600	7.5E-04
8	200	600	4.1E-03
9	300	600	4.5E-02
10	370	600	6.7E-02
11	100	800	7.4E-04
12	200	800	3.4E-03
13	300	800	3.0E-02
14	370	800	4.5E-02
15	100	1000	5.5E-04
16	200	1000	3.2E-03
17	300	1000	7.0E-03

18	370	1000	2.5E-02
19	200	1200	2.9E-03
20	300	1200	1.1E-02
21	370	1200	2.2E-02
22	200	1400	2.1E-03
23	300	1400	4.0E-03
24	370	1400	9.2E-03

5.3.2 Establishing the Process Window from Single Bead Experiment Results

Part porosity is a concern in additively manufactured parts since it affects the fatigue life of the components [94]. Previous work has shown that both process parameters and powder characteristics can influence the part porosity [103][121]. In this work, the process window for AlSi10Mg is defined as the region in process space that produces final parts with limited porosity due to lack of fusion and keyholing. Lack of fusion pores are formed at power-velocity combinations where the melt pool does not fully melt through the powder layer and/or there is insufficient overlap between the adjacent melt tracks. The layer thickness must be changed to eliminate lack of fusion porosity between successive layers while the overlap between the adjacent melt tracks can be controlled by varying the hatch spacing.

In this work, using the cross-section data from the single bead experiments, the lack of fusion region was identified by the melt pools which have a depth less than the nominal powder layer thickness for AlSi10Mg in the EOS process (30 microns, see Table 5-3). Keyhole porosity is formed under very high energy density conditions, where the material in the melt pool vaporizes. Before molten material from above can flow down and fill the void formed from evaporation, the melt pool solidifies resulting in permanent pores characteristically located at the bottom of the melt pool [107]. The keyholing region was identified based on the melt pool width to depth ratio. The cases with a melt pool depth to half-width ratio greater than 1 (indicating a non-semi-circular

geometry) were treated as keyholing melt pools [102]. The procedure for mapping the process window with the above-mentioned criteria is shown in Figure 5-23. This procedure utilizes the melt pool cross-section information from single layer pads experiments. Figure 5-24 shows approximation of the process window based on the information illustrated in Figure 5-23. It should also be noted that the EOS nominal parameters are on the border of keyholing regime based on the information available from these experiments.

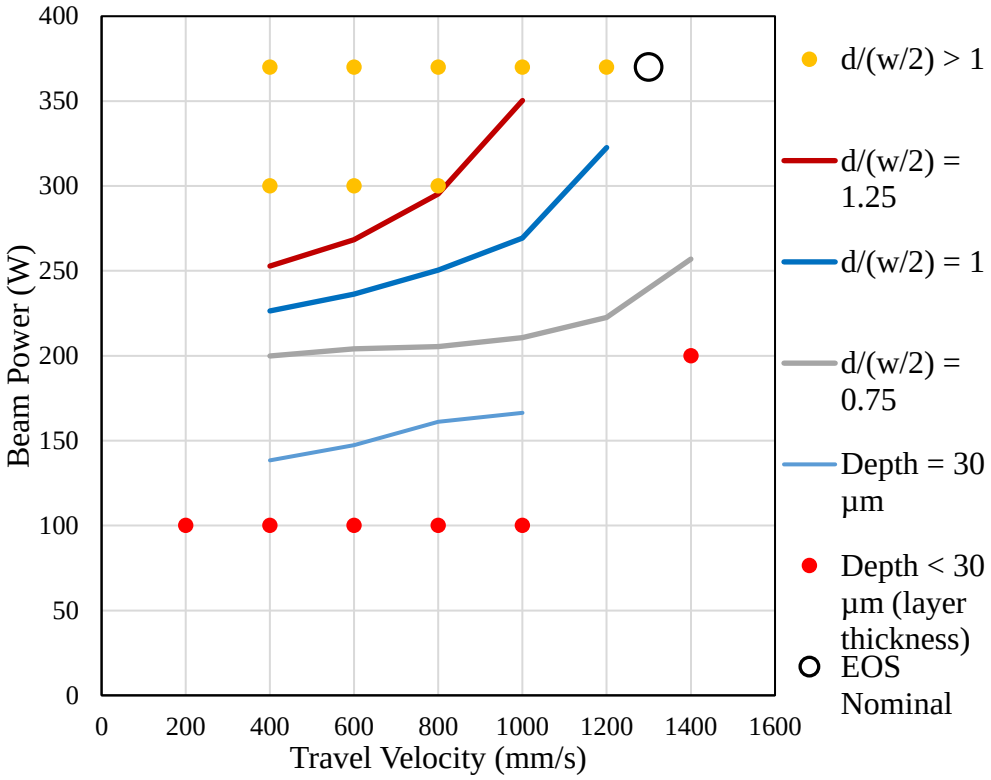

Figure 5-23: Procedure for mapping the process window utilizing information from single bead experiments.

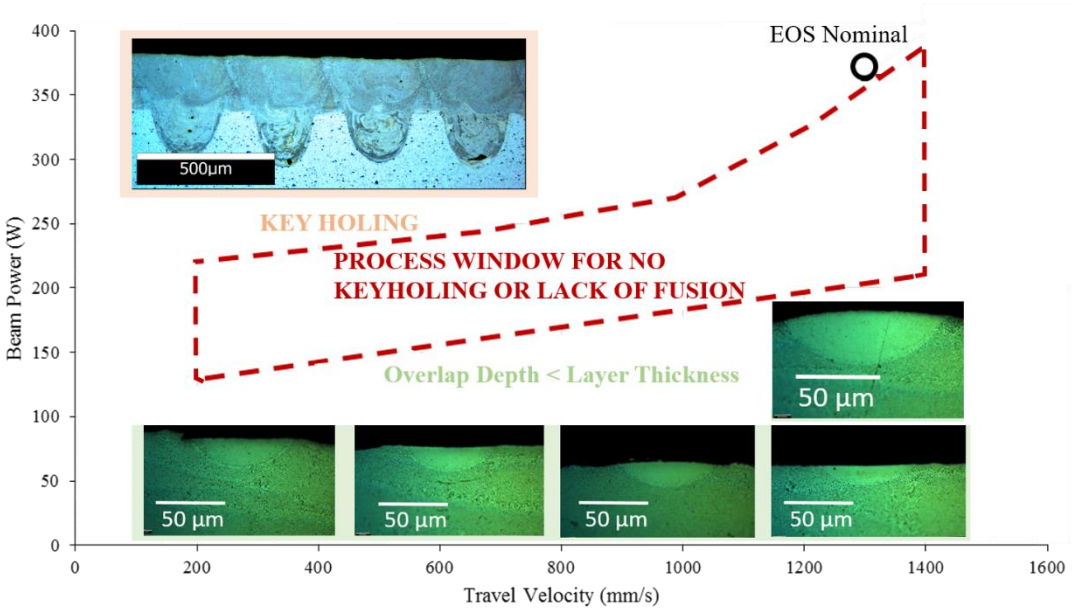

Figure 5-24: Process window for AlSi10Mg depicting the lack of fusion and keyholing regimes for the parameters covered in this research.

5.3.3 Part Quality from Multi-Layer Pads (Solid Blocks)

Multi-layer pads built in this work were used to qualitatively understand final part quality and stress the importance of controlling process parameters such as layer thickness, and hatch spacing for a fixed power and velocity to improve part quality. In these experiments, hatch spacing was adjusted to maintain the overlap percentage between adjacent tracks equivalent to the nominal EOS overlap similar to the single layer pad tests. However, the layer thickness could not be reduced below 20 µm due to the practical constraints resulting from powder size governing the minimum layer thickness choice.

Figure 5-25 illustrates the defects due to under-melting and keyholing porosity for the samples which were built using the parameters that lie outside of the process window shown in Figure 5-24. It is important to note that the under-melting porosity observed in the low power and low velocity sample can be mitigated by decreasing the layer thickness according to melt pool depth. Similarly, keyholing porosity can be eliminated at the higher energy density region of

process space by increasing the beam spot size [102]. From Figure 5-25, it can also be observed that that the extent of keyholing increases with an increase in depth to half-width ratio. In this work, only qualitative results are presented since the main focus is on minimizing the defects by controlling the process parameters systematically. However, this porosity can be quantitatively mapped by measuring the percentage of pores from different samples in the keyholing region.

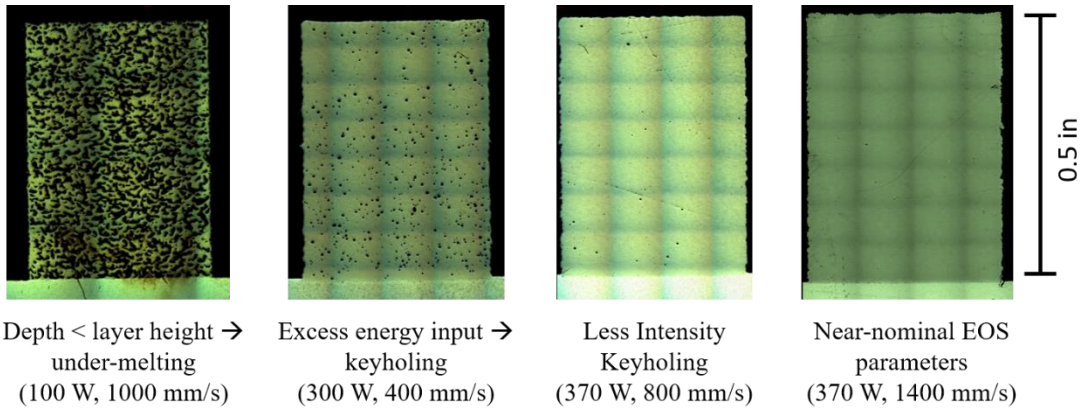

Figure 5-25: Illustration of lack of fusion and keyholing process defects in the multi-layer pads and the improvement in part quality as we approach the process window highlighted in Figure 5-24.

5.3.4 Comparison between Simulations and Experiments for Single Beads

As noted in §5.2.2, there are certain phenomena like convection to the surroundings, radiation, Marangoni flows within the melt pool, and keyhole-mode melting which are not included in the model used in this work. Power which is applied in the simulations is entirely absorbed by the materials, whereas not all the power that is delivered by the laser is absorbed by the material in experiments. Thus, a comparison between the beam input power used in experiments and absorbed power from simulations results in a factor that can be treated as the absorptivity of the material. Since, the model is not a thorough representation of the experiment set up, absorptivity is referred to as effective absorptivity in this work.

The effective absorptivity is estimated for all the melt pool geometry characteristics e.g. width, depth and area. Among available experiments, average width from the surface is considered for the melt pool width and average depth from the single layer pads is considered for the melt pool depth. The variation of absorptivity measured for different melt pool characteristics with depth to half-width ratio is presented in Figure 5-26. The data shows that with increase in depth to half-width ratio, absorptivity increases. Increase in depth to half-width ratio indicated the occurrence of keyholing. During keyholing, due to vaporization of material, a vapor cavity is formed which increases the absorption of the beam. This is different from conduction mode melting [104,107]. This resulted in unrealistic values for absorptivity such as >100% in case of melt pool depth and area when compared with simulations in this work which model conduction based heat transfer.

Using the available information, the effective absorptivity of the material is estimated in the non-keyholing regions as shown in Figure 5-27. Effective absorptivity is almost constant except for one data point which is at 300 W, 1200 mm/s. This can be explained by the fact that this region is close to the key holing regime as discussed above. Thus, this value is not used in estimating the average effective absorptivity value. A summary of the effective absorptivity value estimated from this work is detailed in Table 5-8. Width values between 100 – 150 µm, depth values between 30 – 60 µm and area values between $3x10^{-3}$ and $5x10^{-3}$ mm^2 were considered for this analysis.

Table 5-8: Estimated values for absorptivity estimated from melt pool dimensions in the non-keyholing regime of the process space.

Melt Pool Geometry Considered	Area	Width	Depth
Average Effective Absorptivity (%)	18	19	21
Standard Deviation (%)	1	2	1

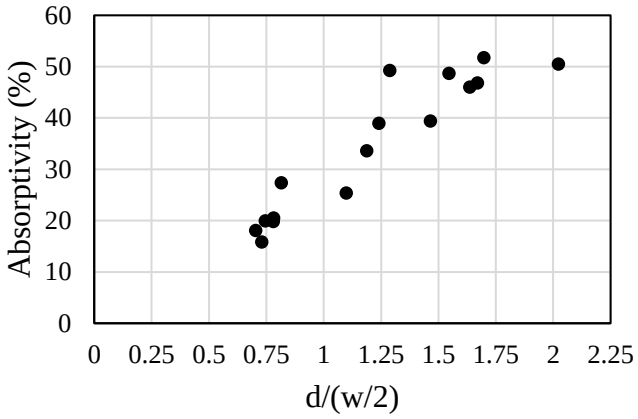

(a)

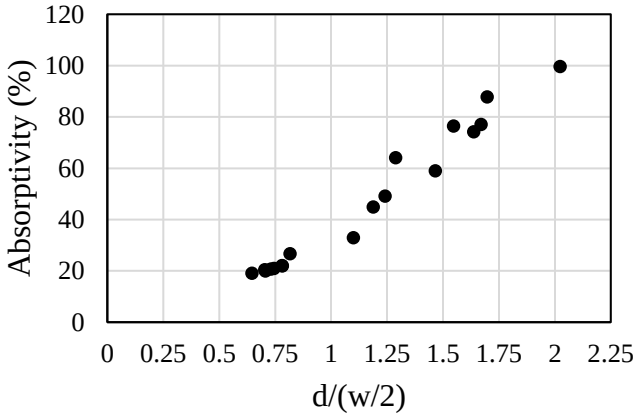

(b)

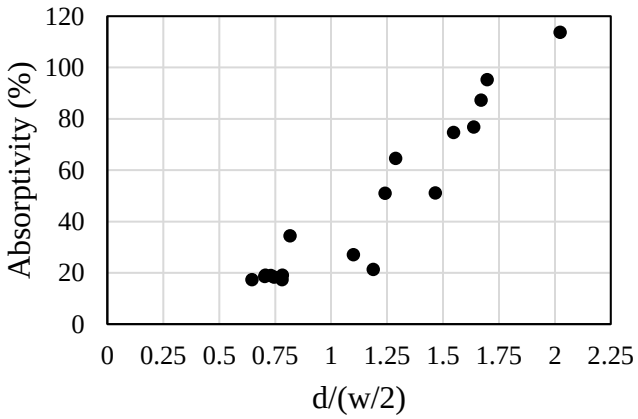

(c)

Figure 5-26: Illustration of the increase in absorptivity estimated from melt pool dimensions: (a) width, (b) depth and (c) area with increase in melt pool cross section aspect ratio.

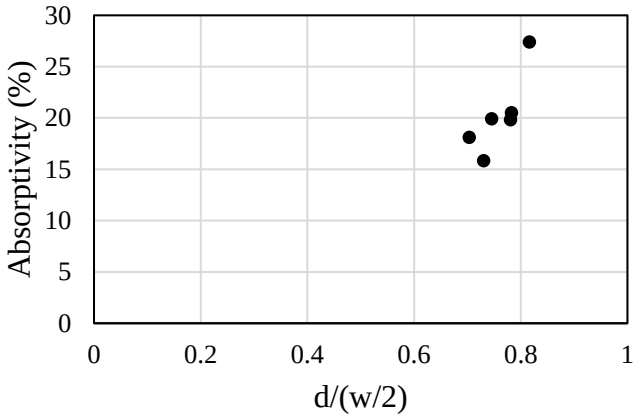

(a)

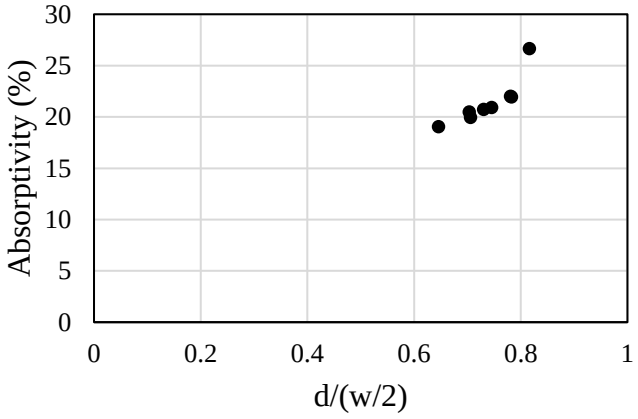

(b)

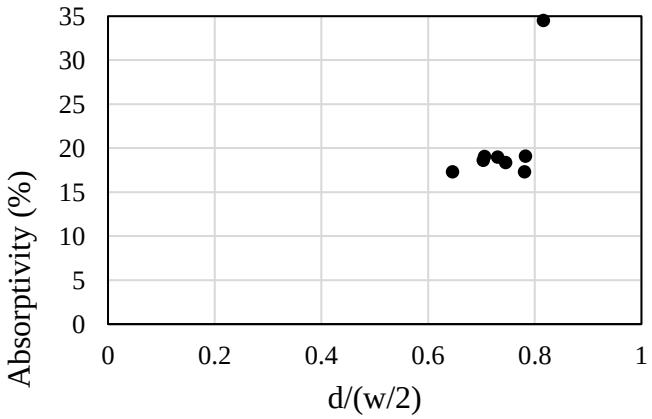

(c)

Figure 5-27: Illustration of the variation in absorptivity estimated from melt pool dimensions: (a) width, (b) depth and (c) area with melt pool cross section aspect ratio in non-keyholing region.

5.3.5 Process Mapping of Solidification Microstructure

This section focuses on controlling the microstructure formed at solidification via process parameter control and demonstrates integrated melt pool geometry and microstructure control in laser melted AlSi10Mg. First, insights from simulations are discussed followed by results from experiments.

5.3.5.1 Process Mapping of Cooling Rates from Simulations

Cooling rates extracted from the tail end of the melt pool are plotted in the power-velocity space using the process mapping approach. In Figure 5-28, it is important to note that lines of constant cooling rate in the P-V space follow the same trends as lines of constant melt pool geometry. Specifically, with an increase in melt pool area, cooling rate decreases and vice-versa. This can be explained by the fact that a bigger melt pool (resulting from higher energy density) will take more time for the energy to dissipate thus resulting in a decrease in the cooling rate. The relationship between melt pool area and cooling rate is illustrated in Figure 5-29.

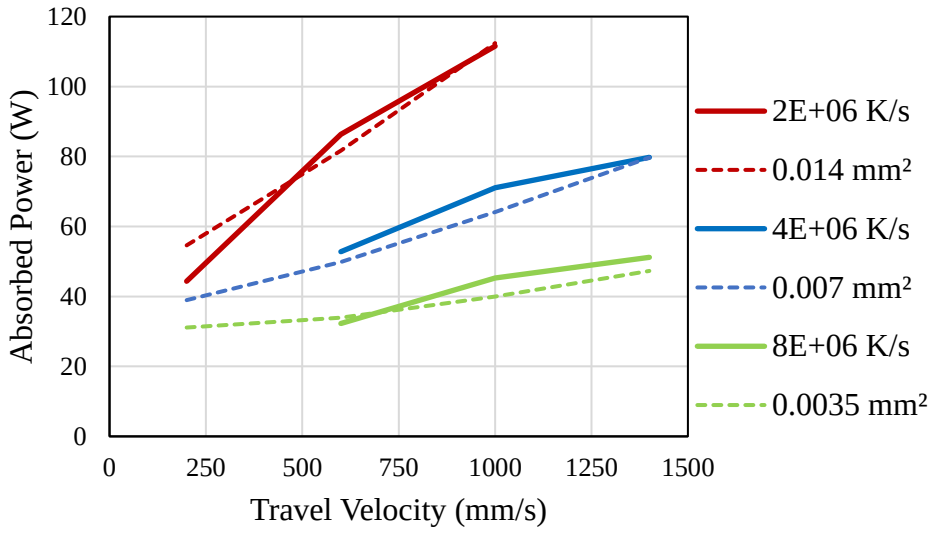

Figure 5-28: Plot illustrating similar trends in process maps for cooling rate and melt pool area.

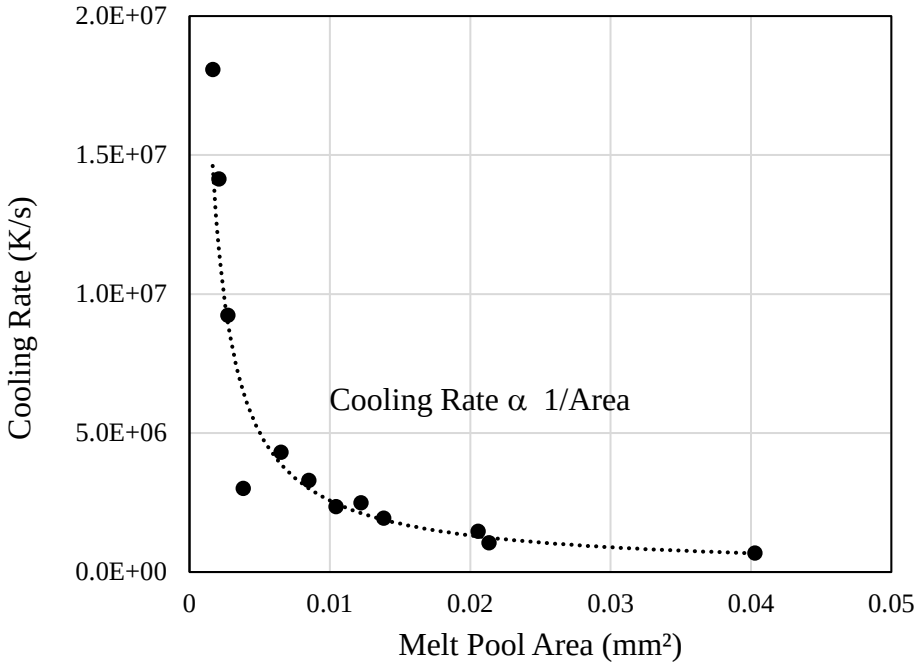

Figure 5-29: Variation of cooling rate with melt pool area estimated from simulations. Data shows that cooling rate is inversely proportional to the area.

5.3.5.2 Experiments

Cellular solidification is prevalent in AlSi10Mg due to the very high thermal gradients owing to the high thermal conductivity of AlSi10Mg. Similar microstructure is reported in previous works by other researchers [38,41,94,122,123]. AlSi10Mg is a hypo-eutectic alloy which leads to the formation of α-Al cells at the beginning of the solidification and Si segregates at the cell boundaries. Silicon at the cell boundaries was confirmed by Aboulkhair et al. [96] through the use of an energy dispersive x-ray detector (EDX). An example cellular microstructure with various phases identified is shown in Figure 5-30.

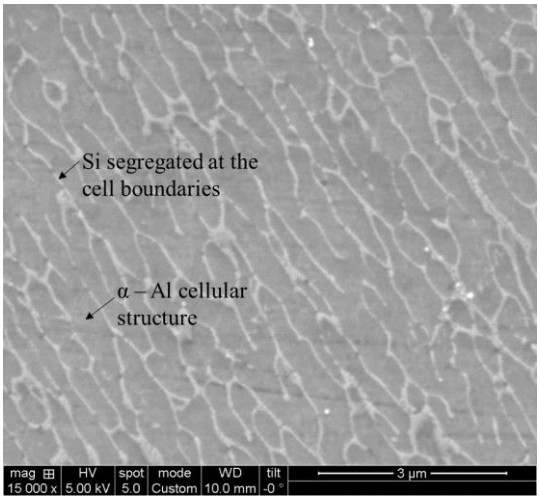

Figure 5-30: Example SEM micrograph illustrating the phases in cellular solidification structure of AlSi10Mg.

Single Beads

Previous work [41] has shown that in single beads, cell spacing varies with cooling rate as per a power relationship with an exponent of -1/3. From Figure 5-29, it can be observed that cooling rate is inversely proportional to area which means cell spacing should be proportional to melt pool area as per power relationship with a factor of 1/3. This is in agreement with the experiment results from single beads demonstrated in Figure 5-31. The error bars represent a 95% confidence interval (CI) about the average cell spacing. Details of the cell spacing measurements used in this plot are provided in Table 5-9. This shows that integrated melt pool geometry and microstructure control concepts are applicable for laser melted AlSi10Mg.

Table 5-9: Summary of cell spacing measurements from cross sections of single bead experiments.

Sample Designation	Power (W)	Velocity (mm/s)	Average Cell Spacing (µm)	Standard Deviation (µm)	Standard Error (µm)
8	200	1400	0.20	0.03	0.01
20	370	1400	0.26	0.04	0.01
13	300	800	0.38	0.06	0.01
21	370	400	0.57	0.10	0.02

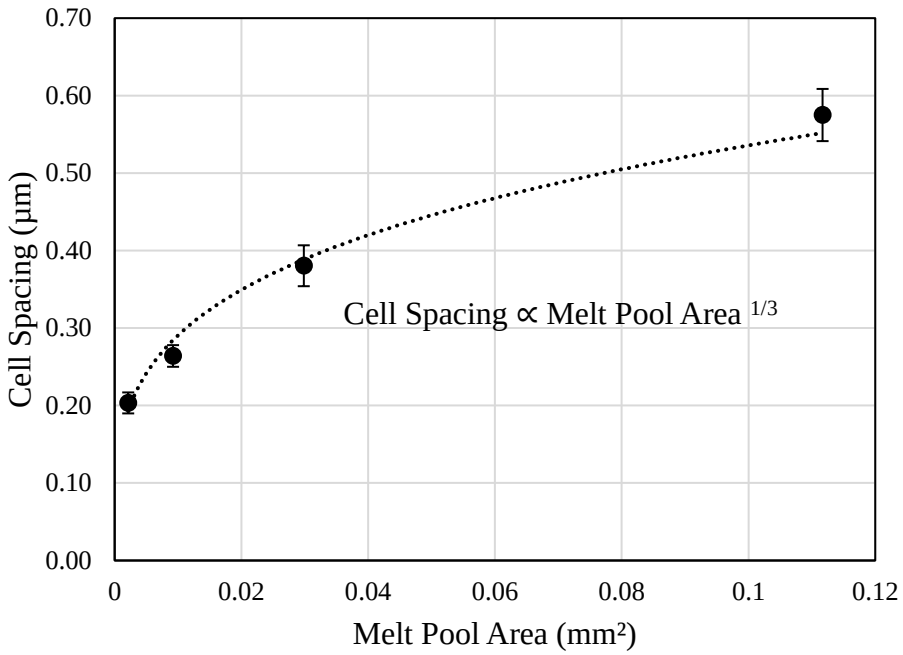

Figure 5-31: Plot showing the relationship between cell spacing and melt pool area. Error bars are 95% CI about the average cell spacing estimate.

Melt pool width is a melt pool characteristic which can be observed during in-situ monitoring via high-speed thermal or visible-light imaging. Cell spacing can be related to melt pool width via the relationship between melt pool widths and melt pool areas shown in Figure 5-32. It is interesting to note that area is proportional to width³ instead of width² for semi-circular melt pools. The reason for this the shape of the melt pool for all the single beads measured in this work. This relationship can be used to link cell spacing to melt pool width as shown in Figure 5-33 and demonstrated in Equation 5.2.

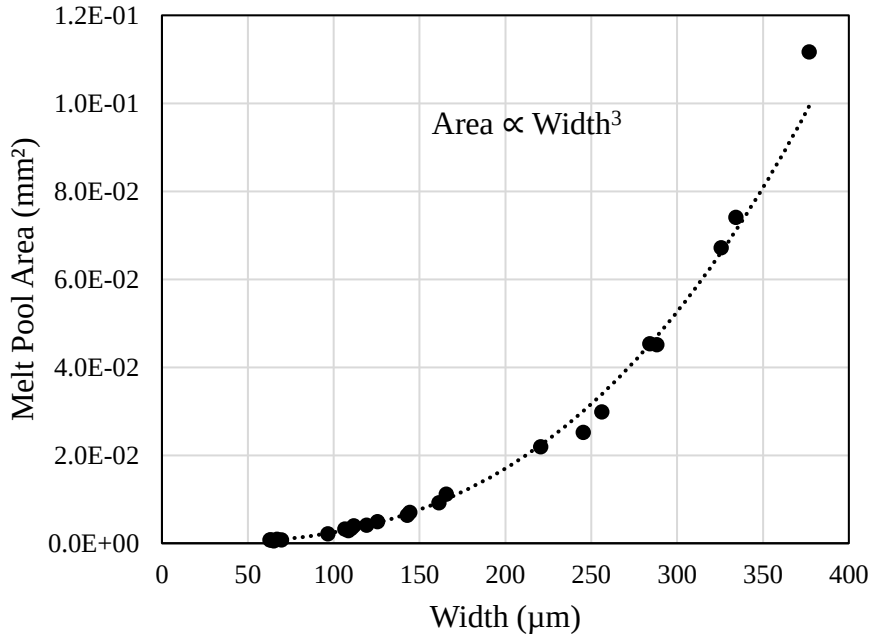

Figure 5-32: Plot showing the variation of melt pool area with melt pool width from single bead experiment cross sections.

$$Cell\ Spacing\ \propto Width \tag{5.2}$$

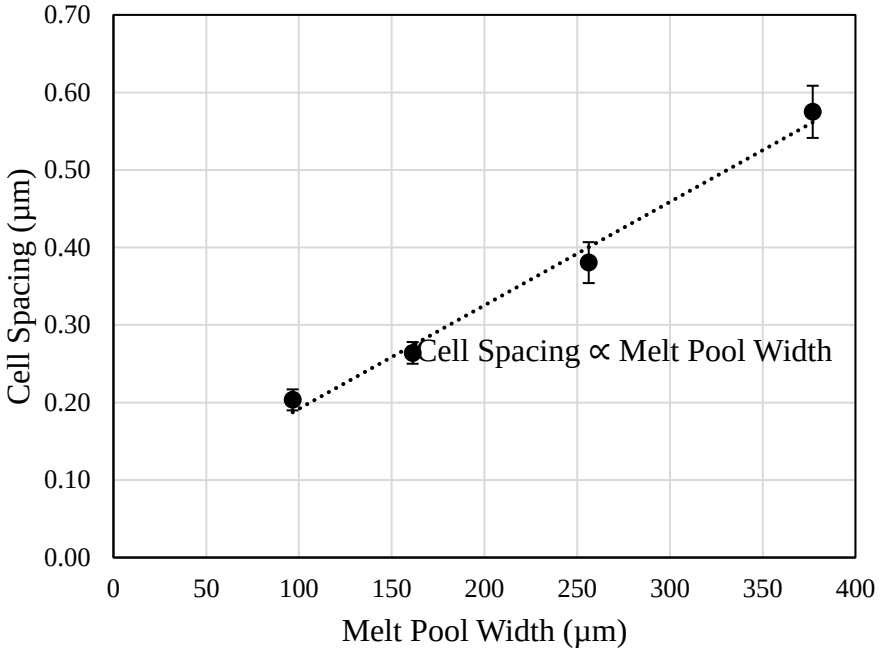

Figure 5-33: Plot showing the linear dependence of cell spacing on melt pool width. Error bars represent a 95% CI about the average cell spacing.

Cell spacing varies linearly with melt pool width according to the data available in the current work. This result implies that by maintaining a constant melt pool width, cell spacing can be held constant. Figure 5-34 shows the comparison of all 4 cell spacing measurements resulting from different cooling rates in the process space.

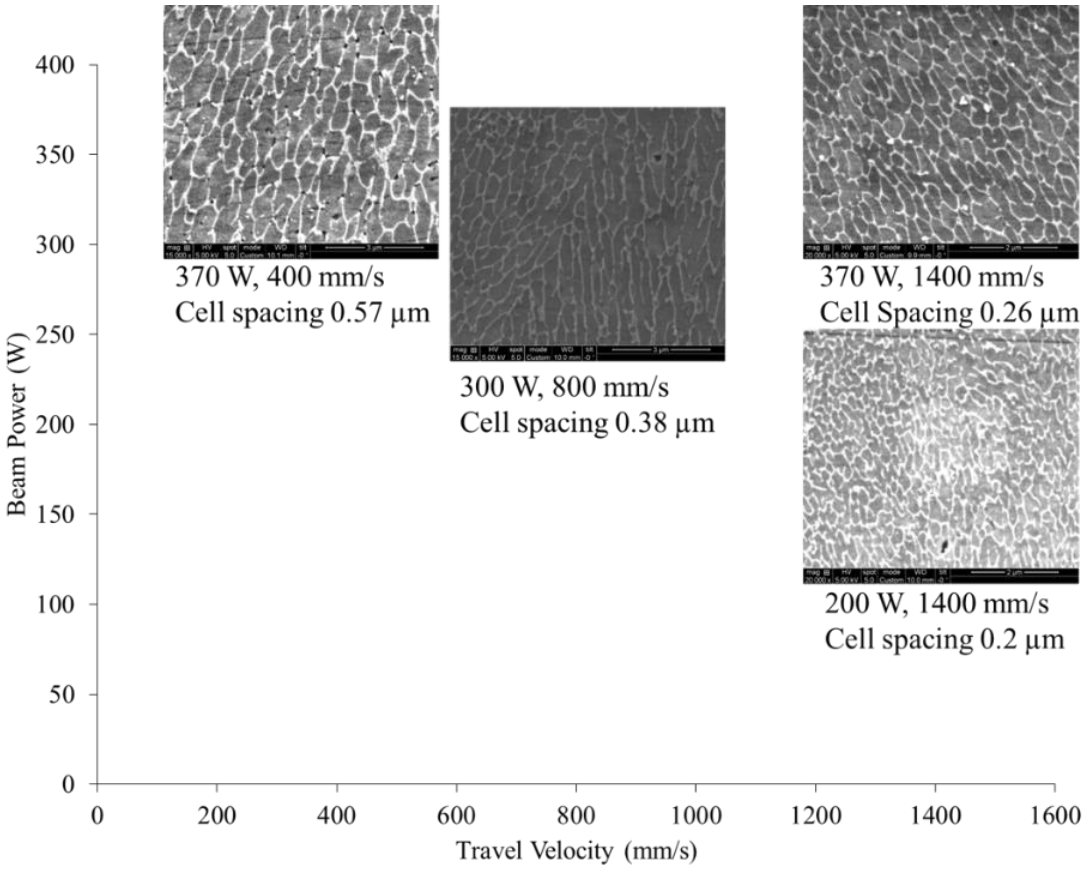

Figure 5-34: Plot showing the variation of cell spacing in power-velocity space for single bead experiments.

Multi-layer pads

For a fixed preheat temperature and beam spot size, single bead results have shown that by maintaining a constant melt pool size, cell spacing will remain constant. This result provides the ability to control the cell spacing in a component based on the mechanical properties required for the application. However, it is important to check if the cell spacing remains constant with constant melt pool size in solid parts too. Similar to the approach used in Ti64 electron beam melting

process, cell spacing control in solid parts was explored before building a component with location-specific control of cell spacing discussed in §5.3.6. Figure 5-35 and Figure 5-36 illustrate the variation of cell spacing with melt pool area and melt pool width at the surface for the multi-layer pads. The error bars represent a 95% confidence interval (CI) about the average cell spacing. The data used in the plots is detailed in Table 5-10. These samples are chosen such that they lie within the no keyholing and lack of fusion window. This resulted in samples with very low variation in cell spacing since cooling rate does not vary by more than a factor of 2 within the good region identified in the processing space in Figure 5-24. Though, the power law exponent is different when compared to single beads, there is still a variation in cell spacing with melt pool area.

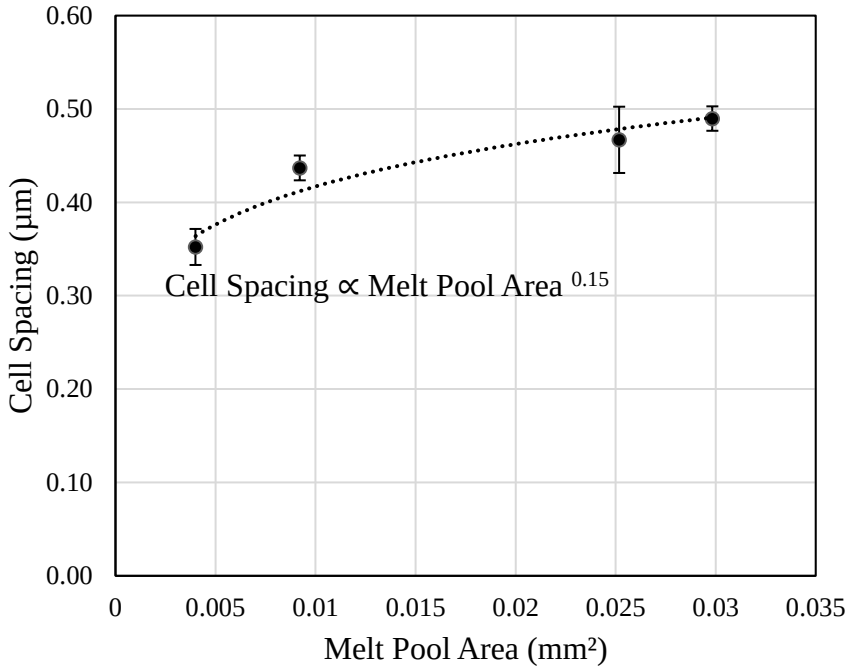

Figure 5-35: Plot showing the variation of cell spacing with melt pool area for multi-layer pad experiments. Error bars represent a 95% CI about the average cell spacing.

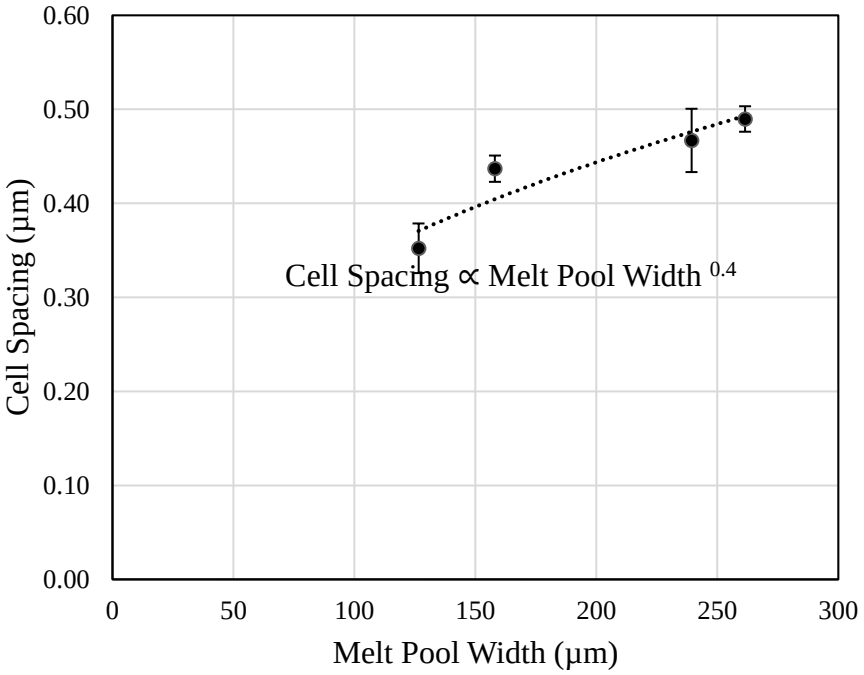

Figure 5-36: Plot showing the variation of cell spacing with melt pool width for multi-layer pad experiments. Error bars represent a 95% CI about the average cell spacing.

Table 5-10: Summary of cell spacing measurements from multi-layer pad experiments.

Sample Designation	Power (W)	Velocity (mm/s)	Average Cell Spacing (µm)	Standard Deviation (µm)	Standard Error (µm)
15	300	800	0.49	0.15	0.01
24	370	1400	0.44	0.07	0.01
18	300	1400	0.35	0.08	0.01
22	370	1000	0.47	0.13	0.02

It is also interesting to note that for similar power-velocity conditions, the cell spacing value increased from single beads to multi-layer pads. It is likely due to coarsening of the microstructure. According to Dantzing et al. [29] " The phenomena, where the length scale of microstructure increases over time, is called coarsening". This might have happened due to the heating to near melting temperature from melting adjacent melt tracks or melt tracks in the next layer. The details of this comparison are shown in Table 5-11. It is important to note that the power law relationship derived for single beads does not hold true for bulk builds. Thus, results from the

bulk blocks are used in designing the cell spacing control in the *flag* component discussed in the following section.

Table 5-11: Comparison of cell spacing measurements from single beads and single layer pads.

Power (W)	Velocity (mm/s)	Average Cell Spacing from Single Beads (µm)	Average Cell Spacing from Multi-Layer Pads (µm)	Ratio of Cell Spacing Between Pads and Single Beads
370	1400	0.26	0.44	1.7
300	800	0.38	0.49	1.3

5.3.6 Location-Specific Solidification Microstructure Control in AlSi10Mg

Micrographs from different regions of the flag are analyzed for cell spacing. A summary of the measurements is provided in Table 5-12. Also, Figure 5-37 provides the illustration of the change in cell spacing with respect to the targeted change. It is important to note that the target ratio of cell spacing variation in this experiment is 1.33 instead of a higher variation like 3 or 4 demonstrated for Ti64 in Chapter 3. This is due to the limitation offered by the machine with respect to the minimum layer thickness that can be used and lack of the equipment to control the beam spot size to avoid keyholing porosity. Thus, it was required to remain within the process window identified in §5.3.2. From the process maps for cooling rate in Figure 5-28, it can observed that the variation of cooling rate within the process window is not sufficient to result in a wide range of cell spacings. Irrespective of the range over which cell spacing is varied, there is agreement between the measured ratio and the target ratio. Measured ratio of cell spacing variation are detailed in Table 5-13. For all the measurement metrics, the measured ratio is on the order of 1.30 – 1.40 when compared to the target ratio of 1.33. Thus, this study demonstrates that location-specific control of cooling rates is possible for AlSi10Mg in the laser melting process.

Table 5-12: Summary of cell spacing measurements from the *Flag*.

Measurement Metric	EQPC			Feret Diameter			Min Feret		
Location Designation	Average (µm)	Standard Deviation (µm)	Standard Error (µm)	Average (µm)	Standard Deviation (µm)	Standard Error (µm)	Average (µm)	Standard Deviation (µm)	Standard Error (µm)
Stars	0.41	0.27	0.01	0.63	0.49	0.02	0.37	0.29	0.01
White Stripes	0.38	0.27	0.01	0.58	0.51	0.02	0.35	0.29	0.01
Red Stripes	0.56	0.19	0.01	0.79	0.35	0.01	0.51	0.20	0.01
Blue Background for Stars	0.57	0.23	0.02	0.84	0.43	0.03	0.50	0.24	0.02

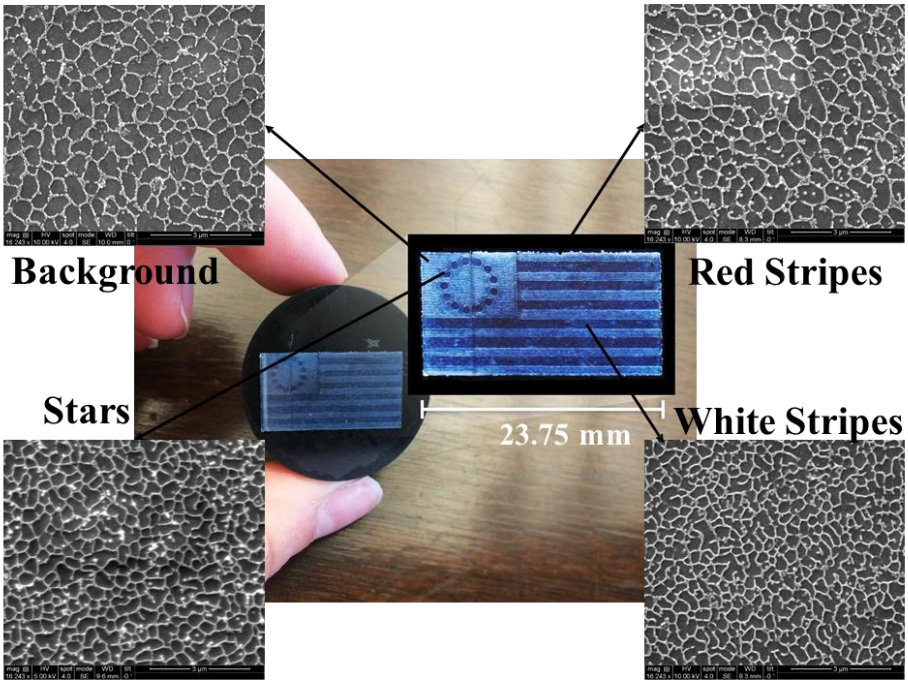

Figure 5-37: Figure demonstrating the control of cell spacing in different locations of the *Flag* component.

Table 5-13: Comparison of cell spacing measurement in different locations of the *Flag*.

Ratio			
Measurement Metric	EQPC	Feret Diameter	Min Feret
Stars	1.00	1.00	1.00
White Stripes	0.92	0.93	0.93
Red Stripes	1.37	1.26	1.35
Blue Background for Stars	1.39	1.34	1.35

Cumulative probability distributions for cell size measurements from different locations of the flag are illustrated in Figure 5-38 – Figure 5-40. It is interesting to note that all the probability curves overlap in the higher cell spacing region whereas, there is a clear distinction in the finer and coarser region measurements in the lower cell spacing region of the plot. The probability of finding a smaller cell in *stars* and *white stripes* is almost twice the probability of finding a smaller cell in the *background* and *red stripes*. This is the main reason that results in a shift in the average measured values for these different locations. One more interesting observation from the plots is, for the coarser regions there is a distinct curvature at the lower cell spacing values which indicates a deviation from a log normal distribution. There is also noticeable deviation from log normal distribution for finer regions at the tail regions.

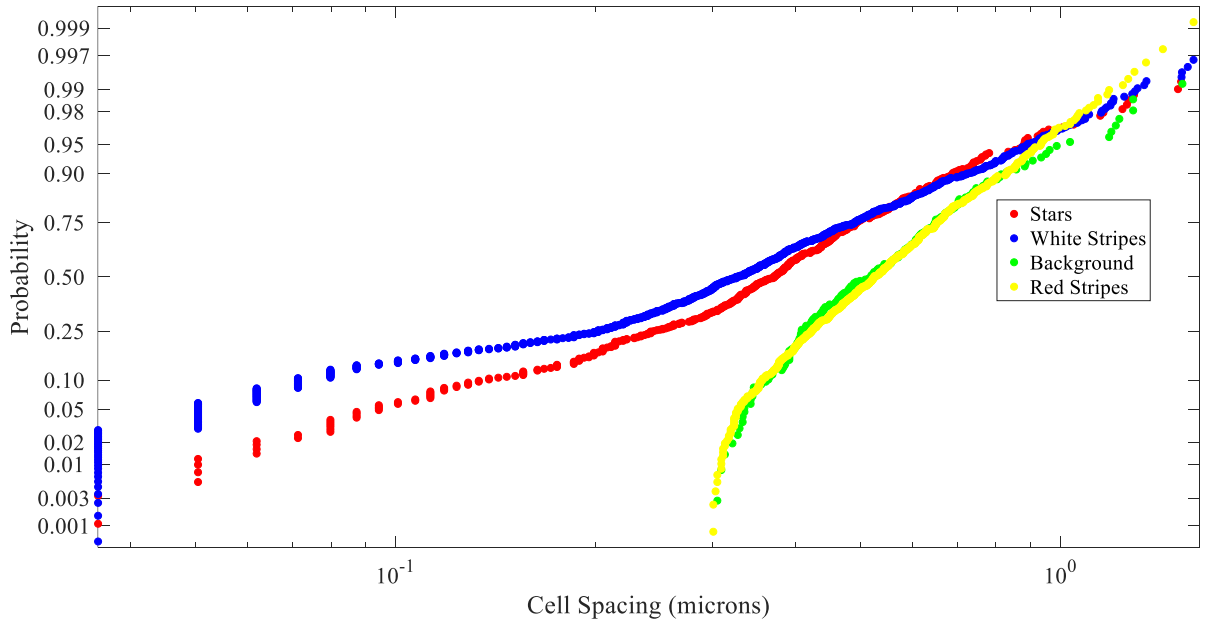

Figure 5-38: Probability plot (cumulative) of EQPC estimate for cell size in the fine and coarse regions of the *Flag* component.

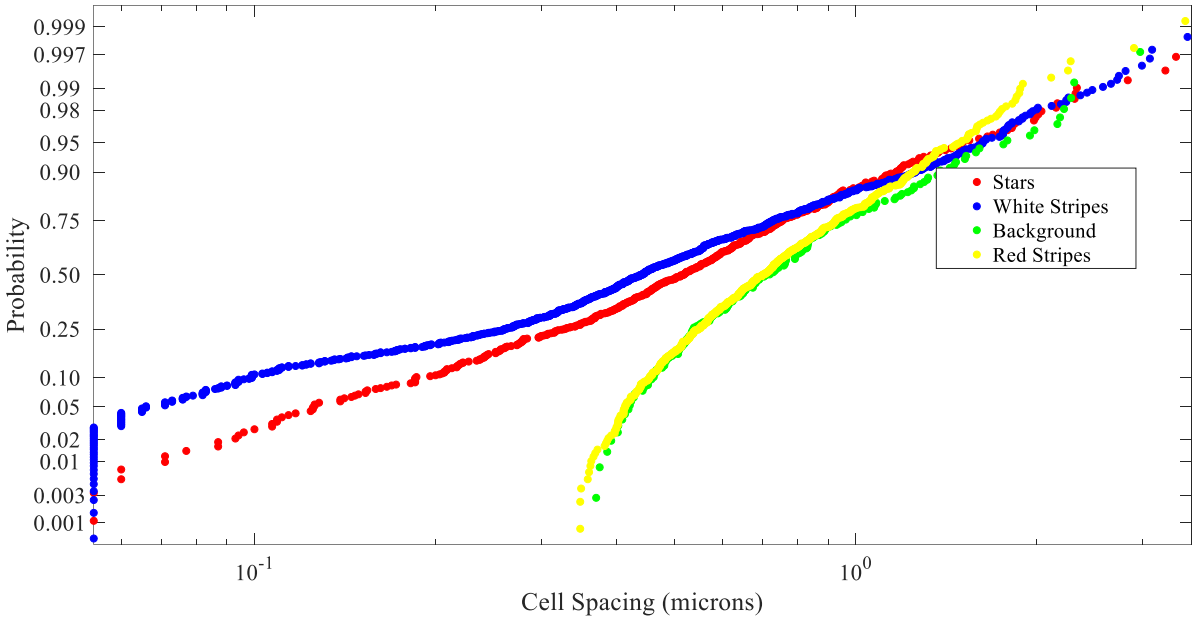

Figure 5-39: Probability plot (cumulative) of maximum caliper size (Feret Diameter) for cells in the fine and coarse regions of the *Flag* component.

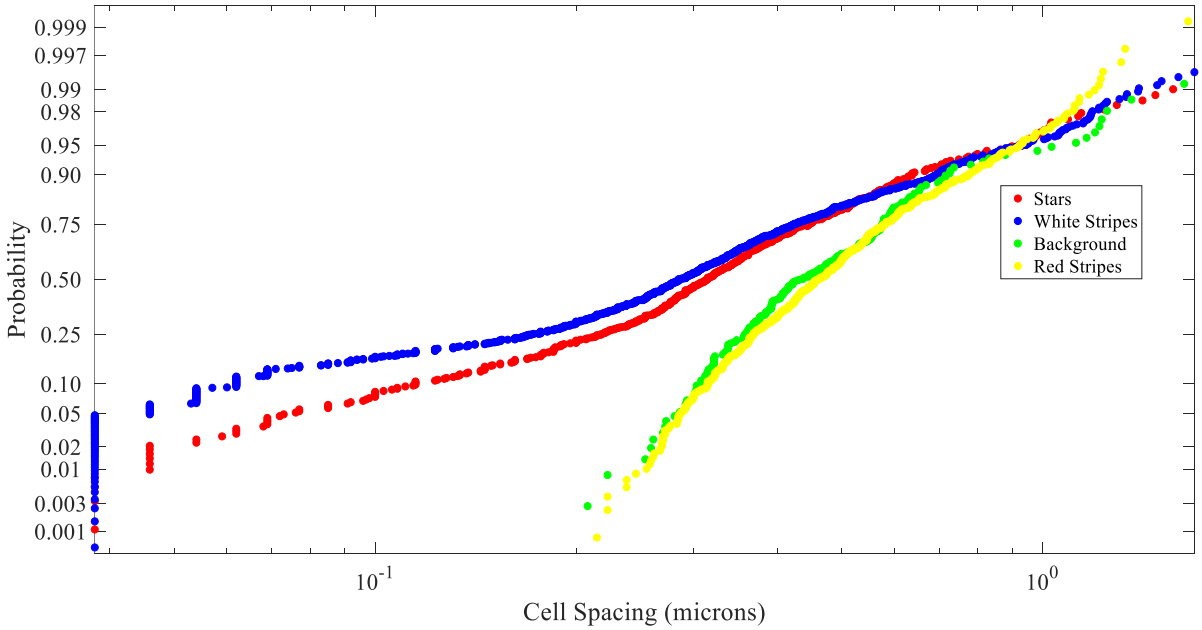

Figure 5-40: Probability plot (cumulative) of minimum caliper size (Min Feret) for cells in the fine and coarse regions of the Flag component.

5.4 Effect of Changing Cell Spacing on Mechanical Properties

Cast Al-Si has coarser microstructure with secondary dendrite arm spacing on the order of tens of microns and the ultimate tensile strength increases with decrease in the secondary dendrite arm

spacing [124]. Kempen et al. [40] compared the cast AlSi10Mg properties to laser melted AlSi10Mg and found that the laser melted AlSi10Mg has better or comparable mechanical properties. Specifically, the ultimate tensile strength and hardness are higher than the as-cast and aged AlSi10Mg. This is attributed to the fine cellular microstructure in laser melted material which has spacing on the order of sub microns. This means, the finer the microstructure is, the better are the mechanical properties. Thus, with decrease in cell spacing, mechanical properties of laser melted AlSi10Mg will improve and hence it is important to understand the control of cell spacing via process parameters.

5.5 Conclusions

It is critical to understand the behavior of an alloy in an additive manufacturing process in order to expand the usable process space for optimizing the part quality and the build rate. This study contributes toward the body of process knowledge of the AlSi10Mg alloy in a power bed laser melting process, utilizing information from both simulations and experiments. The approach developed in this work can be extended to other materials and processes. Different deposit geometries such as single beads, single layer pads, and multi-layer pads are successively built and methodically analyzed for: (i) identifying the process window for a dense and consistent part, (ii) estimating the effective absorptivity of AlSi10Mg in the explored range of the process space by comparing experiments with simulations, (iii) demonstrating integrated melt pool geometry and microstructure control with a focus on control of cell spacing which affects process outcomes such as the hardness of the material.

Another significant result from this study is that cell spacing scales with effective melt pool width in bulk builds which is similar to the result in chapter 5 where prior beta grain size, also controlled by the cooling rate at solidification, scaled with melt pool size. This greatly simplifies

the strategy for controlling cell spacing to one of controlling melt pool size. These results are further used to vary the microstructure methodically in different locations of a single part which was successful. In addition, this integrated melt pool dimension and microstructure control strategy is demonstrated to be achievable by modifying beam variables that are accessible for any user with operational training and unlocked parameter sets on an EOS M290 machine. These concepts should be extendible to other laser powder bed fusion equipment too.

Overall, this knowledge base can be used by a process engineer to optimize the process for desired outputs instead of just using the nominal parameters recommended by the machine manufacturer.

6 Integrated Control of Melt Pool Geometry and Solidification Microstructure in Laser Powder Bed Fusion of Inconel 718

6.1 Overview

In Chapters 3 and 5 , location-specific control of the prior beta grain width and the cell spacing in a single component made up of Ti64 and AlSi10Mg respectively was achieved by means of integrated melt pool geometry and microstructure control. In this chapter, solidification microstructure control through melt pool geometry control is investigated in detail for Inconel 718 (IN718), a nickel super alloy in the laser melting process. First, melt pool geometry control across the available selective laser melting process space was studied utilizing both modeling and experimental techniques. This was followed by examination of solidification conditions that control the microstructure formed at solidification. After that, single bead and multi-layer pad experiments were performed and analyzed for melt pool geometry, variability in melt pool geometry, defect identification and solidification microstructure.

This work (i) identified the regions in available processing space that will minimize the defects due to under-melting and keyholing (ii) established concepts of integrated melt pool geometry and microstructure control in laser melted IN718 with the main focus on control of texture. Results from this work aid in effectively opening up process space for optimizing the quantities of interest during the build rather than just using the nominal parameters recommended by the machine manufacturer.

6.2 Methods

The following section discusses the process mapping approach, finite element model and experiments that are utilized in this Chapter.

6.2.1 Process Mapping Approach

The process mapping technique developed by Beuth et al. [87] relates identified primary process variables: beam power (P), travel speed (V), background temperature, material feed rate or layer thickness and local part geometry to main process outcomes like process precision, build rate, microstructure, and flaw formation [88]. These identified process outcomes are critical in determining the overall part quality. Using this approach, both numerical modeling results and experiments can be mapped with minimal data to characterize a process. These maps are especially useful in opening up the process space and utilizing the available space to meet application-specific requirements [112].

6.2.2 Finite Element Model

Finite element (FE) simulations were run in the ABAQUS [41] environment. This model is based on the thermal model developed by Zachary Francis for simulating beam based AM processes [125]. In this model, a laser beam carrying a specified power moves along the length of the plate in a straight line with a specified travel speed. This simulates the no-added single bead tests where no powder is added to the substrate. In this chapter, a 2D model is used instead of a 3D model to reduce the computation time. The difference between melt pool area and cooling rates estimated from 2D and 3D models is within 10%, which is an acceptable tradeoff for the resulting reduction in simulation time.

In the 2D model, energy delivered by the laser beam is modeled as a concentrated heat flux which is applied at each node along the axis of symmetry as shown in Figure 6-1. A 4 node axisymmetric element for diffusive heat transfer was used in this model. The model is long enough to avoid the effect of free edges on the melt pool. The mesh is biased toward the region of interest and a symmetry condition is imposed on the face that is along the mid-plane of the melt pool,

which allows only half of the melt pool to be modeled, thus saving computation time. The model limitations are similar to that of the 3D model described in Chapter 4.

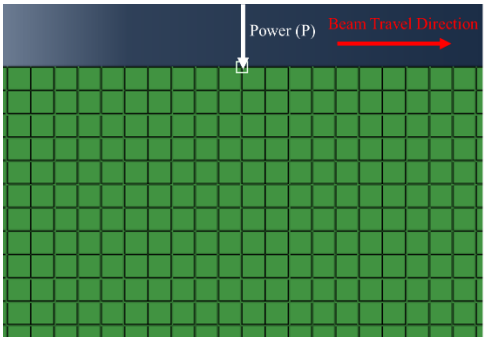

Figure 6-1: Application of concentrated heat flux at a node in 2D model.

The process inputs for the simulations are summarized in Table 6-1. The temperature-dependent thermo-physical properties for IN718 are available from the literature [115]. In this model, the resulting melt pool cross-section is semi-circular, hence melt pool depth is identified at the location of maximum depth as shown in Figure 6-2. Melt pool depth is used to estimate the melt pool area as per Equation 5.1. This is an example melt pool resulting from a laser beam delivering a power of 60 W and travel velocity of 600 mm/s. Along with the melt pool depth, the melt pool length and solidification front are also identified in Figure 6-2. These quantities have significance in relating solidification microstructure to melt pool geometry [28].

Table 6-1: Process parameters for simulations.

Input Parameter	**Range**
Absorbed power (W)	30 - 200
Travel velocity (mm/s)	200 - 1400
Preheat temperature (K)	353
Melting range (K)	1533 - 1609
Latent heat (J/Kg)	227000
Thermal conductivity (W/m K)	8.9 - 29.6 W/m K for T ranging from 298 - 1873 K
Specific heat (J/kg K)	435 -720 J/kg K for T ranging from 298 - 1873 K
Density (kg/m^3)	8190 - 7160 kg/m^3 for T ranging from 298 - 1873 K

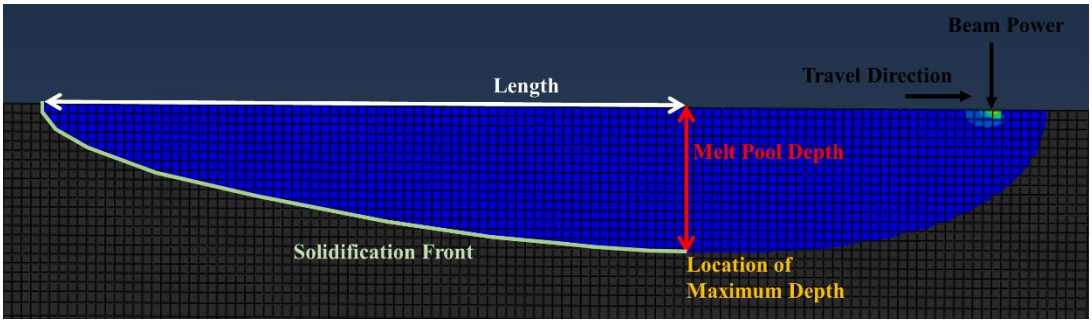

Figure 6-2: Example transverse melt pool image depicting the quantities of interest.

$$melt\ pool\ area = \frac{\pi * depth^2}{2} \tag{5.1}$$

The solidification conditions are extracted from the thermal model to study the as-built microstructure dependence on process parameters. Cooling rates ($\dot{T}$) are estimated using the method outlined in §5.2.2. Previous works by Gockel [28] and Tang et al. [41] on two different AM processes had shown that cooling rates inside the melt pool remains relatively constant with lower cooling rates at the edge of the melt pool. Hence, in the current study, cooling rate values at the tail end of the melt pool are considered for the analysis. Along with the size scale of microstructure, texture is also studied as part of this work. In order to study the variation in texture with change in process parameters, thermal gradient (G) and solidification rate (R) are also estimated from the simulations. Gockel [28] had demonstrated that there is a large variation in thermal gradient along the depth of the melt pool which leads to inconsistent microstructure in a single melt pool. In order to capture the extreme values in the thermal gradient while mapping the morphology, the thermal gradients presented in this work are estimated both at the top surface and at the bottom of the melt pool using the Equation 5.2 [11] and Equation 5.3 respectively. In these equations, ΔT is the solidification interval, v is the beam travel speed, Δx and Δz are the distances between the solidus and liquidus isotherms, respectively, as identified in Figure 6-3.

$$G_{top} = \frac{\Delta T}{\Delta x} = v * \dot{T} \tag{5.2}$$

$$G_{bottom} = \frac{\Delta T}{\Delta z} \tag{5.3}$$

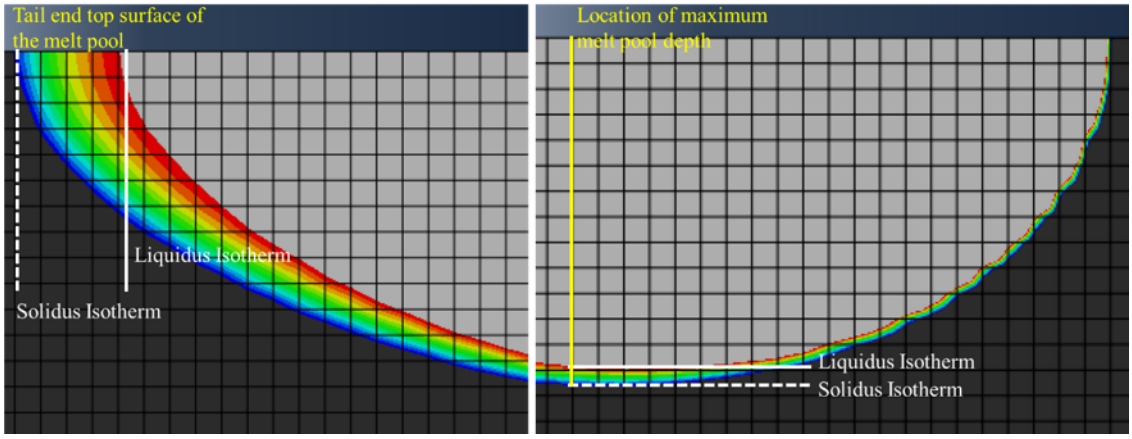

Figure 6-3: (Left) Illustration of the distance between the solidus and liquidus isotherm at the top and (Right) at the bottom of the solidification front.

6.2.3 Experiments

Simple single melt track experiments were performed by varying beam power and velocity on an IN718 substrate without adding any powder. This was done to find the process window that will result in continuous and good quality melt tracks. Process maps to control melt pool geometry were developed using these experiments. Knowledge from the single track experiments was used to deposit solid blocks. These tests were used to study the part porosity and solidification microstructure.

The single bead and multi-layer pad experiments were performed on an EOS M290 machine at Carnegie Mellon University. For these experiments, a .5" x 6" x 6" IN718 plate was procured from Altemp Alloys [126]. Composition of the start plate is detailed in Table 6-2. The feedstock powder used for the multi-layer experiments is spherical, gas atomized powder produced in an inert Argon gas. This is the standard powder supplied by the EOS machine manufacture. The

composition of the powder used in these experiments is outlined in Table 6-3 based on the material analysis information that the manufacturer provided. The build chamber was ventilated with Argon during the experiments. The details of the test layouts and parameters used in these tests are discussed in detail in the following sections.

Table 6-2: Composition of the start plate used in single melt track experiments.

Element	Ni	Fe	Cr	Nb & Ta	Mo	Ti	Al	B, Co, Cu, Mn & Si
Composition/ wt.%	52	19	18	5	3	0.9	0.5	trace amounts

Table 6-3: Composition of the powder used in multi-layer pads (solid block) experiments.

Element	Ni	Fe	Cr	Nb	Mo	Ti	Al	Co, Cu, Mn, Si &C
Composition/ wt.%	52.77	18.5	18.48	5.29	3.10	1.07	0.5	0.19

6.2.3.1 Single Beads

The goal of the experiments is to characterize the melt pool behavior throughout the available process space. The experiment layout is illustrated in Figure 6-4 along with the power-velocity combinations. The numbers inside the pads represent the melting order to avoid any thermal interaction between the pads. The marker labeled “EOS Nominal” in Figure 6-5 is the recommended parameter combination developed by the machine manufacturer for IN718. However, these parameters were not available when the experiments were performed and hence the nominal power and velocity combination for Inconel 625 (IN625) [127] is used for the nominal

case pad test in the layout shown in Figure 6-4. The substrate was heated to a temperature of 353 K and the expected beam spot size is approximately 100 microns.

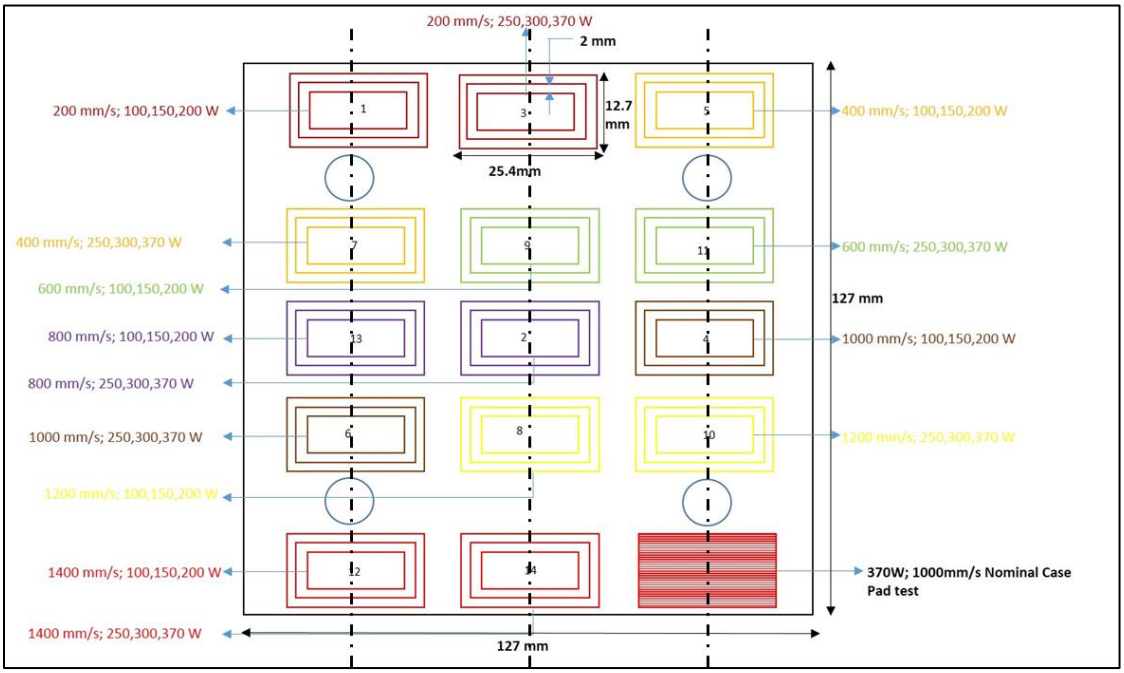

Figure 6-4: Experiment layout for single bead tests along with the power, velocity combinations.

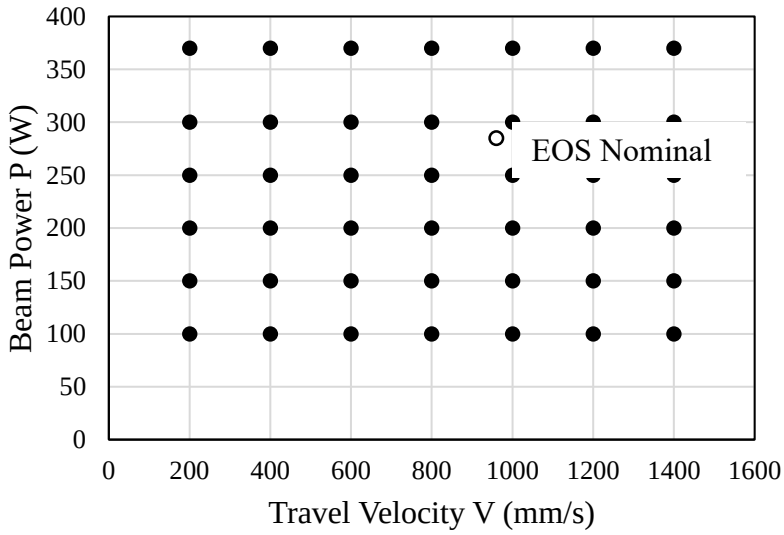

Figure 6-5: Matrix of single bead test points along with the nominal parameters identified in the power-velocity space.

6.2.3.2 Multi-Layer Pads (Solid Blocks)

Multi-layer pads of 10Wx15Lx12.7H mm are built by adjusting the hatch spacing parameter to control the overlap between adjacent melt tracks. Using the melt pool dimensions obtained from the single beads, the hatch spacing was adjusted for the multi-layer pads to match with the nominal overlap. The nominal overlap is the overlap resulting from the melt tracks that are deposited at the nominal process parameter combination specified by the EOS machine manufacturer and it is estimated to be 30% based on the melt pool dimensions calculated from the single bead experiments. The overlap shown in Figure 6-6 refers to the overlap between the adjacent melt tracks which is calculated using the equation shown in the figure. Figure 6-7 illustrates the experiment layout and also provides information about the power, velocity and hatch spacings used for various pads. Other relevant process parameters used in these experiments are outlined in Table 6-4. On the EOS machine, hatch spacings can only be entered as multiples of 10 µm and hence some of the hatch spacing values have to be rounded off to the nearest multiple of 10 µm.

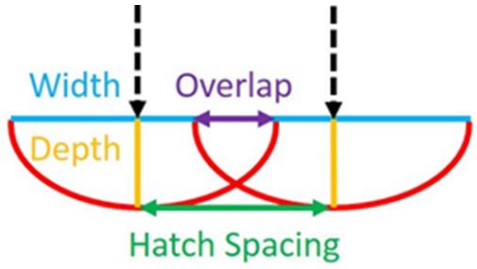

$$Overlap\ (\%) = \frac{(Width - Hatch\ Spacing)}{Width} * 100$$

Figure 6-6: (Left) Illustration of the overlap between the adjacent melt tracks and (Right) Equation to measure the overlap between adjacent melt tracks for a given melt pool width and hatch spacing.

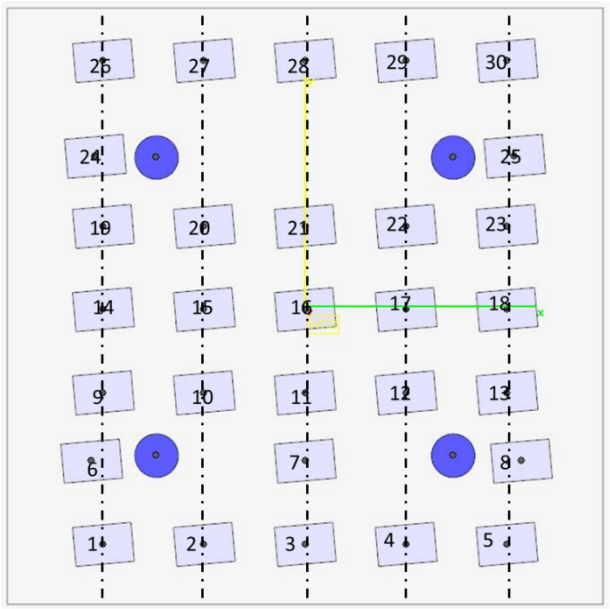

Pad No.	P (W)	V (mm/s)	Hatch Spacing (µm)
1	100	800	70
2	100	400	80
3	100	200	100
4	150	800	80
5	150	600	90
6	100	600	80
7	300	1200	100
8	200	200	190
9	250	200	210
10	150	400	110
11	150	200	160
12	200	1200	70
13	200	1000	80
14	200	800	90
15	200	600	100
16	200	400	140
17	250	1200	80
18	250	1400	80
19	250	800	100
20	250	1000	90
21	250	600	130
22	250	400	180
23	300	1400	90
24	300	1000	110
25	300	800	100
26	300	600	160
27	370	1400	110
28	370	1000	120
29	370	1200	110
30	370	800	120

Figure 6-7: (Left) Layout for multi-layer pad experiments along with pad numbers (Right) Process parameters corresponding to the respective pad numbers in the layout.

Table 6-4: Parameter settings used in the multi-layer pad experiments.

Parameter	Parameter Settings
Layer thickness (µm)	20
Base plate temperature (K)	353
Distance between pads (mm)	10
Sky writing	On
Scan rotation after each layer (°)	67
Focus diameter (µm)	100 [114]

6.2.4 Sample Preparation and Characterization

The black dashed lines across the plate in Figure 6-4and Figure 6-7 are the locations where melt tracks were sectioned to observe the cross-sections of the single bead and multi-layer pad experiments. The sectioning is done using a Wire Electrical Discharge Machine (Wire EDM). All

samples were mounted in Konductomet™ mounting compound via hot compression mounting and polished using a Buehler auto-polisher. The samples were polished using the standard procedure recommended by Buehler, which is provided in Appendix A. Once the samples were polished, they were etched using water-less Kalling's reagent [128] for 45-60 seconds. This etchant consists of 5 grams of Copper Chloride ($CuCl_2$), 100 ml of Hydrochloric Acid and 100 ml of Ethanol.

An Alicona InfiniteFocus optical microscope was used to image the top surface of the single bead melt tracks before sectioning the samples. These images are taken in the middle section of the tracks so they are not close to the turnarounds (edges) and the melt pool has reached a steady state. An example image of the top surface of the no added material single bead is shown in Figure 6-8 (left). The red lines at the border of the melt track were manually identified using GIMP software as a new layer in the image. After that, the layer was filled with black color which resulted in an image as shown in Figure 6-8 (right). Then, the distance between the red lines was measured automatically using an image processing script to calculate the melt pool width along the melt track [70].

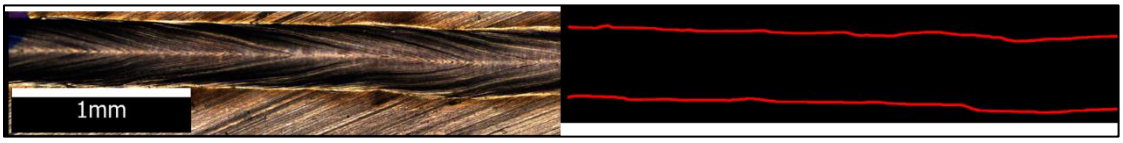

Figure 6-8: (Left) An optical microscope image of the surface of an AlSi10Mg and (Right) melt pool track with the edges manually highlighted in red color and the space between the edges is filled with back color. The melt pool width (distance between the red lines) was measured at every pixel along the length of this image, the results of which were then averaged together. This single bead track was melted using a beam power or 370 W and a velocity of 200 mm/s.

For the single beads, once the surface width measurements were obtained, samples were sectioned and polished to study melt pool geometry and microstructure at the cross section. Polished samples were imaged using an Alicona InfiniteFocus optical microscope. Figure 6-9

shows an example micrograph of the cross section of the single bead sample marked with melt pool geometry characteristics that are of interest. ImageJ software was used to measure the melt pool width, depth and area. The grain widths were measured from the single bead samples using the line intercept method [106]. These results are discussed in detail in the following sections.

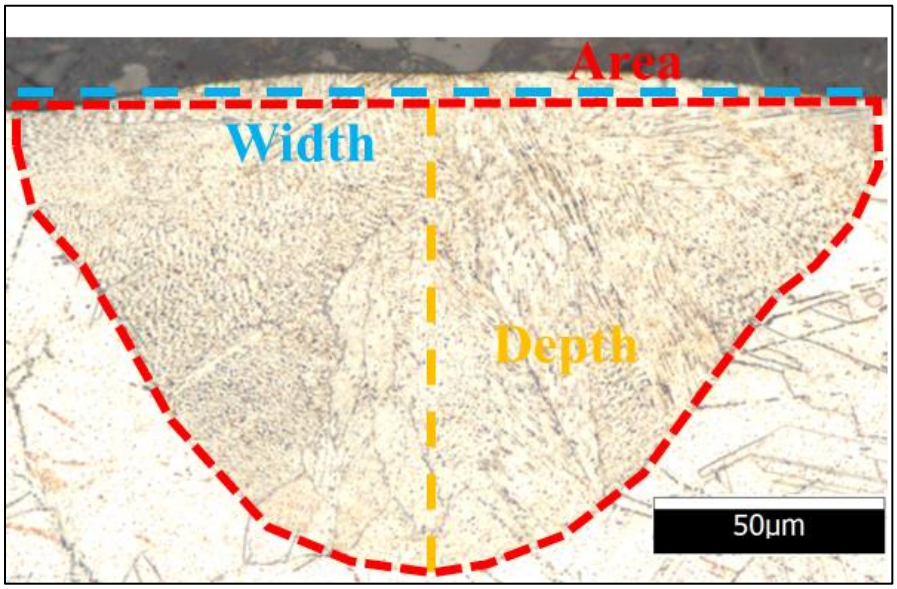

Figure 6-9: An example image of the melt pool cross-sections for single bead with melt pool geometry characteristics marked. This melt pool cross section is from the single bead track melted using a beam power or 250 W and a velocity of 600 mm/s.

For the multi-layer pads, unlike the single bead samples, it was not possible to identify the grains clearly using the Alicona. Hence, other microscopy methods were used such as Scanning Electron Microscopy (SEM) and Electron Back Scatter Diffraction (EBSD). A Quanta 600 SEM was used for obtaining micrographs in the Z-contrast mode. Previous work by Trosch et al. [55] has discussed segregation of the δ-phase (orthorhombic Ni_3Nb) at the grain boundaries and inside the grain for laser melted IN718. Since Nickel and Niobium have different atomic numbers, using Z-contrast aids in identifying solidification features as shown in Figure 6-10. Though these micrographs have provided information on the solidification structure, it was difficult to discern grain boundaries from Z-contrast mode over a large field of interest. Hence, EBSD was used to

obtain information related to the grains over a larger field of interest. The EBSD data was processed using MTEX and the mapping submodule Tango in the Aztec software that is available on the Oxford system. The results associated with the melt pool geometry and microstructure mapping are discussed in detail in the following sections.

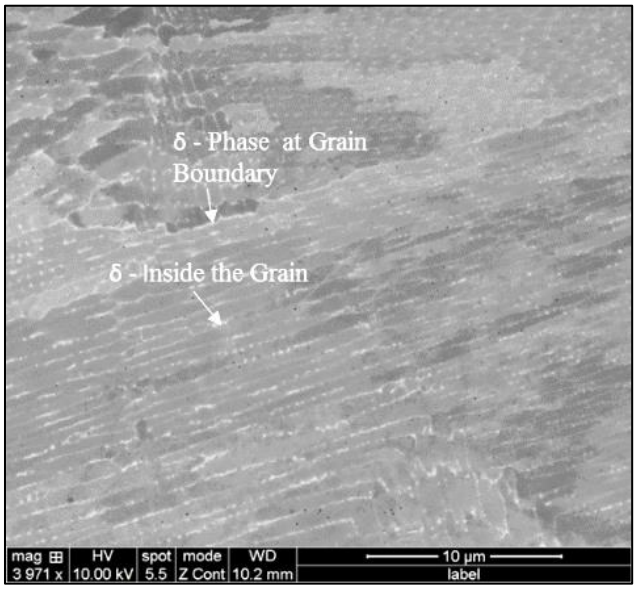

Figure 6-10: Example SEM micrograph illustrating the δ phase in IN718.

6.3 Results

6.3.1 Process Mapping of Melt Pool Geometry

The process maps are developed for the melt pool width, depth and area using the information from the experiments and simulations. These two categories of maps are compared to estimate the effective absorptivity of the material for the simulation set up used in this work.

6.3.1.1 Simulations

The process maps from simulations in this work are developed for melt pool area. Figure 6-11 illustrates the process map for melt pool area resulting from simulations. It can be observed that there are power velocity combinations in the machine process variable space that yield constant melt pool dimensions. Most of the machine manufacturers suggest a standard parameter set to be

used for fabrication for every material the manufacturer supports. However, not all components require the same properties. These parameters need to be changed based on the application of the component and it is important to understand the process input and output relationships to optimize the parameters for the quantity of interest. The process maps can be used to extend the process limits and utilize the full potential of the process to optimize the quantity of interest during the build.

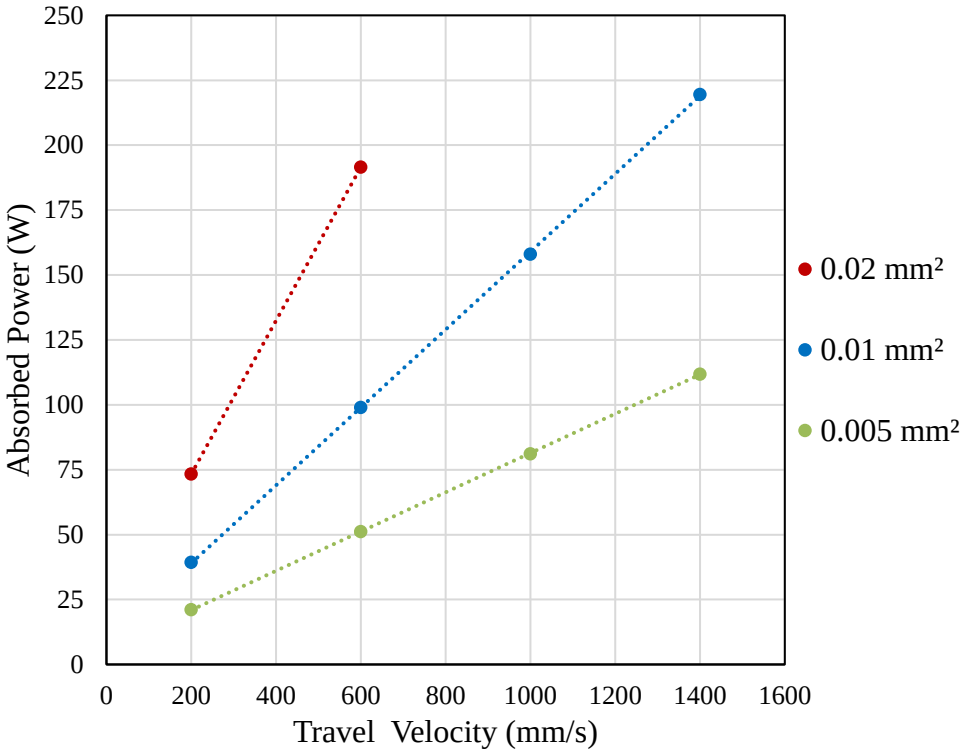

Figure 6-11: Process map for melt pool area resulting from laser melting of IN718. Area remains constant along each line in the map.

6.3.1.2 Experiments

For the melt pool width, measurements are taken on the surface of the melt track and at a single cross-section to map the effect of beam power and travel velocity. The details of these measurements are provided in Appendix B. From these measurements, it can be observed that the melt pool width is higher in the cross-section when compared to the width on the surface for all

the power-velocity combinations used in these experiments. The reason for this behavior is not known. However, this is a good example to emphasize the importance of obtaining the melt pool width at the surface and characterize the melt track over a considerable length rather than looking at one cross-section which either leads to underestimation or over estimation of the melt pool widths. It is worth noting that the lower bounds of the width values are critical values if the user wishes to guarantee an acceptable overlap between adjacent melt tracks and mitigate lack-of-fusion porosity. Also, variability in the melt pool width is low when compared to the variability observed in AlSi10Mg. This shows that melt pool variability depends on the alloy too. Maximum and minimum melt pool width was used to present the variability in the form of process maps. These bounds represent the window in which 95% of the width values are present, assuming that the melt pool width follows a normal distribution. The dashed lines in Figure 6-12 represent the process maps obtained for the upper and lower bounds of melt pool width. From this process map, it can also be observed that the variability in the melt pool width is higher for 150 µm when compared to 200 µm and 250 µm. One more interesting observation from this process map is that the trends for lines of constant melt pool width are similar to the trends observed in lines of constant melt pool widths for AlSi10Mg.

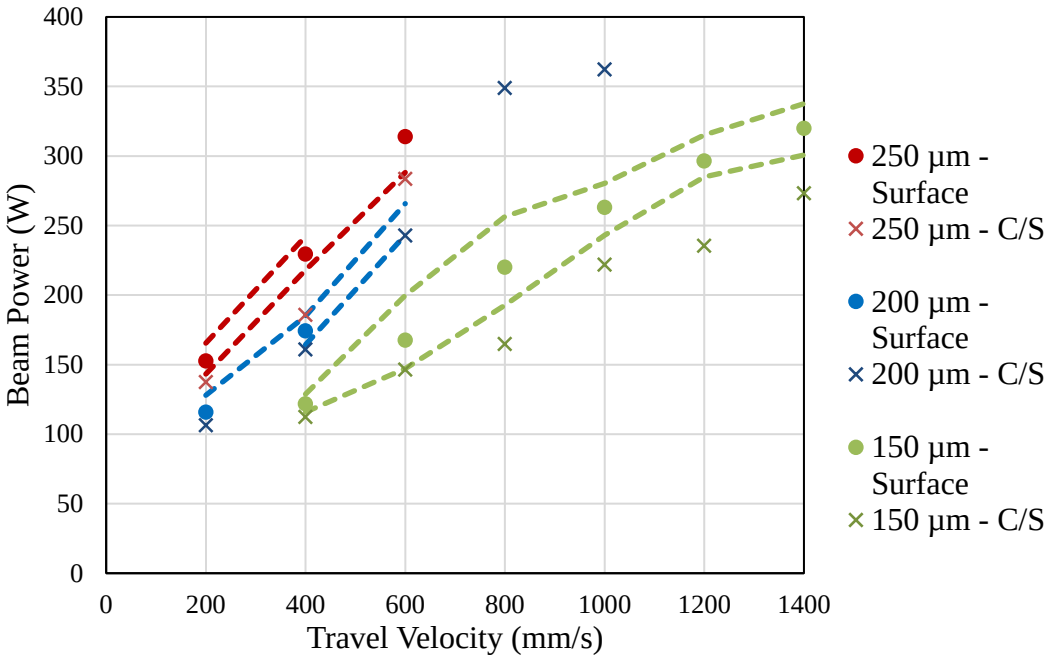

Figure 6-12: Process map for constant melt pool widths at the surface and the cross section for single melt tracks. Dashed lines depict the variation in the melt pool widths.

The discussion on melt pool widths leads into the discussion on melt pool depths. Similar to the variability in the width, variability in the depth is critical to ensure complete melting of powder and overlap between the successive layers. With the available set of experiments, only melt pool width variability was estimated. However, following the procedures explained in Chapter 5, variability in the melt pool depth can also be estimated from the single layer pad experiments. In this work, the process maps for melt pool depth were developed using the cross section depth measurements which are provided in Appendix B. From the depth process map in Figure 6-13, it can be observed that the trends in lines of constant depth are similar to the trends of lines of constant depth presented for AlSi10Mg. This map is especially useful to understand the process region for minimum allowed depth in order to avoid any porosity due to insufficient melting of the powder layer where melt pool depth is less than layer thickness. Application of depth process maps is discussed further in the next section where the process window for no keyholing or lack of fusion is identified.

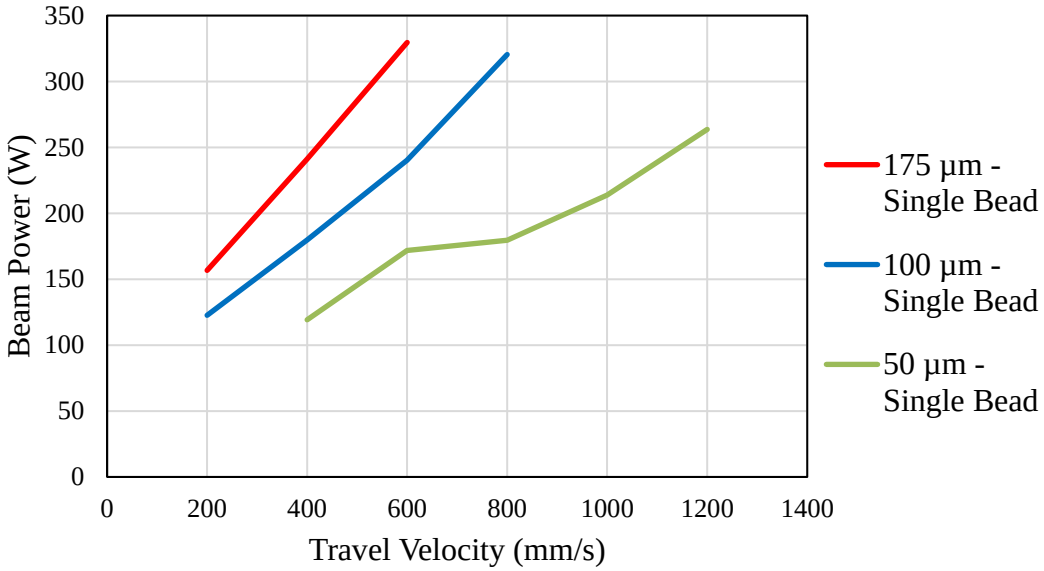

Figure 6-13: Process map for constant melt pool depths for single beads.

Similar to the melt pool width and depth, the melt pool area process maps are developed to study the effect of process variables on the melt pool cross-section area. Figure 6-14 illustrates the process map for melt pool area developed for the data provided in Appendix B. Within the available information from the single bead cross-section, it can be observed that the lines of constant melt pool area follow linear trend. Similar to the melt pool width and depth, trends in lines of constant area are similar to the trends in lines of constant area for AlSi10Mg.

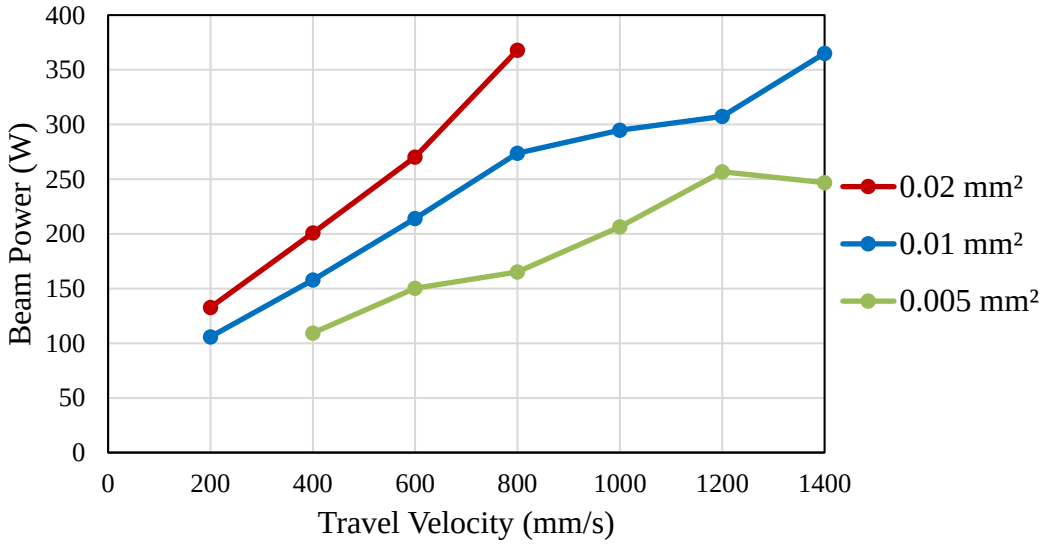

Figure 6-14: Process map for constant melt pool area for single beads.

In summary, results from AlSi10Mg and IN718 for melt pool geometry demonstrate that the nature of process maps remains the same for different alloy systems and the mapping procedures can be applied to different materials. This is discussed in detail in Chapter 7.

6.3.2 Establishing Process Window from Single Bead Experiment Results

Part porosity is a concern in additively manufactured parts since it affects the fatigue life of the components [94]. Previous work has shown that both process parameters and powder characteristics can influence the part porosity [103][121]. In this work, the process window for IN718 is defined as the region in the process space that produces final parts with limited porosity due to lack of fusion or keyholing. Lack of fusion pores are formed at power-velocity combinations where the melt pool does not fully melt through the powder layer and/or insufficient overlap the adjacent melt tracks. The layer thickness must be changed to eliminate the lack of fusion porosity between successive layers while the overlap between the adjacent melt tracks can be controlled by varying the hatch spacing. Whereas, keyholing porosity can be reduced by increasing the spot size [102].

Similar to the process window shown in Chapter 4, the melt pool geometry data from the single bead experiments is used to develop a qualitative process window for IN718 which is shown in Figure 6-15. The lack of fusion region is identified by the melt pools which have a depth less than the nominal powder layer thickness of 40 µm for IN718 on an EOS M290 machine. Usually, both 20 µm and 40 µm layer thicknesses are used for IN718. However, the lack of fusion region identified for 40 µm since, it also includes lack of fusion region for 20 µm layer thickness. Therefore, process window is presented for 40 µm thick powder layers. The keyholing region was identified based on the melt pool width to depth ratio. The cases with melt pool depth to half-width ratio greater than 1 (indicating a non-semi-circular geometry) were treated as keyholing melt pools

[102] [129]. Since the information used for this process window is from a single cross section and keyholing melt pool depth is not consistent throughout the melt track [104], this process window is an approximation, especially at the boundary of the keyholing region.

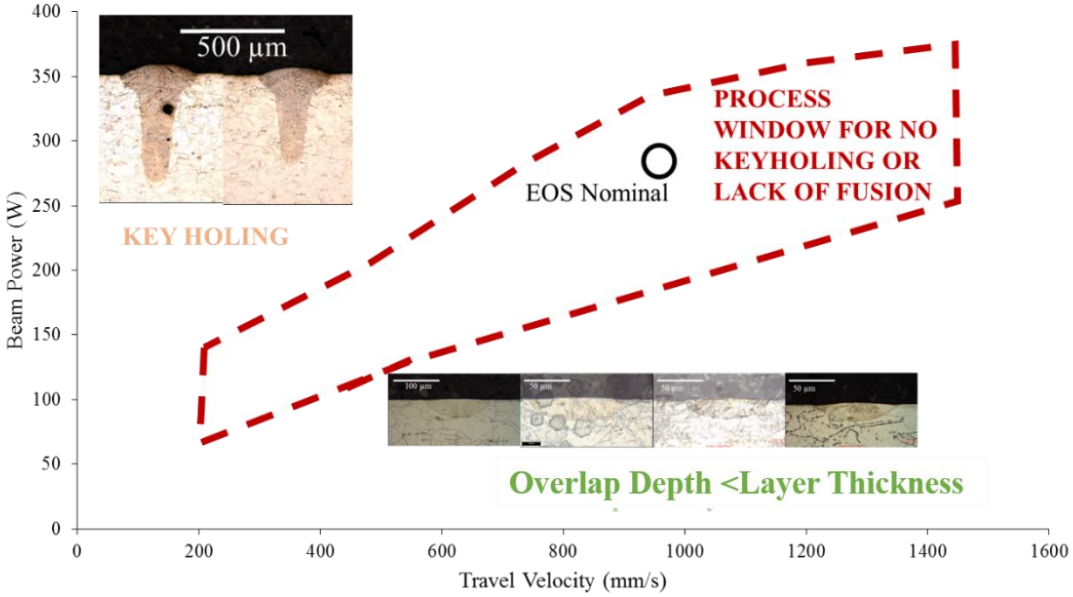

Figure 6-15: Qualitative process window for IN718 depicting the lack of fusion and keyholing regimes for the parameters covered in this research.

6.3.3 Part Quality from Multi-Layer Pads

The multi-layer pads built in this work were used to qualitatively understand final part quality. In these experiments, the hatch spacing was adjusted to maintain the overlap percentage between adjacent tracks equivalent to the nominal EOS overlap of ~30%. Part quality from the multi-layer pads is presented at a single cross-section in the pads. The samples are selected from different regions in the process space as shown in Figure 6-16. The cross section images of the pads (top) and the corresponding cross section images from single beads (bottom) are shown in Figure 6-17.

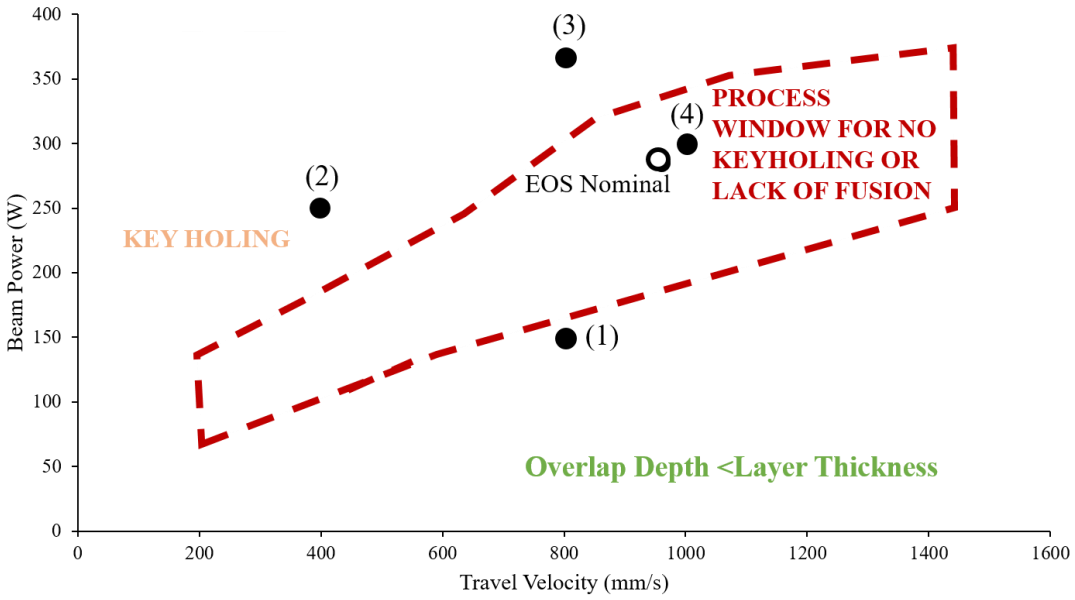

Figure 6-16: Samples of interest identified in different regions of the process space for IN718.

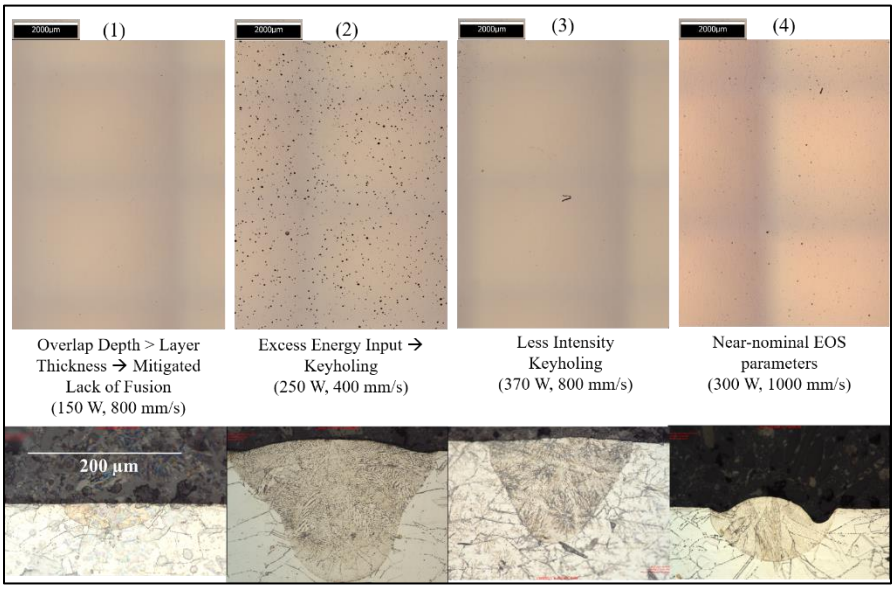

Figure 6-17: (Top) Cross section images of the multi-layer pads illustrating the part quality and (bottom) corresponding single bead cross section images for the same power, velocity combinations used in the pads.

The images from the cross section are used to qualitatively discuss the part porosity at the cross sections and the ability to control the porosity by controlling the process parameters such as beam power, velocity and layer thickness. For example, Sample 1 which is built at 150W and 800

mm/s is actually in the lack of fusion region if layer thickness of 40 µm is used. However, in these experiments 20 µm thick layers are used. This resulted in a part with no lack of fusion defects. The under melting porosity observed in the low power and low velocity sample can also be mitigated by adjusting the hatch spacing [65,103,120] or by decreasing the beam spot size [102] apart from reducing the layer thickness. Figure 6-17 (top) also illustrates the defects due to keyholing porosity for the samples which are built using the parameters that lie in the keyholing region. The quantity of pores in Sample 2 are higher than that of Sample 3 though both are in the keyholing region. This is due to the difference in the shape of the melt pool in both the cases which deviates from the elliptical melt pool assumption used for determining hatch spacing. In addition, there is variability in the melt pool depth due to key holing which also contributes to the deviation from assumption. This keyholing porosity can be eliminated at the higher energy density region of process space by increasing the beam spot size [102]. From Figure 6-17 (top), it can also be observed that that the porosity percentage due to keyholing is not consistent for the two keyholing cases that are presented here. Along with these cases, a cross section image of Sample 4, which is close to nominal build conditions on EOS M290, is also presented. It is interesting to note that there is porosity in this sample though it is well within the process window for no keyholing and lack of fusion. This is potentially due to the bead up at that power-velocity combination at higher length to width ratio of the melt pool [118,119]. In this work only qualitative observations from one single cross section are presented since the main focus is on demonstrating the porosity in the keyholing and lack of fusion regions of the process space and comparing with the sample built at nominal or near nominal processing conditions.

6.3.4 Comparison between Simulations and Experiments for Single Beads

As noted in §5.2.2, there are certain phenomena like convection to the surroundings, radiation, Marangoni flows, keyhole-mode melting which are not included in the model used in this work. The power which is applied in the simulations is entirely absorbed by the materials, whereas not all the power that is delivered by the laser is absorbed by the material in experiments. Thus, a comparison between the beam input power used in experiments and absorbed power from simulations results in a factor that is equivalent to the absorptivity of the material. Since, the model is not a thorough representation of the experiment set up, the absorptivity is referred to as effective absorptivity in this work.

The effective absorptivity is estimated for only melt pool area in this work since a point heat source is used in the simulation model that results in a semi-circular melt pool. The effective absorptivity data presented in Figure 6-18 shows that with increase in depth to half-width ratio, absorptivity increases. The explanation for this is similar to the one provided in §5.3.4 where keyholing led to an increase in estimated absorptivity of the material. Keyholing mode melting is different from conduction mode melting which is the primary heat transfer mode in the current model. Therefore, the absorptivity is estimated from the data points which are in the non-keyholing region as shown in Figure 6-19. The summary of the effective absorptivity values estimated from this work are detailed in Table 6-5.

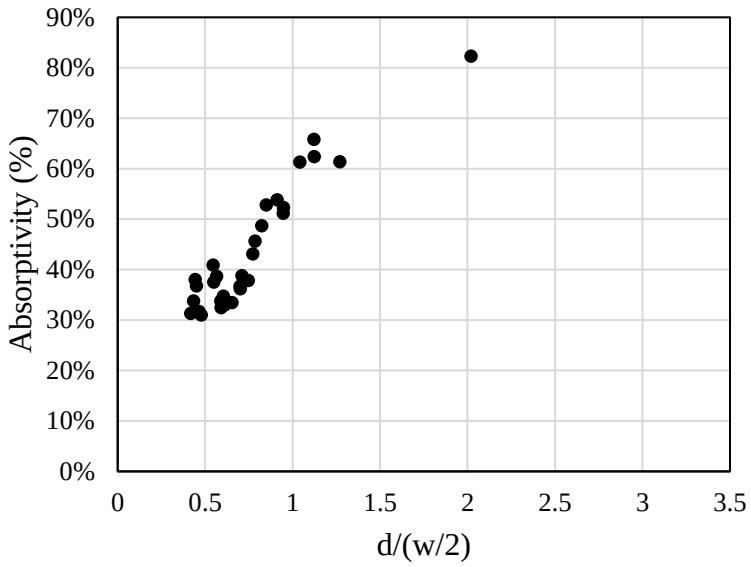

Figure 6-18: Illustration of the increase in absorptivity estimated from melt pool area with increase in melt pool cross section aspect ratio.

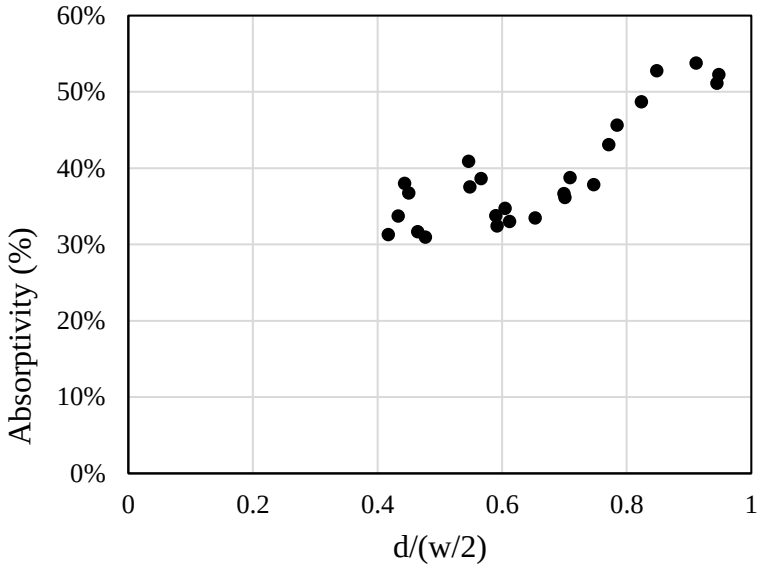

Figure 6-19: Illustration of the variation in absorptivity estimated from melt pool area with melt pool cross section aspect ratio in non-keyholing region.

Table 6-5: Estimated values for absorptivity from melt pool area in the non-keyholing regime of the process space.

Melt Pool Geometry Considered	Area
Average Effective Absorptivity (%)	39%
Standard Deviation (%)	7%

6.3.5 Process Mapping of the Solidification Microstructure

Similar to the work done in Chapters 4 and 5 on Ti64 and AlSi10Mg, in this Chapter, both simulations and experiments are used to understand the solidification microstructure control. First, results from the simulations are discussed followed by the experimental analysis.

6.3.5.1 Process Mapping of Solidification Conditions from Simulations

In order to extend the concept of the integrated melt pool geometry and microstructure control [28] to laser melted IN718, the effect of melt pool area on thermal gradient and cooling rate are plotted explicitly. Figure 6-20 shows the variation of cooling rate with melt pool area obtained from simulations. With an increase in the melt pool area, cooling rate decreases and vice-versa. This can be explained by the fact that for bigger melt pools, resulting from higher energy density, it will take more time for the energy to dissipate thus resulting in a decrease in the cooling rate. This result is similar to the result from Chapter 5(§5.3.5), where cooling rate followed a similar inverse relationship with the melt pool area for AlSi10Mg. This implies that the process maps for cooling rates for IN718 will follow similar trends as process maps for melt pool area in the power-velocity space.

On the other hand, thermal gradients are critical to study the equiaxed to columnar transitions in the microstructure [29]. Figure 6-21 and Figure 6-22 show the variation of thermal gradient with the melt pool area obtained from the simulations. Similar to the cooling rates, thermal gradients also vary with melt pool area. With increase in the melt pool area, thermal gradient decreases and vice-versa. However, the power factor is -0.5 and -1.4 for the thermal gradient in Figure 6-21 and Figure 6-22, when compared to -1 for the cooling rate in Figure 6-20. These relationships are obtained from simulation results. Unlike melt pool geometry, there is no direct comparison to validate these absolute values predicted for thermal gradient and cooling rates with

an experiment measurement. However, results from Chapter 4 demonstrate that the qualitative trends for the solidification conditions inferred from the simulations provide useful insights for interpreting the microstructure. From these figures, it is important to note that the thermal gradients obtained at the top surface of the melt pool are negligible when compared to the thermal gradients estimated at the bottom of the melt pool. To be specific, the thermal gradient at the top surface is an order of magnitude less than the thermal gradient at the bottom of the melt pool. Along the solidification front, the resulting thermal gradient will be lower in the top region of the front when compared to the bottom region.

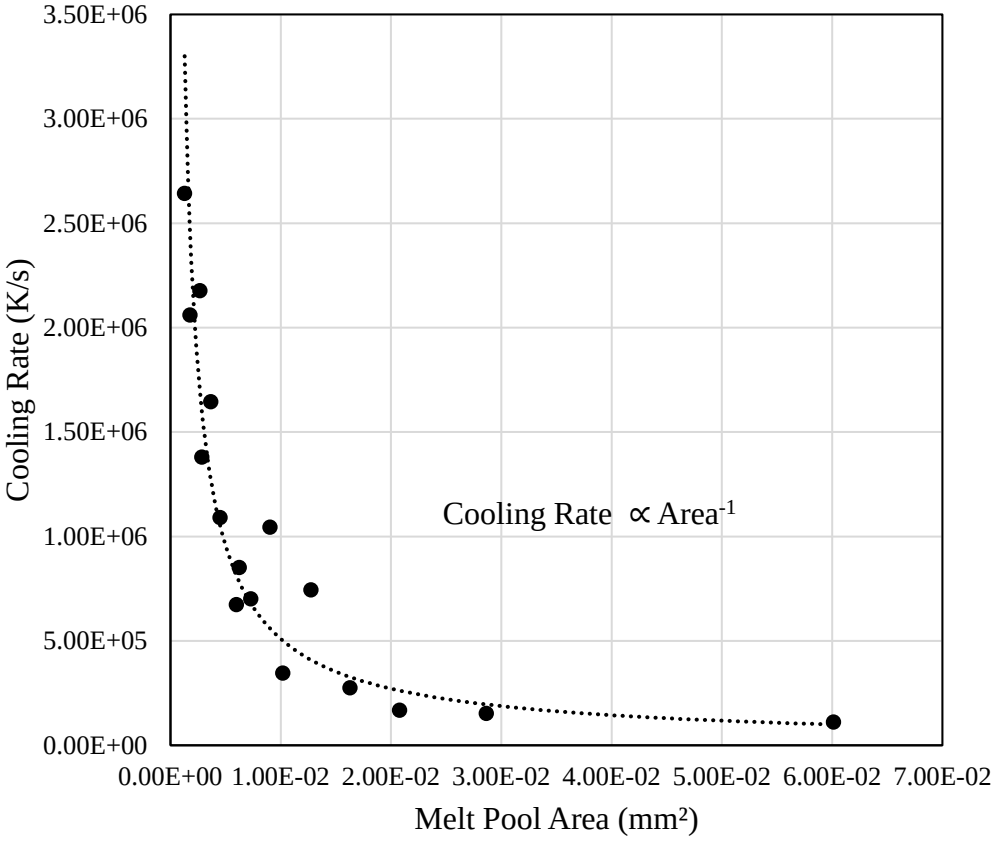

Figure 6-20: Variation of cooling rate at the tail end of the melt pool with melt pool area from the no added material simulation model.

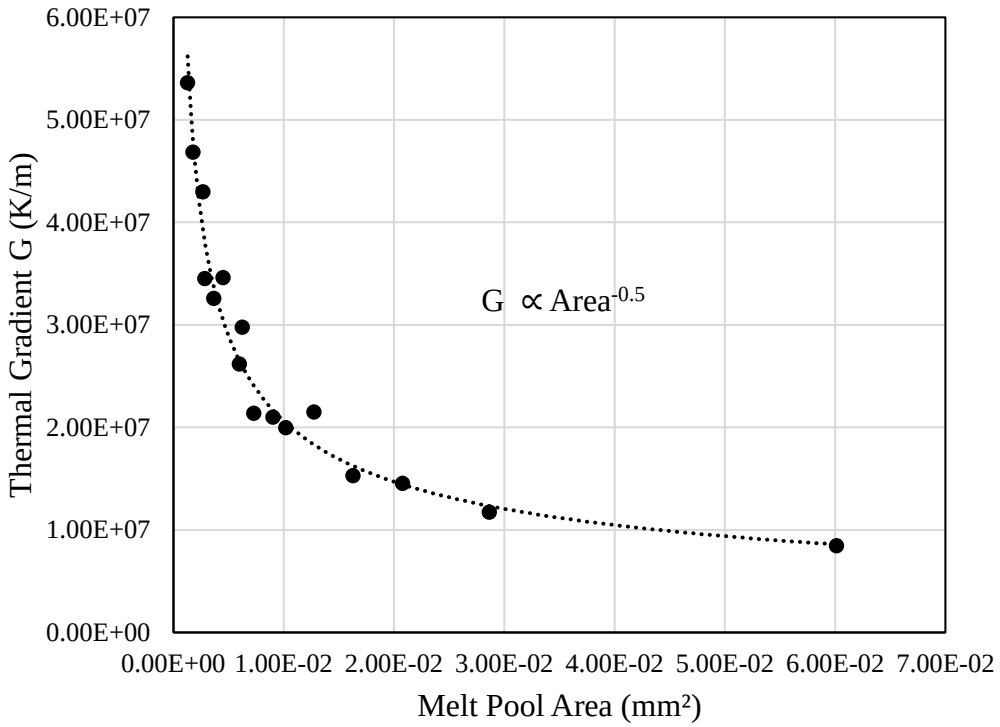

Figure 6-21: Variation of G_z with melt pool area from no added material simulation model.

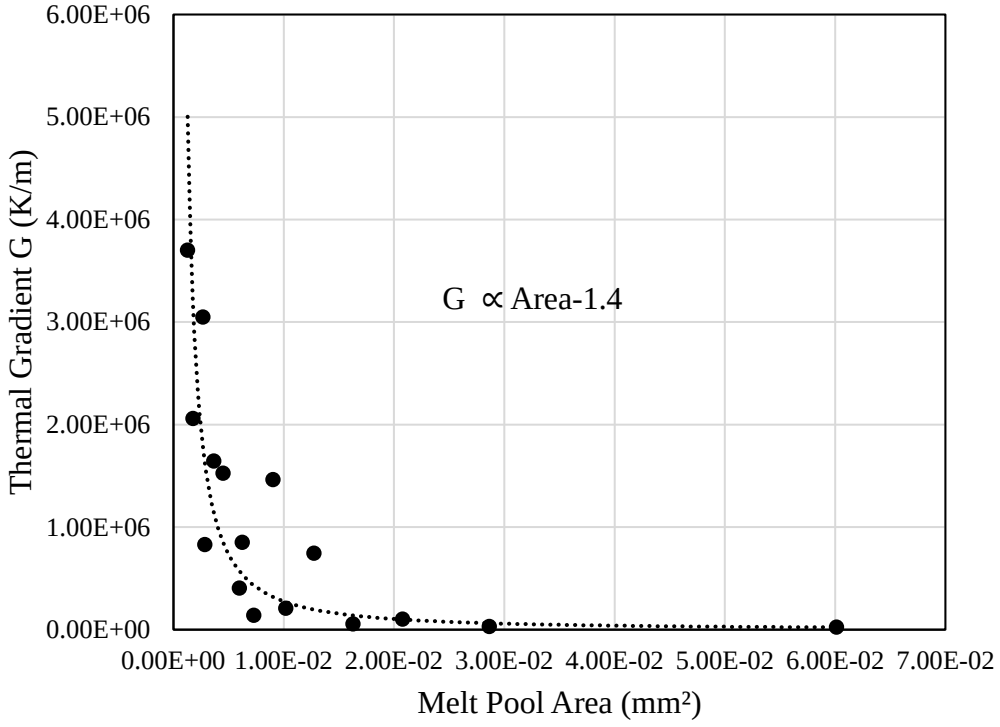

Figure 6-22: Variation of G_x with melt pool area from no added material simulation model.

6.3.5.2 Experiments

Both single bead and multi-layer samples are analyzed to understand the microstructure formed at solidification. In the single beads, simple grain size analysis was performed to understand the relationship between the grain size and the melt pool size. This was followed by more detailed analysis of the grains and the structure inside the grains in multi-layer pads.

Single Beads

Similar to Ti64, in IN718 single beads the grains grow epitaxially from the start plate towards the center of the melt pool as shown in Figure 6-23. In the previous chapters on solidification microstructure control in Ti64 and AlSi10Mg, it was demonstrated that the knowledge from single beads can be used to understand the analysis for solid blocks. And, the relationship between solidification microstructure and melt pool geometry predicted from single beads qualitatively holds true for multi-layer pads or solid builds. The grain widths from single beads are measured to examine if there is a link between the grain size and the melt pool size in IN718.

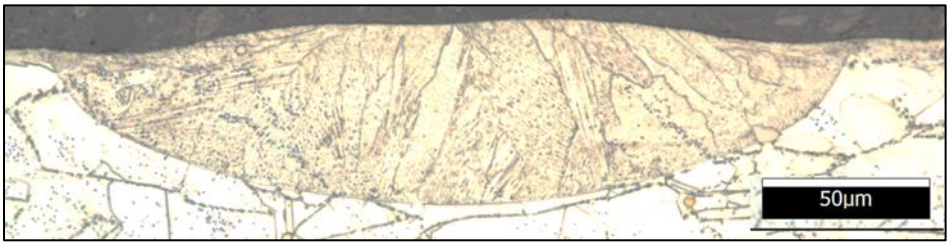

Figure 6-23: Example cross section of the etched melt pool used for estimating the average grain size.

The grain sizes are measured from the melt pools in which grains were clearly identifiable using line intercept method [106]. A line is drawn across the grains in the melt pool and each grain width is measured using ImageJ software. Table 6-6 provides information about both the average grain width along with the beam power and velocity corresponding to the single bead cross section from which grain sizes are measured. Figure 6-24 shows these grain widths plotted with effective

melt pool width. Unlike the result in Chapter 3 for prior beta grain width control in Ti64, in this case, there is no is no distinct relationship between the grain width and effective melt pool width. One possible explanation for the spread in the data in the plot show in Figure 6-24 is based on the fact that grains in the single beads nucleate and grow from the grains in the start plate as shown in Figure 6-25. The arrows show the example grains which continue to grow from the start plate. However, the start plate grain size did not affect the grain size trends in the single bead Ti64 melt pools from electron beam melting. This is likely due to the smaller size grains in the start plate when compared to the prior beta grains in the melt pool. This means apart from thermal conditions, grain size in the start plate seems to affect the grain size in the single beads.

Table 6-6: Average grain size measurements from single bead samples.

Power (W)	Velocity (mm/s)	Average Grain Width (μm)
370	400	18
300	400	13
250	400	9
200	600	13
100	600	8
370	600	14
300	600	10
250	600	9
200	800	9
150	800	10
300	800	12
370	1000	16
300	1000	17
250	1000	12
200	1200	8
200	1400	10
150	1400	9
100	1400	8
370	1400	16
300	1400	14
250	1400	11

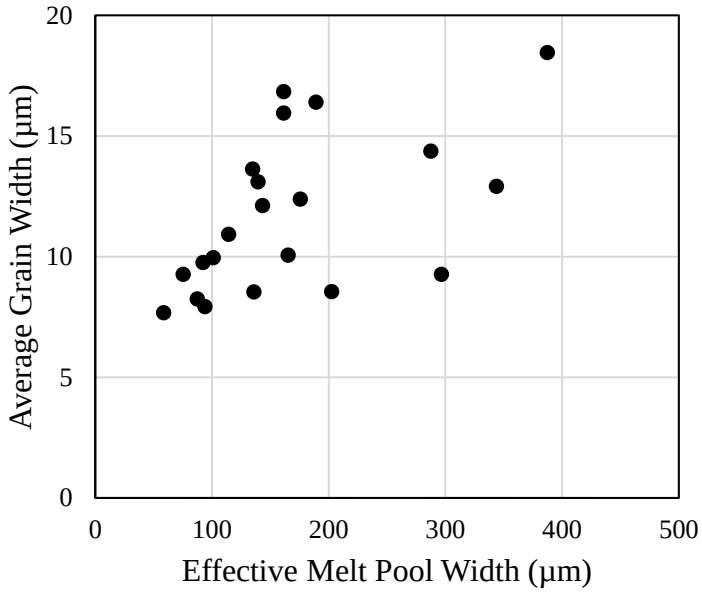

Figure 6-24: Plot of grain width vs. effective melt pool width in IN718 single bead cross section images.

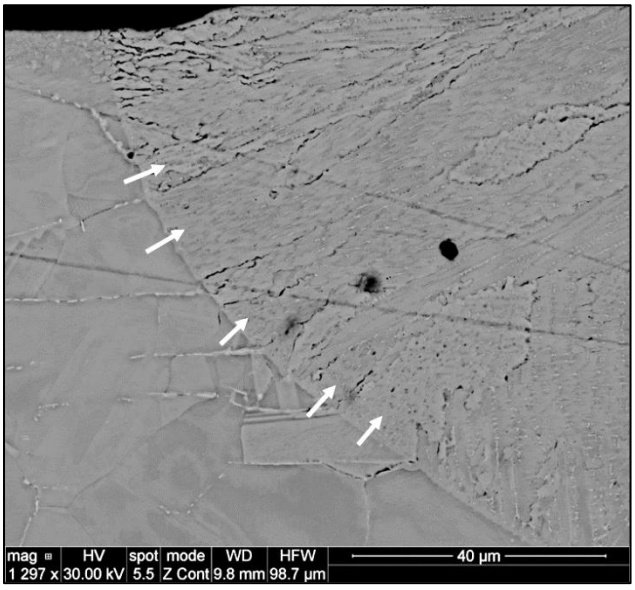

Figure 6-25: Illustration of the epitaxial growth of grains in the single bead samples emphasizing the importance of substrate grain size in determining the grain size in the melt pool.

Multi-layer Pads (Solid Blocks)

The multi-layer pads were analyzed for grain orientation, size and shape. Initially, the goal was to study the change in grain size with change in the process parameters. However, the etchant which

was used for the single beads did not show any observable features in the solid blocks using a light optical microscope. Hence, EBSD was used to study the above mentioned quantities of interest. Since, EBSD is expensive, it was not feasible to analyze all 30 samples. Hence, four samples that are identified within the good region of the processing window in Figure 6-26 are studied in detail for microstructure. Previous work by Gockel [28] had demonstrated that by controlling the shape of the melt pool through length over depth (l/d) ratio, grain morphology can be controlled for prior beta grain widths in Ti64. Hence, the four sample are chosen such that two sets of samples have the same melt pool size and all of them have different melt pool length over depth (l/d) ratios. Length over depth (l/d) values are measured from simulations using the effective absorptivity estimated by comparing the simulations with experiments. It is important to note that the absolute values might not be accurate; however, the relative trends and order of magnitudes can be estimated using this procedure. This assumption can be reinforced by the results in Chapter 5, where the trends between cooling rates and melt pool geometry are supported by results from experiments. Given that the cooling rate is inversely proportional to the melt pool size, it is expected that the sample with a lower melt pool area will result in finer grains when compared to a sample with larger melt pool area. These samples are imaged to capture information related to grain size, shape and orientation.

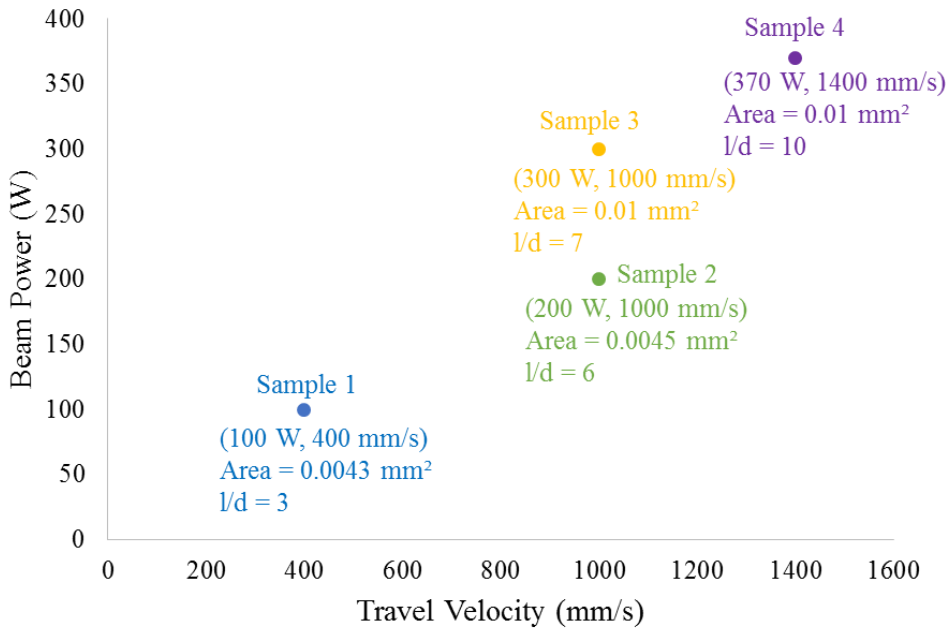

Figure 6-26: Sample chosen for microstructural analysis identified in the process space with estimated melt pool area and aspect ratio.

The samples represent cases with variation in cooling rate and shape (l/d) of the melt pool which results in change in grain morphology as shown in Figure 6-27. In this figure, thermal gradients are presented over a range identified by the arrows instead of one single value. The range here includes the minimum and maximum possible thermal gradient along the solidification front which are estimated from the simulations. Similar to the validity of l/d values, these thermal gradients are qualitative estimates of the relative variation among the samples. To study the grain morphology transition, solidification rate is equally important as the thermal gradient. For the l/d range considered in these experiments, average solidification rate along the solidification front can be assumed to be equal to the beam travel velocity.

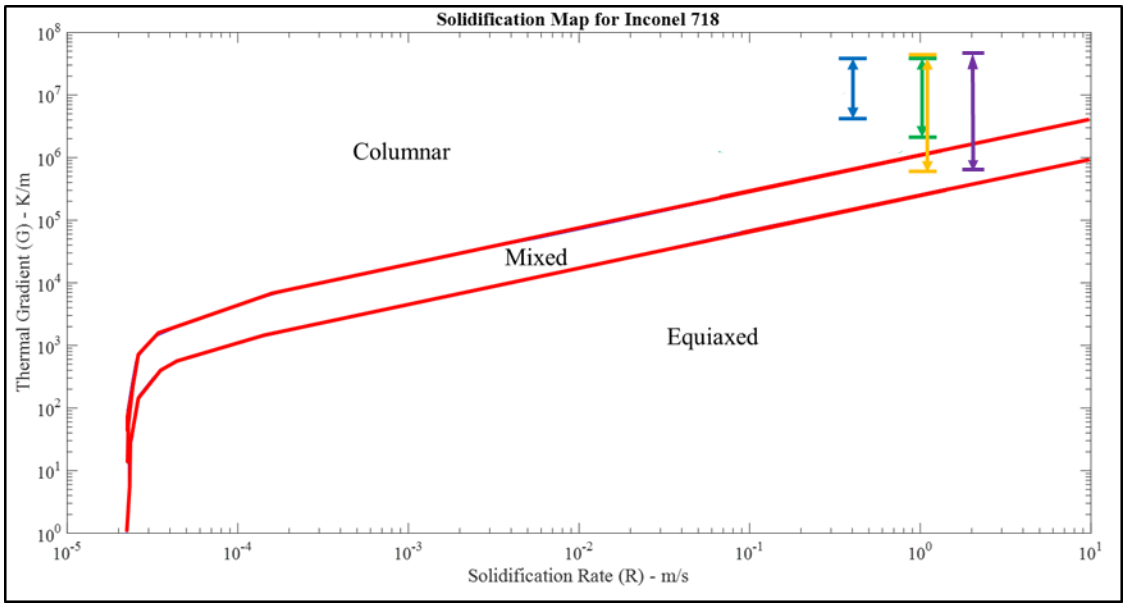

Figure 6-27: CET for IN718 [99] **with the expected morphology identified for the three samples which are analyzed using EBSD scan. The colors correspond to the power velocity combinations in Figure 6-26.**

Grain Orientation

For the grain orientation analysis, raw data is processed for orientation mapping using MTEX [130–132]. For FCC structures, <100> is the favorable crystal growth direction [29]. In AM, orientation of the grains with respect to build direction is of primary interest since columnar dendritic growth is predominant in additively manufactured components [11,30,57]. These dendrites growing along the same direction will result in a columnar grain. This will give rise to anisotropy in the samples. Therefore, inverse pole figures (IPFs) are generated for build direction (Y axis) to understand the sample orientation with respect to crystal orientation. In the IPFs of samples built at (100 W, 400 mm/s) in Figure 6-28 (a) and (200 W, 1000 mm/s) in Figure 6-29 (a), the red colored regions are crystals that are oriented along the <100> direction. This means, the build direction consists of the crystals with <100> orientation. This results in columnar growth in these two samples. This matches well with the qualitative prediction for grain morphology presented in the CET diagram in Figure 6-27. For the sample built at (300 W, 1000 mm/s), and

(370 W, 1400 mm/s) Figure 6-30 (a) and Figure 6-31 (a) respectively, for which the thermal gradient is spanning the mixed and columnar grain growth regions, there is no preferred crystal growth direction and the structure is random. The scale bar beside the IPF represents the intensity of a crystal orientation compared to the intensity of the same crystal orientation in a random structure that consists of all possible crystal orientations. For example, in Figure 6-28 (a), the maximum intensity value of 6 for sample 1 is more when compared to the maximum intensity value of ~2 in Figure 6-30 (a) for the sample 3 and sample 4. This means, along the build direction, <100> texture is stronger in the columnar growth sample when compared to the <100> texture in the sample with random orientation. It is also important to note that the color of one grain is not uniform. There is an orientation gradient within each grain. Orientation data from these samples suggest that, just by changing the primary melting parameters: beam power and velocity, the grain orientation (texture) can be changed.

It is also important to understand the orientation of crystals with respect to non-build directions when understanding texture. For this purpose, pole figures are provided in Figure 6-28 (b), Figure 6-29 (b), Figure 6-30 (b) and Figure 6-31 (c) for all four samples. In the first two samples (Figure 6-28 and Figure 6-29) with columnar growth (strong texture along the build direction), the pole figures show the accumulation of poles along specific directions indicated by the maxima in red color. Whereas, for the samples 3 and 4, the poles figures show random distribution of poles with lower intensity than samples 1 and 2. This can be explained by the weak texture observed in samples 3 and 4. Available data suggests a correlation between the orientation of crystallographic planes and process parameters which gives the ability to alter texture via melt pool geometry control.

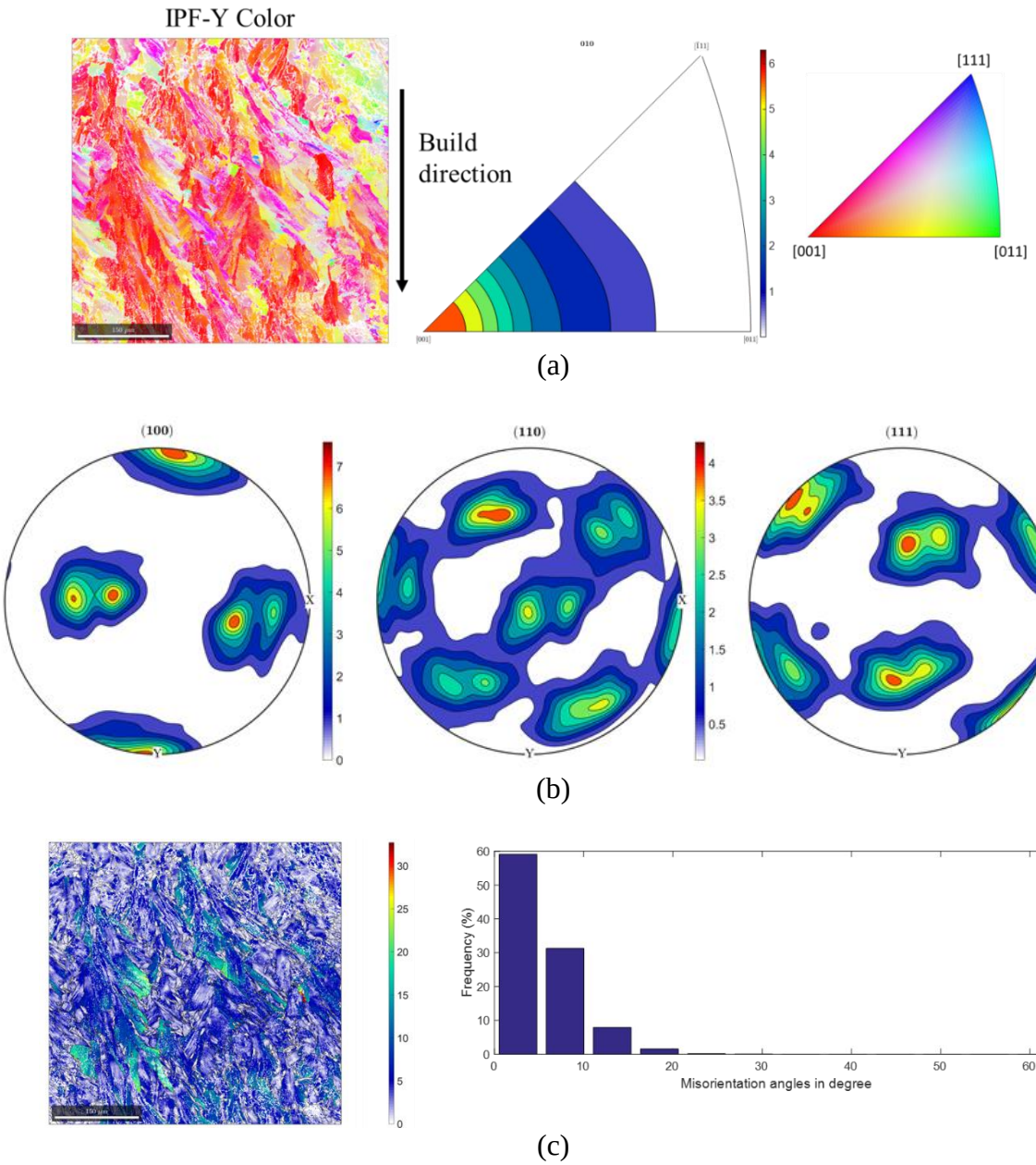

Figure 6-28: (a) IPF-Y Color map (b) Pole Figure and (c) Grain misorientation map and frequency histogram for Sample 1 built at 100 W, 400 mm/s.

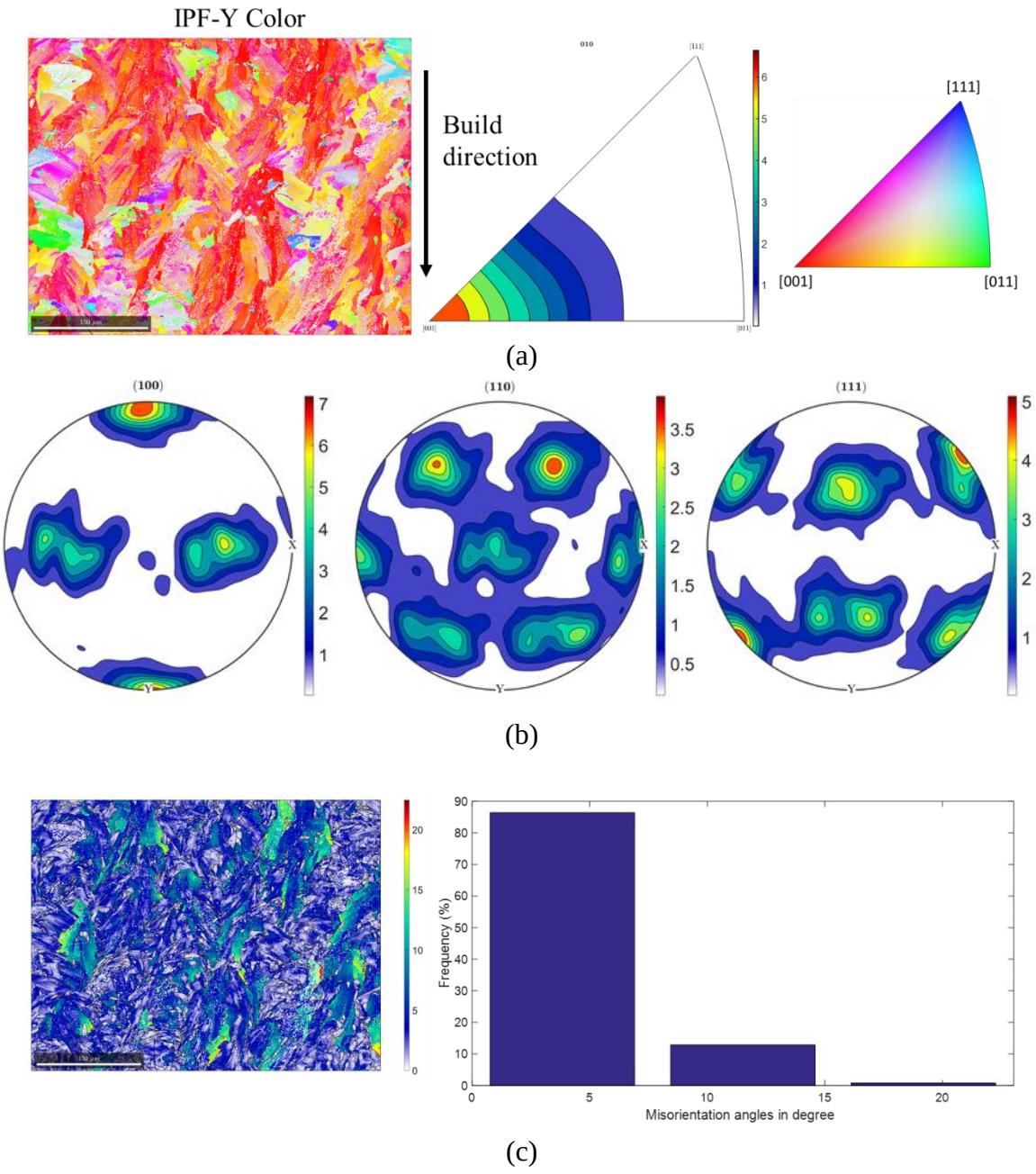

Figure 6-29: (a) IPF-Y Color map (b) Pole Figure and (c) Grain misorientation map and frequency histogram for Sample 2 built at 200 W, 1000 mm/s.

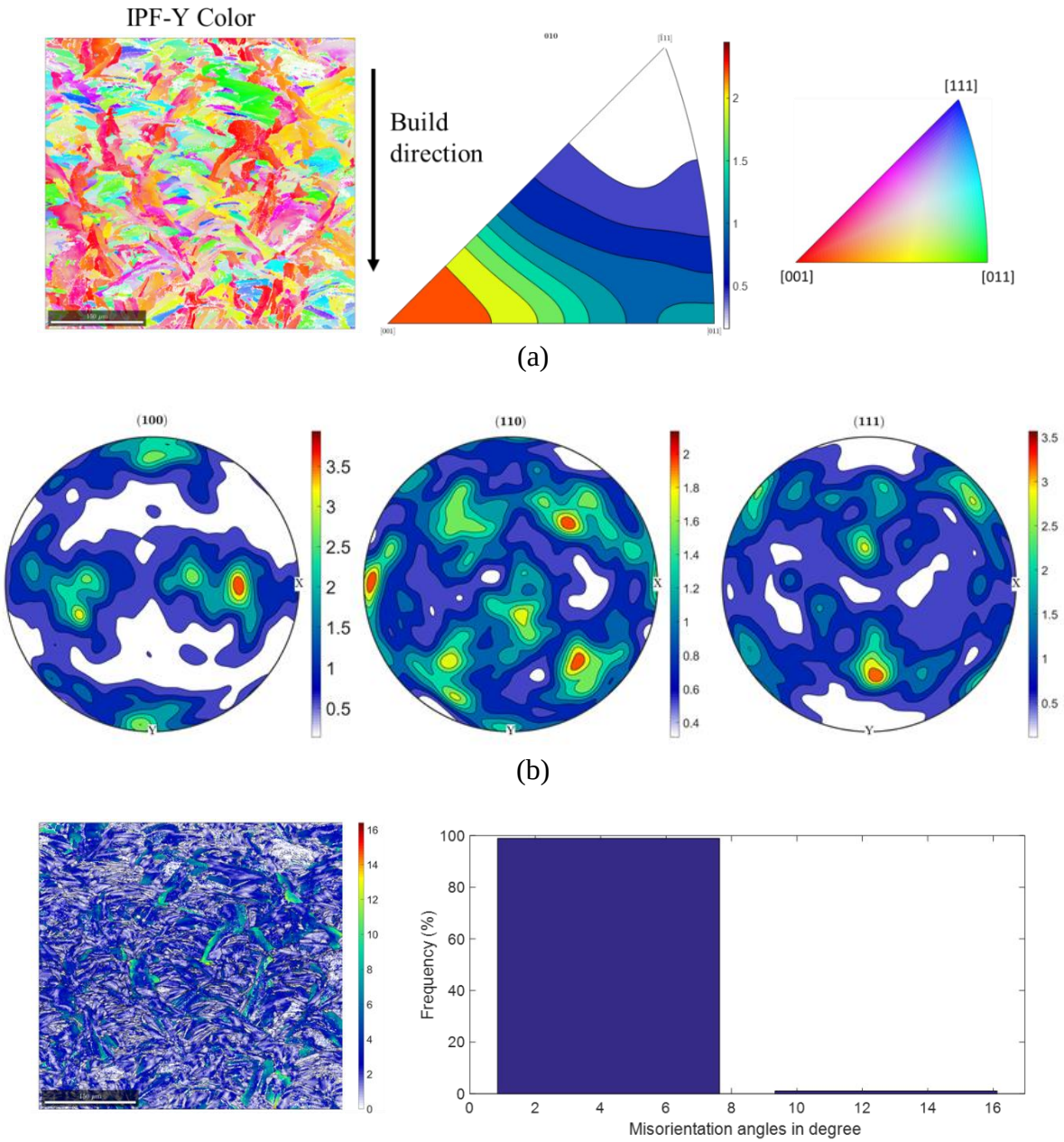

Figure 6-30: (a) IPF-Y Color map (b) Pole Figure and (c) Grain misorientation map and frequency histogram for Sample 3 built at 300 W, 1000 mm/s.

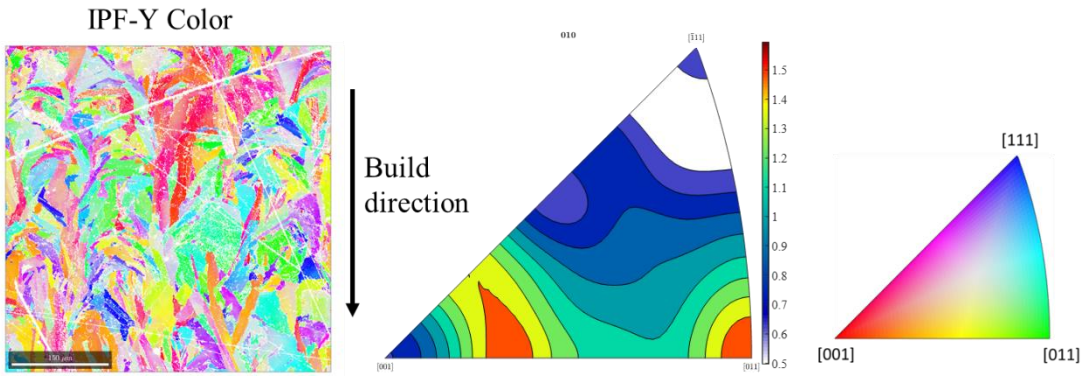

(a)

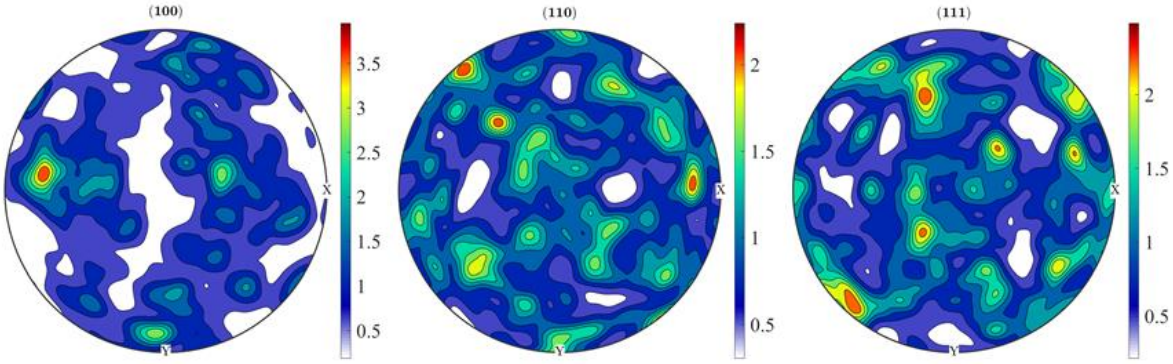

(b)

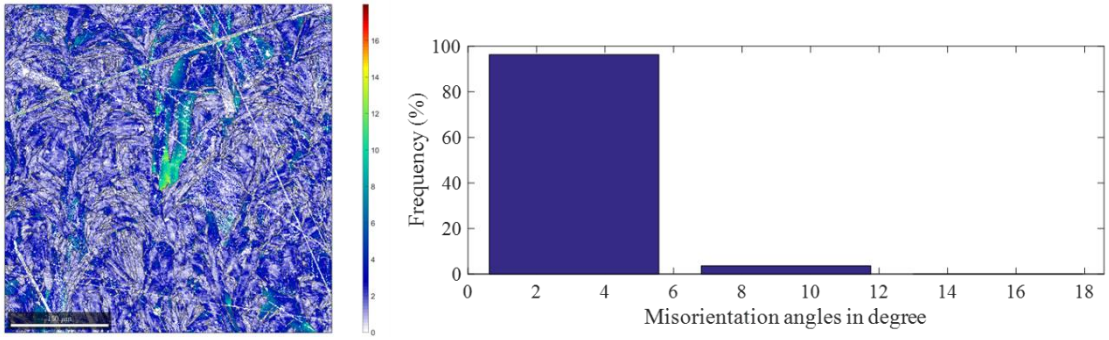

(c)

Figure 6-31: (a) IPF-Y Color map (b) Pole Figure and (c) Grain misorientation map and frequency histogram for Sample 4 built at 370 W, 1400 mm/s.

From the EBSD data, misorientation information is also obtained. Misorientation in this context is the measure of average misorientation of each crystal with respect to its neighboring crystals. This is referred to as intragranular misorientation. Figure 6-28 (c), Figure 6-29 (c), Figure 6-30 (c) and Figure 6-31 (c) show the average misorientation profiles for the four samples along with the frequency histograms. These average misorientation profiles can be used to evaluate the localized strain in the material [133]. The higher the strain, the larger is the misorientation angle. The color bar beside the misorientation map indicated the maximum misorientation angle. It is interesting to note that with an increase in the <100> fiber texture intensity, the maximum value of the misorientation angle increased.

Overall, these results not only demonstrates the link between melt pool geometry and texture in the part, but these also provide information that can be used to develop and validate the solidification and grain growth models for IN718.

Grain Size

The information related to grain size and shape is obtained from the EBSD scan data. All of the analysis is performed using the mapping submodule Tango in Aztec post processing software on an Oxford system. The data was cleaned up to remove the zero solutions where the diffraction patterns were not indexed. A critical misorientation angle of 10° is used to segregate the grains. Grain size is discussed first followed by grain shape. Grain size here refers to the equivalent circular diameter which is measured from the area of each grain.

The probability plot of grain sizes for all four samples is presented in Figure 6-32. The dashed lines in the plot represent log normal distribution for the grain size data whereas, the circle data markers represent the measured grain size data. It is interesting to note that the lower end tail is deviating from the log normal distribution and this is known as lower tail departure. This agrees

well with the observations reported by Subedi on laser melted IN718 [45]. The deviations at the upper tail are negligible. There is a large dispersion in the data which is similar to the observations reported for prior beta grain size in electron beam melted Ti64. However, the deviation from log normal distribution is more in IN718 when compared to Ti64. There are many small grains in IN718 when compared to the grain size distribution in Ti64. This difference can be due to changes in other process parameters that contribute to the grain growth such as hatch spacing and scan layer rotation for electron beam melting of Ti64. Based on the melt pool size, the sample built at 300 W and 1000 mm/s and 370 W and 1400 mm/s are expected to have a higher grain size. However, the grain size distribution plots for the samples built at 300 W and 1000 mm/s and 200 W and 1000 mm/s overlap except at the upper tail and the sample built at 100 W and 400 mm/s which has lower melt pool area has larger grains. This can be explained by the grain morphology which was discussed in the previous section. The sample built at 100 W and 400 mm/s predominantly has columnar grains which grow through multiple layers and coarsen as shown in the IPF-Y in Figure 6-28 (a). The increase in the grain size is also represented by the shift in probability distribution curve towards the larger grain size values on the x-axis. Similarly, the sample 2 has a columnar grain structure when compared to the sample 3 and 4 which is reflected in the grain size probability distributions in Figure 6-32. In case of sample 3 and sample 4, they both have the same cooling rate and have random orientation. However, there is a shift in grain size distribution for these two samples. This can be explained based on the difference in the extent of random growth. These results show that grain growth in laser melted IN718 is a complex process and grain size does not just depend on the cooling rate, but it also depends on the grain morphology. Based on the results observed in Chapter 3 where prior beta grain size increased with decrease in cooling rate, it is likely that if all the samples with predominantly columnar growth are considered, the grain size

should scale might scale with cooling rate. This needs to be verified by analyzing more samples having grains oriented along the build direction.

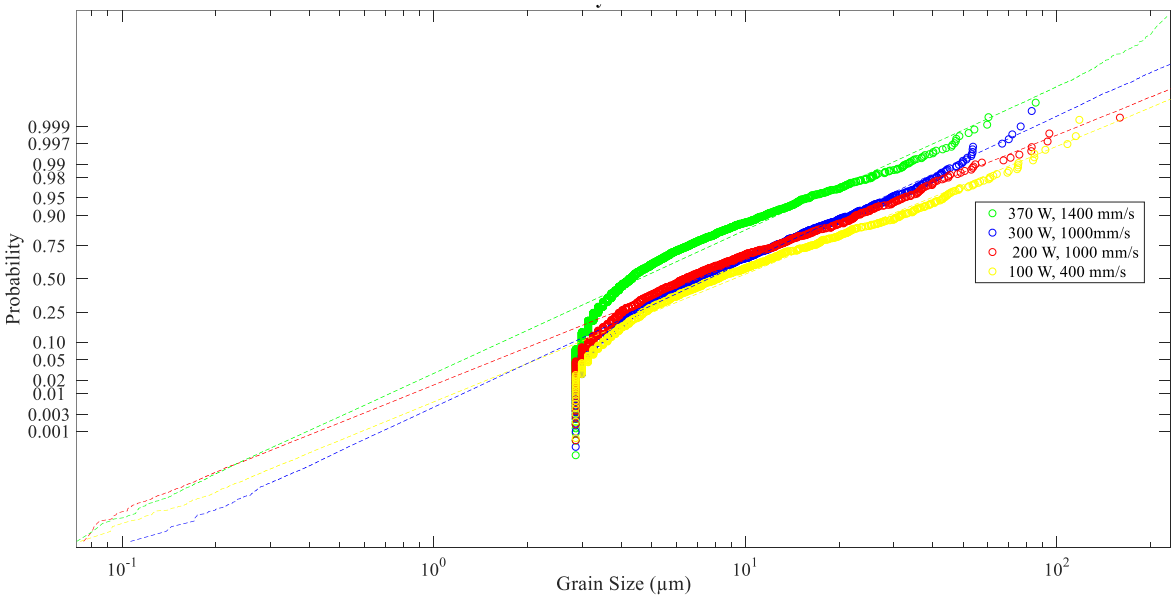

Figure 6-32: Probability plot (cumulative) of the grain sizes from EBSD scan data.

Grain Shape

Grain shape is quantified by using the aspect ratio of the grain. It is the ratio of the minor and major axes of the ellipse that is fit to the grain. Probability plots of the aspect ratio of the grains are presented in Figure 6-33 for all three samples. All four samples consist of elongated grains with aspect ratios greater than 1. However, for sample 4, which has the largest l/d ratio among the 4 samples, the probability curve shifted towards the lower grain aspect ratio. The trends observed in the grain shape cumulative probability plots agrees well with the qualitative grain shapes observed in the IPF-Y pole figures of all the four samples and the grain size distributions.

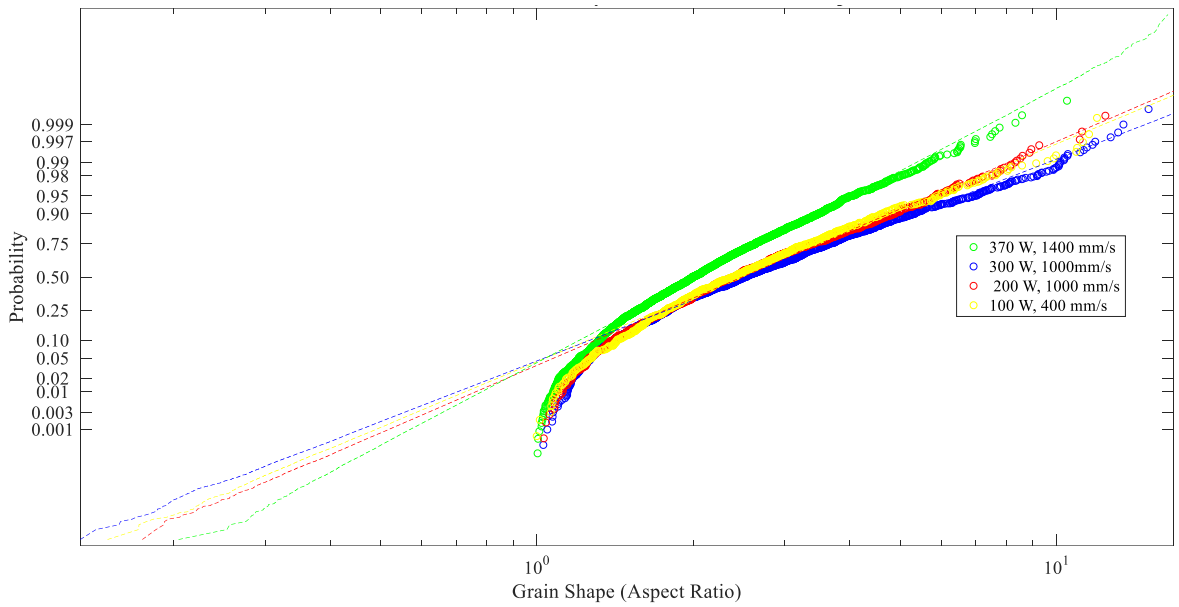

Figure 6-33: Probability plot (cumulative) of the grain aspect ratio from EBSD scan data.

Solidification Structure

Due to the very high cooling rates experienced during the rapid solidification, very fine cellular and dendritic microstructure is formed upon solidification. Figure 6-34 shows an example image for IN718 which consists of solidification structures. This is from the sample which is built at 100 W and 400 mm/s. It is hard to distinguish between cellular and dendritic structures in fine solidification patterns like these where the dendrites does not grow secondary dendrite arms. This is because cross section of dendrite growing out of the page can appear as cellular structure. However, previous work on laser melting of 316L stainless steel had discussed about distinguishing between cellular and dendritic structure from cross section of the sample normal to the beam travel direction [32]. Depending on the growth direction and heat transfer direction, an example dendritic and cellular structures are identified in the Figure 6-34. More detailed analysis is required for accurate identification of dendritic and cellular growths. The example shown in Figure 6-34 is based on the knowledge inferred from previous observations made by Roehling et al. in laser melted 316L stainless steel [32].

Cell spacing and dendrite spacing vary with solidification conditions, e.g. solidification rate and thermal gradient as per the Equations 5.4 and 5.5. They are critical for determining mechanical properties [29]. In these equations, c and k are material constants and V is the solidification rate and G is the thermal gradient.

$$Primary\ dendrite\ arm\ spacing\ (\lambda_1) = cV^{-1/4}G^{-1/2} \tag{5.4}$$

$$Cell\ spacing\ = kV^{-1/3}G^{-1/3} \tag{5.5}$$

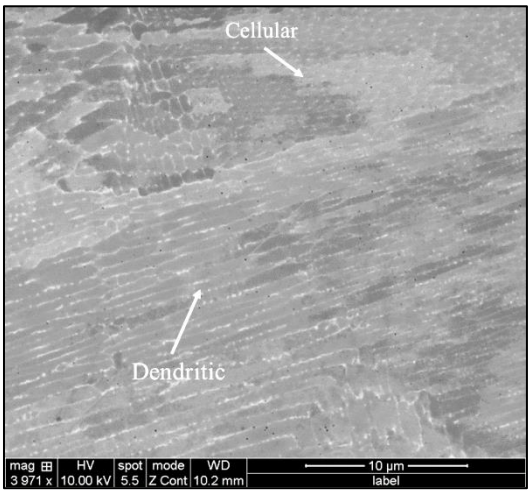

Figure 6-34: Dendritic and cellular solidification structure in IN718.

The cell spacing can be easily related to the solidification time since the power exponent for both solidification rate and thermal gradient is the same. However, in case of primary dendrite arm spacing, such an explicit relationship is not possible. In IN718, both cellular and dendritic structure is observed which made it difficult to represent the solidification structure measurement with one quantity. Previous work done by [50] discussed the variation in columnar dendrite growth with change in beam power and velocity and the subsequent effect on hardness and other properties.

6.4 Conclusions

In this chapter, knowledge obtained from studying AlSi10Mg is extended to IN718 with the main focus on melt pool geometry and microstructure mapping in the beam power and travel velocity space via experiments and finite element modeling of the laser melting process. First, melt pool geometry is mapped in the process space followed by identification of a process window with no keyholing and lack of fusion porosity. There is a very narrow region in the power-velocity space where the defects due to keyholing and lack of fusion are minimized. This is similar to the result observed in AlSi10Mg except for the fact that the process window shifted toward lower powers in IN718 when compared to AlSi10Mg. This is due to the difference in thermal diffusivity of the two materials which changes the susceptibility to keyholing and lack of fusion porosity. After that, melt pool area measurements from simulations and experiments were used to estimate the effective absorptivity of the material in the non-keyholing region of the process space.

The melt pool geometry analysis is followed by studying the solidification conditions in different regions of the power-velocity space. Temperature-related information from the simulations is used to estimate the cooling rate and thermal gradient across the considered range of power-velocity space. This information provided useful insights on the distinct relationship between melt pool size and solidification conditions. Grain size, shape and orientation are studied as part of the microstructure. Results show that by increasing the L/d (length to depth) aspect ratio of the melt pools, anisotropy can be reduced due to the presence of random crystal orientations. This agrees well with the qualitative prediction from IN718 solidification map using the solidification trends estimated from finite element simulations. Grain size analysis results show that grain morphology is also an important factor that controls the grain size along with cooling rate.

This work (i) identified the regions in available processing space that will minimize the defects due to under-melting and keyholing porosity and produce a high quality part (ii) established concepts of integrated melt pool geometry and microstructure control in laser melted IN718 with a main focus on altering the texture via change in melt pool shape. Results from this work aid in effectively opening up process space for optimizing quantities of interest such as texture, surface finish, deposition rate, part properties etc. This in turn will remove the constraint of just using the nominal parameters that are recommended by the machine manufacturer.

7 Framework to Predict Melt Pool Geometry across Alloys and Processing Conditions in Additive Manufacturing

7.1 Overview

With the growing popularity of Additive Manufacturing (AM), new materials are being developed and are pursued for use in the AM equipment. In Chapters 3, 5 & 6, it was demonstrated that for a build to be successful, it is critical to understand the effect of primary process parameters on melt pool geometry. It is also evident that the process maps for melt pool geometry follow the same trends in power-velocity space for Ti64, AlSi10Mg and IN718, irrespective of the fact that these materials have different thermophysical properties and processing conditions. These similar trends in process space served as a motivation to explore for a framework, which would assist in predicting the melt pool geometry like width, depth and area for different process conditions and alloy systems. More importantly, this can be done without performing a large number of experiments and simulations. Based off of the existing literature on welding processes, results from this work provide a preliminary framework for quantifying melt pool geometry over a range of material properties and process settings. This work will provide significant insights on guiding the experiments in order to refine the process parameters further and act as a guide for detailed modeling work.

7.2 Discussion on Methods to Predict Melt Pool Geometry

7.2.1 Analytical Solutions

Rosenthal [60] presented an analytical solution for temperature distribution in the case of a moving point heat source. However, in reality, heat source is distributed instead of a point source. In order to address the distribution effects of the heat source on the temperature field Eagar et al. [62]

developed a modified version of Rosenthal's analytical solution with an additional distribution parameter. In this work, beam spot size is not explored in detail as a process variable. Hence, Rosenthal analytical solution is discussed in detail.

Rosenthal's solution for the temperature distribution resulting from a moving point heat source on a semi-infinite solid is given by Equation 7.1. This solution is developed for the conduction based heat transfer.

$$T - T_0 = \frac{q}{2\pi k} \frac{exp^{-\lambda v(\xi + R)}}{R} \tag{7.1}$$

Where, T = temperature

T_0 = initial temperature of the solid

q = power absorbed by the solid

v = travel velocity of the heat source

k = thermal conductivity of the material

$\frac{1}{2\lambda}$ = thermal diffusivity of the material

ξ = distance of the point of interest from the point source

$R = \sqrt[2]{\xi^2 + y^2 + z^2}$

From this equation, it can be identified that the variables considered in this solutions are beam power, travel velocity, initial temperature of the solid, thermophysical properties of the materials viz. thermal conductivity, density and specific heat. Some of the major assumptions for Rosenthal equation are: (i) thermophysical properties does not change with temperature (ii) beam

power and travel speed are constant [60]. Apart from those two assumptions, it is also important to note that the latent heat effect, surface heat losses, fluid flow inside the melt pool (weld pool) and effects of powder such as size distribution and layer thickness are not included in the derivation of the analytical equation. Thus, when applying the Rosenthal equation to the additive manufacturing processes, it is important to adjust the solution based on a finite element models or experiments where some of the limitations of the analytical solution are addressed. Gockel [28] discussed about adjusting the Rosenthal equation by changing the temperature at which the thermophysical properties are considered to match the analytical solution to the finite element model while predicting melt pool geometry, cooling rates and thermal gradients. Similarly, absorptivity of the material is also a variable which can be modified to adjust the Rosenthal solution when comparing with simulations or experiments.

7.2.2 Comparison between Analytical Solutions and Finite Element Simulations

The finite element simulations considered in this work addresses some of the assumptions used in the Rosenthal analytical equation if not all of the assumptions. In this section, these two models are compared to emphasize the fact that using Rosenthal solution without any prior information can be misrepresentative. The comparison consists of two parts. Firstly, properties at the standard room temperature are used in the Rosenthal equation and the resulting melt pool depth is compared with the melt pool depth from the simulations. Properties at room temperature are considered in this analysis because they are easily available in the literature when compared to temperature dependent properties. After that, the temperature at which the properties are to be used is adjusted until the melt pool depth from Rosenthal solution matches with that predicted by the finite element simulations. In this comparison, the properties of the material which are adjusted in the analytical solution are thermal conductivity, density and specific heat. This comparison is performed at four

different regions in the process space (power-velocity) space as shown in the Figure 7-1. These four points represent the extreme values in the process window. Since, both the models include absorbed power, absorptivity is not considered as a process variable in this comparison. However, when the comparison is between model and the experiment, absorptivity is a critical variable which was discussed in detail in Chapters 5 and 6. Thus, to eliminate the need to add one more variable, comparison of Rosenthal solution is limited to finite element model. Temperature dependent properties are obtained from the data provided in the literature for IN718 material [115].

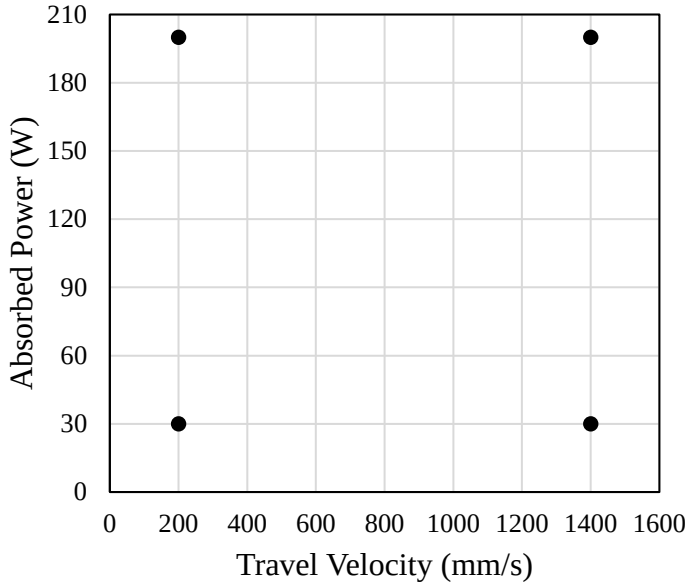

Figure 7-1: Four extreme corners in the process space to capture the behavior across the process space.

Table 7-1outlines the results from the comparison between the melt pool depths predicted by the analytical model and finite element model. Rosenthal fitted temperature is chosen such that the properties at this temperature will result in less than 5% difference when compared to the simulation depths. This difference can be reduced further by adjusting the fitting temperature thought the temperatures in the table are limited to less than 5% difference. It can be observed from the table that the difference between the melt pool depths from simulation and Rosenthal

solution is higher at room temperature properties when compared to the difference at the fitted temperature.

Table 7-1: Comparison between melt pool area estimated from simulations and Rosenthal solution.

Absorbed Power (W)	Travel Velocity (mm/s)	Simulation Depth (in)	Rosenthal Solution for Depth using Properties at Room Temperature (in)	Difference (%)	Fitting Temperature (K)	Rosenthal Solution for Depth using Properties at Fitted Temperature (in)	Difference (%)
30	200	2.7E-03	3.5E-03	31%	1000	2.7E-03	1%
30	1400	1.1E-03	1.4E-03	24%	1100	1.1E-03	2%
200	200	7.7E-03	9.3E-03	21%	1100	7.6E-03	1%
200	1400	3.0E-03	3.5E-03	17%	1000	3.0E-03	1%

It is evident that the Rosenthal prediction for depth is higher than the simulation depth in all the cases. This can be explained by the fact that with increase in temperature, thermal conductivity of IN718 increases. However, this is not accounted for by considering the room temperature conductivity in the analytical solution which led to over estimation of melt pool depth. This case study is a good example to show that, (i) room temperature properties are not suitable to estimate the melt pool dimensions using Rosenthal solution for laser melting of IN718 and (ii) fitting temperature slightly changes with the location in the process space. In summary, depending on the process variables and material properties, the fitting temperature varies. For instance, in AlSi10Mg, thermal conductivity decreases with increase in temperature [115] and this might affect the fitting temperature choice. Study by Ming et al. [65] have reported that room temperature properties resulted in best agreement between experiment and analytical solution prediction for melt pool geometry in AlSi10Mg. This means, in order to use the Rosenthal solution, the material properties have to be adjusted every time when the process variables or the material properties

change. In order to do this, simulations have to be performed at different process variable combinations for every material of interest which can be tedious and time consuming. Thus, it is important to have a framework that utilizes information from the existing simulations and experiments in order to predict the melt pool characteristics for a new alloy system or for a new process variable combination.

7.2.3 Regression Models

Data [68–72] from experiments for different set of materials and processing conditions is used to develop the framework. These are referred to as *training set*. After that, melt pool geometry data available from the previous chapter on IN718 was used to test the prediction capability of the framework. These are referred to as *testing set*. These details are provided in Table 7-2. In this data, the keyholing points are removed since keyholing mode is different from conduction mode melting [104,107]. Though, the approach discussed in this work is for experiments, it can easily be extended to simulations.

Table 7-2: Details of the data used for training and testing.

	Samples from material	**Sample size**
Training Set	IN625, Ti64, SS 316, SS 17-4, and AlSi10Mg	111
Testing Set	IN718	27

Regression is a commonly used supervised learning technique for predicting continuous output values for a given set of inputs. This is done by training the algorithm over available instances of input features and testing it on unseen instances. When linear regression is applied on the training data with 4 input parameters: Power (P), Velocity (V), $k/\rho c$, $T_m - T_0$, it yielded low R^2 values as shown in Figure 7-2 for melt pool area, width and depth. This is possible because linear regression did not adequately capture underlying non-linear structure in the data. Thereafter, regression using

neural networks was applied. Plots in Figure 7-3 show that the prediction performance improved when compared to simple linear regression approach for melt pool width. In case of melt pool area and melt pool depth, linear regression performed well when compared to neural network regression, because, linear regression approach is less sensitive to noise (i.e. variability caused by border line keyholing cases) as compared to neural network approach [138]. Generally speaking, keyholing effect is more significant on melt pool depth and area when compared with melt pool width [102]. However, there is potential for further improvement if better input features are designed for training. This can be possible by decomposing the current feature set from 4 variables to 1 variable using non-dimensionalization and attempting to map output values to the transformed input feature. This approach is discussed in the following sections.

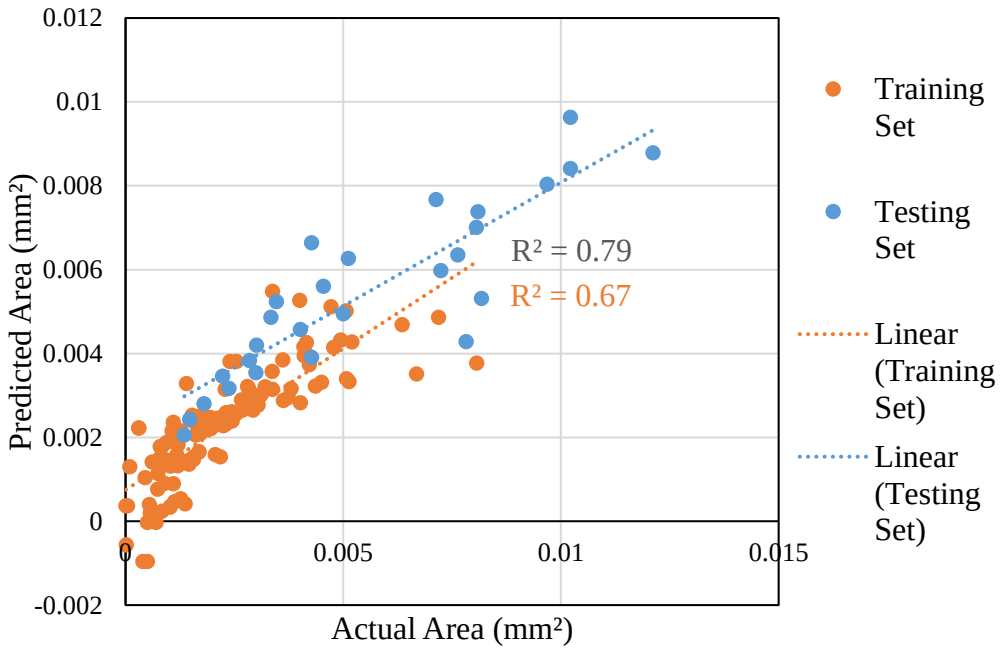

(a)

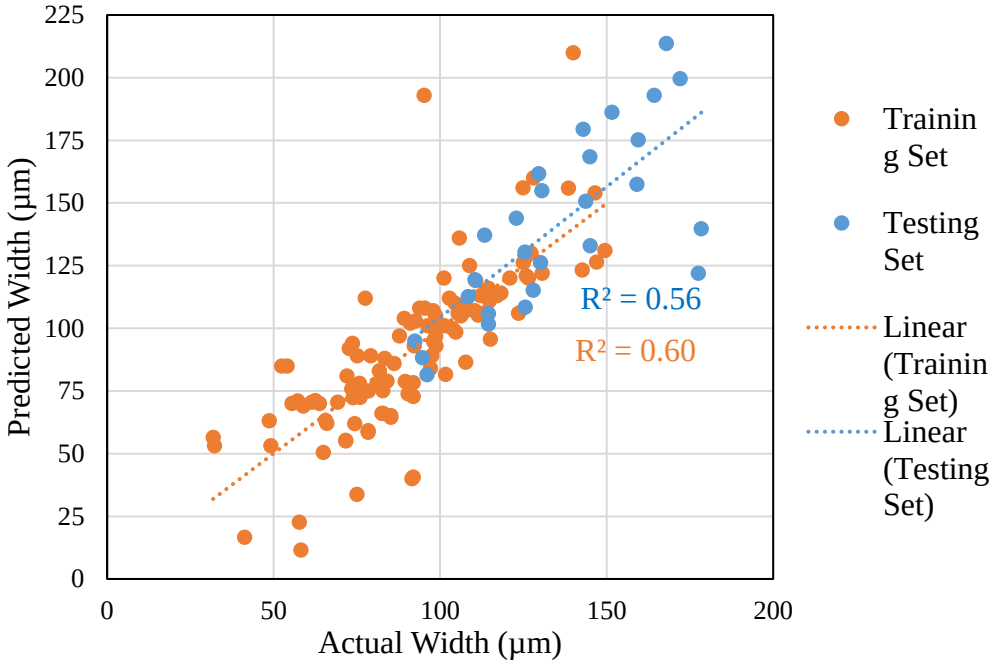

(b)

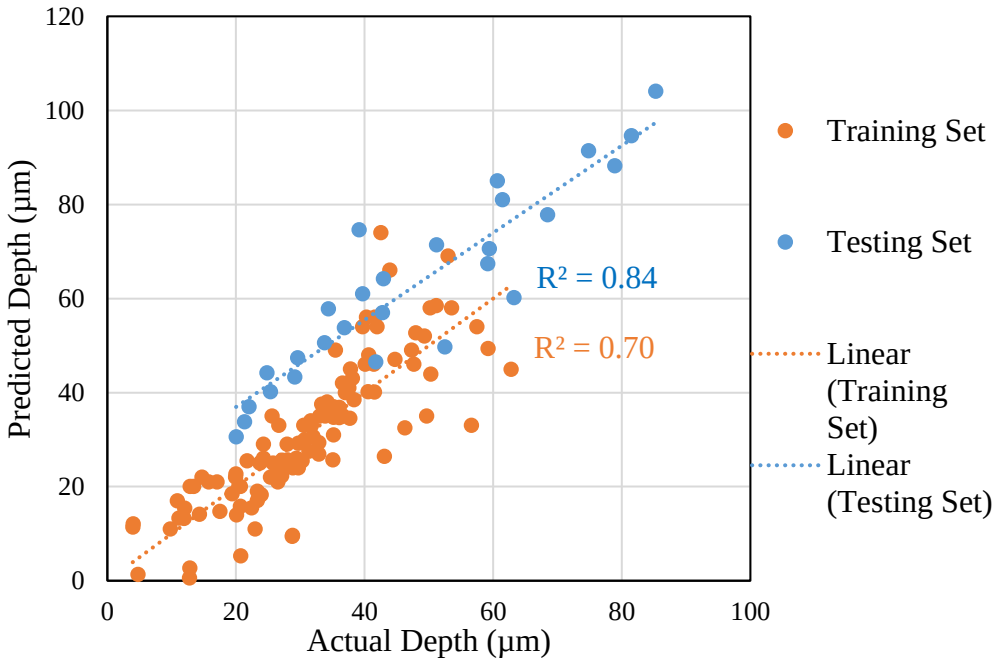

(c)

Figure 7-2: Comparison of predicted vs. actual melt pool dimensions: (a) area, (b) width and (c) depth using linear regression.

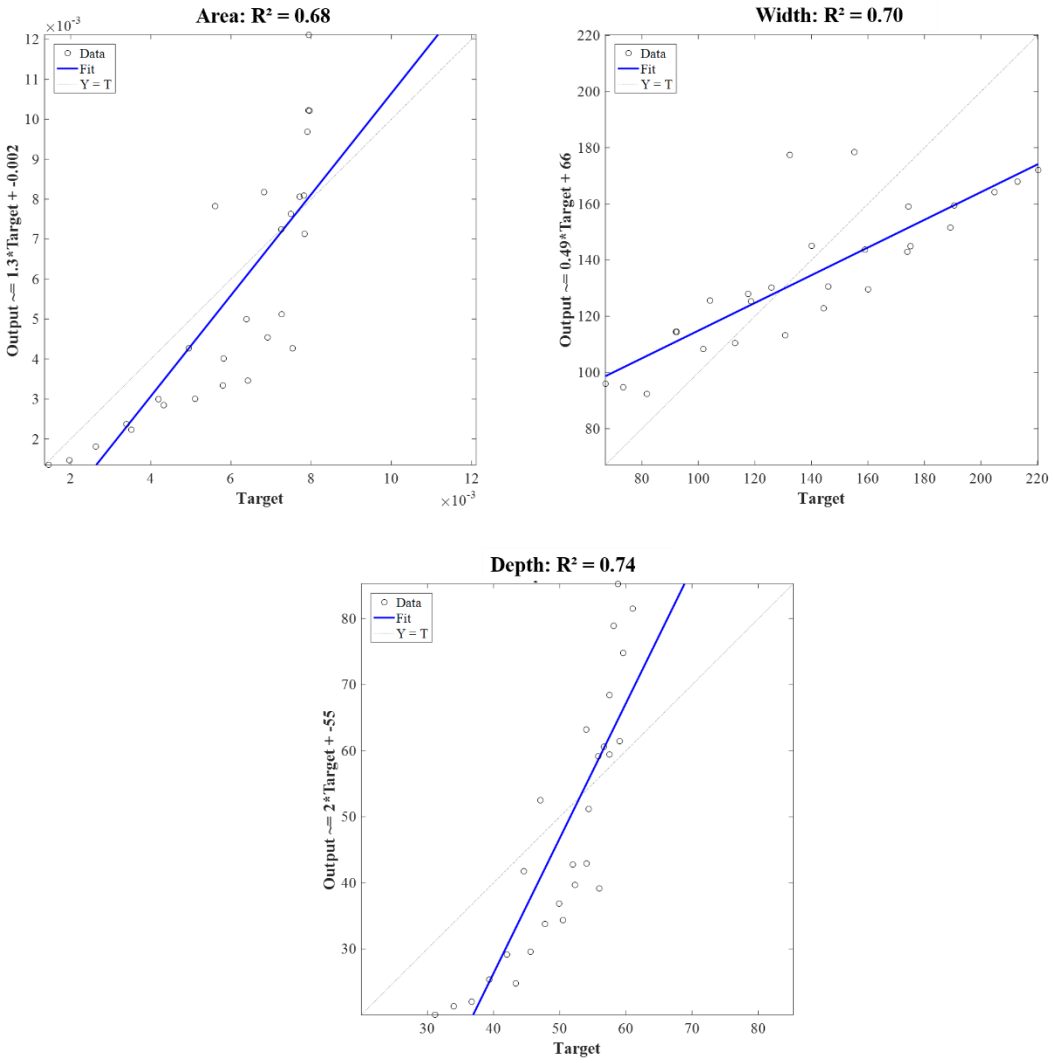

Figure 7-3: Comparison of predicted vs. actual melt pool dimensions using neural network regression.

7.3 Non-Dimensionalization of Process Variables and Melt Pool Geometry

Based off of Rosenthal's analytical solution, Christensen et al. [61] developed dimensionless graphs for predicting melt pool characteristics over a range of welding conditions and material properties. Non-dimensionalized variables developed by Christensen et al. [61] are given by Equations 7.2 – 7.5. In these equations, average of the values between initial part temperature and melting temperature are used for thermo-physical properties. In the current work, this non-

dimensional framework developed for welding processes is applied to laser powder bed processes to predict melt pool geometry for a wide range of materials and process conditions.

$$\eta = \frac{qv}{4\pi\alpha k(T_m - T_0)} \tag{7.2}$$

$$a = \frac{Av^2}{4\alpha^2} \tag{7.3}$$

$$w = \frac{Wv}{2\alpha} \tag{7.4}$$

$$d = \frac{Dv}{2\alpha} \tag{7.5}$$

Where, η = non-dimensionalized operating parameter

q = beam power

v = beam velocity

α = thermal diffusivity

k = thermal conductivity

T_m= melting temperature

T_0 = initial temperature of the solid

A = melt pool area, a = non-dimensionalized melt pool area

W = melt pool width, w = non-dimensionalized melt pool width

D = melt pool depth, d = non-dimensionalized melt pool depth

7.4 Non-linear Regression on Non-Dimensionalized Variables

7.4.1 Neural Network Regression

When using input features generated by non-dimensionalization, overall prediction performance using neural networks improved as shown in Figure 7-4 when compared to Figure 7-3. However, multivariate linear regression still performed better in the case of depth owing to the variability caused by border line keyholing cases. This can be explained based on the result that keyholing affect is more significant on melt pool depth and area when compared with melt pool width [102]. Nevertheless, this example illustrates the significance of using non-dimensionalization to improve the performance of data-driven prediction framework.

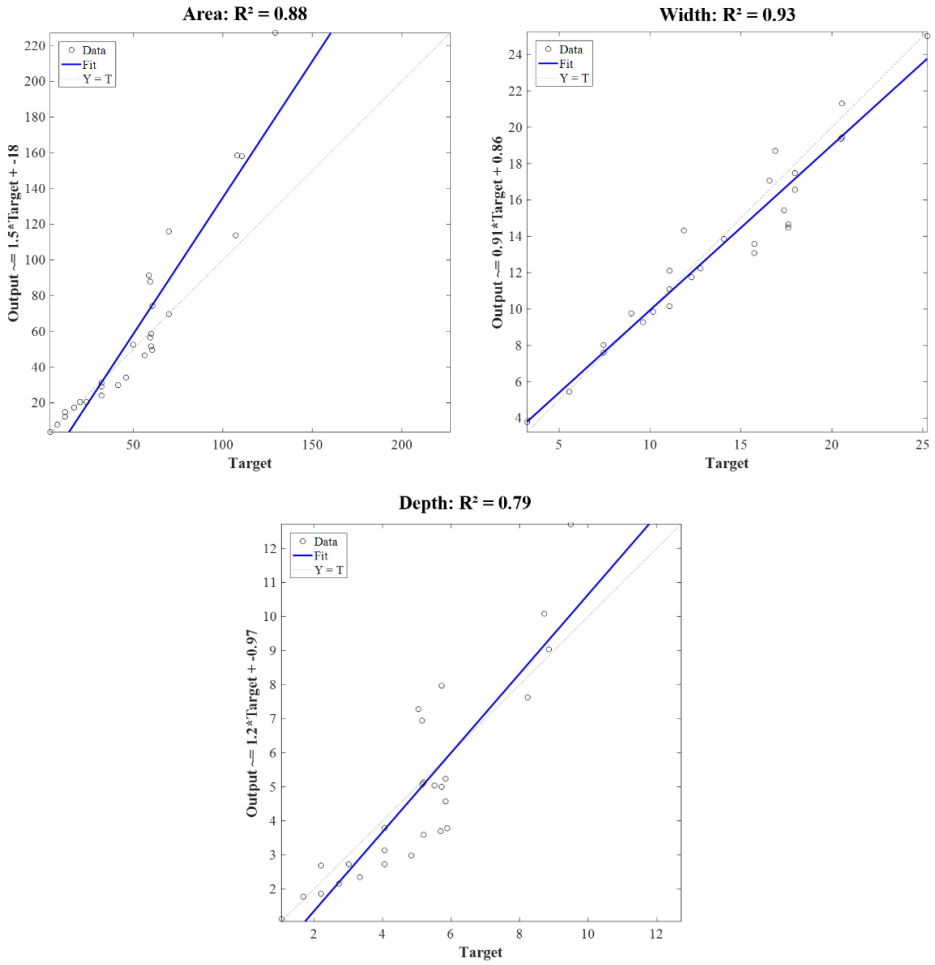

Figure 7-4: Comparison of predicted and actual melt pool dimensions of testing data using neural network regression.

7.4.2 Power Regression

Plots in Figure 7-5 indicate that the performance of power regression for non-dimensionalized input data appears to be better than the neural network regression for the prediction of melt pool geometry for *testing set*. It is also important to note that the process parameter range in the current testing data for IN718 has a narrow band (i.e. beam power: 100 to 370 W and beam travel velocity: 200 mm/s to 1400 mm/s). However, for wider parameter range, especially at high velocities, deviation can be observed from the normalization curve as marked in Figure 7-6. This is also reported in the previous work by Elmer et al. [129]. In such situations, neural network regression or piece wise power regression can potentially capture better the underlying structure of the data, in comparison to a simple universal power fit.

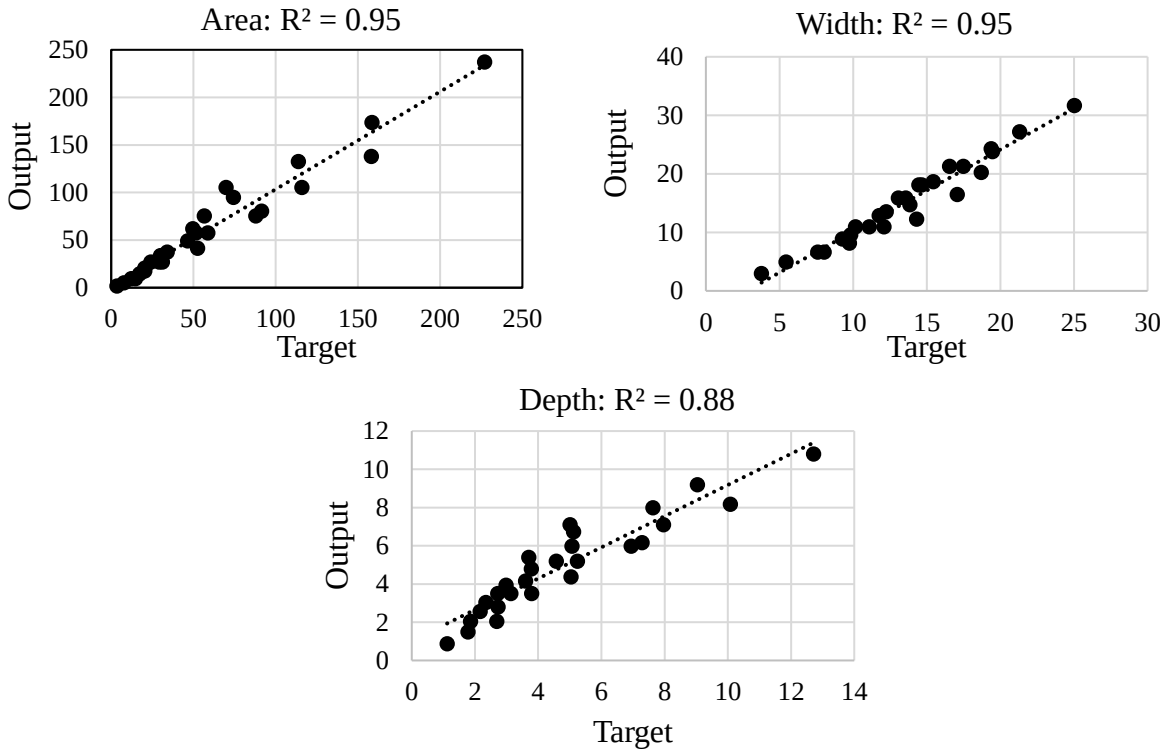

Figure 7-5: Comparison of predicted and actual melt pool dimensions of testing data using power regression.

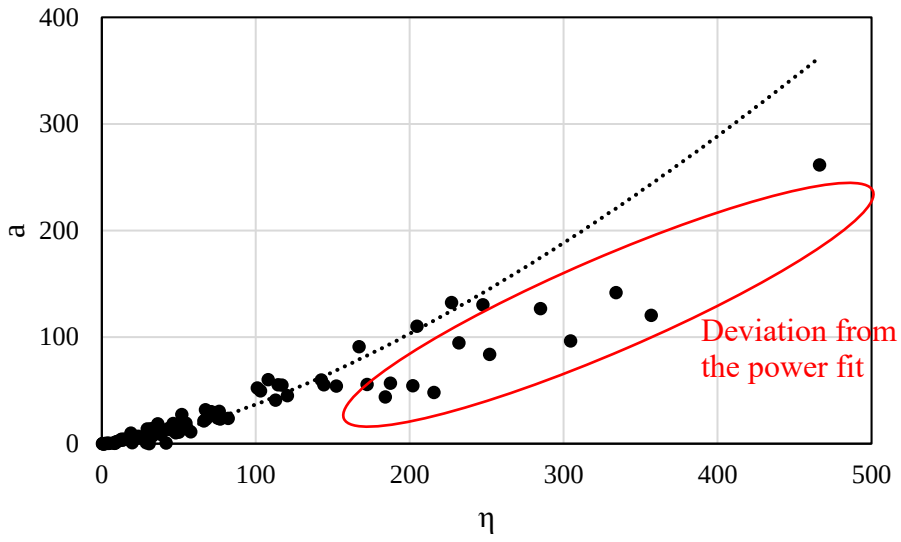

Figure 7-6: Deviation of actual data from the power regression universal fit at higher beam travel velocities.

7.5 Conclusions

Melt pool geometry prediction is critical for controlling part quality in additively manufactured parts. Current methods for estimating the melt pool geometry are based on modifying the analytical solutions or performing time consuming finite element simulations and experiments. In addition, with increasing interest in AM, there is need for optimizing the process for various process outputs such as deposition rate, strength, surface finish and similar other objectives. This requires knowledge of the effect of primary process variables and material properties on the melt pool geometry in order to build a good quality part that does not contain any process induced porosity and has consistent melt pool dimensions. However, there are many combinations of process variables that can possibly be used and performing experiments and simulations at all the possible process variable combinations is not a reasonable solution. Non-dimensionalization methods presented in this work address the above mentioned limitations and assist the user in predicting the melt pool geometry from both simulation results and experiments for different materials and

process variable combinations. These approaches can potentially be used for optimization, sensitivity and uncertainty analysis and prediction algorithms.

Non-dimensionalization is performed on melt pool geometry results from experiment data in laser melting process. Results showed that for the available data size that is relatively small, the prediction performance improved when non-dimensionalized input features are used. Also, the range in which simple power fit regression works is identified. With these contributions, a graphical user interface to the prediction framework, can allow any AM user to estimate the melt pool dimensions for any material or process variable combination. Further, with this interface, the user can also estimate the process maps in power-velocity space for characterizing a process, as discussed in the previous chapters. This predicted result can be refined further via focused experimentation and modeling work.

8 Conclusions and Future Work

8.1 Conclusions

Previous work [28] demonstrated melt pool geometry control and how it can be used for controlling the microstructure of additively manufactured Ti-6Al-4V (a titanium alloy). However, there remained a lack of understanding of (i) its applicability for solid components, (ii) its applicability for new materials, and (iii) how melt pool geometry can be generalized to new materials and process conditions with minimal experimentation.

As mentioned earlier, the experiments and simulations from previous work primarily focused on a single material (Ti-6Al-4V a titanium alloy) and single melt tracks. However, there was no comprehensive understanding on how these results would transfer to solid parts and ultimately for location-specific control of prior beta grain size in a component. In Chapter 3, results are presented that demonstrate that prior beta grain width scales with effective melt pool width in solid builds. This greatly simplifies the strategy for controlling beta grain widths to one of controlling melt pool size. These results are further used to successfully vary the microstructure methodically in different locations of a single part. While Chapter 3 confirmed the applicability of melt pool size control in controlling the prior beta grain width, Chapter 4 tackled the challenges pertaining to prior beta grain width response when varying the microstructure along the build direction. These results enable the user to execute location-specific control of prior beta grain size in a component and this was demonstrated for an example component: the dove tail region of a compressor blade.

In terms of using geometry control to indirectly implement microstructure control in other materials, the current work addressed the existing gaps by applying it to two additional materials

(aluminum alloy - AlSi10Mg and nickel super alloy - IN718) in a laser melting process. Specifically, AlSi10Mg was used to demonstrate solidification structure control through melt pool size control. It was found that cell spacing varies with melt pool width; these results are further used to successfully vary the cell spacing methodically in different locations of a single part. Similarly, IN718 was used to demonstrate texture control through melt pool size control. The presented results showed that grain orientation varied with melt pool aspect ratio (length/depth). Overall, three levels of microstructure control were achieved, starting with the prior beta grain size control in Ti64, followed by cell (solidification structure) spacing control in AlSi10Mg, and ending with texture control in IN718.

While results from integrated melt pool geometry and microstructure control for a component and different materials show promise, whenever there are new process conditions or new materials, in order to map melt pool geometry, either a new set of experiments or simulations are required. To address this, lessons from welding literature have been utilized and applied to additive manufacturing. This resulted in a prediction framework that can be used to enable a preliminary understanding of melt pool geometry for different materials and process conditions with minimal experimentation.

The knowledge developed as part of this work will aid in (i) choosing melting parameters for location-specific control of microstructure to tailor the properties of a part (ii) predicting melt pool geometry with minimal experimentation (iii) predicting the microstructure resulting from process parameters with minimum experimentation. The work presented in this thesis has the potential to reduce the process development and part qualification time, enabling the wider adoption and use of additive manufacturing in industry.

8.2 Future Work

The process mapping approach is presented to both control, and predict, the melt pool geometry and solidification microstructure for three different materials in two different AM processes. More importantly, this can be done with minimal experimentation and modeling work. Therefore, this work is a significant step toward accelerating the process development and qualification timeline. Some of the potential extensions are discussed below:

1. ***Effect of other process parameters:*** Primary melting parameters such as beam power and velocity were explored in this work for microstructure control in three different alloy systems. However, there are other important process parameters such as hatch spacing, beam profile, background/part temperature, and scanning strategy, which also affect the microstructure. The knowledge related to interactions between the primary melting parameters and the other process parameters will provide insights for maintaining consistent microstructure even if the other process parameters need to be changed.
2. ***Design for tailored properties:*** In this work, it was demonstrated that as-built microstructure ranging from solidifications structure, to grain size, to grain morphology can be controlled. However, the application of this is not demonstrated to its full extent as part of this work. It is critical to find an application where there is an opportunity for design/performance optimization and modify the design such that it utilizes the capability of altering the microstructure as needed.
3. ***Effect of post-processing heat treatment:*** All the work presented in this thesis is on as-built microstructure. In the laser melting process, parts are typically stress relieved after the build is completed. Post-stress relief properties should be studied and linked to the as-built microstructure. Additionally, heat treatment for homogenization is prevalent in the

AM industry. The effect of as-built microstructure on post-heat treatment procedures and resulting part properties should be explored systematically.

4. ***Mechanical testing***: Hardness values from the literature are presented in this work as a preliminary metric to understand the effect of changing microstructure on the mechanical properties. However, it is suggested that extensive mechanical testing should be performed to quantify the effect of as-built microstructure on mechanical properties such as tensile strength, fracture toughness, impact resistance, etc.
5. ***Prediction framework for melt pool characteristics:*** The prediction framework presented in this work is applicable to predicting melt pool geometry in laser melting processes. Building on top of that, a similar relationship can be developed for other AM processes such as electron beam melting. Additionally, there is potential to tune current regression tools to further improve the performance of the framework. Such improvements would allow it to be embedded into a process development/optimization software tool.

9 References

[1] "GE in 3D printing push raises Arcam bid, to buy Concept Laser | Reuters" [Online]. Available: http://www.reuters.com/article/us-ge-3dprinting-sweden-idUSKCN12R0LC. [Accessed: 03-Mar-2017].

[2] "What is 3D Printing? The definitive guide | 3D Hubs" [Online]. Available: https://www.3dhubs.com/what-is-3d-printing. [Accessed: 03-Mar-2017].

[3] XJet, "X-Jet technology" [Online]. Available: http://www.xjet3d.com/technology.html. [Accessed: 03-Mar-2017].

[4] Sachs, E., Cima, M., Williams, P., Brancazio, D., and Cornie, J., 1992, "Three Dimensional Printing: Rapid Tooling and Prototypes Directly from a CAD Model," J. Eng. Ind., **114**, pp. 481–488.

[5] 2016, "What is Binder Jetting? | ExOne."

[6] Griffith, M., and Keicher, D., 1996, "Free form fabrication of metallic components using laser engineered net shaping (LENS)," Solid Freeform Fabrication Proceedings, Austin, pp. 125–132.

[7] Taminger, K., and Hafley, R., 2003, "Electron beam freeform fabrication: a rapid metal deposition process," Proceedings of the 3rd Annual Automotive Composites Conference, Troy, pp. 9–10.

[8] "Electron Beam Melting - EBM Process, Additive Manufacturing | Arcam AB" [Online]. Available: http://www.arcam.com/technology/electron-beam-melting/. [Accessed: 03-Mar-2017].

[9] Mahale, T. R., 2009, "Electron Beam Melting of Advanced Materials and Structures, mass customization, mass personalization," PhD Thesis, North Carolina State University.

[10] Heinl, P., Müller, L., Körner, C., Singer, R. F., and Müller, F. A., 2008, "Cellular Ti-6Al-4V structures with interconnected macro porosity for bone implants fabricated by selective electron beam melting," Acta Biomater., **4**(5), pp. 1536–1544.

[11] Al-Bermani, S. S., Blackmore, M. L., Zhang, W., and Todd, I., 2010, "The origin of microstructural diversity, texture, and mechanical properties in electron beam melted Ti-6Al-4V," Metall. Mater. Trans. A Phys. Metall. Mater. Sci., **41**(13), pp. 3422–3434.

[12] Swift-hook, D. T., and Gick, A. E. F., 1973, "Penetration Welding with Lasers," Weld. Res. Suppl., pp. 492–499.

[13] Juechter, V., Scharowsky, T., Singer, R. F., and Körner, C., 2014, "Processing window and evaporation phenomena for Ti-6Al-4V produced by selective electron beam melting," Acta Mater., **76**, pp. 252–258.

[14] "EBM-Built Materials - Arcam AB" [Online]. Available: http://www.arcam.com/technology/electron-beam-melting/materials/. [Accessed: 03-Mar-2016].

[15] Villalon, A., 2005, “Electron beam fabrication of injection mold tooling with conformal cooling channels,” Masters Thesis, North Carolina State University.

[16] “EOS Metal Materials for Additive Manufacturing” [Online]. Available: http://www.eos.info/material-m. [Accessed: 03-Mar-2016].

[17] Boley, C. D., Khairallah, S. A., and Rubenchik, A. M., 2015, “Calculation of laser absorption by metal powders in additive manufacturing.,” Appl. Opt., **54**(9), pp. 2477–82.

[18] Rafi, H. K., Karthik, N. V., Gong, H., Starr, T. L., and Stucker, B. E., 2013, “Microstructures and mechanical properties of Ti6Al4V parts fabricated by selective laser melting and electron beam melting,” J. Mater. Eng. Perform., **22**(12), pp. 3872–3883.

[19] Gu, D. D., Meiners, W., Wissenbach, K., and Poprawe, R., 2012, “Laser additive manufacturing of metallic components: materials, processes and mechanisms,” Int. Mater. Rev., **57**(3), pp. 133–164.

[20] Mudge, R., and Wald, N., 2007, “Laser engineered net shaping advances additive manufacturing and repair,” Weld. J., pp. 44–48.

[21] Dey, N., 2014, “Additive manufacturing laser deposition of Ti-6Al-4V for aerospace repair application,” Masters Thesis, Missouri University of Science and Technology.

[22] Kobryn, P., Ontko, N., Perkins, L., and Tiley, J., 2006, “Additive manufacturing of aerospace alloys for aircraft structures.”

[23] Bandyopadhyay, A., Espana, F., Balla, V., Bose, S., Ohgami, Y., and Davies, N., 2010, “Influence of porosity on mechanical properties and in vivo response of Ti6Al4V implants,” Acta Biomater., **6**(4), pp. 1640–1648.

[24] GE aviation, 2013, “GE jet engine bracket challenge - GrabCAD” [Online]. Available: https://grabcad.com/challenges/ge-jet-engine-bracket-challenge. [Accessed: 03-Mar-2017].

[25] Laureijs, R. E., Roca, J. B., Narra, S. P., Montgomery, C., Beuth, J. L., and Fuchs, E. R. H., 2017, “Metal Additive Manufacturing: Cost Competitive Beyond Low Volumes,” J. Manuf. Sci. Eng., **139**(8).

[26] Ashby, M. F., Evans, A. G., Fleck, N. A., Gibson, L. J., Hutchinson, J. W., and Wadley, H. N. G., 2000, Metal Foams: A Design Guide.

[27] Harrysson, O. L. A., Cansizoglu, O., Marcellin-Little, D. J., Cormier, D. R., and West, H. A., 2008, “Direct metal fabrication of titanium implants with tailored materials and mechanical properties using electron beam melting technology,” Mater. Sci. Eng. C, **28**(3), pp. 366–373.

[28] Gockel, J., 2014, “Integrated Control of Solidification Microstructure and Melt Pool Dimensions In Additive Manufacturing Of Ti - 6Al - 4V,” PhD Thesis, Carnegie Mellon University.

[29] Dantzig, J.A; Rappaz, M., 2009, Solidification, EPFL Press.

[30] Antonysamy, A., 2012, “Microstructure, texture and mechanical property evolution during additive manufacturing of Ti6Al4V alloy for aerospace applications,” PhD Thesis,

University of Manchester.

[31] Campbell, J., 2003, Castings, Elsevier.

[32] Roehling, T. T., Wu, S. S. Q., Khairallah, S. A., Roehling, J. D., Stefan Soezeri, S., Crumb, M. F., and Matthews, M. J., 2017, "Modulating laser intensity profile ellipticity for microstructural control during metal additive manufacturing," Acta Mater., **128**, pp. 197–206.

[33] Hunt, J. D., 1984, "Steady state columnar and equiaxed growth of dendrites and eutectic," Mater. Sci. Eng., **65**(1), pp. 75–83.

[34] Han, Q., and Viswanathan, S., 2008, "Microstructure Prediction in A356 Alloy Castings," Oak Ridge Natl. Lab.

[35] Donachie, M. J., 1988, Titanium : a technical guide, ASM International.

[36] Narra, S. P., Cunningham, R., Christiansen, D., Beuth, J., and Rollett, A. D., 2015, "Toward Enabling Spatial Control of Ti-6Al-4V Solidification Microstructure in the Electron Beam Melting Process," Solid Freeform Fabrication Symposium, Austin, pp. 626–635.

[37] EOS, "Material Data Sheet" [Online]. Available: http://www.agile-manufacturing.com/files/materials/aluminum.pdf. [Accessed: 04-Apr-2016].

[38] Fulcher, B., Leigh, D., and Watt, T., 2014, "Comparison of AlSi10Mg and Al 6061 processed through DMLS," Proceedings of Solid Freeform Fabrication Symposium, Austin, pp. 404–419.

[39] Aboulkhair, N. T., Maskery, I., Tuck, C., Ashcroft, I., and Everitt, N. M., 2016, "The microstructure and mechanical properties of selectively laser melted AlSi10Mg: The effect of a conventional T6-like heat treatment," Mater. Sci. Eng. A, **667**, pp. 139–146.

[40] Kempen, K., Thijs, L., Van Humbeeck, J., Kruth, J. J.-P., Humbeeck, J. Van, and Kruth, J. J.-P., 2012, "Mechanical properties of AlSi10Mg produced by selective laser melting," Phys. Procedia, **39**, pp. 439–446.

[41] Tang, M., Pistorius, P. C., Narra, S., and Beuth, J. L., 2016, "Rapid Solidification: Selective Laser Melting of AlSi10Mg," JOM, **68**(3), pp. 960–966.

[42] Trevisan, F., Calignano, F., Lorusso, M., Pakkanen, J., Aversa, A., Ambrosio, E., Lombardi, M., Fino, P., and Manfredi, D., 2017, "On the Selective Laser Melting (SLM) of the AlSi10Mg Alloy: Process, Microstructure, and Mechanical Properties," Materials (Basel)., **10**(1), p. 76.

[43] Łągiewka, M., Konopka, Z., Zyska, A., and Nadolski, M., 2010, "The influence of modification on the flow and the solidification of AlSi10Mg alloy," Arch. Foundry Eng.

[44] Bhadeshia, H. K. D. H., 2003, "Nickel Based Superalloys" [Online]. Available: http://www.phase-trans.msm.cam.ac.uk/2003/Superalloys/superalloys.html. [Accessed: 22-Apr-2017].

[45] Subedi, S., 2017, "Evaluation of microstructural and mechanical properties of multilayered materials," PhD Thesis, Carnegie Mellon University.

[46] Azadian, S., Wei, L. Y., and Warren, R., 2004, “Delta phase precipitation in inconel 718,” Mater. Charact., **53**(1), pp. 7–16.

[47] Schirra, J. J., Caless, R. H., and Hatala, R. W., 1991, “The effect of laves phases on the mechanical properties of wrought and cast+HIP Inconel 718,” Superalloys 718,625 Var. Deriv., pp. 375–388.

[48] Sundararaman, M., Mukhopadhyay, P., and Banerjee, S., 1997, “Carbide precipitation in nickel base superalloys 718 and 625 and their effect on mechanical properties,” TMS Superalloys 718, pp. 625–706.

[49] Zhang, D., Niu, W., Cao, X., and Liu, Z., 2015, “Effect of standard heat treatment on the microstructure and mechanical properties of selective laser melting manufactured Inconel,” Mater. Sci. Eng. A, **644**, pp. 32–40.

[50] Jia, Q., and Gu, D., 2014, “Selective laser melting additive manufacturing of Inconel 718 superalloy parts: Densification, microstructure and properties,” J. Alloys Compd., **585**, pp. 713–721.

[51] Pédron, J. P., and Pineau, A., 1982, “The effect of microstructure and environment on the crack growth behaviour of Inconel 718 alloy at 650 °C under fatigue, creep and combined loading,” Mater. Sci. Eng., **56**(2), pp. 143–156.

[52] Chaturvedi, M., and Han, Y., 1989, “Creep deformation of Alloy 718,” Superalloys 718, pp. 489–498.

[53] Mannan, S. K., Hibner, E. L., and Puckett, B. C., 2003, “Physical Metallurgy of Alloys 718, 725, 725HS, and 925 for Service in Aggressive Corrosion Environments,” Corrosion, p. 3125.

[54] Amato, K. N. N., Gaytan, S. M. M., Murr, L. E. E., Martinez, E., Shindo, P. W. W., Hernandez, J., Collins, S., and Medina, F., 2012, “Microstructures and mechanical behavior of Inconel 718 fabricated by selective laser melting,” Acta Mater., **60**(5), pp. 2229–2239.

[55] Trosch, T., Strößner, J., Völkl, R., and Glatzel, U., 2016, “Microstructure and mechanical properties of selective laser melted Inconel 718 compared to forging and casting,” Mater. Lett., **164**, pp. 428–431.

[56] Wang, Z., Guan, K., Gao, M., Li, X., Chen, X., and Zeng, X., 2012, “The microstructure and mechanical properties of deposited-IN718 by selective laser melting,” J. Alloys Compd., **513**, pp. 518–523.

[57] Körner, C., 2016, “Additive manufacturing of metallic components by selective electron beam melting — a review,” Int. Mater. Rev., **61**(5), pp. 361–377.

[58] Chlebus, E., Gruber, K., Ku??nicka, B., Kurzac, J., and Kurzynowski, T., 2015, “Effect of heat treatment on the microstructure and mechanical properties of Inconel 718 processed by selective laser melting,” Mater. Sci. Eng. A, **639**, pp. 647–655.

[59] Parimi, L. L., Ravi, G., Clark, D., and Attallah, M. M., 2014, “Microstructural and texture development in direct laser fabricated IN718,” Mater. Charact., **89**, pp. 102–111.

[60] Rosenthal, D., 1946, “The theory of moving source of heat and its application to metal treatment,” Trans. ASME, **43**(11), pp. 849–866.

[61] Christensen, N., Davies, V., and Gjermundsen, K., 1965, “Distribution of Temperatures in Arc Welding,” Br. Weld. J., **12**(2), pp. 54–75.

[62] Eagar, T., and Tsai, N., 1983, “Temperature fields produced by traveling distributed heat sources,” Weld. J.

[63] Sheridan, L. C., 2016, “an Adapted Approach To Process Mapping Across Alloy Systems and Additive Manufacturing Processes,” Masters Thesis, Wright State University.

[64] Kamath, C., 2015, “On the Use of Data Mining Techniques to Build High-Density, Additively-Manufactured Parts,” Inf. Sci. Mater. Discov. Des., **225**, pp. 141–155.

[65] Tang, M., Pistorius, P. C., and Beuth, J., 2017, “Prediction of lack-of-fusion porosity for powder bed fusion,” Addit. Manuf., **14**, pp. 39–48.

[66] Roberts, I. A., Wang, C. ., Esterlein, R., Stanford, M., and Mynors, D. J., 2009, “A three-dimensional finite element analysis of the temperature field during laser melting of metal powders in additive layer manufacturing,” Int. J. Mach. Tools Manuf., **49**(12–13), pp. 916–923.

[67] Zäh, M. F., and Lutzmann, S., 2009, “Modelling and simulation of electron beam melting,” Prod. Eng., **4**(1), pp. 15–23.

[68] Jamshidinia, M., Kong, F., and Kovacevic, R., 2013, “Numerical Modeling of Heat Distribution in the Electron Beam Melting ® of Ti-6Al-4V,” J. Manuf. Sci. Eng., **135**(6), pp. 61010-61010–14.

[69] Michaleris, P., 2014, “Modeling metal deposition in heat transfer analyses of additive manufacturing processes,” Finite Elem. Anal. Des., **86**, pp. 51–60.

[70] Fox, J., 2015, “Transient Melt Pool Response in Additive Manufacturing of Ti-6Al-4V,” PhD Thesis, Carnegie Mellon University.

[71] Soylemez, E., Beuth, J., and Taminger, K., 2010, “Controlling melt pool dimensions over a wide range of material deposition rates in electron beam additive manufacturing,” Proceedings of 21st Solid Freeform Fabrication Symposium, pp. 571–582.

[72] Romano, J., Ladani, L., Razmi, J., and Sadowski, M., 2015, “Temperature distribution and melt geometry in laser and electron-beam melting processes – A comparison among common materials,” Addit. Manuf., **8**, pp. 1–11.

[73] Khairallah, S. A., Anderson, A. T., Rubenchik, A., and King, W. E., 2016, “Laser powder-bed fusion additive manufacturing: Physics of complex melt flow and formation mechanisms of pores, spatter, and denudation zones,” Acta Mater., **108**, pp. 36–45.

[74] Attar, E., 2011, “Simulation of Selective Electron Beam Melting Processes,” PhD Thesis, Universit¨at Erlangen-N¨urnberg.

[75] Körner, C., Attar, E., and Heinl, P., 2011, “Mesoscopic simulation of selective beam melting processes,” J. Mater. Process. Technol., **211**(6), pp. 978–987.

[76] Song, B., Zhao, X., Li, S., Han, C., Wei, Q., Wen, S., Liu, J., and Shi, Y., 2015, "Differences in microstructure and properties between selective laser melting and traditional manufacturing for fabrication of metal parts: A review," Front. Mech. Eng., **10**(2), pp. 111–125.

[77] Wang, F., Williams, S., Colegrove, P., and Antonysamy, A. A., 2013, "Microstructure and mechanical properties of wire and arc additive manufactured Ti-6Al-4V," Metall. Mater. Trans. A Phys. Metall. Mater. Sci., **44**(2), pp. 968–977.

[78] Wauthle, R., Vrancken, B., Beynaerts, B., Jorissen, K., Schrooten, J., Kruth, J. P., and Van Humbeeck, J., 2015, "Effects of build orientation and heat treatment on the microstructure and mechanical properties of selective laser melted Ti6Al4V lattice structures," Addit. Manuf., **5**, pp. 77–84.

[79] Lewandowski, J. J., and Seifi, M., 2016, "Metal Additive Manufacturing: A Review of Mechanical Properties," Annu. Rev. Mater. Res., **46**(1), pp. 151–186.

[80] Rosenthal, I., Stern, A., and Frage, N., 2014, "Microstructure and Mechanical Properties of AlSi10Mg Parts Produced by the Laser Beam Additive Manufacturing (AM) Technology," Metallogr. Microstruct. Anal., **3**(6), pp. 448–453.

[81] Frazier, W. E., 2014, "Metal additive manufacturing: A review," J. Mater. Eng. Perform., **23**(6), pp. 1917–1928.

[82] Safdar, A., 2012, "A study on electron beam melted Ti-6Al-4V," Thesis, Lund University.

[83] Hrabe, N., and Quinn, T., 2013, "Effects of processing on microstructure and mechanical properties of a titanium alloy (Ti-6Al-4V) fabricated using electron beam melting (EBM), Part 2: Energy input, orientation, and location," Mater. Sci. Eng. A, **573**, pp. 271–277.

[84] Hrabe, N., and Quinn, T., 2013, "Effects of processing on microstructure and mechanical properties of a titanium alloy (Ti-6Al-4V) fabricated using electron beam melting (EBM), part 1: Distance from build plate and part size," Mater. Sci. Eng. A, **573**, pp. 264–270.

[85] Sidambe, A. T., Todd, I., and Hatton, P. V., 2016, "Effects of build orientation induced surface modifications on the in vitro biocompatibility of electron beam melted Ti6Al4V," Powder Metall., **59**(1), pp. 57–65.

[86] Bruno, J., Rochman, A., and Cassar, G., 2017, "Effect of Build Orientation of Electron Beam Melting on Microstructure and Mechanical Properties of Ti-6Al-4V," J. Mater. Eng. Perform., **26**(2), pp. 692–703.

[87] Beuth, J., and Klingbeil, N., 2001, "The role of process variables in laser-based direct metal solid freeform fabrication," JOM, **53**(9), pp. 36–39.

[88] Beuth, J., Fox, J., Gockel, J., Montgomery, C., Yang, R., Qiao, H., Soylemes, E., Reeseewatt, P., Anvari, A., Narra, S., and Klingbeil, N., 2013, "Process mapping for qualification across multiple direct metal additive manufacturing processes," Proceedings of Solid Freeform Fabrication Symposium, Austin, pp. 655–665.

[89] Bontha, S., Klingbeil, N. W., Kobryn, P. A., and Fraser, H. L., 2009, "Effects of process variables and size-scale on solidification microstructure in beam-based fabrication of bulky

3D structures," Mater. Sci. Eng. A, **513**–**514**(C), pp. 311–318.

[90] Bontha, S., Klingbeil, N. W., Kobryn, P. A., and Fraser, H. L., 2006, "Thermal process maps for predicting solidification microstructure in laser fabrication of thin-wall structures," J. Mater. Process. Technol., **178**(1–3), pp. 135–142.

[91] Gockel, J., Fox, J., Beuth, J., and Hafley, R., 2015, "Integrated melt pool and microstructure control for Ti-6Al-4V thin wall additive manufacturing," Mater. Sci. Technol., **31**(8), pp. 912–916.

[92] Gockel, J., Beuth, J., and Taminger, K., 2014, "Integrated control of solidification microstructure and melt pool dimensions in electron beam wire feed additive manufacturing of Ti-6Al-4V," Addit. Manuf., **1**–**4**, pp. 119–126.

[93] Kempen, K., Thijs, L., Yasa, E., Badrossamay, M., and Kruth, J.-P., 2011, "Process Optimization and Microstructural Analysis for Selective Laser Melting of AlSi10Mg," Solid Freeform Fabrication Symposium, Austin.

[94] Brandl, E., Heckenberger, U., Holzinger, V., and Buchbinder, D., 2012, "Additive manufactured AlSi10Mg samples using Selective Laser Melting (SLM): Microstructure, high cycle fatigue, and fracture behavior," Mater. Des., **34**, pp. 159–169.

[95] Gong, W., Qi, J., Wang, Z., Chen, Y., Jiang, J., Wang, Z., and Qi, Y., 2017, "Microstructrue and Mechanical Properties of Selective Laser Melting AlSi10Mg," 3rd International Symposium of Space Optical Instruments and Applications: Beijing, China June 26 - 29th 2016, Springer International Publishing, pp. 113–120.

[96] Aboulkhair, N. T. N., Tuck, C., Ashcroft, I., Maskery, I., and Everitt, N. M., 2015, "On the precipitation hardening of selective laser melted AlSi10Mg," Mater. Trans. A, **46**(8), pp. 3337–3341.

[97] Matyja, H., Giessen, B. C., and Grant, N. J., 1968, "Dendrite Spacing in Splat-Cooled Al Alloys," J. Inst. Met., **96**(30).

[98] Dehoff, R. R. R., Kirka, M. M. M., List, F. A. F., Unocic, K. A., and Sames, W. J., 2014, "Crystallographic texture engineering through novel melt strategies via electron beam melting: Inconel 718," Mater. Sci. Technol., **31**(8), pp. 939–944.

[99] Dehoff, R. R., Kirka, M. M., Sames, W. J., Bilheux, H., Tremsin, A. S., Lowe, L. E., and Babu, S. S., 2015, "Site specific control of crystallographic grain orientation through electron beam additive manufacturing," Mater. Sci. Technol., **31**(8), pp. 931–938.

[100] Körner, C., Helmer, H., Bauereiß, A., and Singer, R. F., 2014, "Tailoring the grain structure of IN718 during selective electron beam melting," MATEC Web of Conferences.

[101] Liu, W., and DuPont, J., 2004, "Effects of melt-pool geometry on crystal growth and microstructure development in laser surface-melted superalloy single crystals: Mathematical modeling of single-crystal growth in a melt pool (part I)," Acta Mater., **52**(16), pp. 4833–4847.

[102] Francis, Z., "Effects of Beam Spot Size on Keyholing in Additive Manufacturing," Internal Report, Carnegie Mellon University.

[103] Cunningham, R., Narra, S., Ozturk, T., Beuth, J., and Rollett, A., 2016, "Evaluating the Effect of Processing Parameters on Porosity in Electron Beam Melted Ti-6Al-4V via Synchrotron X-ray Microtomography," JOM, **68**(3), pp. 765–771.

[104] King, W. E., Barth, H. D., Castillo, V. M., Gallegos, G. F., Gibbs, J. W., Hahn, D. E., Kamath, C., and Rubenchik, A. M., 2014, "Observation of keyhole-mode laser melting in laser powder-bed fusion additive manufacturing," J. Mater. Process. Technol., **214**(12), pp. 2915–2925.

[105] Francis, Z., and Beuth, J., 2016, "The Effect of Beam Spot Size on Melt Pool Geometry in Direct Metal Additive Manufacturing Processes," Materials Science & Technology (MS&T).

[106] ASTM Standard E112-13, 2013, Standard test methods for determining average grain size, West Conshohocken, Pennsylvania.

[107] Zhou, J., and Tsai, H.-L., 2007, "Porosity Formation and Prevention in Pulsed Laser Welding," J. Heat Transfer, **129**(8), p. 1014.

[108] Murr, L. E., Esquivel, E. V., Quinones, S. A., Gaytan, S. M., Lopez, M. I., Martinez, E. Y., Medina, F., Hernandez, D. H., Martinez, E., Martinez, J. L., Stafford, S. W., Brown, D. K., Hoppe, T., Meyers, W., Lindhe, U., and Wicker, R. B., 2009, "Microstructures and mechanical properties of electron beam-rapid manufactured Ti-6Al-4V biomedical prototypes compared to wrought Ti-6Al-4V," Mater. Charact., **60**(2), pp. 96–105.

[109] Olsson, U., 2005, "Confidence Intervals for the Mean of a Log-Normal Distribution."

[110] Cunningham, R., Narra, S. P., Beuth, J., and Rollett, A. D., 2016, "Effect of processing parameters on mechancial properties of EBM Ti-6Al-4V," Conference Presentation, TMS, Nashville.

[111] Lütjering, G., 1999, "Property optimization through microstructural control in titanium and aluminum alloys," Mater. Sci. Eng. A, **263**(2), pp. 117–126.

[112] Clymer, D., Beuth, J., and Cagan, J., 2016, "Additive manufacturing process design," Solid Freeform Fabrication 2016: Proceedings of the 27th Annual International, Austin, pp. 1976–1984.

[113] ABAQUS, 2012, "ABAQUS Documentation."

[114] "EOS M 290 - industrial 3D printed parts from metal materials" [Online]. Available: https://www.eos.info/eos-m290. [Accessed: 15-May-2017].

[115] Mills, K. C., 2002, Recommended Values of Thermophysical Properties for Selected Commercial Alloys, Elsevier.

[116] "ASM Alloy Phase Diagram Database™ - ASM International" [Online]. Available: http://www.asminternational.org/home/-/journal_content/56/10192/15469013/DATABASE. [Accessed: 02-Mar-2017].

[117] Dobranich, D., and Dykhuizen, R. C., 1998, Scoping Thermal Calculation of the LENS Process.

[118] Gratzke, U., Kapadia, P. D., Dowden, J., Kroos, J., and Simon, G., 2000, "Theoretical approach to the humping phenomenon in welding processes," J. Phys. D. Appl. Phys., **25**(11), pp. 1640–1647.

[119] Yadroitsev, I., Gusarov, A., Yadroitsava, I., and Smurov, I., 2010, "Single track formation in selective laser melting of metal powders," J. Mater. Process. Technol., **210**(12), pp. 1624–1631.

[120] Cunningham, R., Narra, S. P., Montgomery, C., Beuth, J., and Rollett, A. D., 2016, "Synchrotron-Based X-Ray Microtomography Characterization of the Effect of Processing Variables on Porosity Formation in Laser Power-Bed Additive Manufacturing of Ti-6Al-4V," JOM, **69**(3), pp. 479–484.

[121] Tang, M., Pistorius, P. C., and Beuth, J., 2015, "Geometric Model To Predict Porosity of Part Produced," Mater. Sci. Technol., pp. 129–136.

[122] Aboulkhair, N. T., Maskery, I., Tuck, C., Ashcroft, I., and Everitt, N. M., 2016, "On the formation of AlSi10Mg single tracks and layers in selective laser melting: Microstructure and nano-mechanical properties," J. Mater. Process. Technol., **230**, pp. 88–98.

[123] Kempen, K., Thijs, L., and Yasa, E., 2014, "Process optimization and microstructural analysis for selective laser melting of AlSi10Mg; 2011."

[124] Grosselle, F., Timelli, G., Bonollo, F., and Molina, R., 2009, "Correlation between microstructure and mechanical properties of Al-Si diecast engine blocks," Metall. Sci. Technol., **27**(2), pp. 959–965.

[125] Francis, Z., 2016, "Development of 2D heat source model in ABAQUS for beam based additive manufacturing," Internal Report, Carnegie Mellon University.

[126] "Inconel Alloy 718 - UNS N07718 B50TF14, B50TF15 | Altemp Alloy" [Online]. Available: http://www.altempalloys.com/inconel-718.html. [Accessed: 24-Mar-2017].

[127] Montgomery, C., Beuth, J., Sheridan, L., and Klingbeil, N., 2015, "Process Mapping of Inconel 625 in Laser Powder Bed Additive Manufacturing," Solid Free. Fabr. Symp., pp. 1195–1204.

[128] "Metallographic Etchants" [Online]. Available: http://www.metallographic.com/Etchants/Etchants.htm. [Accessed: 14-Apr-2017].

[129] Elmer, J., Giedt, W., and Eager, T. W., 1990, "The Transition from Shallow to Deep Penetration during Electron Beam Welding," Weld. J., **69**(5), pp. 167–176.

[130] Bachmann, F., Hielscher, R., and Schaeben, H., 2010, "Texture Analysis with MTEX – Free and Open Source Software Toolbox," Solid State Phenom., **160**(FEBRUARY 2010), pp. 63–68.

[131] Mainprice, D., Bachmann, F., Hielscher, R., and Schaeben, H., 2015, "Descriptive tools for the analysis of texture projects with large datasets using MTEX: strength, symmetry and components," Geol. Soc. London, Spec. Publ., **409**(1), pp. 251–271.

[132] Bachmann, F., Hielscher, R., and Schaeben, H., 2011, "Grain detection from 2d and 3d

EBSD data-Specification of the MTEX algorithm," Ultramicroscopy, **111**(12), pp. 1720–1733.

[133] Jorge-Badiola, D., Iza-Mendia, A., and Gutiérrez, I., 2007, "Evaluation of intragranular misorientation parameters measured by EBSD in a hot worked austenitic stainless steel," J. Microsc., **228**(3), pp. 373–383.

[134] Francis, Z., 2016, "Process Mapping of Melt Pool Geometry in Laser Melted SS 316 and SS 17-4," Internal Report, Carnegie Mellon University.

[135] Fisher, B., 2016, "Process Mapping of Melt Pool Geometry at Different Preheat Temperatures in Laser Melted Ti-6Al-4V," Internal Report, Carnegie Mellon University.

[136] Christiansen, D., 2015, "Process Mapping of Melt Pool Geometry in Laser Melted Ti-6A-4V," Internal Report, Carnegie Mellon University.

[137] LeMon, G., 2015, "Process Mapping of Melt Pool Geometry in Laser Melted CoCr," Internal Report, Carnegie Mellon University.

[138] Kalapanidas, E., and Avouris, N., 2003, "Machine Learning algorithms : a study on noise sensitivity," 1st Balcan Conf. Informatics, pp. 356–365.

Appendix A Polishing Procedures

The polishing recipes for Buehler's auto-polisher are provided by Buehler and for Struer's, the procedures taken from ASTM standard for metallography and modified as needed for Struer's auto-polisher

Titanium Alloy (Ti-6Al-4V)

Buehler's Auto-polisher

Polishing Cloth	Suspension and Particle Size
320 Grit	Water (Lubricant)
UltraPol™ Cloth	9 µm diamond spray with activated master met
MicroCloth®	~0.05 Mastermet® Colloidal Silica

Aluminum Alloy (AlSi10Mg)

Struer's Auto-polisher

Polishing Cloth	Suspension and Particle Size
SiC foil + MD - Gekko	Water (Lubricant)
MD - Largo	9 µm DiaPro Allegro/Largo
MD - Mol	3 µm DiaPro Mol R
MD - Nap	1 µm DiaPro Nap R
MD - Chem	0.04 µm OP-U + water (last 15 sec)

Buehler's Auto-polisher

Polishing Cloth	Suspension and Particle Size
320 Grit	Water (Lubricant)
UltraPad	9 µm diamond spray with activated master met
TriDent	3 µm diamond spray with activated master met
TriDent	1 µm diamond spray with activated master met
ChemoMet	0.02 - 0.06 µm Mastermet® Colloidal Silica

Nickel Super alloy Inconel 718 (IN718)

Buehler's Auto-polisher

Polishing Cloth	Solution
240 Grit	Water (Lubricant)
Apex Hercules S	9 µm diamond spray
TriDent	3 µm diamond spray
ChemoMet	0.02 - 0.06 µm Mastermet® Colloidal Silica

Appendix B Melt Pool Geometry Measurements for Inconel 718

P (W)	V (mm/s)	Avg. Width (Above) (µm)	Standard Deviation (µm)	C/S Width (µm)	C/S Depth (µm)	C/S Area (mm^2)
100	200	177	13	190	53	7.8E-03
150	200	248	5	270	157	2.6E-02
200	200	286	5	314	288	4.9E-02
250	200	319	9	353	433	7.2E-02
300	200	364	16	383	470	8.3E-02
370	200	391	11	411	595	1.1E-01
100	400	128	2	141	42	4.3E-03
150	400	178	4	178	63	8.2E-03
200	400	223	5	279	125	2.0E-02
250	400	269	6	294	186	3.5E-02
300	400	277	7	323	236	4.6E-02
370	400	275	6	301	327	5.9E-02
100	600	126	3	132	29	3.0E-03
150	600	145	3	151	43	5.0E-03
200	600	159	5	178	59	7.6E-03
250	600	196	5	204	110	1.6E-02
300	600	247	9	273	161	2.6E-02
370	600	264	17	311	194	3.2E-02
100	800	115	2	122	25	2.4E-03
150	800	130	3	141	37	4.0E-03
200	800	144	4	171	59	7.2E-03
250	800	159	5	180	61	8.1E-03
300	800	172	8	193	82	1.2E-02
370	800	181	5	203	145	2.0E-02
100	1000	92	2	103	22	1.8E-03
150	1000	110	3	123	34	3.0E-03
200	1000	123	2	143	43	4.5E-03
250	1000	145	4	159	68	8.1E-03
300	1000	164	3	180	75	1.0E-02
370	1000	182	3	202	96	1.4E-02
100	1200	95	2	101	21	1.5E-03
150	1200	108	2	118	30	2.8E-03
200	1200	113	3	113	40	3.5E-03
250	1200	130	3	165	39	4.3E-03
300	1200	152	2	170	79	9.7E-03
370	1200	168	3	184	97	1.3E-02
100	1400	96	2	107	20	1.3E-03

150	1400	115	2	122	25	2.2E-03
200	1400	125	2	135	34	3.3E-03
250	1400	131	3	136	51	5.1E-03
300	1400	143	3	166	61	7.1E-03
370	1400	168	3	169	85	1.0E-02